UNIVERSITY OF CALIFORNIA, SAN DIEGO

New insights into the origin, transport and behavior of noble gases: Examples from Monterey Bay, Costa Rica, Iceland, and the Central Indian Ridge

A dissertation submitted in partial satisfaction of the

requirements for the degree Doctor of Philosophy

in

Earth Sciences

by

Evelyn Fueri

Committee in charge:

Professor David R. Hilton, Chair
Professor Donna Blackman
Professor Kevin Brown
Professor Paterno Castillo
Professor Mark Thiemens

2010

ProQuest LLC
789 East Eisenhower Parkway
P.O. Box 1346
Ann Arbor, MI 48106-1346

The dissertation of Evelyn Fueri is approved, and it is acceptable in quality and form for publication on microfilm and electronically:

_____

_____

_____

_____

_____
Chair

University of California, San Diego

2010

DEDICATION

This dissertation is dedicated to my parents,

Anna and Heinz Füri.

TABLE OF CONTENTS

LIST OF FIGURES

LIST OF TABLES

ACKNOWLEDGMENTS

There are many people I would like to thank for their help and guidance during this thesis work. First and foremost is my advisor, David Hilton, who gave me the opportunity to work in his lab and travel to many exotic places around the world for fieldwork and scientific conferences, and who provided the encouragement and advice necessary for me to proceed through the doctoral program and complete my dissertation.

I would like to thank my committee members Donna Blackman, Kevin Brown, Pat Castillo, and Mark Thiemens for their constructive comments on my thesis and their helpful suggestions at our various meetings over the last few years. I would like to acknowledge all my co-authors for their contributions to the work presented in this dissertation; thanks to Kevin Brown, Mike Tryon, Gary McMurtry, Warner Brückmann, Geoff Wheat, Sæmi Halldórsson, Pete Barry, Doshik Hahm, Toby Fischer, Karl Grönvold, Bramley Murton, Jérome Dyment, Christophe Hémond, and James Day for their valuable comments and suggestions. I am also grateful to Bruce Deck and Martin Wahlen for their assistance in carbon isotope analyses.

I was fortunate to participate in several fieldtrips and research cruises to collect samples for the work presented in this dissertation. I would like to thank Carlos Ramirez, Guillermo Alvarado, Karl Grönvold, James Day, Toby Fischer, Zach Sharp, and Kareen Prade for assistance in the field. Many thanks to the captains and crews of the R/Vs *Point Lobos*, *Revelle*, *Melville*, and *Atlantis*, as well as all the scientists who participated in the cruises.

The Fluids and Volatile Laboratory has been a stimulating work environment where I have been fortunate to find myself surrounded by wonderful people. I am immensely grateful to Diana de Leeuw, who taught me everything I know about extracting and analyzing noble gases and who was always available to answer questions. Many thanks to Lillie Jaffe, Dana

Vukajlovich, Pete Barry, Sæmi Halldórsson, and Doshik Hahm for their important support and good company. Special thanks to my labmate and roommate Mary Ray for sharing the joy and pain, and for being an amazing friend!

I was very fortunate to form many wonderful new friendships in San Diego and to keep up old friendships from high school and the ETH. Thanks to all my great friends for your encouragement, patience and support!

And finally, I would like to thank my parents, Anna and Heinz, for always being supportive of my non-conventional career choice, even when they didn't always quite understand what I was doing. I couldn't have done it without you!

Chapter II appeared in full as Füri, E., D.R. Hilton, K.M. Brown, and M.D. Tryon (2009), Helium systematics of cold seep fluids at Monterey Bay, California, USA: Temporal variations and mantle contributions, *Geochemistry Geophysics Geosystems*, 10, Q08013, doi:10.1029/2009GC002557. The dissertation author was the primary investigator and lead author of this paper and conducted all the analyses presented herein.

Chapter III appeared in full as Füri, E., D.R. Hilton, M.D. Tryon, K.M. Brown, G.M. McMurtry, W. Brückmann, and C.G. Wheat (2010), Carbon release from submarine seeps at the Costa Rica fore-arc: Implications for the volatile cycle at the Central America convergent margin, *Geochemistry Geophysics Geosystems,* doi:10.1029/2009GC002810, in press. The dissertation author was the primary investigator and lead author of this paper and conducted all the analyses presented herein.

Chapter IV has been submitted, in full, for publication to *Geochimica et Cosmochimica Acta* as Füri, E., D.R. Hilton, S.A. Halldórsson, P.H. Barry, D. Hahm, T.P. Fischer, and K. Grönvold, Decoupling of the He and Ne isotope systematics of the Icelandic mantle; the role of He depletion, magma mixing, and degassing fractionation. The dissertation author was the primary investigator and lead author of this paper and conducted all the analyses presented herein.

VITA

2004	Master of Science ETH/MSc ETH Swiss Federal Institute of Technology (ETH) Zurich, Switzerland
2004-2010	Graduate Research Assistant Scripps Institution of Oceanography, University of California, San Diego
2005-2010	Teaching Assistant Scripps Institution of Oceanography, University of California, San Diego
2010	Doctor of Philosophy, Earth Sciences Scripps Institution of Oceanography, University of California, San Diego

PUBLICATIONS

Hilton, D.R., C. Ramirez, R.A. Mora Amador, T.P. Fischer, E. Füri, P.H. Barry, and A.M. Shaw, Monitoring of temporal and spatial variations in fumarole helium and carbon dioxide characteristics at Poas and Turrialba volcanoes, Costa Rica (2001-2009), submitted for publication in *Geochemical Journal,* 2010.

Füri, E., D.R. Hilton, S.A. Halldórsson, P.H. Barry, D. Hahm, T.P. Fischer, and K. Grönvold, Decoupling of the He and Ne isotope systematics of the Icelandic mantle; the role of He depletion, magma mixing, and degassing fractionation, submitted for publication in *Geochimica et Cosmochimica Acta*, 2009.

Füri, E., D.R. Hilton, M.D. Tryon, K.M. Brown, G.M. McMurtry, W. Brückmann, and C.G. Wheat (2010) Carbon release from submarine seeps at the Costa Rica fore-arc: Implications for the volatile cycle at the Central America convergent margin, *Geochemistry Geophysics Geosystems*, doi:10.1029/2009GC002810, in press.

Füri, E., D. R. Hilton, K. M. Brown, and M. D. Tryon (2009), Helium systematics of cold seep fluids at Monterey Bay, California, USA: Temporal variations and mantle contributions, *Geochemistry Geophysics Geosystems*, 10, Q08013, doi:10.1029/2009GC002557.

Fischer, T.P., P. Burnard, B. Marty, D.R. Hilton, E. Füri, F. Palhol, Z.D. Sharp, and F. Mangasini (2009) Upper-mantle volatile chemistry at Oldoinyo Lengai volcano and the origin of carbonatites, *Nature*, 459(7243), 77-80.

Füri, E. and the KNOX11RR Scientific Party (2008), Sampling and surveying ridge-hotspot interaction on the Central Indian Ridge, 19°S: Cruise KNOX11RR, *InterRidge News*, 17, 28-29.

PRESENTATIONS

Füri E., D.R. Hilton, K.M. Brown, and M.D. Tryon, (2009), Towards Quantifying Volatile Fluxes and Origins from the Costa Rican Fore-Arc Using Novel Submarine Instrumentation, *Margins TEI: Volatiles in the Subduction Factory*, Mt. Hood (OR), USA.

Füri E., D.R. Hilton, J. Dyment, C. Hémond, and B. Murton, (2009), Ridge-hotspot interaction at the Central Indian Ridge, 20°S: New helium isotope results, *Goldschmidt Conference*, Davos, Switzerland.

Füri E., D.R. Hilton, and K. Grönvold, (2009), Decoupling of noble gases in the Icelandic mantle: new insights from basalts of the neovolcanic zone, *DINGUE Noble Gas workshop*, Nancy, France.

Füri E., D.R. Hilton, and K. Grönvold, (2008), Decoupling of noble gases in the Icelandic mantle: new insights from basalts of the neovolcanic zone, *IAVCEI 2008 – General Assembly*, Reykjavik, Iceland.

Füri E., D.R Hilton, M.D. Tryon, and K.M. Brown, (2007), Towards Quantifying Volatile Fluxes and Origins from the Costa Rica Fore-Arc Using Novel Submarine Instrumentation, *Workshop to Integrate Subduction Factory and Seismogenic Zone Studies in Central America*, Heredia, Costa Rica.

Füri E., D.R. Hilton, M.D. Tryon, and K.M. Brown, (2007), Temporal Controls on the Release of Mantle and Crustal Volatiles from Cold Fluid Seeps at Monterey Bay, California, USA, *International Conference on Evolution, Transfer and Release of Magmas and Volcanic Gases*, Taipei, Taiwan.

Füri E., D.R. Hilton, K.M Brown, and M.D. Tryon, (2005), Helium and Carbon Isotope Systematics of Cold Seep Fluids at Monterey Bay (California, USA), *AGU fall meeting*, San Francisco, USA.

FIELDS OF STUDY

Major Field: Geochemistry

Studies in Isotope Geochemistry
Professors D. Lal, J.D. Macdougall, R. Keeling

Studies in Geology
Professors D.R. Hilton, J.W. Hawkins, P.R. Castillo, S.C. Cande, C.D. Charles

Studies in Marine Chemistry
Professors L. Aluwihare, K. Barbeau, A.Dickson

Studies in Physical Oceanography
Professors M. Hendershott, L.D. Talley, P. Robbins

Studies in Biological Oceanography
Professor P.J. Franks

ABSTRACT OF THE DISSERTATION

New insights into the origin, transport and behavior of noble gases:
Examples from Monterey Bay, Costa Rica, Iceland, and the Central Indian Ridge

by

Evelyn Fueri
Doctor of Philosophy in Earth Sciences
University of California, San Diego, 2010
Professor David R. Hilton, Chair

The study of volatiles in both subaerial and submarine terrestrial samples is central to understanding the compositions of, and interactions between, the mantle-crust-atmosphere system. This dissertation focuses on the origin, transport and behavior of noble gases at four different geologic settings – a) the San Andreas Fault Zone (SAFZ), a transform plate boundary, b) the Costa Rica margin, a convergent plate boundary, c) Iceland, a ridge-centered hotspot, and d) the Central Indian Ridge, a mid-ocean ridge segment near an off-axis hotspot.

Following a brief introduction to the utility of noble gases as geochemical tracers (Chapter I), the helium characteristics of submarine fluid seepage in a strike-slip setting associated with the SAFZ are discussed in Chapter II. Cold seep sites at Extrovert Cliff

(Monterey Bay) were chosen for deployment of submarine flux meters and continuous sampling of fluids over several weeks. We assess the origin of dissolved noble gases in the seep fluids, and determine the cause of any temporal variations of the volatile characteristics.

Chapter III focuses on the He-CO_2 isotope and abundance systematics of submarine cold seep fluids emanating at the Costa Rica fore-arc. We evaluate the origin of dissolved helium and carbon in the fluids, and we estimate the total flux of carbon through fluid venting at mound structures at the fore-arc in order to better constrain the carbon mass balance for the Central America convergent margin.

Chapter IV examines the He-Ne systematics of geothermal fluids and the He-Ne-Ar isotope and relative abundance characteristics of subglacial glasses from the neovolcanic zones and older parts of the crust in Iceland. We investigate the processes contributing to the apparent decoupling of the He and Ne isotope systematics observed previously on the Reykjanes Peninsula and question whether this phenomenon is common to other parts of the neovolcanic zones.

Chapter V investigates the postulated interaction between the Central Indian Ridge (CIR) and the Réunion hotspot, located ~1100 km off-axis to the west. The CIR passed over the hotspot 34 Ma ago, and the goal of this study is to test if CIR basalts still record a Réunion-like helium isotope signature.

Chapter I Introduction

The study of elemental and isotope compositions of noble gases (He, Ne, Ar, Kr, and Xe), in combination with major volatiles (e.g., CO_2), in both subaerial and submarine terrestrial samples is central to understanding the origin and evolution of Earth's atmosphere, the history of planetary differentiation and degassing, and the chemical structure of the mantle. Fumarolic gas discharges, bubbling hot springs, groundwaters, seep fluids, as well as quenched basalt glasses (submarine and subglacial in origin) and various minerals (e.g., olivine, pyroxene) allow access to one of the major geochemical reservoirs of the solid Earth - the mantle - and, through detailed analyses of their volatile isotope and abundance characteristics, have provided fundamental constraints on the compositions of, and interactions between, the mantle-crust-atmosphere system (Allègre et al., 1987). In addition, noble gases are key tools for monitoring earthquake and volcanic activities (e.g., Tedesco et al., 1998; Italiano and Martinelli, 2001) as well as for studying groundwater ages and flow dynamics (e.g., Tolstikhin and Kamenski, 1969; Schlosser et al., 1988; Stute et al., 1995), paleoclimate conditions (Mazor, 1972; Andrews and Lee, 1979), ocean circulation (Jenkins and Clarke, 1976), surface exposure ages (Cerling and Craig, 1994), and tectonic uplift histories (Bruno et al., 1997).

Noble gases are sensitive tracers of volatile sources and geochemical processes due to their 1) scarcity in the solid Earth, 2) inertness, incompatibility, and volatility, and 3) diagnostic isotope ratios in different terrestrial reservoirs (e.g., mantle, crust, and atmosphere). During mantle melting, noble gases will strongly partition into the melt phase (Marty and Lussiez, 1993); subsequently, due to their low solubilities in basaltic magmas (Jambon et al., 1986), exsolution of a vapor phase (such as CO_2) during decompression of an ascending melt will result in rapid loss of noble gases from the melt phase. Thus, noble gases are efficiently

outgassed from the solid Earth, and their passage from mantle to atmosphere is usually considered to be a one-way journey. In this respect they contrast with, and complement, most other geochemical tracers such as CO_2, which appears to be recycled to the (deep) mantle at subduction zones (Hilton et al., 2002; Shaw et al., 2003; de Leeuw et al., 2007). Consequently, noble gas isotope systematics are particularly useful for identifying different terrestrial reservoirs from which volatiles are derived, and for tracing physical processes that may have altered the intrinsic volatile characteristics during transfer to the surface.

In terms of mantle processes, noble gases are a powerful tool to resolve problems associated with magma source history and evolution, degassing processes and mixing between different reservoirs. However, since all magmas lose a fraction of their primary volatile inventory prior to and during eruption, and magmatic systems at depth are inaccessible, we are limited in our understanding of volatile compositions of different mantle reservoirs. Numerous studies have established that mid-ocean ridge basalts (MORB) have higher ratios of radiogenic to non-radiogenic (primordial) isotopes (e.g., $^{4}He/^{3}He$, $^{21}Ne/^{22}Ne$, $^{40}Ar/^{36}Ar$) than ocean island basalts (OIB) (Craig and Lupton, 1976; Sarda et al., 1988; Burnard et al., 1997; Graham, 2002). This is inferred to be the result of more extensive outgassing of the MORB reservoir leading to lower time-integrated $^{3}He/(U+Th)$ and $^{22}Ne/(U+Th)$ ratios compared to the source of OIB. Thus, addition of radiogenic and nucleogenic noble gases (i.e., ^{4}He, ^{21}Ne, and ^{40}Ar) over Earth history has more significantly diluted the primordial noble gas isotope characteristics of the MORB reservoir. In this scenario, noble gas abundances in the OIB source are expected to be higher than in the MORB source. However, a long-standing problem is that many OIB samples have lower helium concentrations than MORB lavas (Porcelli and Ballentine, 2002). In order to explain this discrepancy - which has been termed the “helium paradox” (Anderson, 1998) - it has been proposed that extensive near-surface degassing prior

to and/or during eruption may account for the strong helium depletion in many OIB samples (e.g., Hilton et al., 1997; Hilton et al., 2000; Gonnermann and Mukhopadhyay, 2007). Alternatively, volatiles may be fractionated during partial melting due to different crystal-melt partition coefficients (Hopp and Trieloff, 2008). In this model, helium is depleted relative to neon and argon in OIB parental melts due to a more compatible behavior during partial melting. Consequently, volatile concentrations and elemental ratios observed in MORB and OIB samples may mainly be a reflection of physical processes such as melting, melt-vapor partitioning, and diffusion that can fractionate one volatile element from another, so that determining the primary volatile abundances in different mantle reservoirs is not possible through direct measurements of volcanic materials.

Assessing volatile abundances in the mantle, as well as the volatile fluxes between the mantle and the atmosphere, is critical for understanding the evolutionary history of the mantle and atmosphere. While (light) noble gases appear to be efficiently degassed from the oceanic crust and sediments during subduction (Staudacher and Allègre, 1988; Moreira et al., 2003), subduction zones may act as a conduit for the transfer of carbon into the mantle (Kerrick and Connolly, 2001). Previous studies at the Central America convergent margin have shown that the carbon output flux via volcanism at the volcanic front is only 12-18 % of the carbon which is potentially available by input via the trench (Hilton et al., 2002; Shaw et al., 2003; de Leeuw et al., 2007). This result implies that carbon is efficiently recycled to the (deeper) mantle, i.e., the mantle beyond the zone of arc magma generation, or, alternatively, significant losses of carbon occur at the fore-arc or back-arc. In order to complete a realistic carbon mass balance for subduction zones, it is essential to constrain volatile fluxes at these fore-arc and back-arc regions. Such measurements are critical to evaluate whether volatiles are transferred

to the deep mantle or more efficiently recycled from the subducting slab directly to the atmosphere and hydrosphere.

Volatiles are lost from Earth's mantle predominantly by volcanic and magmatic activity; however, anomalously high concentrations of helium, radon, hydrogen, carbon dioxide, and several other volatiles have also been reported for fluids and gases sampled in regions of amagmatic seismic activity and extensive faulting (King, 1986; Toutain and Baubron, 1999). High He isotope values, i.e., $^{3}He/^{4}He$ ratios significantly greater than crustal production values, show that fault zones play an important role in transferring mantle-derived volatiles to the surface (Kennedy et al., 1997; Kulongoski et al., 2003). Furthermore, several authors have recognized variations in volatile concentrations or fluxes prior to or after earthquakes (Italiano et al., 2001; King, 1978, 1984; Sugisaki et al., 1996), suggesting that changes in fluid provenance, mixing and/or flow histories may be related to seismic events. However, any evaluation of a relationship between geochemical signals and seismic activity requires knowledge of baseline values, where signals are recorded in quiescent periods, together with a high-frequency or quasi-continuous sampling strategy aimed at capturing often transient earthquake-induced changes in the volatile record. Therefore, we have modified submarine fluid flow meters - Chemical and Aqueous Transport Meters (Tryon et al., 2000) and Optical Tracer Injection Systems (LaBonte et al., 2007) - by adding copper sampling coils, so that we can capture fluids for post-recovery analysis of their dissolved noble gas and CO_2 characteristics. The new sampling approach can be used to produce detailed time series records of volatiles in seep fluids and thus, presents an exciting means to better quantify fluxes of mantle volatiles in seismically active areas.

While lakes and groundwaters usually contain a portion of terrigenic (i.e., crustal and/or mantle-derived) noble gases, they are dominated by air-derived noble gases, from both

equilibration with the atmosphere and from excess air entrainment. Since the solubility of noble gases is governed by Henry's law, the equilibrium concentrations of noble gases can be viewed as proxies for the temperature, salinity, and atmospheric pressure (i.e., altitude) prevailing during air-water equilibration. Furthermore, noble gas abundance patterns can also be affected by fluid addition from other sources, or interaction with phases such as gas and oil within the subsurface. Once resolved, the different noble gas components in a water sample bear information on water residence times (i.e., ages), physical conditions prevailing at recharge, and noble gas fluxes from the continental crust and /or Earth's mantle (Kipfer et al., 2002).

The main objective of this dissertation is to study the origin, transport and behavior of volatiles (noble gases and CO_2) at four different geologic settings – a) the San Andreas Fault Zone (SAFZ), a transform plate boundary, b) the Costa Rica margin, a convergent plate boundary, c) Iceland, a ridge-centered hotspot, and d) the Central Indian Ridge, a mid-ocean ridge segment near an off-axis hotspot.

Chapter II discusses temporal variations of the helium characteristics of submarine fluid seepage in a strike-slip setting associated with the SAFZ. Cold seep sites at Extrovert Cliff in Monterey Bay were chosen for deployment of submarine flux meters and continuous sampling of fluids over several weeks. The aims of this study are to (1) establish the feasibility of the modified instrumentation in capturing and preserving submarine fluids for subsequent noble gas and CO_2 analyses and (2) assess if we can produce a near-continuous record of volatile concentrations and isotope variations in a natural system without recourse to conventional high-frequency sampling. We use our quasi-continuous He-Ne record to assess the origin of dissolved noble gases in seep fluids collected near strike-slip faults, as well as to determine the cause of any temporal variations of the volatile characteristics.

In order to obtain helium results on small quantities of fluids, we constructed a new dedicated noble gas extraction/purification system that can be interfaced directly to the preparation line of the noble gas mass spectrometer in the Fluids and Volatile Laboratory. The new ultra-high-vacuum extraction system gives a decrease of a factor of ~10 in the volume of fluid required for helium isotope analyses at the same analytical precision as obtained previously by conventional, 'off-line' noble gas extraction. Thus, we were able to significantly improve the time resolution of our long-term monitoring studies of volatile emissions at seep sites in Monterey Bay and Costa Rica.

Chapter III focuses on the He-CO_2 isotope and abundance systematics of submarine seep fluids emanating at the Costa Rica fore-arc. Seep fluids were sampled at two mud volcanoes (Mound 11 and Mound 12) in copper tubing attached to submarine flux meters operating in continuous pumping mode over a period of 12 months. Additional near-bottom water samples were collected within a tubeworm field at Jaco Scar during an Alvin reconnaissance dive. Fluid venting at the sampling sites is indicated by elevated methane concentrations in the water column (Bohrmann et al., 2002; Schmidt et al., 2005; Mau et al., 2006), high concentrations of dissolved methane and sulfide in sediment pore waters (Hensen et al., 2004; Linke et al., 2005), as well as chemosynthetic communities on the seafloor (e.g., bacterial mats, clams, and/or tubeworms). In this study, we evaluate the origin of dissolved helium and carbon in the seep fluids, and estimate the total flux of carbon (CO_2 plus methane) through fluid venting at mound structures at the Costa Rica fore-arc. The ultimate goals of this study are to better constrain the carbon mass balance for the Central America convergent margin, and hence to determine the fate of carbon during subduction zone processes.

Chapter IV examines the He-Ne systematics of geothermal fluids and the He-Ne-Ar isotope and relative abundance characteristics of subglacial glasses from Iceland. Previous

studies of Icelandic basalts have found trapped neon with a solar-like isotope composition accompanied by helium with $^{3}He/^{4}He$ ratios significantly lower than solar values (Harrison et al., 1999; Dixon et al., 2000; Trieloff et al., 2000; Moreira et al., 2001; Dixon, 2003). However, these studies focused on one segment of Iceland's neovolcanic zones (the Reykjanes Peninsula) whereas the highest $^{3}He/^{4}He$ ratios (i.e., minimal radiogenic He additions) are found in basalts erupted in Central Iceland (Condomines et al., 1983; Kurz et al., 1985; Breddam et al., 2000; Macpherson et al., 2005a) and Vestfirðir - the northwest peninsula of Iceland (Hilton et al., 1999; Ellam and Stuart, 2004). Therefore, in our study, we collected lavas and geothermal fluids from throughout the Icelandic neovolcanic zones and from older parts of the Icelandic crust in order to investigate the likely processes contributing to the apparent decoupling of the He and Ne isotope systematics observed previously on the Reykjanes Peninsula. We consider both elemental and isotopic heterogeneity of the Icelandic mantle source and the possibility of mixing between primordial and depleted/degassed MORB-like mantle components. In addition, we evaluate the effects of atmospheric contamination, nucleogenic isotope addition, and degassing, i.e., the processes that may have modified the primary volatile characteristics en route to the surface.

Chapter V investigates the postulated interaction between the Central Indian Ridge (CIR) and the Réunion hotspot, presently located ~1100 km off-axis to the west. We performed the first extensive helium isotope survey of the CIR axis between 16.7ºS and 20.6ºS, and the adjacent Gasitao, Three Magi, and Rodrigues ridges to the west of the CIR. The CIR passed over the hotspot 34 Ma ago, and the aims of this study are to test if CIR basalts still record a Réunion-like helium isotope signature at the present day, and, if this is the case, to understand the dynamics of mixing between different mantle components in this region of the Indian Ocean Basin. We also evaluate the effects of shallow-level magmatic

processes (i.e., post-eruptive radiogenic ^{4}He in-growth, degassing and fractional crystallization) that play an important role in the helium inventory of any oceanic basalt.

Chapter VI, the final chapter of the dissertation, summarizes the main findings and conclusions of each study, and addresses some of the issues regarding terrestrial noble gases that remain to be explored in future research.

Chapter II Helium systematics of cold seep fluids at Monterey Bay, California (USA): Temporal variations and mantle contributions

II.1 Abstract

We report helium isotope ratios ($^3He/^4He$) as well as helium and neon abundance results for submarine cold seep fluids from Extrovert Cliff in Monterey Bay, California. Samples were collected in copper tubing attached to submarine flux meters operating in continuous pumping mode. Following instrumentation recovery, the tubing was sectioned to produce for the first time a high-resolution time-series of dissolved He and Ne variations over a time-span of several days. Noble gas concentrations are variable, and appear affected by interaction with a hydrocarbon phase within the aquifer. However, it is still possible to resolve the He signal into components associated with air-equilibration, excess air entrainment, and terrigenic fluxes (both crustal and mantle-derived). The mantle He contribution reaches ~25-30 % in some samples (up to 2.3 R_A, where R_A = air $^3He/^4He$). Our quasi-continuous He-Ne record shows remarkable fluctuations over time-scales of only a few hours, and reflects the combined effects of gas stripping by hydrocarbons and an episodic input of mantle-derived fluids.

II.2 Introduction

Degassing of volatiles along seismically-active faults is a common observation. For example, elevated concentrations of helium, radon, hydrogen, mercury, and carbon dioxide have been measured along active fractures in the Earth's crust (King, 1986; Toutain and Baubron, 1999 and references therein). Moreover, several authors have recognized variations in volatile concentrations or fluxes prior to or after earthquakes (Italiano et al., 2001; King,

1978; King, 1984; Sugisaki et al., 1996). Whereas it is tempting to link these phenomena, any evaluation of a relationship between geochemical signals and seismic activity requires knowledge of baseline values, where signals are recorded in quiescent periods, together with a high-frequency or quasi-continuous sampling strategy aimed at capturing often transient earthquake-induced changes in the volatile record.

Helium isotope variations offer great potential as tracers of seismic- or magmatic-induced changes in the Earth's crust. This stems from the huge difference in isotopic values between mantle-derived helium (8 R_A (Graham, 2002), where $R_A = {}^3He/{}^4He$ of air) and helium produced in crustal lithologies by radioactive decay (~0.02 R_A; Andrews, 1985). Changes in crustal properties (e.g., permeability), induced by either seismic or magmatic activity, can potentially affect the balance of helium inputs from mantle and crustal endmembers, resulting in easily perceived variations in $^3He/^4He$ ratios sampled by crustal fluids, such as groundwaters and geothermal waters.

As a result of the sensitivity of helium to assigning fluid provenance, recent attention has turned to assessing its behavior in regions of amagmatic seismic activity and extensive faulting. A key study in this respect in that of Kennedy et al. (1997) who showed that deep pore fluids from the San Andreas Fault (SAF) have high $^3He/^4He$ ratios (up to 4 R_A). Kulongoski et al. (2003), who worked on the western Mojave River Basin located within 30km of the main SAF trace, also reported $^3He/^4He$ ratios significantly greater than crustal production values. These observations indicate that significant fluxes of mantle-derived helium can occur throughout this region of active faulting. Significantly, the flux of helium associated with the SAF appears to be affected by seismic activity, as demonstrated by variations in soil-gas helium concentrations along the fault zone prior to a number of earthquakes (Reimer, 1984; Reimer, 1990). Therefore, if helium isotopes are to realize their full potential as precursors of seismic activity, a new sampling approach is required in order to

produce a near-continuous record of the He isotope characteristics of crustal fluids associated with active faults.

To this end, we address here the helium isotope characteristics of submarine fluid seepage in a strike-slip setting associated with the SAF. The aims of this study are to (1) establish the feasibility of new instrumentation in capturing and preserving submarine fluids for subsequent He isotope analysis, and (2) assess if we can produce a near-continuous record of helium isotope changes in a natural system without recourse to high frequency (and expensive) sampling. For the current study, cold seep sites at Extrovert Cliff in Monterey Bay were chosen for instrumentation deployment and sampling of fluids for their He characteristics. We present a unique quasi-continuous record of the $^{3}He/^{4}He$ ratio over a time-span of several days. We show that the He volatile chemistry of deeply-rooted cold seeps associated with strike-slip faults fluctuates remarkably over time-scales of only a few hours due to the combined effects of variable degrees of noble gas stripping by a hydrocarbon phase in the subsurface and an episodic input of mantle-derived fluids.

II.3 Hydrogeology

Monterey Bay is located within the tectonically-active, roughly 100-km wide, transform plate boundary between the Pacific and North American plates. Tectonic activity in the Monterey Bay region is transpressional to accommodate the oblique convergence of the the two plates (Greene, 1990), which are separated by right-lateral strike-slip faults including the San Andreas, Ascension, San Gregorio, and Monterey Bay fault zones. The occurrence of recent earthquakes within the bay (Greene, 1977; Greene, 1990), together with the disruption of surficial modern mud on the seafloor (Eittreim et al., 2002), shows that these faults are presently active.

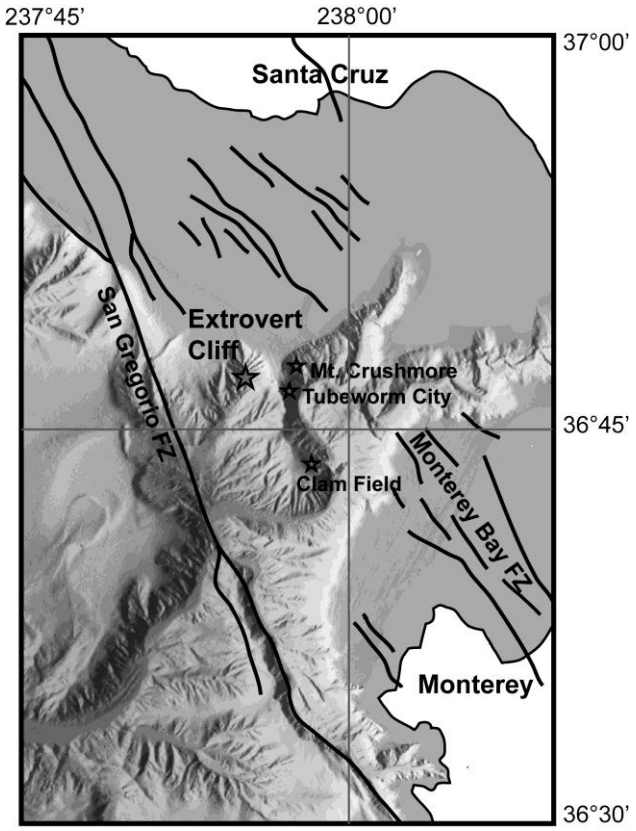

Figure II.1: Bathymetric map of Monterey Bay, California, indicating the location of the cold seep site sampled in this study (Extrovert Cliff) and other active seep sites (Mt. Crushmore, Tubeworm City, and Clam Field) in relation to the San Gregorio and Monterey Bay Fault zones (FZ) (Greene, 1977). Multibeam bathymetry is provided by the Monterey Bay Aquarium Research Institute (MBARI).

There are numerous fluid seeps on the continental slope of Monterey Bay at water depths between 1000-1500m. These are associated with the San Gregorio and Monterey Bay fault zones (Fig. II.1) (Greene et al., 1999; Orange et al., 1999). Greene et al. (1993) proposed that fluid seepage at these various sites within the bay results from a) dewatering of compressed sediments related to the modest compressional component of the Pacific-North America plate motion, b) artesian flow within a confined aquifer (i.e., the Monterey and Purisima Formations) that is recharged in the Santa Cruz mountains, and c) hydrocarbon generation at depth within the organic-rich Monterey Formation.

Previous studies of the pore water chemistry at cold seep sites in Monterey Bay have shown that fluids at most sites are enriched in sulfide, methane and CO_2 (Barry et al., 1997; Gieskes et al., 2005; Martin et al., 1990). Low $\delta^{13}C_{DIC}$ (dissolved inorganic carbon) values in the pore waters result from the production of ^{13}C-depleted bicarbonate by anaerobic oxidation of ascending methane. Furthermore, low $\delta^{13}C_{CH4}$ values (<-70‰; Martin et al., 1997) suggest that methane in Monterey Bay pore fluid samples is largely of microbial origin. However, there seems to be a distinctive contribution of a thermogenic methane component at some seeps, most likely derived from the organic-rich Monterey Formation or Santa Cruz Mudstone (Lorenson et al., 2002; Martin et al., 1997; Stakes et al., 1999). Furthermore, the thermogenic hydrocarbon component suggests potential input of deep fluid from >~2km depth (assuming a geothermal gradient of ~50°C/km and a temperature of 100°C required for thermal degradation of organic matter) (Martin et al., 1997). A deep origin of some seep fluids has also been suggested by Rathburn et al. (2003) on the basis of elevated concentrations of chloride, calcium, and lithium in pore fluids.

In this study, we target the Extrovert Cliff site in Monterey Bay (N36°46.6' W122°05.1') which is a prominent feature at ~950m water depth with a lineament of distinctive seeps showing evidence of advective fluid flow (Fig. II.1). Fluids are venting from an area overlying a young slide scar between the San Gregorio and Monterey Bay fault zones. The seeps are characterized by "blow-out" holes surrounded by chemosynthetic communities, including bacterial mats and associated macrofauna such as vesicomyid clams (Martin et al., 2004; Rathburn et al., 2003).

LaBonte et al. (2007) suggested that fluids at Extrovert Cliff are derived mainly from an overpressured confined aquifer and are channeled upward through a permeable fracture, as indicated by the correlation between observed seep flow rates and tidal height in Monterey Bay. Aquifer-driven flow, redirected by the Monterey Bay fault zone, has also been proposed

as the source of fluid seepage at the nearby Mt. Crushmore and Clam Field sites (Fig. II.1) (Barry et al., 1996; Greene et al., 1993). High-resolution records of the Ba/Ca ratio in shells of vesicomyid clams collected at Clam Field are consistent with topographically-driven fluid flow. Elevated Ba/Ca ratios and corresponding low $\delta^{18}O$ values suggest a period of enhanced fluid flow, reflecting a hydrological response to the increased precipitation at the California coast following the drought of 1988-1990 (Torres et al., 2001). Thus, both flow rate measurements and chemical profiles of clam shells suggest that fluid seepage in this area of Monterey Bay is driven by artesian flow within the Purisima or Monterey formations which are exposed in the nearby Santa Cruz mountains and along the coast-line (Greene, 1977; Greene et al., 1993; Horns and Verosub, 1995).

II.4 Sampling and analytical techniques

In order to collect seep fluids from Extrovert Cliff, we utilized two different instrument packages - Chemical and Aqueous Transport (CAT) meters (Tryon et al., 2001) and an Optical Tracer Injection System (OTIS; LaBonte et al., 2007). These instruments were deployed in March and August 2004 using the ROV *Ventana*, operated from the R/V *Point Lobos*. After periods of between 2 and 18 weeks, the instruments were retrieved from the seafloor for subsequent laboratory determination of flow rates, major ion concentrations and dissolved helium characteristics.

Both the CAT meter and the OTIS are designed to measure seep fluid flow at the seafloor by channeling fluids, sampled via an external collection chamber, through the instrument (Fig. II.2). Entrainment of ambient seawater is avoided by coupling the collection chamber to the seafloor sediment at the focus of the seep. During instrument deployment, the position of the chamber is adjusted such that seep fluids can no longer be seen escaping around the edges.

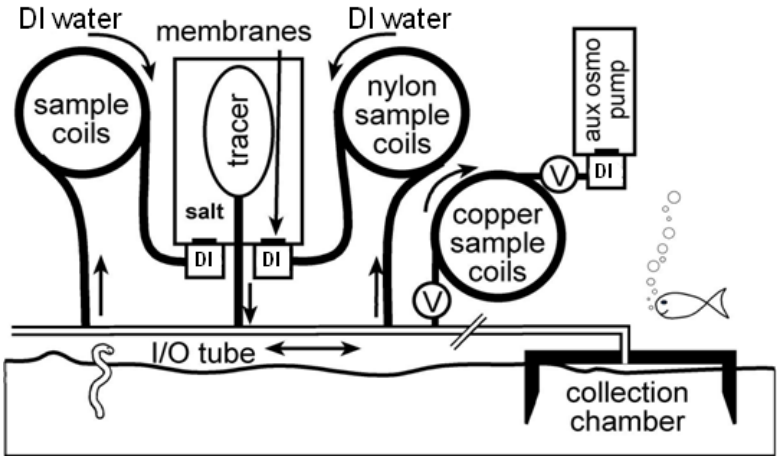

Figure II.2: Schematic of the CAT meter (Tryon et al., 2001) including modifications made for the current study by placing 1/8" diameter copper coils in parallel with existing plastic sampling coils.

The CAT meter is designed to measure fluid flow by determining the degree of dilution of a chemical tracer that is injected by an osmotic pump at a known rate into the fluids venting into or out of the collection chamber placed on the seafloor. The osmotic pump withdraws a sample of the seep fluid/tracer mixture into sample coils, which are initially filled with deionized water. This approach preserves a serial record of the tracer dilution, allowing determination of the flow rates together with the major ion chemistry. It is critical to set the osmotic pump rate close to expected flow rates taking into account the duration of the deployment to ensure that the coil will not be completely filled with seep fluids before the end of the deployment. In such a case, any information about temporal variations in the fluid chemistry would be lost (Tryon et al., 2001).

The OTIS differs in its approach to flow rate determination, using an electronic "time of flight" method. A pulse of fluorescent rhodamine dye tracer is injected into the outlet tubing and travels through the tube with the velocity of the ambient flow. Optical electronics measuring transmittance and fluorescence are used to detect tracer pulses in the passing fluid. The flow rate can be inferred from the time of arrival of each tracer pulse. The OTIS can be

linked in series to a companion CAT meter in order to utilize the sampling coils of the CAT meter (LaBonte et al., 2007).

For the current study, the CAT meter was modified by placing 1/8 inch (1/8”) diameter copper coils filled with DI water in parallel with existing plastic sample coils (Fig. II.2). We use standard 12.7 m (50 feet) coils of 1/8" Cu tubing. These coils can be connected in series to provide the desired storage capacity for each deployment. Seep fluids moving out of the top of the collection chamber are diverted through the Cu-coils which act to capture and preserve dissolved volatiles in solution. The copper coils have virtually zero permeability for helium, and are held at sea bottom pressure on recovery so that gas losses are negligible.

In order to obtain a temporal record of the dissolved volatile content of the seep fluids, the fluid sampling rate within the copper coils was inferred using information on the duration of the deployment and the location of the interface between the deionized water and the saline seep fluid within the coils. For CAT meter 2, the fluid sampling rate in the copper coils is of the order of 11 ml/day. Thus, each section of analyzed coil represents a specific time interval, with 1 m of coil corresponding to ~5 h of fluid sampling.

For a first set of analyses, the copper coils were partitioned into sections of 2-4 m length using standard refrigeration clamps, and attached to an off-line, ultrahigh vacuum system for sample extraction and processing (see Kulongoski and Hilton, 2002). A Swagelok Cajon ultratorr adapter was used to connect the 1/8” diameter copper coil to the 3/8” diameter inlet end of the extraction line. After releasing the refrigeration clamp, the Cu tube was heated so that all water was transferred from the Cu-coils into the vacuum system. A glass trap held at acetone-dry ice temperature was used to isolate water vapor, and a stainless-steel trap held at liquid nitrogen temperature was used to separate the condensable gas fraction (mainly CO_2) from the non-condensable fraction. The non-condensable fraction was purified using activated charcoal traps (held at -196°C) and a Ti getter held at 700°C. A known split (~0.5%) of the

residual non-condensable gas (mainly He and Ne) was collected into an AR-glass breakseal for transfer to a MAP 215 noble gas mass spectrometer for He and Ne analyses. Since all samples were processed "off-line", with only a fraction of the total gas load transferred to the mass spectrometer, 2-4 m long coil sections, containing 5-10 cm^3 of fluid, had to be processed for the measurement of helium and neon on the mass spectrometer. Consequently, the resulting time-resolution of the dissolved volatile signal in the coils was of the order of 10-20 hours.

In order to improve our time-resolution on He isotope and abundance analyses, we constructed a new dedicated extraction system that could be interfaced directly to the noble gas mass spectrometer. The new design was based upon existing instrumentation in the laboratory (see Kulongoski and Hilton, 2002) so that basic analytical protocols remained unchanged. Any released He from the copper coils was processed and inlet directly to the mass spectrometer preparation line giving a decrease of a factor of ~10 in the volume of fluid required for an analysis at the same analytical precision as obtained previously. In this way, we could obtain He results on significantly smaller quantities of fluids (~1 cm^3). This volume of fluid was contained in about 50 cm of 1/8" diameter copper tube, representing an equivalent sampling time-interval of ~2.5 hours.

II.5 Results

Following instrumentation recovery, the first step was determination of flow rates and major ion concentrations in the plastic sampling coils in order to identify which instruments had recorded active seep fluid venting. Our strategy was to target only the copper coils with chemistry altered from seawater values for subsequent helium analyses.

CAT meter 29, deployed in March (15-29 March 2004), showed altered fluid chemistry with elevated B, Ca, Li, Sr and low Mg, K, and S concentrations relative to

seawater (Table II.1). The two CAT meters of the second deployment (29 March to 4 August 2004) both recorded low flow rates and the chemistry of the sampled fluids was similar to ambient seawater. During the August deployment (4-27 August 2004), fluids from both CAT meter 2 and OTIS 14 exhibited highly altered fluid chemistry similar to the March deployment (Table II.1). In addition, the temperature sensor which was mounted inside the external chamber of OTIS recorded an average temperature of 9°C for the cold seep fluids, which is 5°C above ambient bottom seawater temperature (LaBonte et al., 2007). Therefore, we targeted three copper sampling coils (CAT meters 29 and 2 as well as OTIS 14) for dissolved helium analyses.

Table II.1: Chemical content of seep fluids from Extrovert Cliff collected in March 2004 with CAT meter 29 and in August 2004 with CAT meter 2 and OTIS 14[a].

	Seep (CAT 29)	Seep (CAT 2)	Seep (OTIS 14)[b]	Seawater
B	0.56	0.56	0.59	0.42
Ca	14.4	16.0	13.3	10.5
K	5.3	5.6	5.2	10.4
Li	0.04	0.04	0.04	0.03
Mg	26.4	27.1	25.7	54
Na	485	473	482	480
S	3.7	2.3	3.8	28.9
Sr	0.35	0.36	0.34	0.09

[a] The chemistry of the seep fluids is altered from seawater values (IAPSO Standard). Values are shown in mM.

[b] Values were incorrectly tabulated by LaBonte et al. (2007). Correct values are given here.

In Table II.2, we present $^3He/^4He$ ratios as well as helium and neon abundance results for 35 samples from Extrovert Cliff seeps. Results are shown as measured ^4He and Ne concentrations (^4He_m and Ne_m) and measured $^3He/^4He$ ratios (reported as R_m/R_A, where R_m = $^3He/^4He$ ratio measured in the sample and R_A = $^3He/^4He$ ratio of air = 1.4×10^{-6}). Also included in Table II.2 are coil details including the date of deployment and the location of the

Table II.2: Helium and neon characteristics of submarine cold seep fluids from Extrovert Cliff (Monterey Bay, California)[a].

Sample Details[b]	Section in coil (m from inlet end)	Time represented by analyzed section (hours)	$^3He/^4He$ (R_m/R_A)	^4He_m (ncm^3STP/gH_2O)	Ne_m (ncm^3STP/gH_2O)	$(^4He/Ne)_m/(^4He/Ne)_{air}$	f (Ne_m/Ne_i)	$^4He_{terr}$[c] (ncm^3STP/gH_2O)	$^4He_{terr}$[d] (ncm^3STP/gH_2O)	$(R_{terr}/R_A)^3$	$^4He_{terr}$[e] (ncm^3STP/gH_2O)	$(R_{terr}/R_A)^e$
First deployment: 15-29 March 2004												
CAT meter 29 – low-resolution data												
Mont1_29_4	0-3.54		1.29 ± 0.21	69.1 ± 0.8	66.6 ± 0.4	3.60						
Mont1_29_5	3.54-8.04		0.59 ± 0.10	71.0 ± 0.70	77.3 ± 0.6	3.19						
Mont1_29_6	8.04-12.18		0.91 ± 0.14	93.5 ± 1.0	85.8 ± 0.9	3.78						
Third deployment: 4-27 August 2004												
OTIS 14 – low-resolution data												
Mont3_14_1	1.21-5.61		1.62 ± 0.16	81.5 ± 0.9	65.1 ± 0.6	4.34						
Mont3_14_2	15.24-18.94		1.74 ± 0.15	85.1 ± 0.9	72.6 ± 0.4	4.14						
Third deployment: 4-27 August 2004												
CAT meter 2 – low-resolution data												
Mont3_02_2	2.40-5.02	12.0	1.58 ± 0.17	162.4 ± 1.7	346.9 ± 1.2	1.62	1.00	71.2	105.8	1.89	98.4	1.96
Mont3_02_3	5.02-7.72	12.3	1.75 ± 0.22	130.4 ± 1.3	278.6 ± 0.8	1.62	0.80	60.8	87.2	2.12	83.6	2.17
Mont3_02_4	7.72-10.10	10.9	0.91 ± 0.17	87.7 ± 1.0	63.7 ± 0.3	4.78	0.18	76.5	80.7	0.90	82.1	0.90
Mont3_02_5	10.10-13.65	16.2	1.64 ± 0.10	139.1 ± 1.4	312.0± 1.0	1.55	0.90	59.0	89.4	2.00	84.1	2.06
Mont3_02_6	13.65-18.22	20.9	1.04 ± 0.09	56.7 ± 0.7	68.6 ± 0.9	2.87	0.20	44.4	49.1	1.05	50.4	1.05
CAT meter 2 – high-resolution data												
ehes4816	18.22-18.72	2.3	1.17 ± 0.01	43.2 ± 4.3	223.5 ± 20.2	0.67	0.64	−*	10.3	1.71[f]	9.1	1.81[†]
Mont3_02_19	18.72-19.26	2.4	1.50 ± 0.30	23.5 ± 2.3	105.0 ± 9.5	0.77	0.30	2.6	10.5	2.12	11.9	1.99
Mont3_02_22	19.26-19.81	2.4	1.23 ± 0.04	30.5 ± 3.0	193.2 ± 17.8	0.55	0.56	−*	3.0	3.31[f]	2.8	3.49[†]
ehes4826	19.80-20.30	2.3	n.d.	n.d.	n.d.	n.d.						
Mont3_02_20	20.30-20.84	2.4	1.25 ± 0.10	29.7 ± 3.0	152.9 ± 13.8	0.67	0.44	−*	9.1	1.81[f]	9.9	1.75[†]
Mont3_02_21	20.84-21.38	2.4	1.25 ± 0.05	30.6 ± 3.1	199.1 ± 18.0	0.53	0.57	−*	2.0	4.75[f]	1.6	5.65[†]
ehes4836	21.38-21.88	2.3	1.16 ± 0.02	57.2 ± 5.7	238.5 ± 21.6	0.83	0.69	−*	21.5	1.42	19.7	1.46
Mont3_02_26	21.88-22.42	2.4	1.34 ± 0.04	33.5 ± 3.3	151.7 ± 13.7	0.77	0.44	0.6	13.1	1.87	13.9	1.82
Mont3_02_27	22.42-22.96	2.3	n.d.	n.d.	n.d.	n.d.						
ehes4845	22.96-23.46	2.3	1.19 ± 0.02	56.5 ± 5.7	234.3 ± 21.2	0.84	0.68	0.3	21.6	1.50	20.0	1.54
ehes4855	23.46-23.96	2.3	1.20 ± 0.01	25.4 ± 2.5	118.5 ± 10.7	0.74	0.34	1.1	10.3	1.49	11.6	1.44
Mont3_02_18	23.96-24.50	2.4	1.22 ± 0.17	27.3 ± 2.7	165.5 ± 15.0	0.57	0.48	−*	4.6	2.30[f]	5.1	2.17[†]
Mont3_02_25	24.50-25.04	2.4	1.17 ± 0.04	28.6 ± 2.9	134.1 ± 12.1	0.74	0.39	0.3	11.0	1.44	12.1	1.40
ehes4861	25.04-25.54	2.3	1.16 ± 0.01	42.6 ± 4.3	186.6 ± 16.9	0.79	0.54	0.2	16.3	1.42	16.3	1.42
Mont3_02_24	25.54-26.08	2.4	1.24 ± 0.04	24.9 ± 2.5	126.2 ± 11.4	0.68	0.36	−*	8.6	1.69	9.8	1.61

Table II.2: Continued

Sample Details[b]	Section in coil (m from inlet end)	Time represented by analyzed section (hours)	$^3He/^4He$ (R_m/R_A)	^4He_m (ncm^3STP/gH_2O)	Ne_m (ncm^3STP/gH_2O)	$(^4He/Ne)_m/(^4He/Ne)_{air}$	f (Ne_m/Ne_i)	$^4He_{terr}$[c] (ncm^3STP/gH_2O)	$^4He_{terr}$[d] (ncm^3STP/gH_2O)	$(R_{terr}/R_A)^3$	$^4He_{terr}$[e] (ncm^3STP/gH_2O)	$(R_{terr}/R_A)^e$
Mont3_02_27	22.42-22.96	2.3	n.d.	n.d.	n.d.	n.d.						
ehes4845	22.96-23.46	2.3	1.19 ± 0.02	56.5 ± 5.7	234.3 ± 21.2	0.84	0.68	0.3	21.6	1.50	20.0	1.54
ehes4855	23.46-23.96	2.3	1.20 ± 0.01	25.4 ± 2.5	118.5 ± 10.7	0.74	0.34	1.1	10.3	1.49	11.6	1.44
Mont3_02_18	23.96-24.50	2.4	1.22 ± 0.17	27.3 ± 2.7	165.5 ± 15.0	0.57	0.48	−*	4.6	2.30[f]	5.1	2.17[†]
Mont3_02_25	24.50-25.04	2.4	1.17 ± 0.04	28.6 ± 2.9	134.1 ± 12.1	0.74	0.39	0.3	11.0	1.44	12.1	1.40
ehes4861	25.04-25.54	2.3	1.16 ± 0.01	42.6 ± 4.3	186.6 ± 16.9	0.79	0.54	0.2	16.3	1.42	16.3	1.42
Mont3_02_24	25.54-26.08	2.4	1.24 ± 0.04	24.9 ± 2.5	126.2 ± 11.4	0.68	0.36	−*	8.6	1.69	9.8	1.61
Mont3_02_23	26.08-26.62	2.4	1.23 ± 0.03	47.6 ± 4.8	230.8 ± 20.9	0.72	0.67	−*	13.4	1.82[f]	11.9	1.92[†]
Mont3_02_7	26.62-27.12	2.3	1.16 ± 0.02	45.9 ± 5.7	189.3 ± 17.4	0.84	0.55	2.7	19.1	1.38	19.0	1.39
Mont3_02_8	27.12-27.64	2.4	1.19 ± 0.02	33.6 ± 5.5	139.6 ± 13.3	0.83	0.40	3.9	15.2	1.42	16.2	1.39
Mont3_02_9	27.64-28.16	2.4	1.13 ± 0.04	65.6 ± 7.6	238.5 ± 21.9	0.95	0.69	8.1	29.9	1.28	28.1	1.30
Mont3_02_10	28.16-28.68	2.4	1.17 ± 0.03	63.3 ± 7.4	243.5 ± 22.3	0.90	0.70	4.3	26.7	1.40	24.7	1.44
Mont3_02_11	28.68-29.20	2.4	1.13 ± 0.03	55.8 ± 6.7	222.1 ± 20.5	0.87	0.64	3.2	23.2	1.31	22.0	1.33
Mont3_02_12	29.20-29.72	2.4	1.16 ± 0.03	47.9 ± 6.0	186.1 ± 17.3	0.89	0.54	5.6	21.7	1.35	21.6	1.35
Mont3_02_13	27.72-30.24	2.4	1.09 ± 0.02	60.2 ± 7.1	208.9 ± 19.3	1.00	0.60	11.4	30.0	1.18	29.2	1.19
Mont3_02_14	30.24-30.76	2.4	1.20 ± 0.04	54.5 ± 6.8	211.9 ± 19.7	0.89	0.61	4.8	23.7	1.46	22.9	1.48
Mont3_02_15	30.76-31.28	2.4	1.14 ± 0.02	58.2 ± 6.9	222.8 ± 20.5	0.91	0.64	5.3	25.4	1.32	24.2	1.34
Mont3_02_16	31.28-31.80	2.4	1.19 ± 0.03	62.3 ± 7.5	238.2 ± 22.0	0.91	0.69	4.9	26.7	1.45	24.9	1.47
Mont3_02_17	31.80-32.32	2.4	1.17 ± 0.02	63.9 ± 7.3	222.8 ± 20.4	1.00	0.64	11.3	31.2	1.35	30.1	1.36
Seawater at 10°C		1	38.2	162.7	0.81							

[a] All errors are reported at the 1 σ level. Errors for the (R_{terr}/R_A) ratios are ~1.5 % for the low-resolution data and ~15 % for high-resolution data. The larger errors for the high-resolution data are due to the smaller amount of water processed and the correspondingly higher uncertainty on the measured He and Ne concentrations. N.d., no data available

[b] MontX_Y_Z where X is number of deployment, Y is coil ID, and Z is number of sample section. Samples labeled ehesnnn represent the first set of samples run to test the new extraction system.

[c] Values calculated for water-methane interaction and unfractionated excess air with $(He/Ne)_{ex} = 0.288$. For this model, $^4He_{terr}$ values cannot be calculated for the eight samples indicated with asterisks, i.e., the eight samples that fall to the left of the fractionation curve for water-methane interaction (solid line) for starting composition 1 in Figure IV.3.

[d] Values calculated for water-methane interaction and fractionated excess air with $(He/Ne)_{ex} = 0.10$.

[e] Values calculated for water-oil interaction and fractionated excess air with $(He/Ne)_{ex} = 0.14$.

[f] Errors are ≥20%.

analyzed sections within the coil (relative to the inlet end). We utilize CAT meter 2, deployed in August 2004, for detailed (high-resolution) dissolved volatile analyses using the new extraction line. For this particular sampling coil, we report the time interval represented by each coil section in order to resolve any temporal variations of the helium and neon characteristics of the captured fluids.

II.5.1 Volatile characteristics – low-resolution analysis

Low-resolution analyses of a total of ten samples from three instruments (CAT 29; OTIS 14; CAT 2) show that measured helium concentrations (^4He_m) of seep fluids at Extrovert Cliff range from 56 to 162 ncm^3STP/gH_2O. Figure II.3 shows that all these samples are enriched in He relative to air-saturated seawater (38.2 ncm^3 $^4He/gH_2O$ at 10°C; Weiss, 1971), consistent with the chemistry of Extrovert Cliff seep fluids indicating alteration from ambient seawater. Neon abundances (Ne_m) range from 63 to 347 ncm^3STP/gH_2O. Seven out of the ten samples are undersaturated in neon relative to the atmospheric equilibrium concentration of seawater (162.7 ncm^3Ne/gH_2O at 10°C; Weiss, 1971), whereas three samples show significant "excess" neon. In all cases, the air-normalized He/Ne ratio is greater than the seawater-dissolved value.

Measured $^3He/^4He$ ratios in the seep fluids range from 0.59 to 1.75 R_A, and appear significantly higher that the isotopic composition of helium produced in crustal lithologies by radioactive decay (~0.02 R_A; Andrews, 1985). However, correcting the $^3He/^4He$ ratios for the contribution of air-derived helium will result in a shift to lower helium isotope values for samples with measured $^3He/^4He$ ratios < 1 R_A and a shift to higher values for samples with measured $^3He/^4He$ ratios > 1 R_A, respectively. Thus, $^3He/^4He$ ratios greater than 1 R_A in seven seep fluids samples represent minimum estimates for their air-corrected helium isotopic

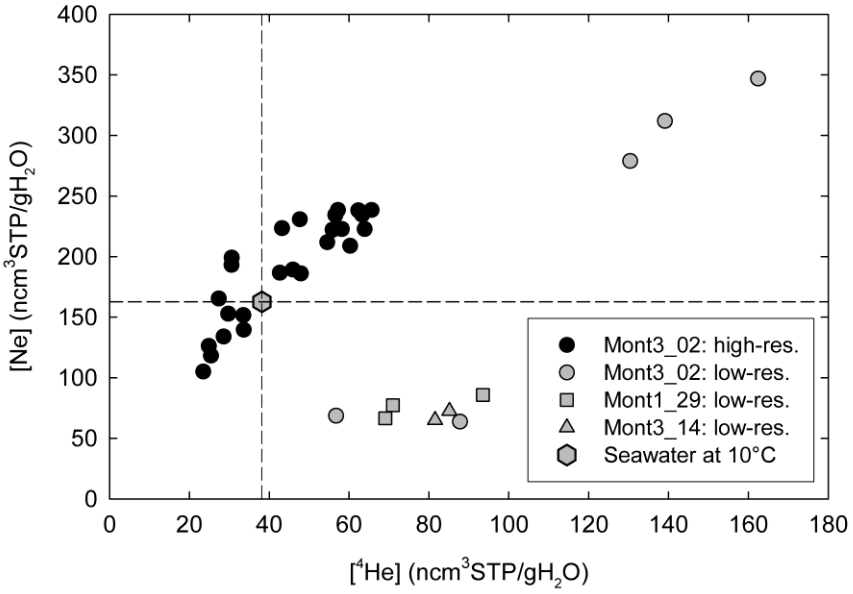

Figure II.3: Measured Ne concentration versus ^{4}He concentration for Extrovert Cliff seep fluid samples collected in three separate copper coils (CAT meter 2, CAT meter 29 and OTIS 14). Dashed lines represent the helium and neon equilibrium concentrations in seawater at 10°C (Weiss, 1971).

composition. These elevated ratios are consistent with the presence of mantle-derived helium in Extrovert Cliff cold seep fluids (see section II.6.2 for discussion).

II.5.2 Volatile characteristics – high-resolution analysis

After refining our extraction procedures (see section II.4), we analyzed 25 adjacent sections of the sampling coil connected to CAT meter 2 in order to obtain a temporal record of the dissolved volatile content with a significantly improved time-resolution. These 25 He analyses cover a total time period of ~2.5 days (i.e., analysis was achieved with a resolution of ~2.5 h). Helium isotope ratios as well as ^{4}He and Ne abundances are reported in Table II.2.

Helium abundances range from 23 to 65 ncm^{3}STP/gH_2O, whereas the neon concentrations vary between 105 and 243 ncm^{3}STP/gH_2O in this part of the sampling coil. Figure II.3 shows that ten samples are depleted in helium relative to ambient air-saturated

seawater (i.e., ^4He_m < 38.2 ncm^3 $^4He/gH_2O$), with a maximum depletion of about 40% in sample Mont3_02_19 (23 ncm^3STP/gH_2O). Furthermore, seven out of these ten samples are also depleted in neon (i.e., Ne_m < 162.7 ncm^3Ne/gH_2O). We note that 12 out of the 25 samples yield an air-normalized He/Ne ratio less than air-equilibrated seawater at 10°C (i.e., $(He/Ne)_m/(He/Ne)_{air}$ < 0.81).

Measured $^3He/^4He$ ratios vary between 1.09 and 1.5 R_A, and are in the range of values obtained for the analyses with a lower time-resolution. Since measured $^3He/^4He$ ratios are greater than 1 R_A for all samples, correcting the helium isotope ratios for the contribution of air-derived helium will result in higher values. Thus, these elevated ratios are again consistent with a contribution of helium originating from the mantle.

II.6 Discussion

II.6.1 Noble gas components in Extrovert Cliff seep fluids

In most natural waters, the dissolved noble gas content is composed of air-derived noble gases - from equilibration with the atmosphere and from excess air entrainment - and variable amounts of terrigenic (i.e., crustal and/or mantle-derived) noble gas components. Furthermore, noble gas concentrations can be affected by other factors such as the temperature and altitude at recharge, the salinity of the fluid, fluid addition from other sources, or interaction with phases such as gas and oil within the subsurface. Although the origin and history of Extrovert Cliff seep fluids remains debatable, we show here that the contribution of the different noble gas components to these seep fluids can be quantified.

In order to resolve our measured helium contents into constituent components, we begin by assuming that fluids emanating at Extrovert Cliff seeps are primarily derived from either the Purisima or Monterey Formation confined aquifers which are exposed along the coast-line of Monterey Bay and in the Santa Cruz mountains (Greene et al., 1993; Greene et

al., 1999; Horns and Verosub, 1995; LaBonte et al., 2007). The high salinity of our samples, together with oxygen ($\delta^{18}O$) stable isotope values of ~0‰, suggests that seawater represents the dominant source of Extrovert Cliff seep fluids. Seawater intrusion may presently occur through outcrops of the aquifers near the coast or, alternatively, the aquifer system may contain "ancient" saline groundwater, topographically driven into the submarine environment by uplift of the Santa Cruz mountains that has tilted the sedimentary sequence to the southwest (Anderson et al, 1990; Orange et al., 1999). Within the recharge zone of the seep fluids, both air-derived helium and neon partition into the water phase according to their equilibrium solubility, which in turn depends on the temperature and salinity of the water as well as on the atmospheric pressure (i.e., altitude). Assuming recharge of saline water at 10°C near sea level, we can calculate the equilibrium concentrations for both helium and neon (Table II.2) (Weiss, 1971).

A notable feature of our results is that measured neon concentrations in 21 out of our 35 samples are greater than the air-equilibration value for seawater at 10°C (Fig. II.3). For example, the sample with the highest measured neon content (Mont3_02_2 = 346.9 ncm^3Ne/gH_2O) has a neon excess of 113% relative to seawater recharged at sea level and a temperature of 10ºC. The observed supersaturation in neon suggests that the total measured noble gas concentrations in our seep fluid samples includes a component of excess-air, i.e., dissolved air bubbles, entrained into the saline groundwater at recharge (Heaton and Vogel, 1981).

While most Extrovert Cliff seep fluid samples show clear evidence of an excess air component, a striking characteristic of the other 14 samples is their significant undersaturation in helium and/or neon relative to equilibrium concentrations and their low He/Ne ratios relative to air-saturated seawater (Fig. II.3 and Table II.2). For these samples, the fluids appear to have lost a fraction of their initial dissolved noble gases acquired at recharge. Furthermore,

helium has been lost preferentially to neon as shown by measured He/Ne ratios < air-saturated water values. One obvious means to deplete, or strip, noble gases from a fluid phase is the interaction of water with a gas or oil phase within the subsurface. Thus, we suggest that the depletion of helium and neon and the resulting elemental fractionation observed in Extrovert Cliff cold seep fluids can be explained by interaction of the fluids with hydrocarbons, either migrating methane (micro-) bubbles or an oil phase, within the aquifer. Indeed, it has been proposed that fluid seepage in Monterey Bay is driven, in part, by hydrocarbon generation at depth within organic-rich units (Martin et al., 1997; Orange et al., 1999). High methane concentrations in pore fluids at cold seep sites in Monterey Bay (Barry et al., 1997; Martin et al., 1997), together with the observation of "blow-out" holes during instrumentation deployment, suggest that Extrovert Cliff is a site of active fluid flow and methane venting. Moreover, Kvenholden et al. (2002) and Lorenson et al. (2002) found petroleum-related hydrocarbons and visible oil in some sediment cores at seep sites within Monterey Bay (e.g., at Clam Field), most likely originating from the Monterey Formation or the Santa Cruz mudstone.

In order to estimate the contribution of the different noble gas components (equilibrium solubility, excess air, terrigenic) in Extrovert Cliff fluids and to establish the terrigenic $^{3}He/^{4}He$ values, we first need to correct the measured elemental ratios for the effect of any noble gas stripping by a hydrocarbon phase. In the following sections, we evaluate two models in which the Extrovert Cliff fluids originate from an aquifer bearing saline water that has interacted with a) methane bubbles, or b) an oil phase within the subsurface. By reconstructing the noble gas characteristics of the fluids prior to interaction with hydrocarbons, we can make a more realistic air-correction to the measured $^{3}He/^{4}He$ ratios which, in turn, will allow us to identify with greater confidence a possible mantle contribution to the measured helium content.

For the proposed models, we assume there is no significant contribution of ^{3}He to the total ^{3}He content in Extrovert Cliff seep fluids from bomb-derived, tritiated water. Although the effect of tritium decay on Extrovert Cliff seep fluids is difficult to assess, as no direct measurements are available, we anticipate that groundwater systems with recharge occurring prior to the 1950s have a tritium level at background levels of ~ 0.5 TU (Andrews and Kay, 1982) (where 1 TU = 1 tritium atom in 10^{18} H atoms). However, nuclear weapons testing during the 1950s and 1960s released copious amounts of tritium into the atmosphere that can be detected in groundwater recharged during this period. For tritiogenic helium to affect seep fluids collected at Extrovert Cliff in 2004, the seep fluids would have to contain a significant fraction of the precipitation from the early 1960s. While the residence time of fluids sampled in this study has not been determined, anticipated flow velocities of groundwaters (≤15 m/a; e.g., Freeze and Cherry, 1979) are much lower than the velocities required for fluids to travel from the recharge region near the coast to the seep site in Monterey Bay (i.e., over a distance of ~20 km) in less than 40 years. Therefore, it is extremely unlikely that the decay of nuclear bomb-derived tritium represents a contribution to the total ^{3}He measured in Extrovert Cliff seep fluids.

II.6.2 Proposed evolution of Extrovert Cliff seep fluids

II.6.2.1 Model 1: Depletion of noble gases in Extrovert Cliff seep fluids due to interaction with methane bubbles

Several recent studies have shown that the noble gas concentration in pore fluids and in seawater surrounding a seep site can be affected by the formation of methane (micro-) bubbles in sediments with a high rate of CH_4 production. For example, Brennwald et al. (2003; 2005) observed a systematic noble gas undersaturation in pore waters of anoxic

lacustrine sediments, whereas Holzner et al. (2008) detected a depletion of noble gases in the water column above an active mud volcano emitting gas bubbles in the Black Sea.

The high rate of methane production at seep sites can lead to the formation of pure CH_4 gas bubbles. Gas exchange between the bubbles and the surrounding pore water in the sediment column can potentially strip dissolved gases from the fluid phase until either the gas bubbles escape or until equilibrium is established between gas concentrations in the bubbles and the surrounding fluid. Stripping can result in the observed noble gas undersaturation in fluids; it can also lead to fractionation of noble gas elemental patterns, due to the systematic increase in water solubility and decrease in diffusion coefficients of the noble gases with increasing atomic mass (Ballentine et al., 2002; Brennwald et al., 2003; Brennwald et al., 2005; Holzner et al., 2008; Leifer and Clark, 2002). Bubbles can preferentially strip helium due to its low solubility and/or high diffusivity, thereby decreasing the He/Ne ratio in the residual water phase.

We model the loss of noble gases in the residual water phase using the Rayleigh fractionation law. Stripping depletes the water phase in noble gases, with the water phase $(He/Ne)_{water}$ ratio given by the following equation:

$$\left(\frac{He}{Ne}\right)_{water} = \left(\frac{He}{Ne}\right)_i f^{(\alpha-1)} \qquad \text{(II.1)}$$

where $(He/Ne)_i$ is the initial fluid phase ratio before gas stripping and f is the fraction of Ne remaining in the fluid phase. The fractionation coefficient (α) for a gas/water system is given by:

$$\alpha = (K_{He}^{\ water} / K_{Ne}^{\ water}) \qquad \text{(II.2)}$$

where K_i^{water} is the Henry's constant for noble gas species i in water.

In order to evaluate if this model is applicable to our dataset, we need to know the initial He/Ne ratio in Extrovert Cliff seep fluids acquired at recharge. However, the air-

equilibration He/Ne value is inappropriate given the observation of excess neon in some samples (section II.5), indicating air bubble dissolution. Therefore, we assume that the sample with the highest measured neon content (Mont3_02_2) has been least affected by stripping and therefore has retained a neon concentration closest to that of the fluids at recharge (i.e., Ne_i = 346.9 ncm^3/gH_2O). This value represents the sum of neon derived from air-equilibration (Ne_{eq}) and entrained excess air (Ne_a). In the following analysis, we assume a recharge temperature of 10°C and take sea level as the altitude of recharge.

Under these assumptions, the values for the equilibrium components He_{eq} and Ne_{eq} at recharge are 38.2 and 162.7 ncm^3/gH_2O, respectively (Weiss, 1971), and the amount of neon entrained by air-bubbles (Ne_a) is 184.2 ncm^3/gH_2O (i.e., the fluids initially contained 113% excess air). The amount of helium from air-bubble entrainment (He_a) is then calculated using the helium-neon ratio in air $(He/Ne)_{ex}$ = 0.288, and is equal to 53.0 ncm^3/gH_2O. Thus, the resulting initial He/Ne of the water at recharge is 0.263.

We can model the effects of methane bubble stripping using equations (II.1) and (II.2) assuming a temperature of 9°C at the water-methane contact and using the coefficients from Smith (1985) to calculate the fractionation coefficient α, i.e., α = 1.234. We plot the corresponding Rayleigh fractionation curve from a starting composition of He_i = 91.2 ncm^3/gH_2O and Ne_i = 346.9 ncm^3/gH_2O (labeled Point 1 in Figure II.4).

Of the 30 samples analyzed for He and Ne contents from CAT meter 2 (Table II.2), eight samples have measured He concentrations (He_m) less than that modeled as remaining in the water phase ($^4He_{water}$) after noble gas stripping by a methane phase. These samples plot to the left of the modeled Rayleigh fractionation curve for water-methane interaction (solid line) as shown in Figure II.4. However, since all of our samples collected with CAT meter 2 are closely related in time (~5 days), we should be able to model their noble gas characteristics from a common starting composition irrespective of the degree of stripping. Therefore, we

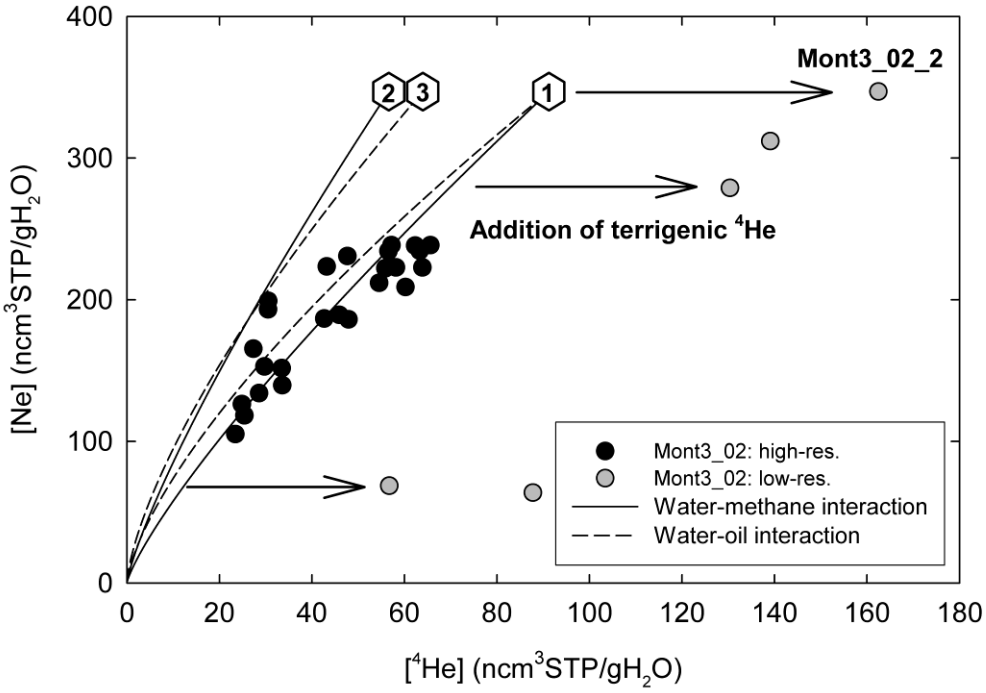

Figure II.4: Measured Ne concentration versus ^{4}He concentration for Extrovert Cliff seep fluids samples collected with CAT meter 2. Rayleigh fractionation curves for both water-methane (solid lines) and water-oil interaction (dashed lines) are shown for a fluid with an initial neon concentration equal to the neon content measured in sample Mont3_02_2 and unfractionated excess air with $(He/Ne)_{ex} = 0.288$ (indicated by 1), fractionated excess air with $(He/Ne)_{ex} = 0.10$ (indicated by 2), and fractionated excess air with $(He/Ne)_{ex} = 0.14$ (indicated by 3).

consider the model starting at Point 1 to be inappropriate to describe our dataset. Consequently, we suggest that a model which adopts either a lower $(He/Ne)_i$ value at recharge or a larger Rayleigh fractionation coefficient is necessary to better explain the observed He-Ne relationships in Extrovert Cliff fluids.

In the first instance, we note that our initial model is based on the assumption that recharge of saline groundwater occurred at 10°C. Assuming a lower temperature at recharge would result in a lower $(He/Ne)_i$ value. For example, the $(He/Ne)_i$ at 0°C is 0.256 in our model. However, for Extrovert Cliff seep fluids, all samples plot to the right of the modeled

Rayleigh fractionation curve for water-methane interaction only if the initial He content is ≤ 56.6 ncm^3/gH_2O, i.e., $(He/Ne)_i$ = 0.163 (Point 2 in Figure II.4). Such an extremely low $(He/Ne)_i$ value cannot be explained by a lower temperature at recharge alone.

Another means to acquire a lower initial He/Ne ratio in Extrovert Cliff fluids is by fractionation of the excess air component entrained at recharge. In our model, we have assumed that the entrained excess air component has an atmospheric composition, i.e., $(He/Ne)_{ex}$ = 0.288, due to the complete dissolution of entrained air bubbles. However, gas excess in groundwaters can be fractionated relative to atmospheric air. Two models have been proposed to describe the fractionation of gas excess in groundwaters, one assuming partial diffusive re-equilibration of groundwater supersaturated by excess air (PR-model; Stute et al., 1995), the other assuming closed-system equilibration of groundwater with entrapped air (CE-model; Aeschbach-Hertig et al., 2000). The first model describes the loss of noble gases by diffusive degassing of the excess air across the groundwater table. In the second scenario, entrained air bubbles dissolve only partially and subsequent equilibration between water and a finite volume of entrapped air in a closed system results in the fractionation of excess air. Both processes result in an enrichment of heavy noble gases relative to light gases. In the case of the PR-model, the light noble gases are lost faster than heavier ones because the diffusivities of the noble gases decrease with atomic mass. Since helium has a particularly high diffusion coefficient, it is strongly depleted in the residual excess air. Thus, the excess air component can, in principle, be characterized by any He/Ne ratio between zero and 0.288, depending on the degree of re-equilibration (Kipfer et al., 2002; Stute et al., 1995). If the CE-model applies, however, the excess air He/Ne ratio is restricted to the range between the atmospheric He/Ne ratio of 0.288 (if the entrapped air volume is completely dissolved) and the value for air-equilibrated saline water (i.e., ~0.23 at 10ºC) (Aeschbach-Hertig et al., 2000).

As mentioned above, our model explains the observed helium contents only if the initial He concentration at recharge is ≤ 56.6 ncm^3/gH_2O (Point 2 in Figure II.4). Thus, to maintain an initial neon abundance of 346.9 ncm^3/gH_2O (observed), the He/Ne ratio of the excess air component must be highly fractionated, i.e., $(He/Ne)_{ex} \leq 0.10$. Such a scenario can be achieved by addition of excess air to air-equilibrated saline water, followed by significant diffusive gas loss (PR model). Using the PR-model from Aeschbach-Hertig et al. (1999) and assuming an excess of 184.2 ncm^3Ne/gH_2O after re-equilibration ($= Ne_m - Ne_{eq}$), we calculate that a large amount of excess air (up to 483 % of Ne saturation), followed by a large degree of diffusive degassing, would be necessary to produce a $(He/Ne)_{ex}$ ratio of 0.10. We note that in the study of Stute et al. (1995), where the PR-model was introduced, initial Ne excesses up to 300% were found. Moreover, since Kipfer et al. (2002) observed that significant fractionation of the excess air component, i.e., He/Ne ≈ 0.14, is possible, we suggest that a noble gas stripping model by methane bubbles, which includes highly fractionated excess air with $(He/Ne)_{ex} \leq 0.10$, is plausible and compatible with the observed He-Ne relationships in Extrovert Cliff fluids. In this case, the PR-model predicts that isotopic fractionation should occur at recharge due to the significantly different diffusivities of the light noble gas isotopes. However, isotopic fractionation has not been observed to date (Kipfer et al., 2002; Peeters et al., 2003). Therefore, we consider that the large He depletion does not have an impact of the initial He isotopic composition of the excess air component.

Thus, if we assume a starting composition of $He_i = 56.6$ ncm^3/gH_2O and $Ne_i = 346.9$ ncm^3/gH_2O and use equations (II.1) and (II.2), we can now calculate the amount of helium remaining in the water phase after stripping of each sample:

$$[^4He]_{water} = (He/Ne)_{water} \times [Ne]_m \qquad \text{(II.3)}$$

where $[Ne]_m$ is the measured neon concentration in each sample.

The amount of terrigenic helium-4 ($^4He_{terr}$) in the fluids is then given by:

$$[^4He]_{terr} = [^4He]_m - [^4He]_{water} \qquad (II.4)$$

The terrigenic helium-3 ($^3He_{terr}$) component in each sample can be estimated from the ^4He concentrations and the $^3He/^4He$ ratios for the different components, assuming that the non-terrigenic helium in Extrovert Cliff fluids has an atmospheric isotopic composition:

$$[^3He]_{terr} = (^4He_m \times R_m) - (^4He_{water} \times R_{water}) \qquad (II.5)$$

where $R_{water} = {}^3He/^4He$ ratio of air $= 1.4 \times 10^{-6}$.

In Table II.2, we tabulate the terrigenic helium-4 ($^4He_{terr}$) component calculated for both starting compositions plotted in Figure II.4 (Points 1 and 2). Note that the amount of terrigenic He cannot be calculated for those eight samples (indicated with asterisks in Table II.2) falling to the left of the fractionation curve starting at Point 1. Consequently, we prefer to adopt the Rayleigh fractionation model starting at Point 2. We note that if the noble gases entrained by air bubbles showed greater fractionation by partial diffusive degassing, i.e., $(He/Ne)_{ex} \ll 0.10$, the resulting values for $[^4He]_{terr}$ would be even higher.

The $^3He/^4He$ ratio of the terrigenic helium component – calculated from equations (II.4) and (II.5) and assuming fractionation starting at Point 2 – is given in Table II.2 (R_{terr}/R_A). The ratio varies from 0.90 to 4.75 R_A (with the majority of samples falling between 1 and 2.3 R_A (n =28) and 2 outliers > 2.3 R_A). Assuming a simple binary mixture of (MORB-like) mantle (8 R_A) and crustal (0.02 R_A) components, we can estimate the fraction of mantle-derived helium relative to the total amount of terrigenic helium in each sample. The mantle contribution to the helium inventory in Extrovert Cliff seep fluids ranges from 11 to 25% for the majority of our samples. Alternatively, the fraction of mantle-derived helium in the seep fluids increases to 34% if the deep helium component originates from the sub-continental lithospheric mantle, which is characterized by a helium isotopic composition of ~6 R_A in the southwestern US (Reid and Graham, 1996). Regardless of the exact $^3He/^4He$ ratio of the

mantle endmember component, an inescapable conclusion of the above analysis is that Monterey seep fluids possess a mixture of He from both mantle and crustal sources.

II.6.2.2 Model 2: Depletion of noble gases in Extrovert Cliff seep fluids due to interaction with oil

An alternative explanation for the depletion of helium and neon in Extrovert Cliff cold seep fluids is that fluids have interacted with an oil phase during flow through the hydrocarbon-rich Monterey Formation or Santa Cruz mudstone. Similar to stripping by methane bubbles, helium and neon will partition between water and an oil phase because the solubilities of noble gases in crude oil are significantly higher than in water (Kharaka and Specht, 1988).

The Rayleigh fractionation coefficient for the He-Ne pair for water that has interacted with an oil phase is given by

$$\alpha = \left(K_{He}/K_{Ne}\right)^{water} / \left(K_{He}/K_{Ne}\right)^{oil} \qquad \text{(II.6)}$$

The solubility constants for helium and neon in crude oil (K_i^{oil}) appear to depend on the oil density, i.e., noble gases are more soluble in lower density oil (higher API gravity) than in heavier oil, and they increase with increasing temperature (Kharaka and Specht, 1988). However, experimentally determined solubilities for noble gases are limited to two crude oils with API gravities of 25° and 34°, whereas oils extracted from the Monterey formation show an extreme variation in API gravity (4° to 33°) (Curiale et al., 1985).

We assume a temperature of 9°C at the water-oil contact and use the coefficients from Smith (1985) and Kharaka and Specht (1988) to calculate the solubility constants for noble gases in water and in heavy oil with an API gravity of 25°. Thus, the fractionation coefficient α is equal to 1.429.

From equations (II.1)-(II.6), we can calculate the contribution of the different noble gas components for a fluid that has interacted with an oil phase within the subsurface. Again, the assumption of an unfractionated atmospheric excess air component entrained at recharge results in negative values in $[^4He]_{terr}$ – in this case for five samples. These five samples plot to the left of the modeled fractionation curve (dashed line) for water-oil interaction and a starting composition of He_i = 91.2 ncm^3/gH_2O and Ne_i = 346.9 ncm^3/gH_2O (Point 1 in Figure II.4). However, if the excess air component has a fractionated He/Ne ratio of ≤ 0.14 (Point 3 in Figure II.4), then the model provides a basis for explaining the observed helium contents of Extrovert Cliff seep fluids. In this case, a $(He/Ne)_{ex}$ ratio of 0.14 results in $^3He/^4He$ ratios of the terrigenic helium component between 0.90 and 5.65 R_A although the majority of samples fall between 1.0 and 2.2 R_A (Table II.2). The values for $[^4He]_{terr}$ and R_{terr}/R_A obtained for water-oil interaction are almost identical to the those calculated for water-methane interaction, and the helium isotopic composition is consistent with a contribution of 12 to 28% mantle-derived helium for the majority of our samples if the mantle endmember is characterized by 8 R_A.

It should be emphasized that variations in subsurface temperatures encountered by oil (25-150°C) do not significantly affect the conclusions reached in this study. We chose a temperature of 9°C (i.e., the temperature of the cold seep fluids at discharge) to model water-oil interaction. For a higher temperature, i.e., a greater depth, the solubility differences between helium and neon in water are lower, resulting in a smaller Rayleigh fractionation coefficient, e.g., α = 1.078 at 50°C. In this case, the excess air component must be even more fractionated (i.e., $(He/Ne)_a \leq 0.08$) for the modeled fractionation curve to explain the observed He-Ne relationships. The resulting values for the terrigenic helium component, however, still range from 1.0 to 2.1 R_A for the majority of our samples.

The general conclusion that emerges from the above discussion is that the helium and neon characteristics observed in Extrovert Cliff fluids can be explained by noble gas stripping due to interaction of the water with either methane or oil within the aquifer. In both cases, the noble gas components consist of air-equilibrated He and Ne, fractionated excess air, and a significant fraction of both mantle-derived and crustal helium.

II.6.3 Temporal variation of the helium and neon characteristics

In this section, we consider the temporal variations of the dissolved volatile content in Extrovert Cliff seep fluids. Figure II.5 shows the variation of the dissolved helium and neon content in one coil of the August deployment (CAT meter 2) over a period of about 5.5 days (136 h). We show results obtained for both longer coil sections (low-resolution analyses) and short coil sections (high-resolution analyses). Also included in Figure II.5 are the flow rate and the tidal height record (i.e., water level) for Monterey Bay (NOAA data; http://tidesandcurrents.noaa.gov/). Time (in hours) is given relative to the start of sampling on 4 August 2004 at 1200 local time.

The measured helium and neon concentrations (^4He_m and Ne_m) fluctuate remarkably over time-scales of only a few hours (Figs. II.5a and II.5b). According to our model, changes in the neon content result from varying degrees of noble gas stripping by hydrocarbons (methane or oil), while fluctuations of the helium content are further affected by a variable addition of terrigenic helium. The temporal record reveals that the degree of noble gas depletion by stripping and/or the contribution of terrigenic helium ($^4He_{terr}$, Fig. II.5b) in Extrovert Cliff seep fluids are highly variable over the given time period. Fluctuations in the degree of stripping are more pronounced and seem to be more episodic during the time period covered by the low-resolution data. Furthermore, the contribution of terrigenic helium appears to increase towards the end of the 5.5-day period. In this respect, we note that LaBonte et al.

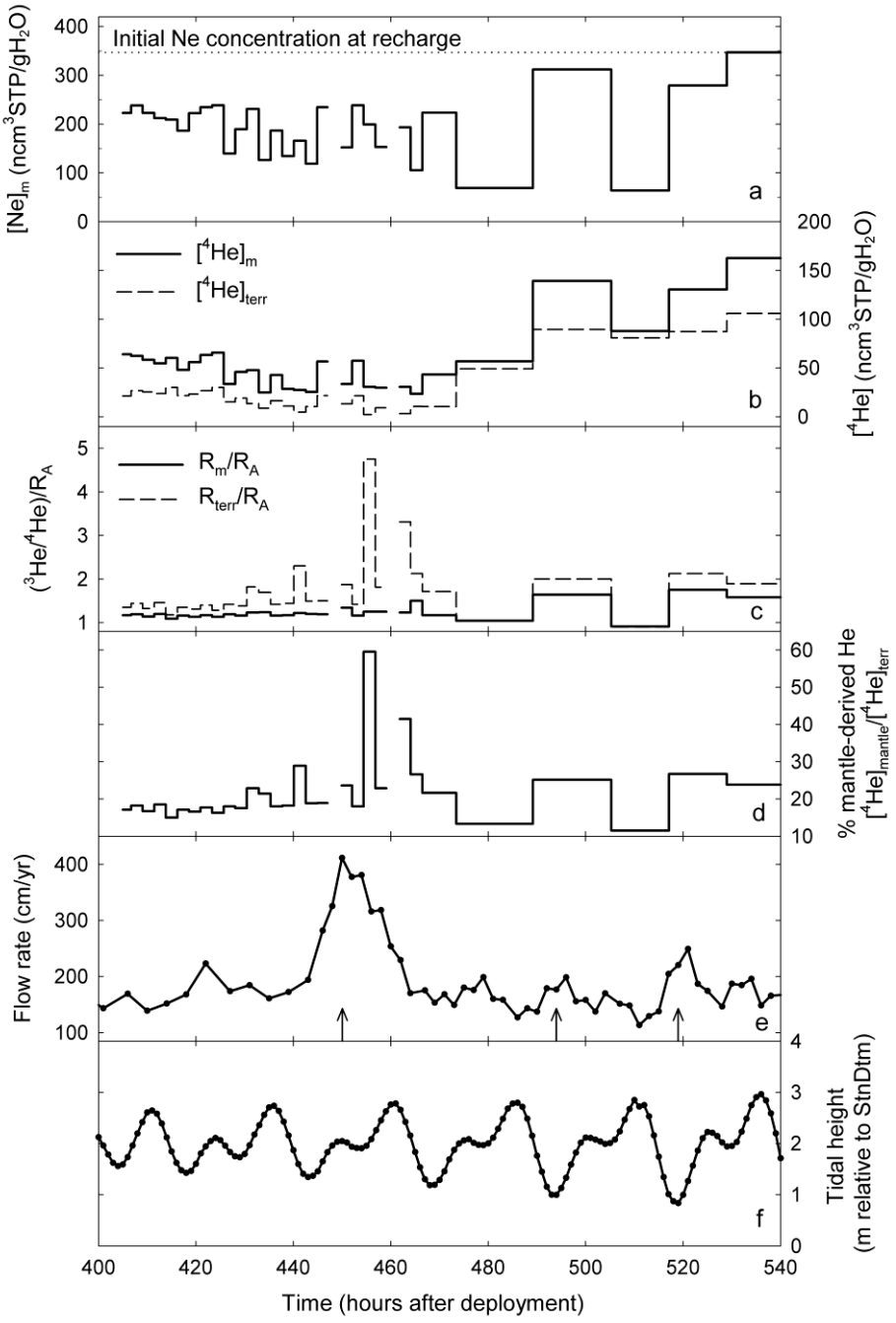

Figure II.5: Temporal variation of a) the measured Ne concentration, b) the measured ^{4}He and calculated terrigenic ^{4}He concentrations, c) the measured ^{3}He/^{4}He ratio (R_m/R_A) and calculated R_{terr}/R_A ratio, and d) the fraction of mantle He in seep fluids collected with CAT meter 2. Also shown are e) the seep flow rate and f) the tidal height record. Time (in hours) is given relative to the start of sampling on 4 August 2004 at 1200 local time. $[^4He]_{terr}$ and R_{terr}/R_m values are shown for water-methane interaction of a fluid with a fractionated excess air component. Arrows indicate times of increased flow rates (see section II.6.3 for details).

(2007) observed a long-term variation in the flow rate and the temperature of seep fluids at Extrovert Cliff. Thus, some of the observed fluctuations in the contribution of terrigenic helium may be related to long-term oscillations that would only be fully revealed by studying a much longer section of the sampling coil. Furthermore, we note that the isotopic characteristics of the dissolved helium vary over time. Measured $^{3}He/^{4}He$ ratios increase from 1.2 to 1.5 R_A within just 2.5 h (e.g., at t = 464 h; Fig. II.5c), and a maximum increase from 0.9 to 1.75 R_A is observed in the data record with the lower time-resolution (at t = 517 h; Fig. II.5c). However, the important point to note in Figure II.5c is that variations in the measured He isotopic composition are subdued due to the large amount of atmospheric helium in the fluids. The terrigenic helium isotope ratio (R_{terr}/R_A, Fig. II.5c) calculated for water-methane interaction, is shifted to higher values than the measured $^{3}He/^{4}He$ ratio for the majority of our samples and shows significantly more pronounced temporal variations. These changes in the isotopic composition of the terrigenic helium component are consistent with fluctuations in the contribution of mantle-derived helium.

The observed variations in the mantle contribution to the He inventory in Extrovert Cliff seep fluids (Fig. II.5d) appear to be related to changes in the flow rate (Fig. II.5e). For example, at t = 450 (hours after deployment), there is a factor of 2.5 increase in flow rate (to ~400 cm/a) with a corresponding spike in R_{terr}/R_A and percentage mantle contribution. At t = 494 and t = 519, there is a more muted increase in flow rate with a correspondingly smaller increase in mantle He contribution. LaBonte et al. (2007) showed that seep flow rates at Extrovert Cliff vary with tidal overburden pressures, i.e., flow rates are high under low tidal load. Variable tidal loading may explain some of temporal variability in the helium and neon characteristics of the seep fluids – particularly at t = 494 and t = 519 (Fig. II.5). Notably, a decrease in tidal forcing appears to drive the release of fluids characterized by higher $^{3}He/^{4}He$

values, presumably from greater depths, into the confined aquifer that is the source of fluid seepage at Extrovert Cliff.

We note, however, that the spike in flow rate between hours 440 to 460 (i.e., the sampling interval covered by samples Mont3_02_18 to Mont3_02_20; Table II.2) cannot be explained by variations of the tidal loading alone (Fig. II.5f). The elevated flow rate over this period does not appear to affect the degree of noble gas stripping, which would lead to variations in the measured neon content (Fig. II.5a), yet it clearly correlates with significantly higher terrigenic $^3He/^4He$ ratios (R_{terr}/R_A) and a greater contribution of mantle-derived helium (Figs. II.5c and II.5d, respectively). We speculate that the increase in flow rate and the associated spike in R_{terr}/R_A can be explained by a significant flux of fluids from a deep source characterized by helium with a higher $^3He/^4He$ value.

II.6.4 Mantle helium at the SAF

Fluids ascending through the faulted crust in the region of the SAF contain mantle-derived helium, as indicated by elevated $^3He/^4He$ ratios observed in groundwater samples collected in central and south-central California (Kennedy et al., 1997), in the Mojave River and East Morongo basins (Kulongoski et al., 2003; Kulongoski et al., 2005) as well as in matrix fluids and mud gas samples from the San Andreas Observatory at Depth (SAFOD) Main Hole (Stute et al., 2005; Thordsen et al., 2005; Wiersberg and Erzinger, 2007). In addition, fluid inclusions in fault zone material collected near and along the SAF between San Francisco and Los Angeles also have $^3He/^4He$ ratios up to 2.5 R_A (Pili et al., 1998). Our new data from Extrovert Cliff show that increased $^3He/^4He$ ratios occur in seep fluids emanating at ~1 km water depth in Monterey Bay, indicating that the high helium isotope province associated with the San Andreas Fault Zone extends well off-shore. We propose that the near-vertical strike-slip faults and subsidiary cross faults that cut across Monterey Bay sub-parallel

to the main San Andreas Fault trace (Greene et al., 1999) represent permeable conduits that allow mantle fluids to leak through the crust and impart elevated $^{3}He/^{4}He$ ratios to aquifers nominally characterized by crustal fluids alone.

Kennedy et al. (1997) and Kennedy and van Soest (2007), on the basis of high $^{3}He/^{4}He$ ratios in water samples from the SAF and the Basin and Range Province, respectively, proposed that mantle fluids can traverse the ductile lower crust along permeable fractures with the resulting high fluid pressures contributing to fault-weakening at seismogenic depths. This hypothesis builds upon the model by Rice (1992), who suggested that continuous migration of fluids from a deep source (i.e., the lower crust or uppermost mantle) through the core of a fault can cause high pore pressures within the slip zone of the fault. However, pore fluid pressures (Zoback et al. 2006), and the proportion of mantle fluids within the core of the SAF (Wiersberg and Erzinger, 2007) are not anomalously high. Therefore, Wiersberg and Erzinger (2007) suggested that mantle-derived fluids may disperse laterally and ascend along more permeable faults in the region. Preferential migration of mantle fluids through the San Gregorio or Monterey Bay fault zones could explain why elevated $^{3}He/^{4}He$ ratios are observed in submarine seep fluids emanating at Extrovert Cliff, ~30 km away from the main SAF trace.

The correlation of high $^{3}He/^{4}He$ ratios with a transient pulse in the flow rate at Extrovert Cliff indicates that the release of mantle-derived fluids is episodic and cannot be explained by pressure changes due to the variable tidal load alone. In this respect, the controlling factor is likely episodic fracturing in the San Gregorio or Monterey Bay fault zones. In such a scenario, continuous ascent of mantle fluids through the crust increases pore fluid pressure until it overcomes the least principle stress, resulting in hydrofracturing and release of fluid (Nur and Walder, 1990). The observation of nonvolcanic tremors beneath the SAF (Nadeau and Dolenc, 2005) may be related to the movement of deeply-sourced fluids, as suggested for subduction zone tremors in Japan (Obara, 2002). Alternatively, episodic tremors

may be caused by slow slip events, in which case fluids possibly play an important role by regulating the shear strength of rock (Rogers and Dragert, 2003).

While it is possible that episodic leakage of mantle fluids at Extrovert Cliff is related to the earthquake-cycle, our temporal record of the helium characteristics is too short to unravel the cause of short-term changes in fluid composition and/or flow rate. Continuous sampling of seep fluids or groundwaters along the SAF over an extended period of time is required to confirm any relationship between geochemical signals and seismic activity in the region.

II.7 Conclusion and implications

The Extrovert Cliff deployments demonstrate that both the modified CAT meter and OTIS, with the addition of gas sampling capability, successfully capture submarine fluids for postrecovery analysis of their noble gas characteristics.

The quasi-continuous record of the volatile chemistry of Extrovert Cliff seep fluids reveals that the helium and neon abundances are highly variable over time. The observed noble gas characteristics of Extrovert Cliff seep fluids can be explained by both water-methane and water-oil interaction within the aquifer. While the helium and neon characteristics are dominated by variable degrees of noble gas fractionation by stripping, there is clear evidence for a significant contribution of mantle-derived helium. The observed transient pulse in the release of mantle fluids could be related to episodic fault rupture.

The significant variability in noble gas concentrations, isotopic composition and flow rates of the seep fluids demonstrates the necessity for continuous sampling over longer time periods in order to detect transient earthquake-induced changes in the volatile record at fault zones.

II.8 Acknowledgements

We are grateful to the National Undersea Research Program (NURP) of NOAA (National Oceanographic and Atmospheric Administration) for funding instrument development and sea-going activities (grant UAF040034). Captain and crew of MBARI's R/V *Point Lobos* and the ROV *Ventana* team are thanked for their professional support at sea. Analytical developments in the Fluids & Volatiles Laboratory and sample analysis costs were supported by NSF (OCE-0242034). We thank F. Italiano, S. Gilfillian, and an anonymous reviewer for comments.

This chapter appeared in full as E. Füri, D. R. Hilton, K. M. Brown, and M. D. Tryon (2009), Helium systematics of cold seep fluids at Monterey Bay, California, USA: Temporal variations and mantle contributions, *Geochemistry Geophysics Geosystems*, 10, Q08013, doi:10.1029/2009GC002557. The dissertation author was the primary investigator and lead author of this paper and conducted all of the analyses presented herein.

Chapter III Carbon release from submarine seeps at the Costa Rica fore-arc: Implications for the volatile cycle at the Central America convergent margin

III.1 Abstract

We report total dissolved inorganic carbon (DIC) abundances and isotope ratios, as well as helium isotope ratios ($^3He/^4He$), of cold seep fluids sampled at the Costa Rica fore-arc in order to evaluate the extent of carbon loss from the submarine segment of the Central America convergent margin. Seep fluids were collected over a 12-month period at Mound 11, Mound 12, and Jaco Scar using copper tubing attached to submarine flux meters operating in continuous pumping mode. The fluids show *minimum* $^3He/^4He$ ratios of 1.3 R_A (where R_A = air $^3He/^4He$), consistent with a small but discernable contribution of mantle-derived helium. At Mound 11, $\delta^{13}C_{\sum CO2}$ values between -23.9 to -11.6 ‰ indicate that DIC is predominantly derived from deep methanogenesis and is carried to the surface by fluids derived from sediments of the subducting slab. In contrast, at Mound 12, most of the ascending dissolved methane is oxidized due to lower flow rates, giving extremely low $\delta^{13}C_{\sum CO2}$ values ranging from -68.2 to -60.3 ‰. We estimate that the carbon flux (CO_2 plus methane) through submarine fluid venting at the outer fore-arc is 8.0×10^5 g C $km^{-1}yr^{-1}$, which is virtually negligible compared to the total sedimentary carbon input to the margin and the output at the volcanic front. Unless there is a significant but hitherto unidentified carbon flux at the inner fore-arc, the implication is that most of the carbon being subducted in Costa Rica must be transferred to the (deeper) mantle, i.e., beyond the depth of arc magma generation.

III.2 Introduction

Subduction zones represent the major avenues for geochemical cycling between Earth's major external reservoirs - the oceans, sediments and oceanic/continental crust - and Earth's interior, i.e., both shallow and deep mantle. Water and other volatiles (e.g., carbon, nitrogen, and sulfur), released from the subducting crust and sediments as the oceanic lithosphere descends into the mantle and experiences progressively higher pressures and temperatures, control fundamental processes in the subduction zone. At shallow levels, the water and carbon fluxes influence the formation and destruction of gas hydrates, and support chemosynthetic vent communities in the outer fore-arc region (Judd and Hovland, 2007; Judd, 2003). At greater depths, excess pore fluid pressures reduce the strength of faults and may control the updip limit of the seismogenic zone (e.g., Byrne et al., 1988; Moore and Safer, 2001; Ranero et al., 2008). Deeper still, volatiles released from the subducting slab may serpentinize the over-riding plate and promote the generation of hydrous partial melts in the mantle wedge (Tatsumi and Eggins, 1995). Finally, any volatiles that are not lost by fluid flow, dehydration, decarbonation reactions and/or magma generation at the volcanic front will be carried into Earth's deep mantle.

The fate of carbon during subduction zone processes is a poorly known component of Earth's natural carbon cycle. Estimates of the total carbon flux associated with volcanism at the Central America volcanic front have shown that the output flux is only 12 - 18% of the carbon which is potentially available by input via the trench (Hilton et al., 2002; Shaw et al., 2003; de Leeuw et al., 2007). This result indicates that either carbon is efficiently recycled to the (deeper) mantle, i.e., the mantle beyond the zone of arc magma generation, or significant losses of carbon occur in the fore-arc or back-arc regions. Significantly, thermodynamic modeling by Gorman et al. (2006) predicts efficient release of CO_2 from the top of the subducting slab at relatively shallow depths (i.e., between ~65 and 80 km depth) beneath the

fore-arc in Central America, and de Leeuw et al. (2007) argued that subducted sediments do not represent a direct source of CO_2 to the back-arc region. Therefore, direct measurements of volatile fluxes and compositions in the fore-arc region are critical for completing the carbon mass balance for the Central America convergent margin. The numerous submarine fluid venting sites offshore Nicaragua and Costa Rica are obvious targets for assessing the carbon flux at the outer fore-arc region.

In this contribution, we report the dissolved volatile characteristics of well-mapped fluid venting sites (Mound 11, Mound 12, and Jaco Scar; Figure III.1) at the submarine segment of the Costa Rica fore-arc margin. Measurements of the $^{3}He/^{4}He$ ratios and $\delta^{13}C_{\sum CO2}$ values are used to assess the provenance of dissolved helium and carbon, respectively, dissolved in the seep fluids. In addition, through use of an innovative sampling approach coupling copper sampling coils to submarine flux meters (Tryon et al., 2002; Füri et al., 2009), we evaluate the extent of temporal variability in the volatile characteristics over a 12-month period. The observed DIC abundances, together with previous estimates of methane fluxes (Mau et al., 2006), allow limits to be placed on the total flux of carbon (CO_2 plus methane) released via submarine fluid venting at mound structures at the Costa Rica outer fore-arc. This flux estimate represents an important element of the total fore-arc flux and provides essential input to help complete the carbon mass balance for the Central America convergent margin.

III.3 Geologic setting and background

At the Costa Rica margin, the Cocos Plate subducts beneath the Caribbean Plate at a convergence rate of ~85 mm/yr (DeMets, 2001; Kimura et al., 1997). Generation of the oceanic lithosphere at two different spreading centers and interaction with the Galápagos hotspot results in along-strike variations in the morphology of the incoming Cocos Plate. Relatively smooth oceanic crust, originating from the East Pacific Rise, subducts northwest of

the Nicoya Peninsula in Costa Rica. Further to the southeast, the incoming plate, generated at the Cocos-Nazca spreading center, exhibits a rough surface with numerous seamounts (von Huene et al., 2000). The subduction of seamounts causes severe deformation and subduction erosion of the over-riding plate (Fisher et al., 1998; Ranero and von Huene, 2000; von Huene et al., 2000). Mass removal from the upper plate results in subsidence, extension and formation of normal faults, which may act as pathways for ascending fluids (Mc Intosh and Silver, 1996; Ranero and von Huene, 2000).

The incoming sedimentary section of the Cocos Plate is relatively thin (~380 m). It can be divided into three units: the uppermost unit is composed of diatomaceous ooze with ash and sand layers, the underlying unit consists of silty clay with ash layers, and the lowermost unit comprises calcareous and siliceous ooze (Kimura et al., 1997). Results obtained during Ocean Drilling Program (ODP) Leg 170 revealed that nearly the entire column of incoming sediments is underthrust beneath the toe of the Caribbean Plate without frontal offscraping or sediment accretion, indicating that the Costa Rica margin is either non-accretionary or that underplating may be taking place further landward (Kimura et al., 1997; Vannucchi and Tobin, 2000). Underthrusting leads to rapid compaction of the upper hemipelagic sediments and dewatering of pore water within the first few kilometers of subduction (Shipley and Moore, 1986; Shipley et al., 1990; McIntosh and Sen, 2000; Saffer et al., 2000; Saito and Goldberg, 2001; Spinelli and Underwood, 2004). In addition to mechanically induced shallow dewatering near the toe of the over-riding plate, deep-sourced fluids are released by mineral dehydration reactions and phase transformations at depths of ~10 to 15 km (between ~60-140ºC) (Spinelli and Saffer, 2004; Spinelli and Underwood, 2004). While some of the deeply sourced fluids migrate along the décollement towards the deformation front (Chan and Kastner, 2000), most of the fluids released during dehydration reactions ascend through the over-riding plate along deep-penetrating faults, producing numerous fluid venting sites on the

continental slope of Costa Rica (Ranero et al., 2008). Detailed surveying of the seafloor off-shore Nicaragua and Costa Rica has revealed that fluid seepage is associated with mounds (i.e., cone-shaped or slightly elongated edifices, typically ≤1 km wide and 50–100 m high), faults, seamount subduction scars, and slope failures (Kahn et al., 1996; Bohrmann et al., 2004; Klaucke et al., 2008; Sahling et al., 2008; Ranero et al., 2008).

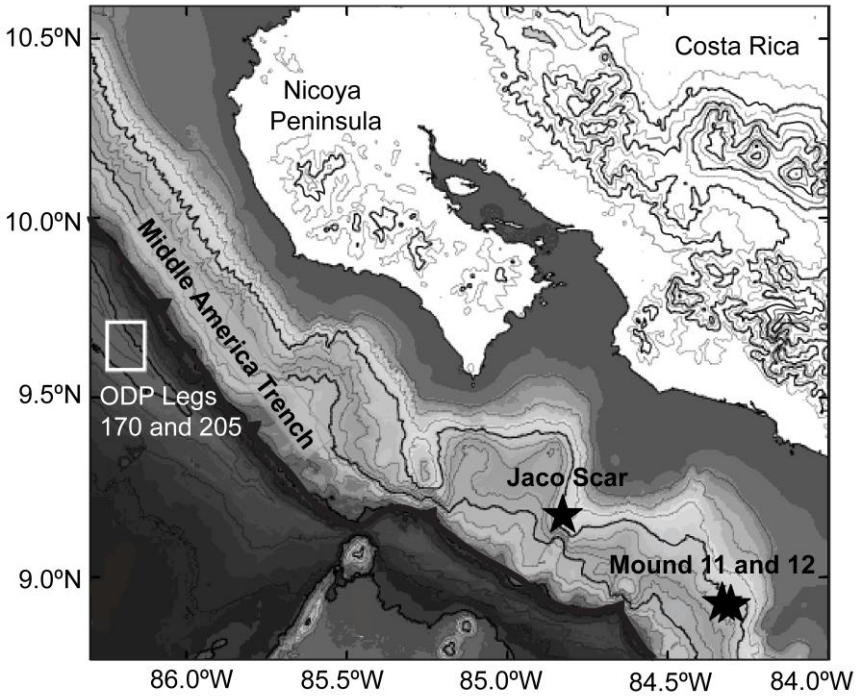

Figure III.1: Regional map of the Costa Rica segment of the Central America convergent margin showing the locations of Mound 11, Mound 12, and Jaco Scar, as well as ODP legs 170 and 205 (Kimura et al., 1997), at the outer fore-arc.

In this study, we target Mound 11, Mound 12 and Jaco Scar for sampling of seep fluids for their dissolved volatile characteristics. The three sampling sites are located southeast of the Nicoya Peninsula, ~30 km arc-ward from the Middle America Trench (Figure III.1). Jaco Scar is an 8 km-wide erosive structure formed by the subduction of a seamount (Huehnerbach et al., 2005). The landslide headwall consists of two distinct scarps at water depths between 800 and 1900 m (Bohrmann et al., 2005). Mound 11 and Mound 12 are two

mud volcanoes located at 1000 m water depth. Mound 12 has a cone-shaped summit several hundred meters in diameter that rises ~50 m above the seafloor, whereas Mound 11 is significantly smaller with two distinct summits that are about 15 m (11a) and 25 m (11b) high (Tryon et al., 2006; Tryon et al., 2009).

The seep sites at Mound 11, Mound 12 and Jaco Scar are characterized by the presence of authigenic carbonates and chemosynthetic communities (e.g., bacterial mats, vesicomyid clams, and/or tubeworm colonies) on the seafloor, as well as elevated methane concentrations in the water column (Bohrmann et al., 2002; Schmidt et al., 2005; Mau et al., 2006; Mau et al., 2007) and high concentrations of dissolved methane and sulfide in sediment pore waters (Hensen et al., 2004; Linke et al., 2005). Uniquely, gas hydrates and methane of a primarily thermogenic origin were recovered at Mound 11 (Schmidt et al., 2005). A deep origin of the methane-rich seep fluids emanating at Mound 11 was also proposed by Hensen et al. (2004) on the basis of the observed chlorinity depletion and boron enrichment, combined with the $\delta^{18}O$ and δD isotope composition of the fluids. The chemistry was interpreted to reflect fluid formation by clay-mineral dehydration within the subducted sediments and subsequent fluid ascent through the upper plate along deep-seated faults from ≥12 km depth, i.e., from a source depth near the updip limit of the seismogenic zone (e.g., Newman et al., 2002). However, seep fluid sampling at Mound 11 in 2005/6 revealed an unusually high B/Li ratio of the fluids, suggesting that the source may be a mixture of subducted sediment and eroded upper plate material (Tryon et al., 2009). Taken together, these observations indicate that Mound 11 may be one of the most active and deepest sourced fluid venting sites along the Central America convergent margin.

Previous attempts to quantify fluxes of fluids and chemical species (e.g., methane) at the mounds in the outer fore-arc region were based on observed methane concentrations in the near-bottom water (Mau et al., 2006) or involved geochemical modeling of measured heat

fluxes and concentration profiles in pore waters (Hensen et al., 2004; Linke et al., 2005; Ranero et al., 2008). However, published fluid flux estimates for five of the major mound structures (Mound Culebra, Mound 10, Mound 11, Mound 12, Mound Quepos) (Hensen et al., 2004; Linke et al., 2005; Mau et al., 2006) vary over several orders of magnitude between different sites and even at particular seep locations (Hensen et al., 2004; Mau et al., 2006).

III.4 Sampling and analytical techniques

Seep fluids were collected at Mound 11 and Mound 12 utilizing Chemical and Aqueous Transport (CAT) meters (see Tryon et al. (2001) for description) operating in continuous pumping mode. The submarine flux meters were deployed during cruise AT-11-28 in June 2005 using DSV *Alvin* operated from R/V *Atlantis*. After a period of 12 months, the instruments were retrieved from the seafloor for subsequent laboratory determination of flow rates, major ion concentrations and dissolved volatile (helium, neon and CO_2) characteristics. Additional near-bottom water samples were collected within a tubeworm field at Jaco Scar using major Ti-bottles during Alvin Dive 4131.

The CAT meter is designed to measure seep fluid flow at the seafloor by channeling fluids, sampled via a collection chamber placed over the focus of the seep, through the instrument. Plastic sampling coils preserve a serial record of major ion concentrations and seep fluid flow rates (inferred from the degree of dilution of a chemical tracer), whereas 1/8 inch diameter copper coils capture fluids for determination of dissolved volatile characteristics over the duration of the deployment (see Füri et al. (2009) for details on sampling procedures). We note that volatile anomalies are not significantly attenuated by diffusion or dispersion in the copper tubing, as discussed by Barry et al. (2009). The characteristic diffusion length (x) for helium in fresh water at 5°C is ~40 cm for a 12-month deployment ($x = \sqrt{Dt}$ where $D = 5.1 \times 10^{-5}$ cm^2/s (Jähne et al., 1987) and t = time). Thus, the helium signal may be slightly

impacted, and aliquots collected early during a deployment will experience greater diffusive smearing of a helium pulse compared to later samples. Dispersion of the signal is a potentially greater problem, with differential flow between water close to the tubing wall versus that in the center of the tube acting to smear out sharp concentration gradients. However, diffusion tends to counter this effect in small diameter tubes at low flow rates (Cussler, 1984). Furthermore, Tryon et al. (2001) found that dispersion and diffusion were insignificant during a 70-day submarine tracer test using 2.4 mm diameter tubing at a flow rate of ~1 m/day.

Following instrumentation recovery, the copper tubing was sectioned to produce a quasi-continuous temporal record of the dissolved volatile content. Based on the duration of the deployment and the location of the interface between the saline seep fluid and the deionized water which initially filled the coils, we calculated at fluid sampling rate of ~0.9 ml/day. Thus, each section of analyzed copper coil represents a specific time interval, with 0.4 m of coil corresponding to ~1 day of fluid sampling.

Copper coils were cut and sealed into sections of ~0.4 m length using refrigeration clamps, and attached to an ultra high vacuum system for sample extraction and processing (see Kulongoski and Hilton, 2002; Füri et al., 2009). The extraction system was interfaced directly to the noble gas mass spectrometer preparation line, so that the total helium and neon load released from the Cu coils was transferred to the MAP 215 noble gas mass spectrometer. Helium and neon abundances as well as the $^{3}He/^{4}He$ ratios were determined for a subset of seep fluid samples. Sample $^{3}He/^{4}He$ ratios and $^{4}He/^{20}Ne$ ratios were calibrated against air standards of known amount run under identical experimental conditions.

All fluid samples were acidified to ensure release of the total CO_2; consequently, CO_2 amounts represent the total dissolved inorganic carbon content. The CO_2 fraction of each sample was collected during the extraction procedure by freezing into a pyrex break-seal for transfer to a dedicated purification and measurement system. A variable temperature trap was

used to separate CO_2 from any other species after which the $\sum CO_2$ abundances were measured manometrically in a calibrated volume. The $\delta^{13}C_{\sum CO2}$ values, reported relative to the international reference standard Vienna Pee Dee Belemnite (VPDB), were measured from an aliquot of this gas using a VG Prism stable isotope mass spectrometer or a Delta V Isotope Ratio mass spectrometer.

III.5 Results

Following instrumentation recovery, the first step was determination of flow rates and major ion concentrations in the plastic sampling coils in order to identify which flux meters had recorded active seep fluid venting. In Table III.1, we show the chemical composition of seep fluids collected at mounds 11 and 12.

Table III.1: Chemical content of seep fluids from Mound 11a (CAT meter R29) and Mound 12 (CAT meters S28 and I22), as well as seawater values (IAPSO Standard) (Tryon et al., 2006; 2009).

	R29	S28	I22	Seawater
Cl (mM)	397	554	551	546
Ca (mM)	6.0	10.2	10.3	10.3
K (mM)	7.1	10.4	10.5	10.2
Mg (mM)	30	53	53	53
Na (mM)	322	478	473	470
B (μM)	881	397	422	416
Li (μM)	18.1	25.6	25.4	25.2
Sr (μM)	44.6	86.5	80.5	90.2

Fluids sampled at Mound 11a (CAT R29) show a low salinity and altered fluid chemistry with elevated B and low Ca, K, Mg, Na, Li and Sr concentrations relative to seawater. Flow rates were 2-5 cm/yr through most of the 12-month record. However, increased flow rates were measured near the beginning and end of our record, as well as in mid-October 2005 (Figure III.3c). At Mound 12, coil S28 recorded highly variable flow rates;

however, the chemistry of the sampled fluids is similar to seawater throughout the deployment. The sampling chamber connected to coil I22, also from Mound 12, was accidentally flipped over on October 9th 2005 during ROV operations on the site. Thus, after this date, CAT meter I22 sampled ambient bottom seawater, and the fluids are expected to have a seawater-like volatile content.

Since only CAT meter R29, deployed at Mound 11a, sampled fluids with chemistry altered from seawater values, we targeted this particular sampling coil for detailed volatile analyses in order to resolve any temporal variations of the dissolved CO_2 content of the captured fluids (section III.6.2).

III.5.1 Helium and neon abundances

Helium and neon results for a subset of submarine seep fluids collected at Mound 11a, Mound 12, and Jaco Scar are reported in Table III.2. Results are shown as measured ^4He and ^{20}Ne concentrations (^4He_m and $^{20}Ne_m$).

Measured helium concentrations (^4He_m) of seep fluids collected at mounds 11a and 12 range from 47.7 to 54.3 ncm^3STP/gH_2O, whereas the neon concentrations vary between 179.5 and 228.7 ncm^3STP/gH_2O (Table III.2). The helium and neon abundances are slightly higher than expected values for ambient air-saturated seawater (i.e., $[^4He]_{SW}$ = 40.3 ncm^3STP/gH_2O and $[^{20}Ne]_{SW}$ = 158.8 ncm^3STP/gH_2O at 5°C; Weiss, 1971), even for sample I22-1, which was collected after the sampling chamber had been decoupled from the seafloor. Near-bottom water samples from Jaco Scar, on the other hand, are significantly oversaturated in helium ($[^4He]_m \approx 85$ ncm^3STP/gH_2O) and depleted in neon ($[^{20}Ne]_m \approx 115$ ncm^3STP/gH_2O) relative to air-equilibrated seawater. Thus, these fluids show elevated $^4He/^{20}Ne$ ratios compared to ambient seawater, while the $^4He/^{20}Ne$ ratios of samples from the mounds are similar to or slightly lower than seawater values.

Table III.2: Helium and neon systematics of submarine seep fluids, Costa Rica.

Sample ID	$^3He/^4He$ (R_m/R_A)	$[^4He]_m$ ncm^3STP/gH_2O	$[^{20}Ne]_m$ ncm^3STP/gH_2O	$^4He/^{20}Ne$
Mound 11a: CAT meter R29				
R29-1	1.34 ± 0.03	47.9 ± 6.0	179.5 ± 18.3	0.27
R29-2	1.21 ± 0.03	47.8 ± 5.8	199.7 ± 20.3	0.24
R29-3	1.22 ± 0.03	52.8 ± 6.4	216.9 ± 22.0	0.24
R29-4	1.22 ± 0.03	54.3 ± 6.5	228.7 ± 23.2	0.24
R29-5	1.04 ± 0.02	49.7 ± 3.4	197.2 ± 20.1	0.25
Mound 12: CAT meter S28				
S28-1	1.24 ± 0.03	50.1 ± 6.0	222.8 ± 22.6	0.23
Mound 12: CAT meter I22				
I22-1	1.06 ± 0.03	50.5 ± 6.2	206.0 ± 20.9	0.25
Jaco Scar: Alvin Dive 4131				
Alvin major bottle	1.31 ± 0.03	84.4 ± 0.9	114.0 ± 1.2	0.74
Alvin major bottle	1.23 ± 0.06	86.7 ± 0.9	115.5 ± 1.2	0.75
Seawater (5°C)	1	40.3[a]	158.8[a]	0.25

All errors are reported at the 1 σ level. The smaller errors for $[^4He]_m$ and $[^{20}Ne]_m$ for the samples from Jaco Scar are due to the larger amounts of fluids processed and the correspondingly lower uncertainty on the measured gas concentrations.
[a] Amount of gas absorbed per volume of seawater when the partial pressure of the gas is 1 atm (Weiss, 1971), assuming an air-equilibration temperature of 5ºC. Note that the solubilities do not change significantly with temperature, e.g., $[^4He]_{eq}$ = 39.3 ncm^3STP/gH_2O at 15ºC.

III.5.2 $^3He/^4He$ ratios

Measured helium isotope ratios are reported in Table III.2 as R_m/R_A, where R_m = $^3He/^4He$ ratio measured in the sample and R_A = $^3He/^4He$ ratio of air = 1.4×10^{-6}.

The $^3He/^4He$ ratios range from 1.04 to 1.34 R_A and appear significantly higher that the isotope composition of helium produced in crustal lithologies by radioactive decay (~0.05 R_A; Andrews, 1985). Measured helium isotope ratios in water samples are usually corrected for the presence of atmosphere-derived helium – from air directly or water. By monitoring the sample He/Ne ratio and, assuming all the neon is derived from air or air-equilibrated water, the atmospheric helium component can be subtracted from the sample helium utilizing the known

He/Ne ratio of air or air-saturated water, respectively (Hilton, 1996). However, noble gas concentrations in pore fluids and seawater at submarine cold seep sites can be affected by the presence of methane gas bubbles (Brennwald et al., 2003; Han et al., 2004; Brennwald et al., 2005; Schmidt et al., 2005; Holzner et al., 2008; Füri et al., 2009). Gas exchange between the bubbles and the surrounding pore water in the sediment column can potentially strip dissolved gases from the fluid phase until either the gas bubbles escape or until equilibrium is established between gas concentrations in the bubbles and the surrounding fluid. Thus, stripping can decrease noble gas concentrations in pore fluids, and it can also lead to fractionation of noble gas elemental patterns, due to the systematic increase in water solubility and decrease in diffusion coefficients of the noble gases with increasing atomic mass (Ballentine et al., 2002; Leifer and Clark, 2002; Brennwald et al., 2003; Brennwald et al., 2005; Holzner et al., 2008). Bubbles preferentially strip helium due to its low solubility and/or high diffusivity, thereby decreasing the He/Ne ratio in the residual pore water. As escaping methane bubbles dissolve in the water column, however, helium is expected to be transferred to the bottom water at an early stage because it diffuses much faster out of the bubbles than neon.

We suggest that the neon depletion in near-bottom water samples collected at Jaco Scar indicates that seep fluids emanating at the Costa Rica margin have lost a fraction of their dissolved noble gases by interaction with methane bubbles. The helium enrichment, on the other hand, may be caused by noble gas dissolution from rising methane bubbles and/or addition of a terrigenic (i.e., crustal and/or mantle-derived) helium component. Since the noble gas elemental ratio prior to noble gas stripping for the deeply-sourced seep fluids is unknown, the observed $^{3}He/^{4}He$ ratios in our samples cannot be corrected for the presence of atmosphere-derived helium. However, subtracting the atmospheric helium component from the sample helium will result in a shift to higher helium isotope ratios for samples with

measured $^3He/^4He$ ratios > 1 R_A. Thus, all $^3He/^4He$ ratios which are greater than the atmospheric value represent minimum estimates for the air-corrected helium isotope composition. Therefore, these elevated ratios are consistent with a small but discernable contribution of mantle-derived helium (8 R_A; Graham et al., 2002) to fluids emanating along the submarine section of the Costa Rica fore-arc (see section III.6.1.1 for discussion).

III.5.3 Carbon abundances and isotope ratios

The $\sum CO_2$ abundances (i.e., total dissolved inorganic carbon) and carbon isotope ratios are reported in Table III.3 together with information on the specific sampling interval represented by each section of the analyzed coil. Thus, the sampling coils have preserved a record of the temporal variations of the dissolved carbon characteristics of the captured fluids.

Measured $\sum CO_2$ concentrations in the seep fluid samples range from 0.006 to 0.34 cm^3STP/gH_2O (Table III.3, Figure III.2). Fluids in coils R29 and S28 are supersaturated in $\sum CO_2$ with respect to seawater (i.e., $[\sum CO_2]_{SW} \approx 0.06$ cm^3STP/gH_2O in water from the deep Pacific; Simpson and Broecker, 1973), indicating addition of extraneous carbon. However, one near-bottom water sample collected at Jaco Scar and bottom seawater collected at Mound 12 with coil I22 appear to be undersaturated in $\sum CO_2$ relative to seawater. During our survey dives, we observed dense forests of vestimentiferan tubeworms and clam fields at Jaco Scar as well as extensive tubeworm colonies at Mound 12. Thus, the CO_2 depletion in the bottom seawater may results from uptake of DIC by the seep biota. The carbon isotope composition of one fluid sample collected at Jaco Scar is similar to ambient seawater (i.e., $\delta^{13}C_{\sum CO2} \approx 0.3$ ‰; Kroopnick, 1985), whereas the $\delta^{13}C_{\sum CO2}$ values of all other seep fluids samples range from -11 to -68‰. However, we note that extremely low $\delta^{13}C_{\sum CO2}$ values (< -60‰) are only observed in one sampling coil at Mound 12 (i.e., CAT meter S28).

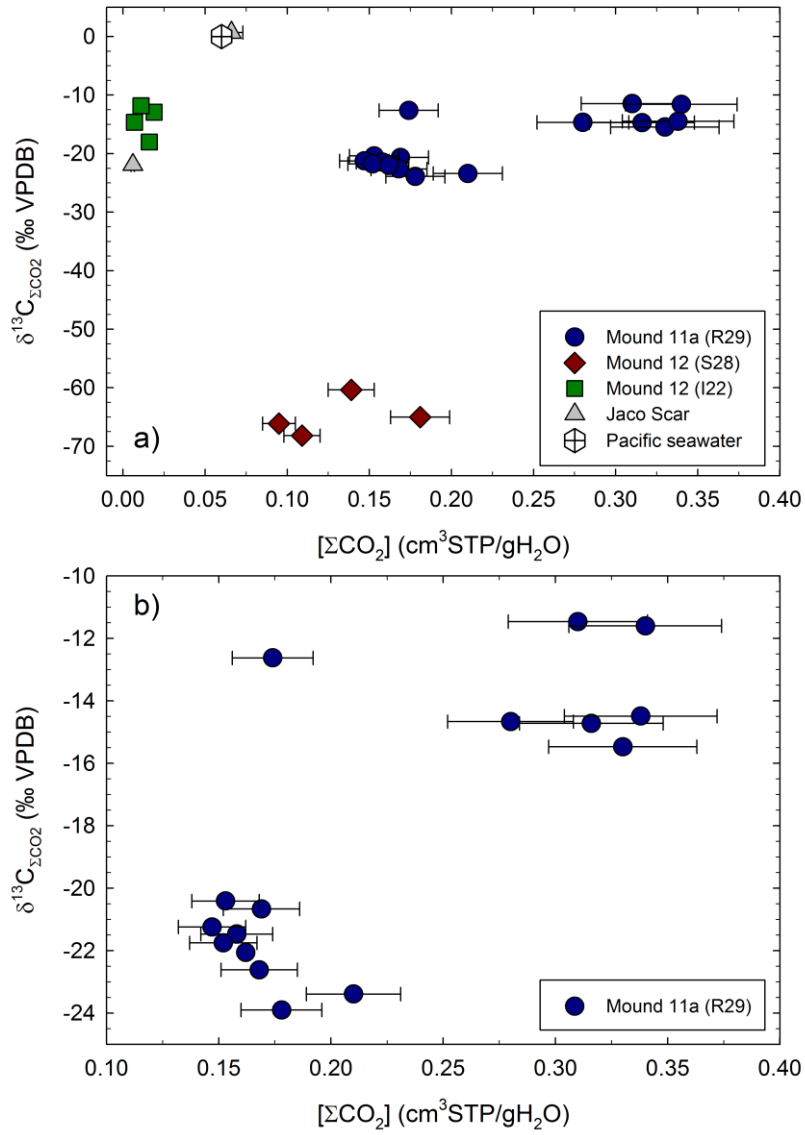

Figure III.2: a) Carbon isotope composition, $\delta^{13}C_{\sum CO2}$, versus measured $\sum CO_2$ (i.e., total dissolved inorganic carbon concentrations) for seep fluids collected at Mound 11a (CAT meter R-29), Mound 12 (CAT meters S28 and I22), and Jaco Scar (Alvin major Ti-bottles), as well as deep Pacific seawater (Kroopnick, 1985; Simpson and Broecker, 1973), and b) expanded version showing the data for Mound 11a (CAT meter R-29) only. Errors are shown at the 1σ level.

Table III.3: Carbon systematics of submarine seep fluids, Costa Rica.

Sample ID	Section in coil (m from inlet)	Time elapsed after deployment (days)	$[\sum CO_2]$ $cm^3STP/\ gH_2O$	$\delta^{13}C_{\sum CO2}$ (‰ VPDB)
Mound 11a: CAT meter R29				
R29-1	136.75-137.16	30 (07/10/05)	0.17 ± 0.02	-12.62 ± 0.02
R29-2	106.17-106.58	106 (09/24/05)	0.31 ± 0.03	-11.46 ± 0.02
R29-6	105.76-106.17	107 (09/25/05)	0.28 ± 0.03	-14.67 ± 0.02
R29-7	105.36-105.76	108 (09/26/05)	0.18 ± 0.02	-23.90 ± 0.03
R29-8	104.95-105.36	109 (09/27/05)	0.21 ± 0.02	-23.39 ± 0.02
R29-9	103.73-104.95	110 (09/28/05)	0.34 ± 0.03	-11.60 ± 0.02
R29-10	102.51-103.73	113 (10/01/05)	0.17 ± 0.02	-20.66 ± 0.03
R29-11	101.29-102.51	116 (10/04/05)	0.32 ± 0.03	-14.72 ± 0.02
R29-12	100.07-101.29	119 (10/07/05)	0.15 ± 0.02	-20.41 ± 0.04
R29-13	98.85-100.07	122 (10/10/05)	0.16 ± 0.02	-21.47 ± 0.02
R29-14	97.64-98.85	125 (10/13/05)	0.17 ± 0.02	-22.61 ± 0.04
R29-15	96.42-97.64	128 (10/16/05)	0.15 ± 0.02	-21.24 ± 0.04
R29-16	95.20-96.42	131 (10/19/05)	0.15 ± 0.02	-21.75 ± 0.05
R29-3	75.72-76.12	182 (12/09/05)	0.33 ± 0.03	-15.47 ± 0.01
R29-4	45.38-45.78	258 (02/21/06)	0.34 ± 0.03	-14.49 ± 0.02
R29-5	0-0.41	371 (06/15/06)	0.16 ± 0.01	-22.06 ± 0.01
Mound 12: CAT meter S28				
S28-1	136.75-137.16	30 (07/10/05)	0.14 ± 0.01	-60.35 ± 0.02
S28-2	13635-136.75	31 (07/11/05)	0.18 ± 0.02	-65.02 ± 0.07
S28-3	135.94-136.35	32 (07/12/05)	0.11 ± 0.01	-68.18 ± 0.03
S28-4	135.53-135.94	33 (07/13/05)	0.10 ± 0.01	-66.11 ± 0.04
Mound 12: CAT meter I22				
I22-4	1.34-1.75	367 (06/11/06)	0.007 ± 0.001	-14.65 ± 0.29*
I22-3	0.94-1.34	368 (06/12/06)	0.011 ± 0.001	-11.83 ± 0.47*
I22-2	0.53-0.94	369 (06/13/06)	0.019 ± 0.001	-12.96 ± 0.33*
I22-1	0.13-0.53	370 (06/14/06)	0.016 ± 0.001	-18.03 ± 0.01
Jaco Scar: Alvin Dive 4131				
Alvin major bottle			0.006 ± 0.001	-21.90 ± 0.01
Alvin major bottle			0.066 ± 0.007	0.68 ± 0.02
Pacific seawater			0.06[a]	~0.3[b]

* $\delta^{13}C_{\sum CO2}$ values were determined on a Delta V Isotope Ratio mass spectrometer; all other $\delta^{13}C_{\sum CO2}$ values were determined on a VG Prism stable isotope mass spectrometer.

[a] Simpson and Broecker (1973)

[b] Kroopnick et al. (1985)

III.6 Discussion

Our survey of submarine seep fluids demonstrates that the volatile chemistry of fluids emanating at the Costa Rica margin shows significant spatial and temporal variability. In the following sections, we (1) evaluate the origin of dissolved volatiles in the seep fluids, and (2) attempt to quantify the fore-arc carbon output through submarine fluid venting.

III.6.1 Origin of dissolved volatiles

III.6.1.1 Mantle helium release at the Costa Rica fore-arc

Helium isotopes are a powerful tool to recognize mantle-crust interactions in a variety of geotectonic settings. The rare isotope (^{3}He) is essentially primordial and retained in the Earth's interior whereas ^{4}He is continuously produced by the decay of U and Th. Thus, any ^{3}He/^{4}He ratio in terrestrial fluids greater than the local crustal production rates (i.e., ratios significantly greater than values of ~0.05 R_A; Andrews, 1985) indicates the presence of mantle-derived helium.

Seep fluids collected at Mound 11, Mound 12, and Jaco Scar show *minimum* helium isotope ratios of 1.3 R_A (see section III.5.2), suggesting that mantle-derived helium is released by submarine fluid venting at the Costa Rica fore-arc. Furthermore, groundwaters collected on the Nicoya Peninsula and the adjacent coast also show ^{3}He/^{4}He ratios between 0.45 and 3 R_A, which equates to a mantle contribution up to ~38 % of the total He in these fluids (Hilton et al., 2009). Magmatic activity can be ruled out as the source of mantle helium in this region. Notably, however, high ^{3}He/^{4}He ratios (i.e., greater than crustal production rates) have previously been reported for other fore-arc regions, such as SW Japan (Matsumoto et al., 2003; Dogan et al., 2006; Umeda et al., 2006; Umeda et al., 2007), New Zealand (Giggenbach et al., 1993), the Nankai Trough (Kastner et al., 1993), the Cook Inlet of Alaska (Poreda et al., 1988), and the Solomon Islands (Trull et al., 1990). In fore-arc regions, slab-derived fluids

may acquire mantle helium during their ascent through the serpentinized mantle wedge. While seismic velocities along the Nicoya Peninsula are consistent with the presence of a serpentinized fore-arc mantle wedge in Costa Rica, the continental Moho intersects the downgoing oceanic slab ~100 km arc-ward from the trench at a depth of 30–34 km (DeShon and Schwartz, 2004). Mound 11, Mound 12 and Jaco Scar are located significantly closer to the trench and thus, a mantle wedge is not present beneath the sampled seep locations. However, it has previously been suggested that the Costa Rica margin contains several oceanic igneous basement complexes, formed from a primitive mantle source (Sinton et al., 1997; Kerr et al., 1998; Hauff et al., 2000). The Nicoya Complex marks the westernmost edge of the Caribbean Large Igneous Province (CLIP)**,** an oceanic plateau produced by massive volcanism over the Galápagos hotspot. It formed between 95 and 83 Ma and consists of tholeiitic volcanics (pillow lavas and massive sheet flows), locally intruded by gabbros and plagiogranites (Hauff et al., 2000; Sinton et al., 1997). In addition, lavas described as komatiites have been located on the Nicoya Peninsula (Alvarado et al., 1997). In contrast, the Quepos Complex (65-59 Ma; Hauff et al., 2000), further to the southeast, is thought to represent an accreted seamount of the early Galápagos hotspot track (Sinton et al., 1997). Olivine separates of two enriched picrites collected at Quepos show high $^{3}He/^{4}He$ ratios of ~12 R_A, consistent with a helium contribution from the Galápagos hotspot (Hauff et al., 2000b). Thus, if the fore-arc basement rocks in Costa Rica can be linked to the Galápagos hotspot or the CLIP, fluids derived from compaction and/or dehydration of subducting slab sediments and eroded fore-arc material may acquire a high-^{3}He signature during serpentinization within the subduction channel and upper plate.

Alternatively, Umeda et al. (2006) proposed that aqueous fluids generated by dehydration of the downgoing slab may entrain helium derived from the mantle lithosphere portion of the down-going plate. As the fluids migrate to the surface, the original $^{3}He/^{4}He$ ratio

is lowered by addition of radiogenic ^{4}He from the crust and/or mixing with shallow fluids. Thus, mantle helium released through submarine fluid venting at the Costa Rica fore-arc possibly originates from the lithospheric mantle of the Cocos Plate. Kennedy et al. (1997; 2007) showed that crustal faulting plays an important role in the transfer of mantle-derived helium through the crust. In this case, normal faults within the toe of the Caribbean Plate would represent the permeable conduits that allow mantle fluids to leak through the crust and impart elevated $^{3}He/^{4}He$ ratios to the seep fluids emanating at Mound 11, Mound 12 and Jaco Scar. We note that assessing the helium provenance for fluids released along the Costa Rica fore-arc is the topic of continuing studies (e.g., Hilton et al., 2009) and is beyond the scope of this contribution.

III.6.1.2 Dissolved inorganic carbon in Costa Rica seep fluids

The DIC content of seep fluids emanating at the Costa Rica fore-arc may be derived from a number of potential sources. These include: 1) seawater, 2) methanogenesis, 3) in situ oxidation of marine organic matter, 4) anaerobic methane oxidation, 5) precipitation/dissolution of authigenic carbonates, and/or 6) the mantle. The isotope composition of the DIC can, in principle, be used to distinguish between these possibilities and identify its origin. However, interplay of various processes and mixing of DIC derived from several sources severely impedes a definitive assessment of the origin of DIC in the seep fluids sampled at Mound 11, Mound 12, and Jaco Scar.

The carbon isotope composition, $\delta^{13}C_{\sum CO2}$, of the collected seep fluids is significantly lower than that of eastern Pacific seawater (~0.3 ‰ at 1 km depth; Kroopnick, 1985), except for one near-bottom water sample collected at Jaco Scar. Consequently, ocean bottom water can be ruled out as the dominant source of DIC in the fluids sampled at mounds 11 and 12.

Methanogenesis by bacterial CO_2 reduction below the sulfate reduction zone,

$$CO_2 + 4H_2 \rightarrow CH_4 + H_2O, \qquad \text{(III.1)}$$

probably represents the principal mechanism for biogenic methane formation in marine sediments (Whiticar and Faber, 1986). Methanogenesis produces isotopically depleted methane ($\delta^{13}C_{CH4}$ = -110‰ to -50‰) and a ^{13}C-enriched DIC pool due to a fractionation effect of about 60‰ (Whiticar, 1999). At the Costa Rica fore-arc, methane and residual DIC are likely carried from depth to the surface at cold seep sites by upward flow of fluids derived from sediments of the subducting slab (Hensen et al., 2004). Indeed, previous work has shown that DIC in pore waters at Mound 11 has an isotopic signature of methanogenesis, with $\delta^{13}C_{DIC}$ values up to +20‰ (Han et al., 2004). However, the $\delta^{13}C_{\sum CO2}$ values observed in our study at mounds 11 and 12 are significantly lower, i.e., between -11 to -68‰, suggesting that a significant fraction of DIC in our samples is derived from oxidation of ascending isotopically depleted methane.

One of the main biogeochemical processes within the sediments at cold seep sites is the microbially-mediated anaerobic oxidation of methane via sulfate reduction according to the reaction (Boetius et al., 2000):

$$CH_4 + SO_4^{2-} \rightarrow HCO_3^- + HS^- + H_2O. \qquad \text{(III.2)}$$

Thus, when fluid flow rates are low, the ascending dissolved methane is completely oxidized by this process, which generates DIC with a $\delta^{13}C$ range reflecting mainly the isotope composition of oxidized methane. At Mound 11, bottom water methane has a carbon isotope ratio of ~ -45‰, whereas $\delta^{13}C_{CH4}$ values at Mound 12 are about 30‰ lower ($\delta^{13}C_{CH4} \approx$ -75‰), indicating a deep (thermogenic) source of methane, i.e., methane generation by degradation of organic matter within the subducted slab (Han et al., 2004; Schmidt et al., 2005). Therefore, $\delta^{13}C_{\sum CO2}$ values between -68‰ to -60‰ in seep fluids collected at Mound 12 appear consistent with a significant contribution of carbon derived from oxidation of thermogenic methane.

Aside from anaerobic methane oxidation, microbial oxidation of marine organic

matter can produce ^{13}C-depleted DIC in the pore waters of deep-sea sediments. Above and within the zone of sulfate reduction, oxidation of sedimentary organic matter produces DIC that inherits the low $\delta^{13}C$ values of the organic carbon (-20‰ to -25‰), assuming little or no fractionation during organic matter oxidation:

$$CH_2O + SO_4^{2-} \rightarrow \sum CO_2 + S^{2-} + 2H_2O, \qquad \text{(III.3)}$$

where CH_2O represents organic matter. While organic matter degradation likely represents an important source of DIC for the sampled seep fluids, $\delta^{13}C_{\sum CO2}$ values at Mound 12 are significantly lower than is possible if the DIC originates from oxidation of sedimentary organic matter alone.

We note that extensive carbonate crusts and large carbonate rocks were observed during our survey of Mound 12, whereas Mound 11a showed less extensive carbonate cover. Precipitation of authigenic carbonate may remove a significant fraction of DIC; however, this process has a negligible effect on the isotope composition of the dissolved carbon phases (Emrich and Vogel, 1970). Dissolution of carbonate minerals, on the other hand, has a variable influence on the carbon isotope composition of the DIC in bottom waters, depending on the $\delta^{13}C$ value of the carbonate that is being dissolved.

Our study shows that the DIC characteristics of seep fluids emanating at the Costa Rica margin show significant spatial variability. At Mound 11, both the DIC concentrations and the $\delta^{13}C_{\sum CO2}$ values of the fluids collected in coil R29 are much higher than in coil S28 at Mound 12 (Table III.2; Figure III.2). Furthermore, pore fluids sampled at Mound 11 show alkalinities of ~5 mM, whereas significantly higher alkalinities between 30 and 40 mM were measured at Mound 12 (Tryon et al., 2009). Given that the two mounds are just 1 km apart, fluids are expected to be derived from the same source. We suggest that at both mounds, isotopically-depleted methane and ^{13}C-enriched DIC produced by deep methanogenesis are carried from depth to the surface by upward flow of fluids derived from sediments of the

subducting slab. Since Mound 12 is older and is becoming less active, most of the ascending dissolved methane is likely oxidized via sulfate reduction, generating DIC with $\delta^{13}C_{\sum CO2}$ values between -68‰ to -60‰ at this site. Furthermore, anaerobic methane oxidation increases the alkalinity and leads to the precipitation of authigenic carbonates. In contrast, Mound 11 is young and more active, and fluids were sampled on a relatively fresh mud flow. Thus, the higher $\delta^{13}C_{\sum CO2}$ values are consistent with a large contribution of DIC originating from deep methanogenesis (with $\delta^{13}C_{DIC}$ values up to +20‰ (Han et al., 2004); see above), only slightly diluted by DIC derived from anaerobic oxidation of methane and/or oxidation of marine organic matter. In addition, high helium isotope values in fluids collected at Mound 11 and Mound 12 as well as Jaco Scar (see section III.5.2) are consistent with a small contribution of mantle-derived volatiles. Thus, a fraction of the dissolved carbon likely originates from the mantle ($\delta^{13}C \approx -6.5$‰; Marty and Jambon, 1987).

III.6.2 Temporal variations of the dissolved carbon content

Time-series studies at a number of locations have revealed that gas and fluid emission at cold seep sites is not a continuous process but exhibits strong variability at different timescales (Tryon et al., 1999; Tryon et al., 2002; Leifer et al., 2004; LaBonte et al., 2007; Solomon et al., 2008; Füri et al., 2009). To date, little is known about the causes of these variations. Correlations between seep fluid flow rates and tides have been observed at a number of seep sites (Tryon and Brown, 2001; Tryon et al., 2001; LaBonte et al., 2007). In contrast, Füri et al. (2009) proposed that a transient pulse in the flow rate at Extrovert Cliff (Monterey Bay) results from the release of mantle-derived fluids caused by fault rupturing. In addition, Solomon et al. (2008) and Tryon et al. (1999; 2002) suggested that seep flow rates can be significantly affected by localized changes in sediment permeability as a result of gas hydrate and carbonate precipitation, as well as the presence of free gas in the sediment pore

space. As discussed above, we observed extensive carbonate crusts at the summit of Mound 12 during our survey dives in 2005 and 2006, whereas Mau et al. (2006) noted little carbonate precipitation during previous seafloor surveys. Furthermore, episodic free gas expulsions were observed at mounds 11 and 12 in spring 2009 (Levin, pers. comm.). These observations show that fluid and gas emissions at the Costa Rica fore-arc are highly variable over time.

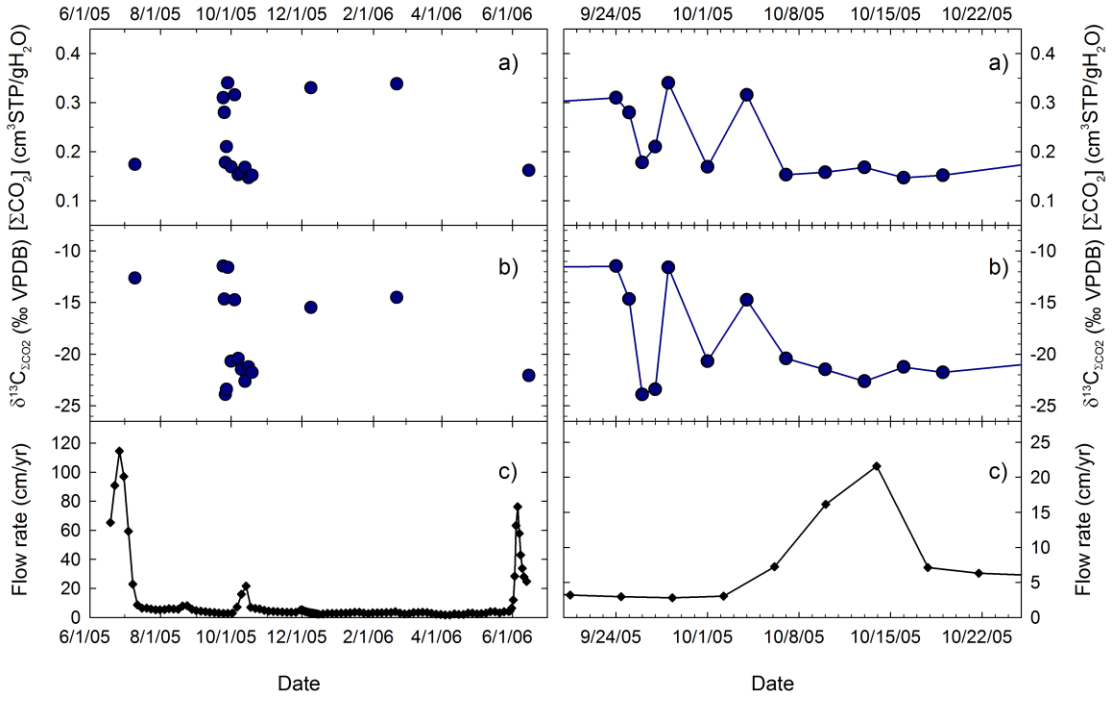

Figure III.3: Variation of a) the measured $\sum CO_2$ concentration, b) the carbon isotope composition, $\delta^{13}C_{\sum CO2}$, and c) the flow rate for seep fluids collected at Mound 11a with CAT meter R29 over the 12-month deployment period (left), and during the high flow rate event in mid-October 2005 (right).

Our new carbon isotope and abundance results and related flow rate data for fluids emanating at Mound 11a show that the carbon chemistry of seep fluids fluctuates remarkably over time. Figure III.3 shows the variation of the DIC characteristics of fluids collected at Mound 11a (CAT meter R29) as well as the flow rate over the 12-month deployment period. The temporal record reveals that both the DIC concentration (Figure III.3a) and the isotope

composition (Figure III.3b) of the fluids vary over time. For most samples, low DIC abundances correlate with low $\delta^{13}C_{\sum CO2}$ values (Figure III.2b; Figure III.3). We note that the carbon characteristics appear to be controlled by the fluid flow rate (Figure III.3c); increased flow rates near the beginning and end of our record, as well as in mid-October 2005, result in decreased DIC concentrations. However, detailed analyses from September 24th to October 19th (Table III.2; Figure III.3) reveal that the carbon flux appears to be perturbed before the onset of the spike in flow rates.

Previous studies have shown that the efficiency of methane oxidation at cold seep sites depends on the rate of upward fluid flow. At high flow velocities (>100 cm/yr), the ascending fluids push the zone of anaerobic methane oxidation to shallow sediment depths or even through the sediment-water interface, so that a significant methane fraction can be expelled into bottom water (Luff and Wallmann, 2003). In this case, due to the lower alkalinity production, super-saturation with respect to carbonates is diminished so that carbonate precipitation is not as extensive.

Low DIC concentrations at high flow rates observed in our temporal record obtained at Mound 11a appear consistent with decreased methane oxidation. Since only a small fraction of methane is oxidized under these conditions, the $\sum CO_2$ pool is expected to become enriched in ^{12}C (i.e., yielding lower $\delta^{13}C_{\sum CO2}$ values) as the light carbon isotope is preferentially utilized during methane oxidation. Alternatively, low DIC abundances and correspondingly low $\delta^{13}C_{\sum CO2}$ values may indicate that less ^{13}C-enriched DIC is supplied from methanogenesis within the subducted sediments.

III.6.3 Mass balance calculations and implications for the carbon flux at the Costa Rica fore-arc

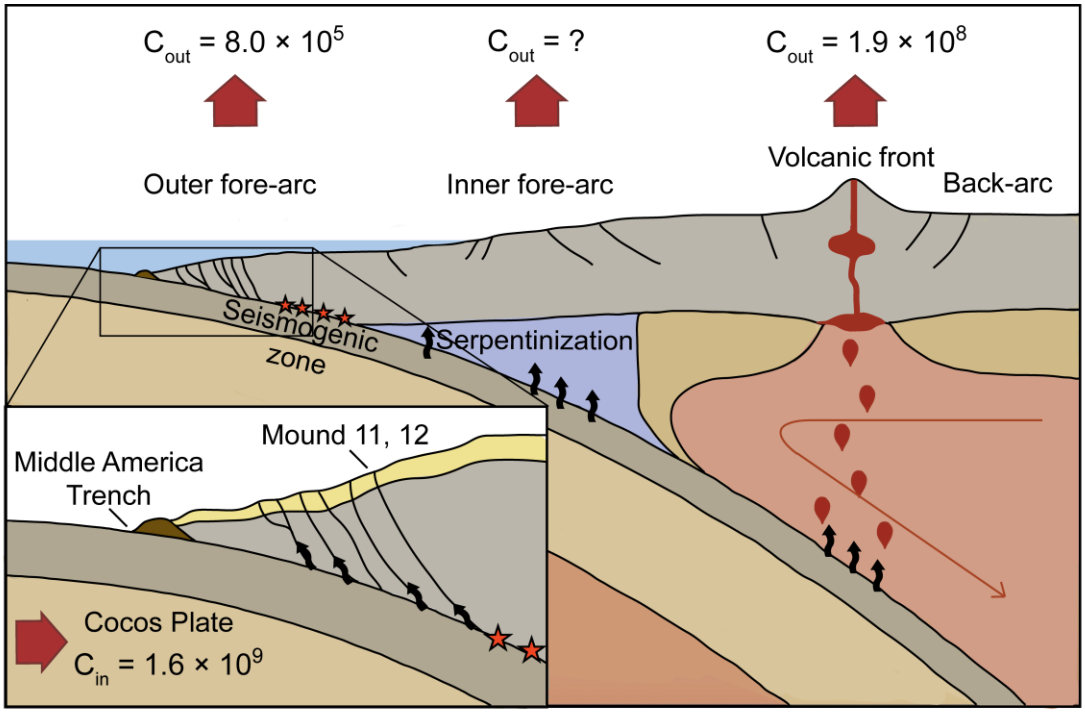

Figure III.4: Simplified cartoon illustrating the carbon input and output fluxes (in g C km^{-1} yr^{-1}) at the Central America convergent margin. The insert shows the location of Mound 11 and Mound 12, ~30 km arc-ward from the Middle America trench. The total sedimentary carbon input to the margin is estimated at 1.6 × 10^9 g C km^{-1} yr^{-1} (Li and Bebout, 2005). The carbon output through submarine fluid venting at the outer fore-arc is 8.0 × 10^5 g C km^{-1} yr^{-1} (this study), whereas the volcanic front carbon flux derived from the subducted slab (i.e., marine carbonates and sedimentary organic carbon) is equal to ~1.9 × 10^8 g C km^{-1} yr^{-1} (Hilton et al., 2002; Shaw et al., 2003) (see section III.6.3 for details). Subducted sediments do not represent a direct source of CO_2 to the back-arc region (de Leeuw et al., 2007).

The input flux of sedimentary carbon into the Costa Rica subduction zone can be estimated from 1) the masses and lithologies of the incoming sediment pile on the Cocos Plate, 2) the total carbon concentration (sedimentary organic carbon and marine carbonates) of the subducting lithologies, and 3) present-day subduction rates. Li and Bebout (2005)

characterized the carbon concentration and isotope composition of sediments recovered offshore of Costa Rica during ODP Leg 170. By integrating the carbon content of the ~380 m thick sediment section, the total sedimentary carbon input to the Costa Rica margin is estimated at 1.6×10^9 g C km^{-1} yr^{-1}. However, subducting oceanic crust may also represent a significant input flux of carbon since carbonate veining and/or calcite precipitation associated with hydrothermal alteration affect the upper oceanic crust progressively with age (Alt and Teagle, 1999).

A fraction of the subducted carbon will be returned to the surface by magmatism at the volcanic front. The CO_2 output flux for the 310 km long volcanic front in Costa Rica can be derived from SO_2 flux measurements (= 1.1×10^9 mol/yr; Zimmer et al., 2004) and observed average CO_2/SO_2 molar ratios at volcanic arcs worldwide (= 5; Hilton et al., 2002). This flux is estimated at 2.1×10^8 g C km^{-1} yr^{-1}. However, the carbon released via the front may originate, in part, from the mantle wedge (M), as well as from slab-derived marine limestone (L) and sedimentary organic carbon (S), and possibly subducting oceanic crust. Hilton et al. (2002) and Shaw et al. (2003) assessed the carbon provenance for geothermal fluids collected along the Costa Rica volcanic front using the three end-member (M-L-S) model of Sano and Marty (1995), and concluded that 6 - 10% of the carbon output is derived from the mantle wedge (see Hilton et al. (2002) for details). Thus, the volcanic front carbon flux derived from the subducted slab (i.e., marine carbonates and sedimentary organic carbon) is equal to ~1.9×10^8 g C km^{-1} yr^{-1} (Figure III.4). In other words, the output flux via the front is only ~12 % of the total carbon which is potentially available by sediment input via the trench. In a more recent analysis, de Leeuw et al. (2007) estimated the relative proportions of the three incoming sediment units required to satisfy the L/S ratio for the volcanic output in Costa Rica. They argued that the top 74 m section of the uppermost sediment unit (Unit U1) is not involved in supplying the output CO_2 flux to the volcanic front, and only the upper 19 m

out of the total 290 m of the lowermost sediment unit (U3) are needed to maintain the required L/S ratio. Thus, most of Unit U3, together with the altered oceanic basement, is carried past the zone of arc magma generation. Consequently, the influence of subducting oceanic crust as a contributor to the volcanic carbon flux can be neglected. In contrast, a significant fraction of the uppermost unit (U1) of the down-going sedimentary sequence is removed before reaching the zone of arc magma generation, consistent with the lack of a ^{10}Be signal in Costa Rica arc lavas (Morris et al., 2002). If this analysis is correct, then we suggest that the carbon content of the uppermost 74 m of Unit U1 alone, i.e., 6.9×10^7 g C km^{-1}yr^{-1} (Li and Bebout, 2005; de Leeuw et al., 2007), represents the flux of carbon that is potentially available to supply the fore-arc region in Costa Rica.

The total carbon emission from seep sites at the outer fore-arc in Costa Rica can be estimated by combining the CO_2 flux observed in our study at Mound 11a with estimates for the methane output from Mau et al. (2006). As the entire margin offshore Nicaragua and Costa Rica has been extensively surveyed, and the distribution of seep sites well-mapped (Klaucke et al., 2008; Ranero et al., 2008; Sahling et al., 2008), we assume that our estimates encompass the major fraction of submarine carbon release. However, we caution that our CO_2 flux estimates are based on data from a single mound, and we exclude emissions from other seep structures (landslides, seamount subduction scars, and faults; Sahling et al., 2008). Furthermore, there is a significant temporal and spatial variability of measured carbon (CO_2 and methane) concentrations in seep fluids and in the water column at mud extrusions (Mau et al., 2006; Mau et al., 2007). Since fluid venting is highly variable both in space and in time, extrapolation of data from only one site may produce estimates with large uncertainties. In addition, CO_2- and methane-rich fluids might also be lost through channels in sediments and fractures in carbonates (Mau et al., 2006) and/or via flow along the décollement zone towards the deformation front (Kopf et al., 2000); this fraction of the carbon output is not captured by

our mass flux instruments on the seafloor. Also, methane may be stored in marine gas hydrates at continental margins (Milkov et al., 2003), and a fraction of the (methane-derived) carbon likely precipitates as authigenic carbonates at cold seep sites (Han and Suess, 1989; Luff and Wallmann, 2003) and/or is taken up by the seep biota (e.g., Southward et al., 1981).

In spite of these caveats, we can still derive first-order estimates of the methane-related carbon flux from the outer fore-arc using the approach of Mau et al. (2006). For the latest estimate of 77 mounds observed along a ~460 km long stretch of the continental slope at the Central America margin (Klaucke et al., 2008; Ranero et al., 2008; Sahling et al., 2008), we calculate a total methane output of 3.1×10^7 mol/yr. This output estimate is based on average methane emissions (4×10^5 mol/yr; Mau et al., 2006) observed at four mounds (Mound 10, Mound 11, Mound 12, and Mound Culebra). This corresponds to a methane-related carbon flux equal to 8.0×10^5 g C $km^{-1}yr^{-1}$.

For Mound 11, we calculate that the $\sum CO_2$ emission ranges from ~110 to 3100 mol/yr. This estimate is based on flow rates (2.7 - 25 cm/yr) and $\sum CO_2$ concentrations (0.15 – 0.34 cm^3STP/gH_2O) observed during our 12-month deployment, combined with first-order estimates of the total area covered by bacterial mats (500-1700 m^2; Mau et al., 2006) at the seep site. However, we note that for most of our record, flow rates are low (i.e., between 2 and 5 cm/yr), and the corresponding $\sum CO_2$ output then lies between ~110 to 800 mol/yr. Extrapolated over the 77 mound structures along the 460-km long section of the Central America margin, we estimate a *maximum* total CO_2 output of 2.4×10^5 mol/yr, corresponding to a carbon flux of 6.1×10^3 g C $km^{-1}yr^{-1}$. Notably, this value is two orders of magnitude less than the methane-related flux.

Thus, the total carbon emission (CO_2 plus methane) from mounds at the Costa Rica margin is of the order of 8.0×10^5 g C $km^{-1}yr^{-1}$ (Figure III.4). This flux represents ~1% only of the amount of carbon that is potentially available to the fore-arc region via the uppermost 74

m of sediment layer U1 (i.e., 6.9×10^7 g C $km^{-1}yr^{-1}$), assuming the analysis of de Leeuw et al. (2007). Alternatively, compared to the total sedimentary carbon input to the subduction zone in Costa Rica (1.6×10^9 g C km^{-1} yr^{-1}; Figure III.4; Li and Bebout, 2005), the carbon loss through fluid seepage at mound structures at the outer fore-arc is virtually negligible. Consequently, we conclude that the submarine section of the Costa Rica fore-arc does not represent a pathway for significant carbon loss from the subducting slab. Complementary studies are needed on the subaerial segment of the fore-arc to assess the volatile release from the slab under more extreme P-T conditions.

III.7 Conclusions

Our new He-CO_2 isotope and relative abundance results for submarine seep fluids allow us to assess the origin and fluxes of volatiles at the outer fore-arc in Costa Rica. Elevated helium isotopes ratios in fluids emanating at Mound 11, Mound 12 and Jaco Scar are consistent with a small but discernable component of mantle-derived helium. Mantle helium in this region may be derived from the lithospheric mantle segment of the subducting Cocos Plate or from oceanic igneous basement rocks related to the Galápagos hotspot or the CLIP. At the mounds, the carbon isotope composition of DIC shows that isotopically-depleted methane and ^{13}C-enriched DIC produced by deep methanogenesis are carried from depth to the surface by upward flow of fluids derived from sediments of the subducting slab. Due to low fluid flow rates at Mound 12, most of the ascending dissolved methane is oxidized, resulting in extremely low $\delta^{13}C_{\sum CO2}$ values. In contrast, at the more active Mound 11, the ascending DIC is only slightly affected by biogeochemical processes in near-surface sediments.

Through use of an innovative sampling approach coupling copper sampling coils to submarine flux meters, we are able to produce a quasi-continuous temporal record of the

volatile chemistry of seep fluids emanating at Mound 11 and Mound 12. The remarkable temporal variability of the carbon and fluid emissions from the studied mounds demonstrates the necessity for long-term, continuous sampling in order to understand and quantify fluid and volatile emissions at submarine seep sites.

We estimate that the carbon loss (CO_2 plus methane) through submarine fluid venting at mound structures at the Costa Rica fore-arc is significantly less than the amount of carbon that is potentially available by subducted sedimentary input via the trench. Taken together, estimates of the carbon flux at the outer fore-arc (this study), the volcanic front (Hilton et al., 2002; Shaw et al., 2003), and the back-arc (de Leeuw et al., 2007) at the Central America convergent margin represent $\leq$ ~12% of the total sedimentary carbon input into the subduction zone. Unless there is a significant but hitherto unidentified carbon flux at the inner fore-arc, i.e., between the submarine fore-arc and the volcanic front, our observations suggest that most of the carbon entering the Costa Rica subduction zone must be recycled to the (deeper) mantle.

III.8 Acknowledgments

We gratefully acknowledge NSF (grant OCE-0242034) for support of this work. We thank captain and crew of the R/V *Atlantis* and the DSV *Alvin* team for their professional support at sea. Martin Wahlen and Bruce Deck are thanked for assistance with stable isotope measurements. Comments from associate editor Eli Silver and an anonymous reviewer helped improve the manuscript. This is SOEST Contribution No. 7804.

This chapter appeared in full as Füri, E., D.R. Hilton, M.D. Tryon, K.M. Brown, G.M. McMurtry, W. Brückmann, and C.G. Wheat (2010), Carbon release from submarine seeps at the Costa Rica fore-arc: Implications for the volatile cycle at the Central America convergent margin, *Geochemistry Geophysics Geosystems,* doi:10.1029/2009GC002810, in press. The dissertation author was the primary investigator and lead author of this paper and conducted all the analyses presented herein.

Chapter IV Decoupling of the He and Ne isotope systematics of the Icelandic mantle: the role of He depletion, magma mixing and degassing fractionation

IV.1 Abstract

We present new He-Ne data for geothermal fluids and He-Ne-Ar data for basalts from throughout the Icelandic neovolcanic zones and from older parts of the Icelandic crust. Geothermal fluids, subglacial glasses, and phenocrysts are characterized by a wide range in helium isotope ratios ($^3He/^4He$) encompassing typical MORB-like ratios through values as high as 36.8 R_A (where R_A = air $^3He/^4He$). Although neon in geothermal fluids is dominated by an atmospheric component, samples from the northwest peninsula show a small excess of nucleogenic ^{21}Ne, likely produced in-situ and released to circulating fluids. In contrast, geothermal fluids from the neovolcanic zones show evidence of a contribution of mantle-derived neon, as indicated by $\delta^{20}Ne$ enrichments up to 3% compared to air. The neon isotope composition of subglacial glasses reveals that mantle neon is derived from both depleted MORB-mantle and a primordial, 'solar' mantle component. However, binary mixing between these two endmembers can account for the He-Ne isotope characteristics of the basalts only if the $^3He/^{22}Ne$ ratio of the primordial mantle endmember is lower than in the MORB component. Indeed, the helium to neon elemental ratios ($^4He/^{21}Ne^*$ and $^3He/^{22}Ne_s$, where $^{21}Ne^*$ = nucleogenic ^{21}Ne and $^{22}Ne_S$ = 'solar'-derived ^{22}Ne) of the majority of Icelandic subglacial glasses are lower than theoretical values for production within Earth's mantle, as observed previously for other OIB samples. Helium may be depleted relative to neon in high-$^3He/^4He$ ratio parental melts due to either more compatible behavior during low-degree partial melting or more extensive diffusive loss relative to the heavier noble gases. However, Icelandic glasses show higher $^4He/^{40}Ar^*$ ($^{40}Ar^*$ = radiogenic Ar) values for a given $^4He/^{21}Ne^*$

value compared to the majority of other OIB samples: this observation is consistent with extensive open-system equilibrium degassing, likely promoted by lower confining pressures during subglacial eruptions of Icelandic lavas. Taken together, the He-Ne-Ar systematics of Icelandic subglacial glasses are imprinted with the overlapping effects of helium depletion in the high-$^{3}He/^{4}He$ ratio parental melt, binary mixing of two distinct mantle components, degassing fractionation and atmosphere contamination. However, it is still possible to discern differences in the noble gas characteristics of the Icelandic mantle source, with MORB-like He-Ne isotope features prevalent in the Northern Rift Zone and a sharp transition to more primitive 'solar-like' characteristics in central and southern Iceland.

IV.2 Introduction

Studies of trace element, radiogenic isotope, and noble gas characteristics of mid-ocean ridge basalts (MORB) and oceanic basalts (OIB) have revealed that domains exist within Earth's mantle which have experienced different evolutionary histories (e.g., Zindler and Hart, 1986; Hofmann, 1997). Noble gases represent powerful tracers of these heterogeneities with basalts from ocean islands such as Iceland, Hawaii, Galápagos, Samoa, and Réunion having high $^{3}He/^{4}He$ ratios, and MORB lavas having lower $^{3}He/^{4}He$ values equal to 8 ± 1 R_A (where $R_A = {}^{3}He/^{4}He$ of air $= 1.4 \times 10^{-6}$; Graham, 2002). Additionally, OIB magmas have lower $^{21}Ne/^{22}Ne$ values for a given $^{20}Ne/^{22}Ne$ ratio (i.e., a lower nucleogenic to primordial neon ratio) than MORB melts, suggesting that the OIB source has evolved with both a higher time-integrated $^{3}He/(U+Th)$ and $^{22}Ne/(U+Th)$ ratio compared to the source of MORB.

The helium and neon isotope signatures of MORB and OIB are consistent with the notion that remnants of primordial gases of presumably solar-like composition are preserved within Earth's mantle (Sarda et al., 1988; Honda et al., 1991; Honda et al., 1993). However,

radiogenic ^{4}He and ^{21}Ne in-growth from the decay of U and Th will have altered the initial composition over Earth history. Since production of nucleogenic ^{21}Ne in the solid Earth is coupled to that of radiogenic ^{4}He (with a constant $^{4}He/^{21}Ne$ production ratio of $\sim 2.2 \times 10^{7}$; Yatsevich and Honda, 1997), the present-day mantle $^{3}He/^{4}He$ and $^{21}Ne/^{22}Ne$ ratios should be correlated. In other words, if Earth's mantle remained an essentially closed-system after the initial outgassing, an increase in $^{21}Ne/^{22}Ne$ should be accompanied by a concomitant decrease in $^{3}He/^{4}He$. Indeed, Honda et al. (1993) noted a strong correlation between He and Ne isotopes for some OIB; steeper trajectories in three isotope neon space (i.e., low $^{21}Ne/^{22}Ne$ ratios for a given $^{20}Ne/^{22}Ne$ value) were characterized by samples with high $^{3}He/^{4}He$ ratios. However, more recent studies have revealed a lack of correlation between He and Ne, at locations such as Iceland (Harrison et al., 1999; Dixon et al., 2000; Trieloff et al., 2000; Moreira et al., 2001; Dixon, 2003), the East Pacific Rise (Niedermann et al., 1997), and the Manus Basin (Shaw et al., 2001). This apparent decoupling between helium and neon may bear fundamental information on the nature of mantle source regions, mantle dynamics, and the degassing history of the Earth.

Studies of Icelandic subglacial basalts (Harrison et al., 1999; Dixon et al., 2000; Trieloff et al., 2000; Moreira et al., 2001; Dixon, 2003) have discovered trapped neon with a solar-like isotope composition accompanied by helium with $^{3}He/^{4}He$ ratios $< 20\ R_A$, i.e., significantly lower than solar values (either proto-solar values of $120\ R_A$; Mahaffy et al., 1998 or meteoritic ratios of $280\ R_A$; Black, 1972). The apparent decoupling of the He-Ne isotope systematics of these lavas has been explained by either a) elemental and isotopic heterogeneity of the mantle source, or b) binary mixing between a relatively undegassed, primordial mantle endmember and a second endmember characterized by depleted/degassed MORB-mantle (Dixon, 2003; Moreira et al., 2001). The first scenario requires that the OIB source itself is heterogeneous with respect to the helium to neon elemental ratio ($^{3}He/^{22}Ne$), leading to

domains in Earth's mantle with different $^{3}He/^{4}He$ and $^{21}Ne/^{22}Ne$ ratios. Alternatively, the He-Ne signature may result from mixing between two endmembers with distinct He-Ne isotope and elemental compositions, i.e., a low-$^{3}He/^{22}Ne$ ratio primordial mantle component and a high-$^{3}He/^{22}Ne$ ratio MORB-like endmember. Notably, all previous studies focused on one segment of Iceland's neovolcanic zones (the Reykjanes Peninsula) whereas the highest $^{3}He/^{4}He$ ratios (i.e., minimal radiogenic He additions) are found in basalts erupted in Central Iceland (Condomines et al., 1983; Kurz et al., 1985; Breddam et al., 2000; Macpherson et al., 2005a) and Vestfirðir - the northwest peninsula of Iceland (Hilton et al., 1999; Ellam and Stuart, 2004). Thus, any model of the nature of the Icelandic mantle source that incorporates He-Ne constraints needs to consider noble gas variations from regions other than the Reykjanes Peninsula, given trace element and radiogenic isotope evidence of the occurrence of mantle source heterogeneities throughout the Icelandic neovolcanic zones (Hards et al., 1995; Kerr et al., 1995; Thirlwall, 1995; Chauvel and Hémond, 2000; Kempton et al., 2000).

In order to examine in more detail the apparent He-Ne decoupling observed in Reykjanes Peninsula subglacial lavas, we present new noble gas data for subglacial glasses and geothermal fluids from throughout the neovolcanic zones and from older parts of the Icelandic crust. In contrast to helium isotopes in geothermal fluids and lavas which appear to provide a robust tracer of variations in the Iceland mantle source, the neon (and argon) isotope data are mostly masked by addition of an atmospheric component. However, it is still possible to discern the underlying processes controlling the He-Ne relationships: helium depletion relative to neon (and argon) in the high-$^{3}He/^{4}He$ ratio parental melt, followed by binary mixing between the primordial mantle component and a depleted/degassed MORB-like endmember at shallower depths, and extensive open-system equilibrium degassing. We show that the combined action of these effects leads to decoupling of the Ne isotope signal of the Icelandic mantle from that provided by helium isotopes.

IV.3 Geologic setting and background

Iceland is a subaerial section of the Mid-Atlantic Ridge, and is associated with high basaltic melt production and, hence, anomalously thick crust (Darbyshire et al., 2000). Geophysical studies have revealed the presence of a cylindrical zone of low P- and S-wave velocities beneath Iceland, consistent with upwelling of anomalously hot mantle. However, while some models suggest that the seismic velocity anomaly extends from the core-mantle boundary to the surface (Helmberger et al., 1998; Bijwaard and Spakman, 1999; Zhao, 2004), others point to a shallow 'plume' of upwelling mantle (Foulger et al., 2000). Recently, Montelli et al. (2006) proposed that these conflicting interpretations can be explained by fluctuations in the activity of the Icelandic hotspot, i.e., the strength of the seismic velocity anomaly can vary with depth as a result of distinct plume pulses (Ito, 2001). Irrespective of the depth of origin of the low P- and S-wave velocity anomalies, the center of the hotspot is hypothesized to be currently located in Central Iceland (Tryggvason et al, 1983). Significantly, this region has the highest $^{3}He/^{4}He$ ratios (up to ~34 R_A; Condomines et al., 1983; Kurz et al., 1985; Breddam et al., 2000; Macpherson et al., 2005a) yet observed for the neovolcanic zones.

Geochemical and isotopic heterogeneities observed in Icelandic lavas and in submarine basalts along the Reykjanes Ridge to the south of Iceland have been interpreted to result from mixing between so-called hotspot mantle material and depleted MORB mantle. As Iceland is approached from the south, basalts record a systematic increase in a number of geochemical parameters, such as La/Sm, $^{206}Pb/^{204}Pb$, $^{87}Sr/^{86}Sr$, and $^{3}He/^{4}He$ ratios (from 11.0 to 17.6 R_A), as well as a decrease in $^{143}Nd/^{144}Nd$ ratios: these trends are considered to reflect a change from normal MORB-like characteristics to those more akin to OIB features (Hart et al., 1973; Schilling, 1973; Sun et al., 1975; Taylor et al., 1997; Hilton et al., 2000; Thirlwall et al., 2004). North of Iceland, Kolbeinsey Ridge basalts show a decrease in $^{87}Sr/^{86}Sr$ and $^{3}He/^{4}He$ ratios, and an increase in $^{143}Nd/^{144}Nd$ ratios with increasing distance from Iceland.

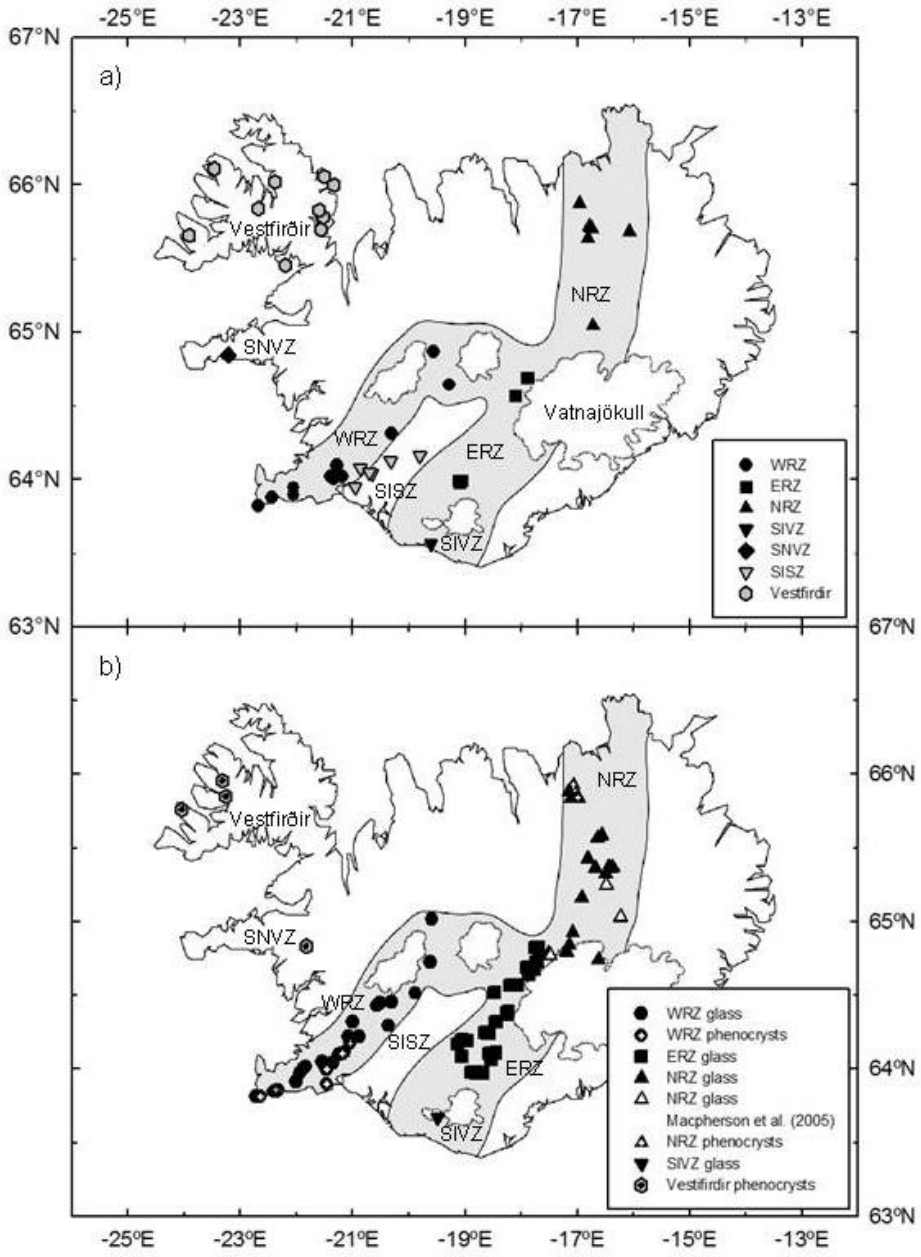

Figure IV.1: Map of Iceland showing the neovolcanic zones. These include the axial rift zones, i.e., the Western (WRZ), Eastern (ERZ), and Northern rift zones (NRZ), as well as the off-axis volcanic zones, i.e., the South Iceland Volcanic Zone (SIVZ) and the Snæfellsnes Volcanic Zone (SNVZ). Also shown are the South Iceland Seismic Zone (SISZ) and Vestfirðir - the northwest peninsula. Sampling locations for a) geothermal fluids and b) basaltic glass and phenocrysts are indicated. Black symbols refer to samples collected within the neovolcanic zones. Grey symbols indicate sampling locations in older parts of the Icelandic crust. Open triangles show location of samples from the NRZ previously analyzed for helium by Macpherson et al. (2005a).

Notably, Pb isotopes show no such relationship and provide no evidence for systematic mixing between depleted asthenospheric mantle and Icelandic hotspot material (Mertz et al., 1991; Macpherson et al., 2005b). Furthermore, other studies have revealed that trace element and Sr-Nd-Pb-Hf isotope variations of Icelandic basalts can be attributed to chemical and isotopic heterogeneities within the mantle source itself, and that MORB-like mantle may not contribute significantly to the generation of Icelandic lavas (Hards et al., 1995; Kerr et al., 1995; Thirlwall, 1995; Chauvel and Hémond, 2000; Kempton et al., 2000).

Recent volcanism in Iceland has occurred along two types of so-called neovolcanic zones: 1) axial rift zones, which represent the landward extensions of the Mid-Atlantic Ridge, and 2) off-rift volcanic zones. The axial rift zones cross the island from southwest to northeast and connect the Reykjanes Ridge in the southwest to the Kolbeinsey Ridge in the north. In southern Iceland, the rift zone can be subdivided into the Western (WRZ) and Eastern (ERZ) rift zones that are separated by a transform fault system, the South Iceland Seismic Zone (SISZ) (Fig. IV.1). The Icelandic rift zone system continues northwards from the Vatnajökull glacier along the Northern Rift Zone (NRZ) towards the Tjörnes Fracture Zone that links the Icelandic rift system to the Kolbeinsey Ridge. The off-rift zones are the South Iceland Volcanic Zone (SIVZ) and the Snæefellsnes Volcanic Zone (SNVZ). The SIVZ is a direct continuation of the Eastern Rift Zone, whereas the SNVZ is entirely intraplate and is not connected to the presently-active plate boundary (Einarsson, 2008).

IV.4 Sampling and analytical techniques

IV.4.1 Geothermal fluids

Geothermal fluids were sampled over three periods (summer 2006, 2007, and 2008) along the Icelandic neovolcanic zones (WRZ, ERZ, NRZ, SIVZ, SNVZ), the South Iceland Seismic Zone (SISZ), and Vestfirðir - the northwest peninsula of Iceland (Fig. IV.1a). We

collected samples from a) 10 fumaroles, b) 15 bubbling hot pools, c) 4 water springs, d) 6 mud pots, and e) 15 geothermal wells, making a total of 50 individual localities (i.e., 71 samples including duplicates; Table IV.1). Geothermal fluids were collected in evacuated low-He diffusivity 1720-glass flasks following procedures designed to minimize air contamination (see Hilton et al., 2002, for details on sampling procedures).

In the laboratory, an ultra high vacuum (UHV) extraction line was employed for noble gas extraction (Kulongoski and Hilton, 2002). A glass trap held at acetone-dry ice temperature was used to isolate water vapor, and a stainless-steel trap held at liquid nitrogen temperature was used to separate the condensable gas fraction (mainly CO_2) from non-condensable volatiles. A split of the non-condensable gas fraction was collected in a pyrex glass breakseal for transfer to a VG5400 mass spectrometer for neon isotope measurements. The remaining non-condensable gas was purified using activated charcoal traps (held at -196°C) and a Ti getter held at 700°C. A calibrated aliquot (~0.5%) of this fraction was expanded into an AR-glass breakseal for transfer to a MAP 215 noble gas mass spectrometer for He isotope analysis.

Prior to He isotope analysis, the gas was released into the MAP 215 mass spectrometer preparation line for further purification by sequential exposure to a 750ºC hot Ti-getter, an activated charcoal trap (held at -196ºC), a SAES getter, and a cryogenic trap lined with activated charcoal (held at <20 K). Helium was released from the cryogenic trap by increasing the temperature to 35 K, whereas Ne was released at 90 K. Sample $^{3}He/^{4}He$ ratios and $^{4}He/^{20}Ne$ ratios were measured in static mode and calibrated against standard aliquots of air run at least twice a day under identical experimental conditions. The blank contribution to the ^{4}He signal was less than 3 % for all geothermal samples, except for three samples collected at Landmannalaugar (ICE08-26) and Köldukvíslabotnar (ICE08-17 and -18), which were heavily contaminated by air (see section IV.5.1.1).

We targeted 22 geothermal samples collected in 2006 for subsequent Ne isotope measurements on a modified VG5400 mass spectrometer running in peak jumping mode (Craig et al., 1993) (Table IV.2). Gas released from the pyrex breakseals was first exposed to a Ti-Zn sponge that was cooled from 750° to 450°C, after which the heavy noble gases were trapped onto a stainless-steel frit kept at liquid nitrogen temperature (-196ºC). The remaining volatiles were exposed to a SAES getter, and He and Ne were subsequently trapped onto a He-cooled cryogenic trap (<20 K). Neon was released from this trap by increasing the temperature to 90 K. Reproducibility of the Ne analyses was monitored using an air standard measured after every eight or less sample runs, and sample neon isotope compositions were determined by normalization to the air standard. All results take into account corrections for procedural blanks and contributions to ^{20}Ne and ^{22}Ne due to doubly charged ^{40}Ar and CO_2, respectively. The $^{40}Ar^{++}/^{40}Ar^{+}$ ratio was 0.25 and the CO_2^{++}/CO_2^{+} ratio was 0.013. HF and H_2O are resolved from ^{20}Ne; thus, no corrections for these species were required. Procedural blank contributions to the ^{20}Ne signal throughout these experiments were less than 2% for the majority of the samples (n = 14), and only two samples showed blank contributions greater than 5% (i.e., samples ICE-17 and ICE-11 showed ^{20}Ne blank contributions of 6% and 9%, respectively).

IV.4.2 Basaltic glasses and olivine phenocrysts

We collected subglacial basaltic glasses and/or phenocryst-bearing lavas from 89 locations along the WRZ (n = 28), ERZ (n = 28), NRZ (n = 27), SIVZ (n = 1), and Vestfirðir (n = 5) (Table IV.3; Fig. IV.1b). A total of 77 glasses, as well as 5 clinopyroxene and 15 olivine phenocryst samples, were analyzed for their helium isotope and abundance characteristics by crushing. For three locations on the WRZ (Miðfell, Þrengsli, and Mælifell), helium analyses were carried out on both glasses and phenocryst phases from the same sample, whereas both olivine and pyroxene phases were analyzed for four samples from

Vestfirðir. In part, the large sample load was processed to help identify volatile-rich samples for subsequent Ne-Ar abundance and isotope measurements. In the case of glasses, we selected fresh chips, free of phenocrysts and surface alteration, using a binocular microscope. For phenocrysts, we made sure that crystals did not have any adhering matrix. In all cases, an effort was made to choose a small number of large grains to minimise the surface area to volume ratio and help preserve vesicles and/or inclusions in the samples.

After pre-cleaning in a 1:1 acetone-methanol mixture, approximately 500 mg of glass or 1-3 g of olivine phenocrysts, respectively, were loaded into on-line, electro-magnetic crushers (see description by Scarsi, 2000) connected to the preparation line of the MAP 215 noble gas mass spectrometer and pumped overnight to UHV. Crushing of the samples was achieved by externally accelerating a magnetized steel slug up and down within the crusher for 2 minutes at a frequency of ~120 impacts per minute. The volatiles released upon crushing were purified in the mass spectrometer preparation line, and helium and neon abundances, as well as the $^{3}He/^{4}He$ ratios, were determined on a MAP 215 noble gas mass spectrometer (see section IV.4.1 for details). Prior to each individual sample run, an analytical blank of the entire system was measured. The blanks were $\leq 0.5 \times 10^{-9}$ $cm^{3}STP^{4}He$, and the blank contribution to the ^{4}He signal was less than 5 % for the majority of the samples; however, 14 out of 97 samples showed a blank contribution between 7 and 50 % due to low He contents and/or small sample sizes.

For subsequent analyses of Ne and Ar abundances and isotope ratios, we targeted 44 helium-rich glasses with high $^{3}He/^{4}He$ ratios between 8.5 and 25.9 R_A from the WRZ (n = 15), ERZ (n = 11), NRZ (n = 17), and SIVZ (n = 1) (Table IV.4). Between ~300 mg and 1 g of fresh glass chips were loaded into screw-type crushers (constructed from modified Nupro vacuum valves; see Stuart et al., 1994) which were evacuated to UHV and kept at 100°C overnight. Neon and argon abundances and isotope ratios (as well as He abundances) were

determined on a modified VG5400 mass spectrometer (see Craig et al., 1993, and section IV.4.1 for details). In order to maximize noble gas yields, noble gases were released from samples by single-step crushing in vacuo using an external hydraulic press capable of 5 tons pressure. Procedural blanks were run prior to each individual sample and averaged $(5 \pm 1) \times 10^{-10}$ cm^3STP for ^4He; $(12 \pm 5) \times 10^{-12}$ cm^3STP for ^{20}Ne; and $(6 \pm 2) \times 10^{-9}$ cm^3STP for ^{40}Ar. Blank contributions were (significantly) less than 20% of sample yields in most cases. For blank contributions > 20%, owing to low intrinsic gas contents and/or sample sizes of some samples, results are listed in italics in Table IV.4. We note that the helium abundance data presented in Table IV.4 are typically not as accurate and precise as those in Table IV.3 because procedures were optimized for neon and argon analyses.

IV.5 Results

IV.5.1 Geothermal fluids

We report $^3He/^4He$ ratios and He abundances (for water samples) of Icelandic geothermal fluids in Table IV.1. Sample locations are shown in Figure IV.1a, and the data set is plotted as a function of latitude in Figure IV.2. Neon isotope ratios, determined for the samples collected in 2006, are given in Table IV.2.

IV.5.1.1 $^3He/^4He$ ratios

All measured $^3He/^4He$ ratios (reported as R_m/R_A where R_m = measured $^3He/^4He$ of sample and R_A = $^3He/^4He$ of air) have been corrected for the effects of atmospheric contamination using the X-factor, where X is the air-normalized He/Ne ratio multiplied by the ratio of the Bunsen coefficients, assuming an air-equilibration temperature of 10ºC (see Hilton, 1996, and Table IV.1 for details). For the majority of our samples, air-normalized He/Ne ratios are high (i.e., $X \geq 10$), which results in only minor corrections for atmospheric

helium. Most air-corrected $^3He/^4He$ ratios (reported as R_c/R_A) of Icelandic geothermal fluids range from typical MORB-values (8 ± 1 R_A; Graham, 2002) up to 27.4 R_A. However, 11 samples (marked with asterisks in Table IV.1) show significantly lower $^3He/^4He$ ratios due to air contamination or addition of radiogenic helium; these samples are considered suspect and are not included in further discussions.

The criteria we adopt here to recognize severe air contamination are low air-normalized He/Ne values (i.e., X-values ≤ 5) and $^3He/^4He$ ratios that are significantly lower than duplicate samples or other samples from the same general region. Thus, a total of 10 samples (i.e., all samples collected at Landmannalaugar, Köldukvíslabotnar, and Laugarhóll, as well as samples PBICE-4 and PBICE-15) are considered to be overwhelmingly contaminated by air-derived He. We note that previous studies reported $^3He/^4He$ ratios between 15.6 and 23.7 R_A for samples from Landmannalaugar and a value of 26.0 R_A for a steam sample from Köldukvíslabotnar (Polak et al., 1976; Poreda et al., 1992). Low $^3He/^4He$ ratios and He/Ne values, however, were reported previously by Hilton et al. (1998) for Laugarhóll. In contrast, sample ICE-34 from Laugaland (Vestfirðir) shows a low $^3He/^4He$ ratio of 3.4 R_A yet a relatively high X-value of 11.4. Similar helium isotope values (between 3.7 to 3.9 R_A) for this location have been observed previously by Hilton et al. (1998), who suggested that the low $^3He/^4He$ ratios at Laugaland point to a significant contribution of radiogenic helium to the geothermal fluids.

In general, our new helium isotope data for Icelandic geothermal fluids agree with the regional pattern observed in previous studies (Polak et al., 1976; Torgersen and Jenkins, 1982; Sano et al., 1985; Hilton et al., 1990; Marty et al., 1991; Poreda et al., 1992; Hilton et al., 1998). MORB-like $^3He/^4He$ ratios between 8.4 and 10.4 R_A are observed in geothermal fluids along the NRZ and in the single sample from the off-rift SNVZ (Table IV.1; Fig. IV.2), similar to the range in helium isotope ratios reported by Hilton et al. (1990) and Poreda et al.

Table IV.1: He characteristics of Icelandic geothermal fluids.

Location	Latitude (N)	Longitude (W)	Sample ID[a]	Sample Type[b]	$^3He/^4He$ R_m/R_A[c]	X[d]	$^3He/^4He$ R_c/R_A[e]	$[^4He]_c$[f] cm^3STP/gH_2O $(\times 10^{-5})$
Western Rift Zone (WRZ)								
Nesjavellir (Borehole)	64°05'45.6"	021°16'48.0"	ICE-3	B	14.75	839	14.77 ± 0.18	
Nesjavellir (Bubbling pool)	64°05'36.6"	021°16'28.3"	ICE08-11	G	13.97	84.5	14.13 ± 0.07	
			ICE08-12	G	13.48	59.0	13.69 ± 0.10	
Svartsengi (Borehole HSH11)	63°52'32.8"	022°26'06.6"	ICE-5	B	14.67	383	14.70 ± 0.13	
			ICE-6	B	14.24	214	14.30 ± 0.05	
Reykjanes (Fumarole)	63°49'06.7"	022°41'04.7"	PBICE-1	G	8.99	10.1	9.69 ± 0.38	
			PBICE-2	G	11.91	137	11.97 ± 0.58	
Krísuvík (Fumarole)	63°53'43.1"	022°03'19.2"	PBICE-3	G	13.87	194	13.92 ± 0.73	
			PBICE-4*	G	2.62	2.3	3.50 ± 0.12	
Krísuvík (Bubbling pool)	63°53'43.1"	022°03'19.3"	ICE08-14	G	13.83	63.3	14.03 ± 0.13	
			ICE08-15	G	13.89	205	13.95 ± 0.10	
Hengill (Bubbling pool)	64°01'12.1"	021°23'41.6"	PBICE-9	G	12.27	14.7	12.39 ± 0.26	
			PBICE-12	G	12.67	19.3	13.18 ± 0.21	
Hengill (Fumarole)	64°00'25.0"	021°20'30.4"	ICE08-22	G	15.69	84.7	15.86 ± 0.17	
Little Geysir (Bubbling pool)	64°18'38.4"	020°18'08.8"	PBICE-13	G	16.59	72.8	16.77 ± 0.31	
			PBICE-14	G	15.99	70.0	16.17 ± 0.19	
Kerlingafjöll (Bubbling pool)	64°38'37.0"	019°17'17.1"	PBICE-10	G	14.22	28.7	14.61 ± 0.28	
Hveravellir (Bubbling pool)	64°51'55.6"	019°33'29.7"	PBICE-11	G	13.68	32.1	14.01 ± 0.26	
Hveragerði (Fumarole)	64°01'20.1"	021°11'38.5"	PBICE-16	G	16.89	51.1	17.15 ± 0.23	
			PBICE-8	G	17.08	40.7	17.41 ± 0.23	
Eastern Rift Zone (ERZ)								
Landmannalaugar (Fumarole)	63°58'52.2"	019°05'21.3"	PBICE-5*	G	1.26	2.5	1.39 ± 0.09	
Landmannalaugar (Spring)	63°59'32.7"	019°06'01.7"	ICE08-26*	W	1.24	3.4	1.35 ± 0.07	17.50
Landmannalaugar (Fumarole)	63°59'21.2"	019°06'42.1"	ICE08-29*	G	3.28	4.6	3.92 ± 0.07	
Landmannalaugar (Pool)	63°59'26.8"	019°03'46.4"	ICE08-30*	W	4.28	3.4	5.64 ± 0.04	680.1
Köldukvíslabotnar (Borehole)	64°34'15.2"	018°06'39.9"	ICE08-17*	B	3.04	3.0	4.05 ± 0.32	6.3
			ICE08-18*	B	2.19	4.7	2.51 ± 0.10	10.9
Vonarskarð (Fumarole)	64°41'32.3"	017°53'47.5"	ICE08-16	G	17.27	33.4	17.77 ± 2.89	
			ICE08-21	G	18.86	50.5	19.22 ± 0.27	
Vonarskarð (Spring)	64°41'26.8"	017°52'53.9"	ICE08-13	W	15.41	11.8	16.74 ± 0.25	191.9
Northern Rift Zone (NRZ)								
Krafla (Borehole 20)	65°42'16.3"	016°44'42.4"	ICE-11	B	8.86	72.1	8.97 ± 0.08	
			ICE-12	B	8.75	121	8.81 ± 0.08	
Krafla (Borehole 13)	65°42'31.4"	016°45'38.7"	ICE-10	B	5.58	7.94	6.24 ± 0.08	
			ICE-17	B	8.84	158	8.89 ± 0.05	
Krafla (Fumarole)	65°43'18.2"	016°47'15.5"	PBICE-20	G	8.36	144	8.40 ± 0.17	
Krafla (Mud pot)	65°43'18.0"	016°47'15.5"	ICE08-06	G	8.89	314	8.91 ± 0.07	
Krafla (Fumarole)	65°43'09.9"	016°47'17.4"	ICE08-10	G	10.36	2361	10.36 ± 0.27	
Námafjall (Mud pot)	65°38'30.5"	016°48'35.8"	PBICE-15*	G	3.10	4.0	3.63 ± 0.06	
Námafjall (Mud pot)	65°38'26.9"	016°48'34.7"	ICE08-03	G	9.27	28.0	9.58 ± 0.10	
Námafjall (Fumarole)	65°38'26.8"	016°48'30.4"	ICE08-02	G	10.26	558	10.28 ± 0.11	
Theystareykir (Mud pot)	65°52'33.2"	016°57'24.2"	PBICE-7	G	8.58	23.0	8.86 ± 0.18	
Theystareykir (Mud pot)	65°52'23.0"	016°58'12.7"	ICE08-09	G	10.10	242	10.13 ± 0.04	
Askja, Viti crater (Bubbling pool)	65°02'40.4"	016°43'31.4"	PBICE-18	G	9.08	130	9.13 ± 0.17	
Askja, Viti crater (Bubbling pool)	65°02'48.0"	016°43'29.2"	ICE08-05	G	9.70	550	9.71 ± 0.07	
Kverkfjöll (Mud pot)	64°40'30.1"	16°41'33.6"	ICE08-19	G	8.37	131	8.43 ± 0.05	
	64°40'30.1"	16°41'33.6"	ICE08-20	G	9.06	103	9.14 ± 0.09	
South Iceland Volcanic Zone (SIVZ)								
Seljavellir (Borehole)	63°33'56.1"	019°36'31.1"	ICE-8	B	18.46	69.9	18.72 ± 0.07	6232.5
			ICE-9	B	19.02	107	19.19 ± 0.06	4502.9

Table IV.1: Continued

Location	Latitude (N)	Longitude (W)	Sample ID[a]	Sample Type[b]	$^3He/^4He$ R_m/R_A[c]	X[d]	$^3He/^4He$ R_c/R_A[e]	$[^4He]_c$[f] cm^3STP/gH_2O ($\times 10^{-9}$)
Snæfellsnes Volcanic Zone (SNVZ)								
Lýsuhóll (Borehole)	64°50'40.7"	023°13'10.6"	ICE-18	B	9.09	646	9.11 ± 0.11	
			ICE-7	B	9.34	672	9.34 ± 0.11	
South Iceland Seismic Zone (SISZ)								
Hæðarendi (Borehole)	64°04'31.8"	20°51'36.3"	ICE-22	B	18.62	283	18.69 ± 0.42	
Selfoss (Borehole)	63°56'46.3"	020°57'38.3"	PBICE-17	B	16.92	8.8	18.55 ± 0.27	
			PBICE-19	B	17.79	62.0	18.01 ± 0.33	
Þjórsardalslaug (Bubbling pool)	64°09'41.7"	019°48'41.4"	ICE08-27	G	21.67	114	21.86 ± 0.23	
			ICE08-28	G	21.74	110	21.93 ± 0.23	
Flúðir (Borehole)	64°07'45.3"	020°19'25.0"	ICE08-23	B	17.21	36.7	17.67 ± 0.11	793.5
Ormsstaðir (Borehole)	64°02'29.9"	020°39'46.3"	ICE08-25	B	21.27	39.6	21.80 ± 0.23	3262.4
Eyvik (Borehole)	64°02'48.4"	020°41'59.4"	ICE08-24	B	22.04	119	22.22 ± 0.09	8645.6
Northwest peninsula (Vestfirðir)								
Hveravik (Spring)	65°41'54.1"	21°33'35.2"	ICE-23	W	24.09	74.2	24.40 ± 0.55	1316.4
			ICE-24	W	24.02	59.7	24.41 ± 0.80	1544.9
Laugarhóll (Bubbling pool)	65°46'51.5"	21°31'13.2"	ICE-25*	G	8.43	5.16	10.22 ± 0.24	
			ICE-26*	G	8.73	4.32	11.06 ± 0.18	
Goðdalur (Spring)	65°49'39.8"	21°35'30.2"	ICE-28	W	15.48	6.01	18.37 ± 0.61	179.1
Gjögur (Bubbling pool)	66°00'01.7"	21°19'12.5"	ICE-29	G	15.83	38.5	16.22 ± 0.37	
			ICE-30	W	15.61	18.6	16.44 ± 0.58	457.0
Krossnes (Bubbling pool)	66°03'01.7"	21°30'22.5"	ICE-31	G	26.76	42.4	27.38 ± 0.44	
			ICE-33	G	26.38	48.7	26.91 ± 0.62	
Laugaland (Bubbling pool)	66°01'11.7"	22°23'43.8"	ICE-34*	G	3.39	11.4	3.62 ± 0.08	
Heyardalur (Bubbling pool)	65°50'23.0"	22° 40'39.9"	ICE-36	W	16.32	11.7	17.75 ± 0.62	323.7
Laugar, Orkubú Vestfjarða (Borehole)	66°06'40.6"	23°27'17.4"	ICE-37	B	11.11	5.63	13.30 ± 0.30	8659.3
Laugardalsá (Borehole)	65°39'23.0"	23°54'36.7"	ICE-38	W	23.59	31.2	24.34 ± 0.52	1389.3
Reykhólar (Borehole)	65°27'15.8"	22°11'52.7"	ICE-39	B	12.93	12.2	13.99 ± 0.50	172.9

[a] Samples labeled ICE-X, PBICE-X, and ICE08-X were collected in 2006, 2007, or 2008, respectively. The 11 samples indicated with asterisks are considered to be contaminated by air-derived helium (i.e., X<5) or addition of radiogenic helium (see section IV.5.1.1).

[b] Samples are designated: G = gas, W = water, and B = collected from a borehole.

[c] R_m/R_A is the measured $^3He/^4He$ ratio divided by the $^3He/^4He$ ratio in air.

[d] $X = (^4He/^{20}Ne)_{measured}/(^4He/^{20}Ne)_{air} \times \beta_{Ne}/\beta_{He}$, where β represents the Bunsen coefficient from (Weiss, 1971), which is the volume of gas absorbed per volume of water at a pressure of 1 atm assuming an air-equilibration temperature of 10°C. Note that β_{Ne}/β_{He} does not change significantly with temperature, e.g., β_{Ne}/β_{He} = 1.29 at 5ºC and β_{Ne}/β_{He} = 1.25 at 10ºC.

[e] R_c/R_A is the air-corrected He isotope ratio = $[(R_{M/}R_A \times X) - 1)/(X - 1)]$.

[f] He concentrations are air-corrected, where $[He]_c = ([He]_m(X - 1))/X$.

Table IV.2: Neon characteristics of select geothermal fluids from Iceland[a].

Location	Sample ID	[^{20}Ne] cm^{3}STP/gH$_2$O ($\times 10^{-9}$)	^{21}Ne/^{22}Ne	^{20}Ne/^{22}Ne	δ^{21}Ne[b]	δ^{20}Ne[c]
WRZ						
Nesjavellir	ICE-1		0.0299 ± 0.0005	10.05 ± 0.05	3.10	2.55
Svartsengi	ICE-6		0.0297 ± 0.0005	9.97 ± 0.07	2.41	1.73
NRZ						
Krafla	ICE-11		0.0297 ± 0.0004	9.89 ± 0.06	2.41	0.92
	ICE-12		0.0299 ± 0.0004	9.93 ± 0.04	3.10	1.33
Krafla	ICE-10		0.0300 ± 0.0004	10.07 ± 0.04	3.45	2.76
	ICE-17		0.0302 ± 0.0004	10.09 ± 0.05	4.14	2.96
SNVZ						
Lýsuhóll	ICE-18		0.0297 ± 0.0003	9.79 ± 0.04	2.41	-0.10
	ICE-7		0.0300 ± 0.0004	9.95 ± 0.05	3.45	1.53
SISZ						
Hædarendi	ICE-21		0.0297 ±0.0005	9.96 ± 0.06	2.41	1.63
	ICE-22		0.0295 ± 0.0003	9.79 ± 0.06	1.72	-0.10
Seljavellir	ICE-9	179.2 ± 0.4	0.0297 ± 0.0003	9.77 ± 0.06	2.41	-0.31
Vestfirðir						
Hveravik	ICE-23	75.2± 1.2	0.0296 ± 0.0003	9.89 ± 0.05	2.07	0.92
Laugarhóll	ICE-25		0.0297 ± 0.0003	9.74 ± 0.06	2.41	-0.61
Goðdalur	ICE-28	126.3 ± 2.4	0.0297 ± 0.0003	9.78 ± 0.05	2.41	-0.20
Gjögur	ICE-29		0.0295 ± 0.0003	9.74 ± 0.09	1.72	-0.61
	ICE-30	104.1 ± 0.6	0.0300 ± 0.0004	9.86 ± 0.06	3.45	0.61
Krossnes	ICE-33		0.0298 ± 0.0003	9.84 ± 0.05	0.41	0.62
Laugaland	ICE-34		0.0295 ± 0.0004	9.79 ± 0.04	1.72	-0.10
Heyardalur	ICE-36	117.2 ± 0.7	0.0296 ± 0.0003	9.81 ± 0.04	2.07	0.10
Laugar, Orkubú Vestfjarða	ICE-37	6517 ± 104	0.0299 ± 0.0004	9.85 ± 0.06	3.10	0.51
Laugardalsá	ICE-38	188.7 ± 1.9	0.0295 ± 0.0004	9.79 ± 0.04	1.72	-0.10
Reykhólar	ICE-39	60.4 ± 0.4	0.0296 ± 0.0004	9.83 ± 0.05	2.07	0.31

[a] All errors are reported at the 1 σ level.
[b] $\delta^{21}Ne = \{(^{21}Ne/^{22}Ne)_{sample}/(^{21}Ne/^{22}Ne)_{air} - 1\} \times 100$.
[c] $\delta^{20}Ne = \{(^{20}Ne/^{22}Ne)_{sample}/(^{20}Ne/^{22}Ne)_{air} - 1\} \times 100$.

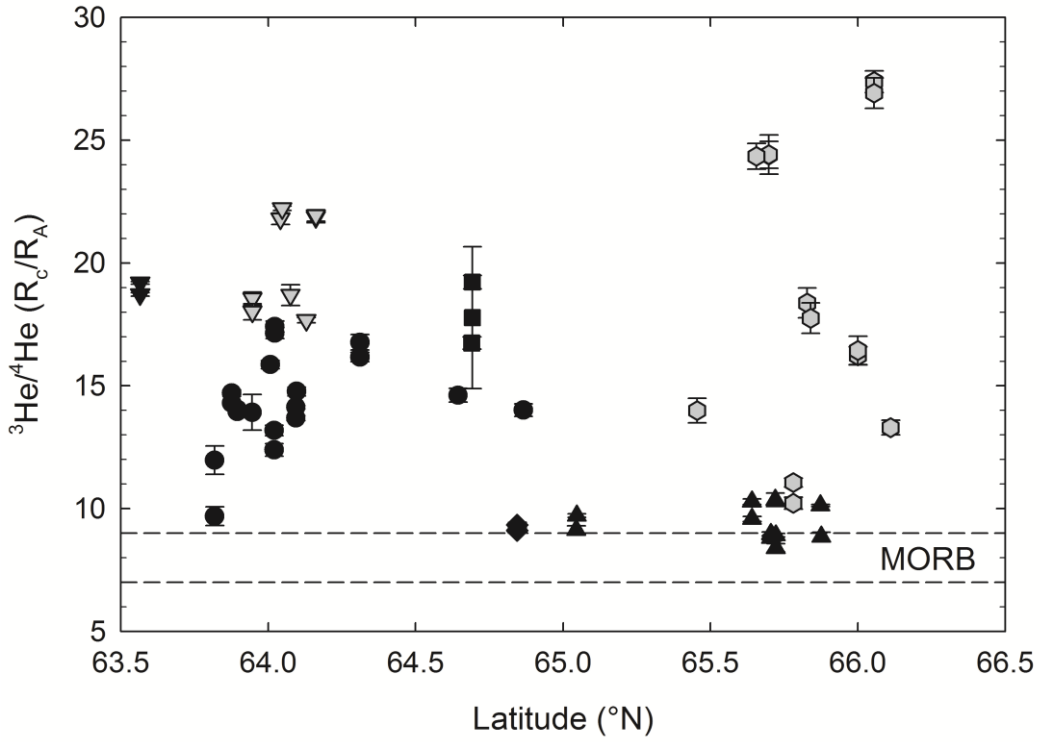

Figure IV.2: Helium isotope ratios ($^3He/^4He$) of Icelandic geothermal fluids as a function of latitude. Symbols as in Figure IV.1a. Errors are given at the 1 σ level.

(1992). South of the NRZ, the $^3He/^4He$ ratios increase to values of 16.7-19.2 at Vonarskarð and remain higher than typical MORB values along the WRZ (9.7 - 17.4 R_A). We note that the $^3He/^4He$ ratio of ~17.4 R_A measured at Hveragerði is slightly higher than the value reported previously for this location (14.9 R_A; Marty et al., 1991). The highest helium isotope ratios (≥ 20 R_A) in our study are found within the SISZ and Vestfirðir, away from the neovolcanic zones. Our results for these regions agree with the data from Hilton et al. (1990; 1998) and Poreda et al. (1992); for example, the highest helium isotope ratio observed in our study (27.4 R_A at Krossnes in Vestfirðir) is comparable to the values of 28.8 R_A and 30.4 R_A reported previously for the same location. Only one water sample from Goðdalur (Vestfirðir) shows a

significantly higher value of 18.4 R_A than observed before (6.3 – 9.5 R_A; Hilton et al., 1998). However, the water samples collected by Hilton et al. (1998) at Goðdalur were heavily contaminated by air-derived helium, as indicated by their low air-normalized He/Ne values of ~1.1. We note that Hilton et al. (1990; 1998) proposed that high $^3He/^4He$ ratios within the SISZ and Vestfirðir result from the release of magmatic volatiles via incipient mantle melting rather than dispersion by groundwater flow from the neovolcanic zones.

IV.5.1.2 Neon isotopes

The $^{20}Ne/^{22}Ne$ ratios, determined for a subset of geothermal samples from 17 locations, range from air-like values (9.8) to 10.1, whereas the $^{21}Ne/^{22}Ne$ ratios are slightly higher than air (0.0290) and vary between 0.0295 and 0.302 (Table IV. 2). In Figure IV.3a, we illustrate the deviation of the neon isotope composition of a given sample from the air value using the $\delta^{20}Ne$ and $\delta^{21}Ne$ notation (see details in Poreda and Dibrozolo, 1984). The mass fractionation line is drawn on the assumption that mass fractionation effects are twice as large in $^{20}Ne/^{22}Ne$ as in $^{21}Ne/^{22}Ne$ (see Sarda et al., 1988, for details). The Ne isotope compositions of Icelandic geothermal fluids differ from those predicted for mass fractionated neon of atmospheric origin. All samples are displaced from air towards higher ^{21}Ne values, with excesses in ^{21}Ne between 1.5 and 4% compared to the atmospheric composition. However, $^{20}Ne/^{22}Ne$ ratios of the majority of fluids collected in Vestfirðir are similar to atmospheric values; thus, these fluids appear to be dominated by atmospheric neon supplemented with a small proportion of nucleogenic ^{21}Ne. In contrast, geothermal fluids from the neovolcanic zones (WRZ, NRZ, and SNVZ) plot near the MORB 2ΠD43 trajectory of Sarda et al. (1988). These samples show $^{20}Ne/^{22}Ne$ enrichments up to 3% compared to air, consistent with a neon component derived from the mantle, albeit heavily diluted by atmospheric neon.

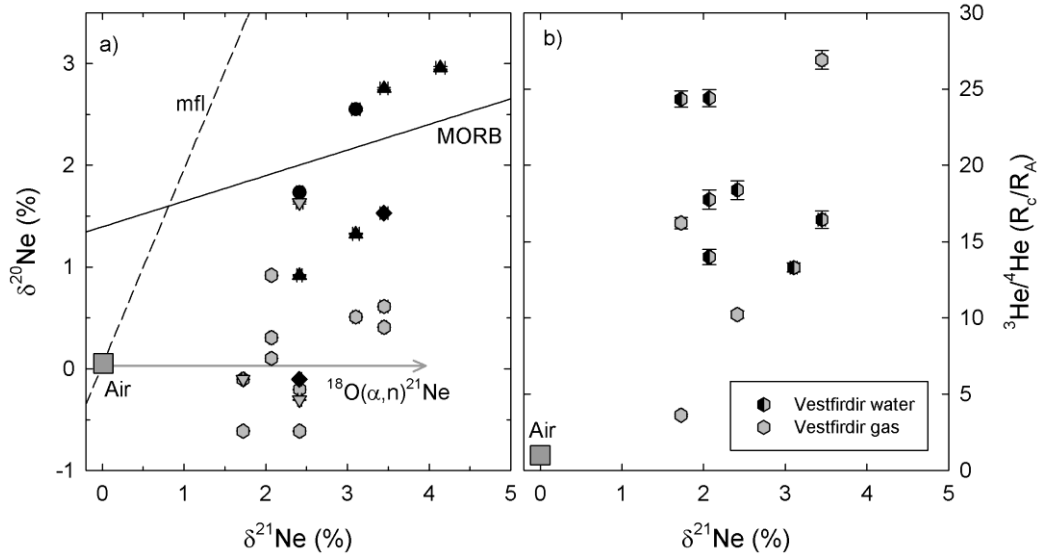

Figure IV.3: a) Neon enrichment (in %) of Icelandic geothermal fluids relative to air. Neon isotope enrichments are shown in the delta notation, where $\delta^{i}Ne = [(^{i}Ne/^{22}Ne)_{sample}/(^{i}Ne/^{22}Ne)_{air} - 1] \times 100$ ($^{i}Ne = ^{20}Ne$ or ^{21}Ne). Also shown are the mass fractionation line (mfl.; dashed line) and the MORB (2ΠD43) trajectory (solid line; Sarda et al., 1988). Addition of nucleogenic ^{21}Ne is characterized by a shift to higher $\delta^{21}Ne$ values. Symbols as in Figure IV.1a. b) $^3He/^4He$ (R_c/R_A) versus $\delta^{21}Ne$ for geothermal fluids from Vestfirðir.

IV.5.2 Basaltic glasses and phenocrysts

Helium isotope ratios and abundance results for 77 basaltic glasses, as well as 5 clinopyroxene and 15 olivine phenocryst samples are reported in Table IV.3 with sample locations shown in Figure IV.1b. Neon and argon concentrations and isotope ratios for a subset of 44 glass samples are given in Table IV.4.

IV.5.2.1 Helium

Our new helium data fall within the range of values reported previously for phenocrysts and subglacial basalt glasses from Iceland (Condomines et al., 1983; Kurz et al., 1985; Poreda et al., 1986; Harrison et al., 1999; Dixon et al., 2000; Trieloff et al., 2000; Moreira et al., 2001; Dixon, 2003; Macpherson et al., 2005a). The He contents fall in the

range (0.1 to 14) × 10^{-9} cm^3STP/g in olivine and clinopyroxene phenocrysts, while the glasses are significantly more gas-rich and yield He concentrations up to 3450 × 10^{-9} cm^3STP/g. Olivine, clinopyroxene and glass samples are characterized by a wide range in $^3He/^4He$ ratios encompassing typical MORB-like values through high-^3He hotspot values up to 36.8 R_A (Table IV.3; Fig. IV.4). We note that 11 glasses from the NRZ and ERZ, as well as one pyroxene sample from Vestfirðir, show significantly lower $^3He/^4He$ ratios than other samples from the same general locations. Since these 11 glasses (marked with asterisks in Table IV.3) also yield the lowest He concentrations (i.e., [He] ≤ 5 × 10^{-9} cm^3STP/g), they are more susceptible to contamination by radiogenic He, and thus, are considered suspect and are not included in further discussions.

Helium isotope ratios are exclusively higher than MORB values along the WRZ. Phenocrysts and glass samples yield a wide range of $^3He/^4He$ ratios between 10.3 (Grindavik) and 21.0 R_A (Arnarbæli). Along the NRZ, $^3He/^4He$ ratios of glasses and olivine phenocrysts are predominantly MORB-like in the north and show a trend of increasing values towards Central Iceland, up to 19.7 R_A at Dyngjufjöll Ytri. This value is in excellent agreement with the $^3He/^4He$ ratio of 19.6 R_A obtained previously by Breddam et al. (2000) for this location. We note that the distribution of high $^3He/^4He$ ratios coincides with the zone of low P- and S-wave velocities in the mantle beneath Iceland (e.g., Tryggvason et al, 1983; Wolfe et al., 1997), confirming that the high helium isotope values outline the lateral distribution of upwelling hotspot mantle (Breddam et al., 2000). However, all glass samples from the ERZ and the single glass sample collected within the SIVZ also show helium isotope ratios ≥ 18 R_A, as noted previously (Kurz et al., 1985; Breddam et al., 2000). Breddam et al. (2000) proposed that these high $^3He/^4He$ ratios result from the southward migration of hotspot mantle material along the propagating ERZ.

Table IV.3: Helium isotope and abundance systematics of Icelandic basalts[a].

Sample	Phase	Location	Lat (N)	Lon (W)	Amount processed (g)	$^3He/^4He$[b] (R/R_A)	[He] cm^3STP/g ($\times 10^{-9}$)
WRZ							
SKARD-1	glass	Skarðsmýrarfjall	64°02´37.6"	021°21´29.9"	0.5054	12.94 ± 0.26	9.27 ± 0.08
VIF-1	glass	Vífilsfell	64°02´55.4"	021°32´24.8"	0.5059	12.97 ± 0.18	45.18 ± 0.13
MID-1	glass	Miðfell	64°10´28.9"	021°02´50.9"	0.4974	16.65 ± 0.20	3177 ± 2
	glass				0.0674	17.22 ± 0.03	3447 ± 1
	olivine				1.0263	16.23 ± 0.62	10.44 ± 0.01
	olivine				1.0565	17.28 ± 0.37	11.11 ± 0.01
MID-2	glass	Arnarfell	64°13´02.3"	021°04´12.1"	0.3027	15.58 ± 0.46	35.35 ± 0.12
MID-3	glass	Kálfstindar	64°13´06.2"	020°53´08.9"	0.5041	14.06 ± 0.15	868.19 ± 0.34
NES-1	glass	Nesjavellir	64°06´01.1"	021°14´50.4"	0.51	15.75 ± 0.18	139.64 ± 0.08
OLF-1	glass	Ölfusvatnsfjöll	64°06´57.0"	021°08´26.4"	0.5066	14.49 ± 0.08	258.17 ± 0.08
BUR-1	olivine	Búrfell	63°53´59.5"	021°27´43.9"	1.031	13.05 ± 0.42	2.69 ± 0.01
THREN-1	glass	Þrengsli	64°00´04.8"	021°27´45.4"	0.502	13.62 ± 0.29	48.80 ± 0.28
	olivine				1.0345	12.59 ± 0.55	5.04 ± 0.03
REY-1	glass	Reykjanes viti	63°48´44.6"	022°42´49.2"	0.3104	14.20 ± 0.05	623.43 ± 3.01
D-2	olivine	Háleyjarbunga	63°48´55.6"	022°38´43.0"	1.0921	14.34 ± 0.30	7.71 ± 0.02
GRIN-1	olivine	Grindavik	63°50´45.7"	022°24´50.2"	1.0092	10.27 ± 0.66	0.57 ± 0.01
VATN-1	olivine	Vatnsheiði	63°51´33.6"	022°22´18.5"	1.0254	11.92 ± 0.41	3.28 ± 0.01
HRA-1	glass	Hraunsvik	63°51´06.9"	022°22´07.2"	0.4973	14.16 ± 0.10	27.06 ± 0.01
ISO-1	olivine	Ísólfskáli	63°51´38.7"	022°19´03.9"	1.0221	16.30 ± 0.63	6.09 ± 0.03
MAE-1	glass	Mælifell	64°06’25.4"	021°10’54.9"	0.3305	12.48 ± 0.25	400.04 ± 0.16
	olivine				1.0608	12.94 ± 0.19	14.37 ± 0.02
	cpx				0.9542	12.44 ± 0.33	12.37 ± 0.01
LON-1	glass	Lönguhlíðar	63°58'18.2"	021°56'42.2"	0.48	15.49 ± 0.17	24.74 ± 0.12
KLE-1	glass	Kleifarvatn	63°54'40.4"	022°00'43.5"	0.57	12.64 ± 0.23	3.19 ± 0.05
HEL-2	glass	Helgafell	64°00'57.8"	021°50’32.8"	0.51	12.37 ± 0.26	7.91 ± 0.12
ICE08R-07	glass	Stakur	63°59'47.2"	021°53’19.4"	0.45	11.43 ± 0.17	15.53 ±0.08

Table IV.3: Continued

Sample	Phase	Location	Lat (N)	Lon (W)	Amount processed (g)	$^{3}He/^{4}He^{b}$ (R/R_A)	[He] cm^3STP/g ($\times 10^{-9}$)
A1	glass	Ármannsfell	64°19'13.5"	020°59'43.9"	0.58	15.26 ± 0.14	168.51 ± 1.97
A2	glass	Þórólfsfell	64°26'55.6"	020°31'02.1"	0.50	14.01 ± 0.14	154.03 ± 3.79
A3	glass	Hlöðufell	64°25'44.4"	020°34'13.3"	0.51	15.18 ± 0.15	29.23 ± 0.49
A4	glass	Fagradalsfjöll-1	64°27'10.2"	020°18'22.0"	0.49	15.36 ± 0.24	24.23 ± 0.21
A6	glass	Bláfell	64°30'56.3"	019°53'16.2"	0.49	15.36 ± 0.23	50.36 ± 0.23
A8	glass	Þverbrekknamúli-2	64°43'23.6"	019°36'52.7"	0.45	14.52 ± 0.26	22.08 ± 0.29
A9	glass	Arnarbæli	65°00'50.9"	019°35'20.7"	0.44	21.05 ± 0.09	831.47 ± 9.65
STAK-1	glass	Stakksá	64°17'41.5"	020°21'53.3"	0.51	14.73 ± 0.82	4.93 ± 0.11
NRZ							
Th-29	olivine	Þeistareykir	65°55'51.6"	017°04'21.5"	3.0363	6.11 ± 0.47	0.14 ± 0.01
BORG-1	olivine	Borgarhaun	65°50'33.1"	016°59'33.0"	1.0047	7.91 ± 0.35	1.97 ± 0.01
KVIH-1	glass	Kviholafjoll	65°50'24.6"	016°59'10.4"	0.512	9.39 ± 0.15	13.04 ± 0.03
NAL-837	glass	Kviholafjoll	65°50'24.6"	016°59'10.4"	0.4943	9.41 ± 0.25	26.08 ± 0.02
NAL-213	glass	Hvammsfjöll	65°21'49.8"	016°40'26.7"	0.4432	12.49 ± 0.17	85.51 ± 0.15
NAL-216	glass	Hvammsfjöll	65°21'38.7"	016°41'11.4"	0.4229	12.84 ± 0.06	578.61 ± 0.17
NAL-263	glass	V-Skógamannafjöll	65°34'56.0"	016°33'53.1"	0.4133	9.25 ± 0.04	2826.9 ± 3.5
NAL-265	glass	V-Skógamannafjöll	65°35'17.8"	016°33'55.8"	0.4433	9.01 ± 0.05	91.63 ± 0.35
NAL-281	glass	Herðubreiðarfjöll	65°22'10.7"	016°22'29.5"	0.4225	10.36 ± 0.18	1255.0 ± 0.5
NAL-440	glass	Hrímalda	64°55'29.4"	017°05'08.1"	0.413	8.84 ± 0.14	4.68 ± 0.01
NAL-455	glass	Kverfjöll	64°44'18.3"	016°37'20.1"	0.4534	2.27 ± 0.10*	5.04 ± 0.03
NAL-458	glass	Búrfell	65°34'04.0"	016°38'34.7"	0.386	3.04 ± 0.14*	5.07 ± 0.03
NAL-460	glass	Þeistareykir/Kistufjall	65°52'45.0"	017°09'20.2"	0.50	4.91 ± 0.27*	2.96 ± 0.01
NAL-461	glass	Þeistareykir/Lambafjall	65°50'18.7"	017°06'45.2"	0.4217	4.27 ± 0.20*	2.74 ± 0.02
NAL-500	glass	Gæsavatn	64°46'50.2"	017°30'40.7"	0.3323	17.57 ± 0.35	205.34 ± 0.12
NAL-537	glass	Herðubreiðarfjöll	65°21'29.8"	016°24'03.4"	0.3925	11.40 ± 0.05	277.95 ± 0.14
A26	glass	Vonarskarð	64°41'32.3"	017°53'47.5"	0.52	19.89 ± 0.57	186.36 ± 2.57
A27	glass	Kirkjufellsvatn	63°58'44.5"	018°53'46.6"	0.48	19.67 ± 0.32	115.50 ± 0.66

Table IV.3: Continued

Sample	Phase	Location	Lat (N)	Lon (W)	Amount processed (g)	$^3He/^4He$[b] (R/R_A)	[He] cm^3STP/g ($\times 10^{-9}$)
A28	glass	Klappagil	63°58'26.9"	018°47'31.9"	0.49	1.87 ± 0.16*	4.09 ±0.03
A29	glass	Hörðufell	63°58'08.5"	018°40'47.1"	0.50	8.76 ± 2.51*	1.09 ±0.01
A30	glass	Hellnaá	64°03'41.0"	018°32'02.4"	0.49	18.59 ± 0.53	5.72 ± 0.06
A31	glass	Hrútabjörg	64°06'37.1"	018°27'41.7"	0.52	12.17 ± 0.49*	3.09 ± 0.09
A32	glass	NW of Grænifjallgarður	64°06'20.8"	018°30'55.5"	0.50	18.07 ± 0.07	132.44 ±7.15
A33	glass	Breiðbak	64°06'21.4"	018°34'07.2"	0.48	18.99 ± 0.57	3.79 ± 0.04
A34	glass	Hnausar	64°05'16.0"	019°03'15.0"	0.48	10.55 ± 0.32*	2.30 ± 0.02
A35	glass	Sigalda	64°10'19.8"	019°08'18.7"	0.16	20.59 ± 0.24	193.15 ± 0.82
A36/ICE08R-23	glass	Heljargjá	64°19'19.8"	018°27'37.8"	0.46	19.65 ± 0.40	6.05 ± 0.21
A37/ICE08R-24	glass	Miklagljúfur	64°19'13.8"	018°25'57.4"	0.47	19.23 ± 0.61	8.31 ± 0.07
A38/ICE08R-25	glass	Fellsendavatn	64°11'18.5"	018°57'25.2"	0.46	2.19 ± 0.18*	2.55 ± 0.01
ICE08R-20	glass	Fontur, craters	64°15'06.3"	018°39'08.4"	0.49	1.16 ± 0.08*	2.41 ± 0.03
SIVZ							
RET-1/VES-1	glass	Réttarfell (Þórsmörk)	63°40'19.5"	019°29'32.4"	0.50	18.93 ± 0.22	90.56 ± 4.54
Vestfirðir							
ICE08R-01	olivine	Bjarnardalsá	64°50'02.0"	021°29'20.8"	0.7751	20.34 ± 1.04	2.02 ± 0.01
	cpx				0.9002	14.78 ± 0.68	1.91 ± 0.02
ICE08R-02	olivine	Selárdalur	65°45'43.6"	024°02'35.1"	1.172	34.92 ± 0.17	1.50 ± 0.06
	cpx				1.0146	36.76 ± 1.19	3.55 ± 0.03
ICE08R-03	olivine	Vatnseyri	65°51'05.0"	023°15'12.2"	0.9535	26.08 ± 1.34	0.40 ± 0.01
ICE08R-04b	olivine	Ekkisdalur	65°57'24.3"	023°19'07.0"	0.995	36.38 ± 1.42	1.08 ± 0.08
	cpx				0.9921	2.70 ± 0.06	0.67 ± 0.07
Lambadalur	olivine	Dýrafjörður syðri	-	-	0.9469	21.64 ± 1.82	0.20 ± 0.01
	cpx				1.2008	21.39 ± 1.15	0.61 ± 0.03

[a] All errors are reported at the 1 σ level.
[b] Glass samples indicated with asterisks contain low magmatic gas contents and data is not considered in further discussions.

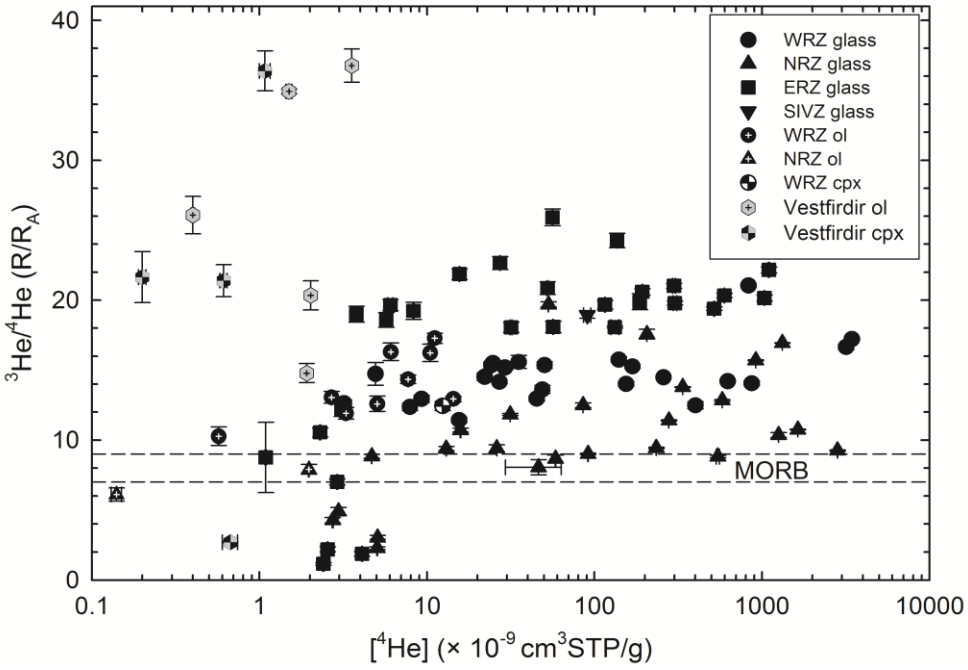

Figure IV.4: Helium isotope ratios (^{3}He/^{4}He) versus helium concentrations for basaltic glasses as well as olivine and pyroxene phenocrysts. Errors are given at the 1 σ level.

Significantly higher helium isotope ratios (> 30 R_A) are observed in olivine and clinopyroxene phenocrysts from Tertiary lavas in Vestfirðir, away from the Icelandic neovolcanic zones. The highest ^{3}He/^{4}He ratio of 36.8 ± 1.2 R_A at Selárdalur agrees with the values of 37.7 R_A and 37.0 R_A reported previously for the same location by Hilton et al. (1999) and Ellam and Stuart (2004), respectively. Other samples from Vestfirðir have ^{3}He/^{4}He values that vary between 2.7 and 36.4 R_A. We note that pyroxenes from Bjarnardalsá and Lambadalur have lower ^{3}He/^{4}He ratios than cogenetic olivines. This may indicate that the pyroxenes crystallized after the olivines from a melt that was influenced by addition of crustal He, as suggested by Gasparon et al (1994). An additional consideration is that ^{4}He from alpha-decay of groundmass U and Th may be implanted into the rims of both olivine and pyroxene grains. Such an effect could

be significant for phenocrysts of Tertiary age. If this He is liberated by crushing then the $^{3}He/^{4}He$ ratios would represent minimum values.

Our data confirm that basalts collected along the three segments of the Icelandic axial rift zones have distinct helium isotope signatures, with the highest $^{3}He/^{4}He$ ratios found near Central Iceland and along the ERZ. In general, subglacial basalts and phenocrysts from the neovolcanic zones show a similar range in helium isotope ratios to the geothermal fluids collected nearby. For example, the highest $^{3}He/^{4}He$ ratio obtained for geothermal fluids from the ERZ (19.22 R_A at Vonarskarð) agrees with the isotope ratio measured in basaltic glass at the same location (19.89 R_A). In contrast, geothermal fluids collected at Reykjanes (11.97 R_A) show slightly lower $^{3}He/^{4}He$ ratios than basaltic glass and olivine phenocrysts collected nearby (14.20 and 14.34 R_A at Reykjanes viti and Háleyjarbunga, respectively).

IV.5.2.2 Neon

Neon concentrations for 44 subglacial basalt glasses vary over three orders of magnitude from (16 to ~16,000) × 10^{-12} $cm^3STP^{20}Ne/g$ as shown in Figure IV.5. In this plot, we illustrate the deviation of the neon isotope composition of a given sample from the air value using the $\delta^{20}Ne$ and $\delta^{21}Ne$ notation (see details in Poreda and Dibrozolo, 1984). We note that samples from the ERZ have air-like Ne isotope compositions, regardless of neon abundances. Along the WRZ, glasses have high $\delta^{20}Ne$ and $\delta^{21}Ne$ values (up to 23 and 36%, respectively) for a wide range of neon concentrations. Glasses from NRZ, on the other hand, show neon isotope enrichments only at low neon concentrations. In other words, along the NRZ, the lowest concentration samples are the least contaminated by air. This effect has been observed previously in studies of submarine glasses (e.g., Shaw et al., 2001; Macpherson et al., 2005b).

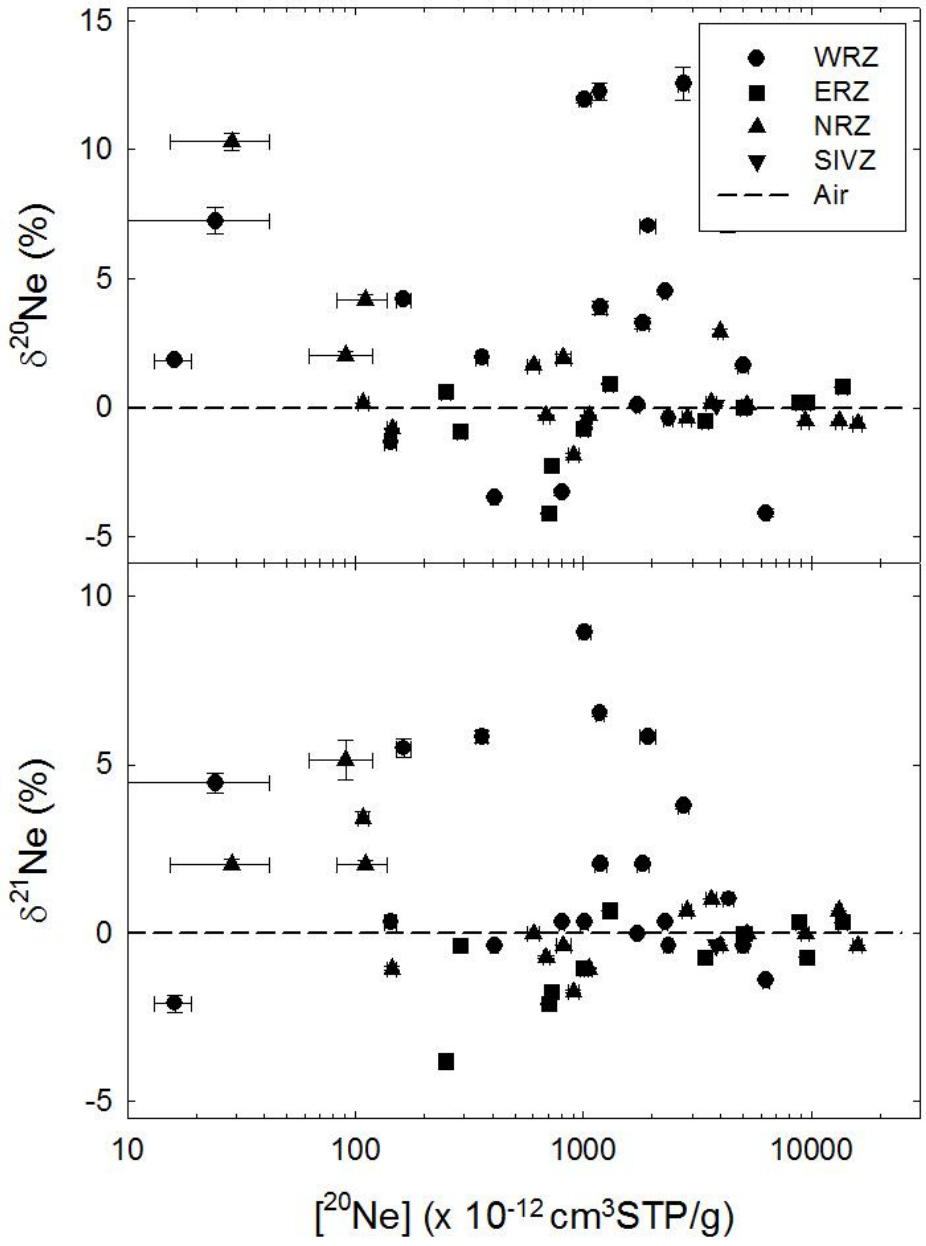

Figure IV.5: Neon isotope enrichment (in %) of Icelandic subglacial glasses relative to air as a function of ^{20}Ne concentration. Neon isotope enrichments are shown in the delta notation where $\delta^{i}Ne = [(^{i}Ne/^{22}Ne)_{sample}/(^{i}Ne/^{22}Ne)_{air} - 1] \times 100$ ($^{i}Ne = ^{20}Ne$ or ^{21}Ne). The dashed line represents air (i.e., $\delta^{20}Ne$ and $\delta^{21}Ne = 0$). Errors are given at the 1 σ level.

In Figure IV.6, we show the $^{20}Ne/^{22}Ne$ and $^{21}Ne/^{22}Ne$ ratios of Icelandic subglacial glasses in a three-isotope plot. The $^{20}Ne/^{22}Ne$ ratios range from air-like values (9.8) to 11.0, whereas the $^{21}Ne/^{22}Ne$ ratios lie between the atmospheric ratio (0.0290) and 0.316. We note that sample A2 shows an even higher $^{20}Ne/^{22}Ne$ ratio of 12.0; duplicate analysis, however, yielded an atmospheric isotope ratio (Table IV.4) and so this sample is excluded from further consideration. Figure IV.6 provides further illustration that neon in most samples erupted along the ERZ is air-like. Sample RET-1 from the SIVZ also lies within error of the air value. However, a significant number of samples from the WRZ and NRZ show non-atmospheric neon isotope ratios. Within error, these samples fall between the MORB trajectory defined by mid-ocean ridge popping rock 2ΠD43 (Moreira et al., 1998) and the line joining the solar wind isotope composition to atmosphere, suggesting that neon in Icelandic basalts could be derived from a mixture of depleted MORB-mantle and a relatively undegassed, 'solar' mantle component (see section IV.6.1). We note that the highest $^{20}Ne/^{22}Ne$ ratio (11.0 ± 0.3), measured in sample MID-1 from the WRZ, is significantly lower than the values for solar wind neon (13.8; Benkert et al., 1993; Kallenbach et al., 1997) and Ne-B (12.5; Black, 1972), i.e., the values proposed for primordial neon in Earth's mantle. In previous studies of glasses from the same locality (Dagmálafell, Miðfell), Harrison et al. (1999) reported $^{20}Ne/^{22}Ne$ ratios up to 13.7 in samples Dice 10 and 11, whereas Trieloff et al. (2000) and Parai et al. (2000) obtained values up to 12.8 and 12.2, respectively. However, the study by Harrison et al. (1999) appears to have over-estimated the $^{21}Ne/^{22}Ne$ ratios (likely due to low Ne sensitivity of the mass spectrometer and contamination by a ^{21}Ne-enriched spike); thus, these high values are controversial (Trieloff et al., 2000; Harrison et al., 2003). Furthermore, the highest $^{20}Ne/^{22}Ne$ ratios observed in all previous studies were released during the final stages of step-wise crushing experiments; total gas $^{20}Ne/^{22}Ne$ ratios (i.e., $^{20}Ne/^{22}Ne$ ratios integrated over all crushing steps) range from 10.4 to 11.7, and are comparable to our data obtained by single-

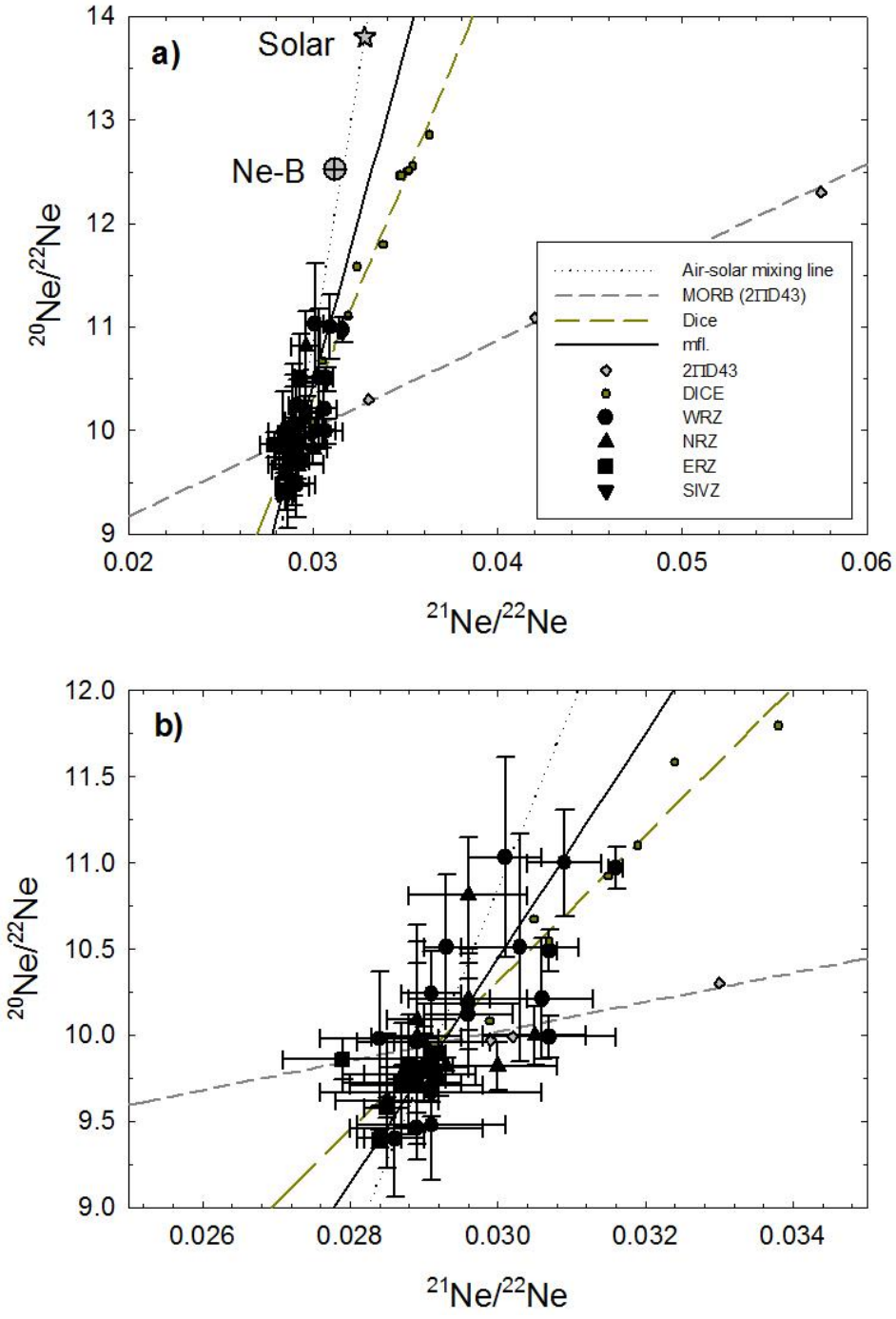

Figure IV.6: Three isotope neon plot for basaltic glasses with $^{20}Ne/^{22}Ne$ versus $^{21}Ne/^{22}Ne$ including a) the solar value and Ne-B, and b) expanded version. Also shown are the air-solar mixing line, the MORB (2ΠD43) trajectory (Sarda et al., 1988), the Dice trajectory (Trieloff et al., 2000), and the mass fractionation line (mfl.).

step crushing. We note that our glasses from Miðfell (MID-1) fall onto the Dice trajectory of Trieloff et al. (2000), confirming that our neon data agree with previous findings.

The Dice results led Ballentine and Barfod (2000) and Sarda (2004) to propose that most glass samples (MORB and OIB) contain both large vesicles, bearing atmosphere-derived noble gases, and smaller vesicles which carry the mantle component. Thus, the neon isotope ratios obtained in our study by single-step crushing (i.e., the method employed to maximize noble gas yields), likely represent mixtures of atmospheric and mantle-derived neon residing in distinct vesicle generations. Consequently, the highest $^{20}Ne/^{22}Ne$ ratio measured in sample MID-1 in our study represents a minimum estimate for the neon isotope composition of the Icelandic mantle source.

IV.5.2.3 Argon

The Icelandic subglacial glasses yield a wide range in ^{40}Ar concentrations from (~14 to 9000) × 10^{-9} cm^3STP/g (Table IV.4; Fig. IV.7). The highest Ar contents are found in glasses from the NRZ (NAL-263, -281, -595), and are significantly higher than typical MORB values ([^{40}Ar] ~ 1200 × 10^{-9} cm^3STP/g; Sarda et al., 1985; Staudacher et al., 1986; Allègre et al., 1987).

There is a large range in Ar isotope compositions ($^{40}Ar/^{36}Ar$); the highest $^{40}Ar/^{36}Ar$ measured is 1334 while the lowest ratios are undistinguishable from the atmospheric Ar composition (295.5). All measured $^{40}Ar/^{36}Ar$ ratios are significantly lower than MORB and OIB source estimates, which are ~32,000 - 40,000 (Burnard et al., 1997; Trieloff et al., 2003) and 6600 - 8000 (Trieloff et al., 2000; 2003), respectively, indicating that a large component of argon in all Icelandic glass samples is atmosphere-derived. Figure IV.7a shows that the majority of glasses from the ERZ and NRZ have only slightly elevated $^{40}Ar/^{36}Ar$ ratios compared to atmospheric values. However, three samples from the NRZ show significantly

higher values of ~340 to 590, and sample A22/ICE08R-17 from the ERZ yields a $^{40}Ar/^{36}Ar$ ratio of ~1100. Along the WRZ, a number of samples have $^{40}Ar/^{36}Ar$ ratios higher than air. The highest $^{40}Ar/^{36}Ar$ ratio (1334.5 ± 2.4) is observed in sample MID-1, which is the sample with the highest $^{20}Ne/^{22}Ne$ values. In previous studies, Burnard et al. (1994) observed $^{40}Ar/^{36}Ar$ ratios up to 2200 ± 200 in a basaltic glass sample from Miðfell, whereas Harrison et al. (1999) obtained significantly higher $^{40}Ar/^{36}Ar$ ratios up to 4900 and 6500 for the same locality, comparable to the lowest estimates for the OIB mantle source (~6600; Trieloff et al., 2003).

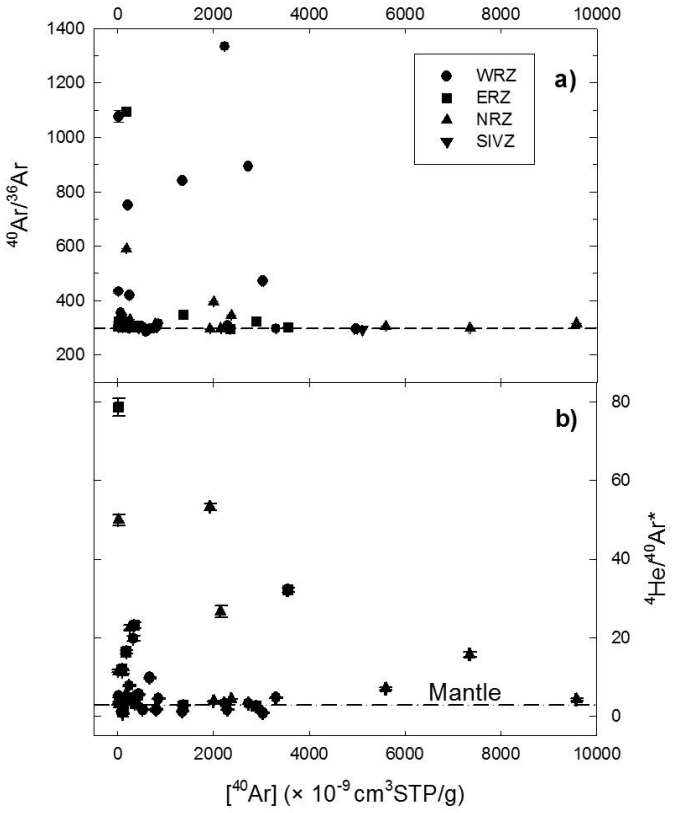

Figure IV.7: a) $^{40}Ar/^{36}Ar$ and b) $^{4}He/^{40}Ar^{*}$ as a function of ^{40}Ar concentrations in basaltic glasses. Also shown is the theoretical $^{4}He/^{40}Ar^{*}$ production ratio (~2.9) calculated for the upper mantle on the basis of U, Th and K concentrations (Jochum et al., 1983; Graham, 2002). Errors are shown at the 1 σ level.

Table IV.4: Neon and argon systematics of Icelandic subglacial glasses[a].

Sample[b]	Amount processed (mg)	[^{4}He] cm^{3}STP/g (× 10^{-9})	[^{20}Ne] cm^{3}STP/g (× 10^{-12})	^{21}Ne/^{22}Ne	^{20}Ne/^{22}Ne	[^{40}Ar] cm^{3}STP/g (× 10^{-9})	^{40}Ar/^{36}Ar	^{38}Ar/^{36}Ar	^{4}He/^{40}Ar*
WRZ									
SKARD-1	389.7	13.45 ± 0.23	803.84 ± 26.39	0.0291 ± 0.0010	9.48 ± 0.32	240.0 ± 1.7	297.7 ± 2.0	0.1875 ± 0.0020	7.7 ± 0.2
VIF-1	487.6	13.97 ± 0.24	162.76 ± 11.36	0.0306 ± 0.0007	10.21 ± 0.35	85.4 ± 0.5	346.2 ± 2.1	0.1874 ± 0.0014	1.1 ± 0.1
MID-1	362.2	929.20 ± 0.24	1181.36 ± 42.04	0.0309 ± 0.0005	11.00 ± 0.31	1357.0 ± 5.0	840.9 ± 4.0	0.1866 ± 0.0010	1.1 ± 0.1
	309.3	1555.10 ± 26.10	2745.39 ± 133.45	0.0301 ± 0.0005	11.03 ± 0.58	3027.8 ± 11.5	741.8 ± 3.1	0.1877 ± 0.0011	0.8 ± 0.1
	518.6	5884.03 ± 94.85	1918.48 ± 142.86	0.0307 ± 0.0001	10.49 ± 0.12	2728.7 ± 9.5	894.2 ± 3.6	0.1893 ± 0.0008	3.2 ± 0.1
	505.8	5559.18 ± 199.30	1013.05 ± 58.20	0.0316 ± 0.0001	10.97 ± 0.12	2234.0 ± 9.2	1334.5 ± 2.4	0.1906 ± 0.0008	3.2 ± 0.1
MID-2	340.7	9.23 ± 0.02	1719.85 ± 32.67	0.0290 ± 0.0006	9.81 ± 0.20	444.6 ± 3.1	296.6 ± 1.9	0.1878 ± 0.0017	5.4 ± 0.1
MID-3	335.1	160.52 ± 2.70	4327.65 ± 241.56	0.0293 ± 0.0003	10.50 ± 0.42	2290.9 ± 9.9	309.0 ± 1.1	0.1879 ± 0.0011	1.6 ± 0.1
NES-1	344.1	35.54 ± 2.70	1190.07 ± 69.72	0.0296 ± 0.0007	10.18 ± 0.15	671.0 ± 2.9	297.1 ± 1.1	0.1878 ± 0.0011	9.7 ± 0.2
OLF-1	502.6	99.33 ± 0.60	*24.37 ± 17.51*	*0.0303 ± 0.0008*	*10.51 ± 0.66*	27.2 ± 0.3	1076.4 ± 21.6	0.1839 ± 0.0041	5.0 ± 0.2
THREN-1	312.3	21.31 ± 0.15	1821.18 ± 110.76	0.0296 ± 0.0006	10.12 ± 0.30	810.0 ± 3.4	300.4 ± 1.1	0.1884 ± 0.0010	1.6 ±0.1
REY-1	365.2	77.31 ± 1.90	6322.84 ± 193.61	0.0286 ± 0.0004	9.40 ± 0.34	4974.7 ± 37.7	295.4 ± 1.5	0.1877 ± 0.0008	-
	287.8	60.27 ± 0.36	5006.47 ± 286.95	0.0289 ± 0.0003	9.96 ± 0.68	3303.4 ± 13.3	296.6 ± 0.7	0.1879 ± 0.0009	4.7 ± 0.1
HRA-1	304.7	32.41 ± 0.61	2281.38 ± 55.54	0.0291 ± 0.0004	10.24 ± 0.25	591.1 ± 2.7	287.1 ± 1.5	0.1830 ± 0.0011	-
MAE-1	335.8	15.83 ± 0.27	*16.18 ± 2.98*	*0.0284 ± 0.0008*	*9.98 ± 0.39*	14.8 ± 0.6	433.0 ± 7.3	0.1830 ± 0.0030	3.4 ± 0.2
A1	550.2	172.50 ± 5.72	359.38 ± 21.35	0.0307 ± 0.0009	9.99 ± 0.12	329.3 ± 1.6	303.6 ± 0.6	0.1908 ± 0.0006	19.7 ± 0.7
A2	585.9	536.27 ± 14.50	72.16 ± 4.69	0.0393 ± 0.0001	12.01 ± 1.04	208.6 ± 1.0	750.8 ± 2.4	0.1918 ± 0.0008	4.2 ± 0.1
	1163.9	242.99 ± 6.97	2362.64 ± 108.54	0.0289 ± 0.0001	9.76 ± 0.06	854.4 ± 3.6	315.8 ± 0.7	0.1868 ± 0.0006	4.4 ± 0.1
	631.8	40.70 ± 0.53	142.70 ± 8.11	0.0291 ± 0.0015	9.67 ± 0.14	61.8 ± 0.3	353.9 ± 0.7	0.1923 ± 0.0010	4.0 ± 0.1
A6	594.0	21.96 ± 0.77	1012.79 ± 38.74	0.0291 ± 0.0001	9.72 ± 0.11	526.0 ± 1.6	303.3 ± 0.6	0.1891 ± 0.0005	1.6 ± 0.1

Table IV.4: Continued

Sample[b]	Amount processed (mg)	[^{4}He] cm^{3}STP/g (× 10^{-9})	[^{20}Ne] cm^{3}STP/g (× 10^{-12})	^{21}Ne/^{22}Ne	^{20}Ne/^{22}Ne	[^{40}Ar] cm^{3}STP/g (× 10^{-9})	^{40}Ar/^{36}Ar	^{38}Ar/^{36}Ar	^{4}He/^{40}Ar*
A9	480.1	343.07 ± 9.32	408.07 ± 16.37	0.0289 ± 0.0009	9.46 ± 0.09	247.3 ± 1.1	419.3 ± 0.6	0.1935 ± 0.0007	4.7 ± 0.1
NRZ									
KVIH-1	517.7	15.78 ± 0.26	*28.72 ± 13.31*	*0.0296 ± 0.0008*	*10.81± 0.34*	*20.1 ± 0.5*	*300.3 ± 1.5*	*0.1859 ± 0.0019*	49.9 ± 1.4
NAL-837	426.3	7.71 ± 0.02	*90.56 ± 27.92*	*0.0305 ± 0.0007*	*10.00 ± 0.17*	*13.7 ± 0.4*	*310.9 ± 1.2*	*0.1902 ± 0.0021*	11.4 ± 0.3
NAL-216	388.2	620.24 ± 17.28	603.95 ± 37.91	0.0290 ± 0.0009	9.96 ± 0.09	258.2 ± 1.1	330.7 ± 0.5	0.1893 ± 0.0010	22.5 ± 0.6
NAL-263	475.6	2637.41 ± 178.91	13213.92 ± 460.90	0.0292 ± 0.0001	9.75 ± 0.04	9578.7 ± 15.8	316.3 ± 0.5	0.1884 ± 0.0006	4.2 ± 0.3
NAL-281	406.1	963.73 ± 40.69	15949.74 ± 706.43	0.0289 ± 0.0001	9.74 ± 0.04	7349.3 ± 24.3	298.0 ± 0.4	0.1872 ± 0.0005	15.7 ± 0.7
NAL-355*	352.4	*6.18 ± 0.01*	686.75 ± 23.97	0.0288 ± 0.0009	9.77 ± 0.35	109.7 ± 0.8	306.7 ± 2.1	0.1896 ± 0.0021	1.6 ± 0.1
NAL-356*	389.7	23.30 ± 0.39	1054.13 ± 42.24	0.0287 ± 0.0005	9.77 ± 0.30	655.3 ± 4.9	292.7 ± 1.9	0.1867 ± 0.0015	-
NAL-496*	342.8	*1.13 ± 0.01*	*110.45 ± 27.66*	*0.0296 ± 0.0008*	*10.21 ± 0.29*	*13.8 ± 0.5*	*304.0 ± 1.8*	*0.1863 ± 0.0029*	2.9 ± 0.1
NAL-500	360.7	142.84 ± 2.46	3986.09 ± 124.81	0.0289 ± 0.0004	10.09 ± 0.33	1927.1 ± 6.0	295.9 ± 1.6	0.1843 ± 0.0011	53.2 ± 0.9
NAL-537	491.1	337.93 ± 18.73	5213.13 ± 271.15	0.0290 ± 0.0001	9.81 ± 0.04	2150.2 ± 9.4	297.3 ± 0.6	0.1850 ± 0.0004	26.6 ± 1.5
NAL-584	498.1	149.53 ± 5.66	145.09 ± 6.74	0.0287 ± 0.0008	9.72 ± 0.24	101.5 ± 0.5	340.4 ± 1.0	0.1900 ± 0.0008	11.2 ± 0.4
NAL-585	418.2	30.18 ± 0.51	816.54 ± 58.45	0.0289 ± 0.0006	9.99 ± 0.55	138.2 ± 0.6	311.8 ± 1.1	0.1909 ± 0.0016	4.2 ± 0.1
NAL-595	586.3	1384.15 ± 49.26	9410.98 ± 387.89	0.0290 ± 0.0001	9.75 ± 0.04	5595.6 ± 14.2	306.3 ± 0.5	0.1886 ± 0.0006	7.0 ± 0.3
NAL-611	671.5	1486.36 ± 27.40	3642.70 ± 197.91	0.0293 ± 0.0001	9.82 ± 0.05	2370.3 ± 9.1	345.9 ± 0.6	0.1867 ± 0.0004	4.3 ± 0.1
NAL-688*	320.8	87.03 ± 1.46	904.17 ± 48.43	0.0285 ± 0.0007	9.62 ± 0.39	791.2 ± 5.4	313.5 ± 2.1	0.1883 ± 0.0016	1.9 ± 0.1
NAL-828	846.5	485.03 ± 20.48	108.10 ± 5.65	0.0300 ± 0.0008	9.82 ± 0.14	179.9 ± 0.8	591.1 ± 1.1	0.1918 ± 0.0012	5.4 ± 0.2
HSH92-15	483.1	1930.04 ± 69.21	2840.15 ± 134.67	0.0292 ± 0.0001	9.76 ± 0.11	2006.0 ± 8.6	395.9 ± 0.8	0.1863 ± 0.0005	3.8 ± 0.1
ERZ									
A11	749.7	94.19 ± 2.22	5055.22 ± 179.12	0.0290 ± 0.0001	9.80 ± 0.05	2344.9 ± 4.6	295.4 ± 0.6	0.1862 ± 0.0005	-

Table IV.4: Continued

Sample[b]	Amount processed (mg)	[^{4}He] cm^{3}STP/g (× 10^{-9})	[^{20}Ne] cm^{3}STP/g (× 10^{-12})	^{21}Ne/^{22}Ne	^{20}Ne/^{22}Ne	[^{40}Ar] cm^{3}STP/g (× 10^{-9})	^{40}Ar/^{36}Ar	^{38}Ar/^{36}Ar	^{4}He/^{40}Ar*
A13/ICE08R-09	531.8	46.72 ± 1.93	726.64 ± 27.41	0.0285 ± 0.0003	9.58 ± 0.06	368.2 ± 2.5	308.1 ± 0.3	0.1910 ± 0.0005	3.1 ± 0.1
ICE08R-13	497.8	580.59 ± 23.97	3437.15 ± 120.04	0.0288 ± 0.0001	9.75 ± 0.05	1378.3 ± 2.9	349.4 ± 1.2	0.1871 ± 0.0007	2.7 ± 0.1
A19/ICE08R-14	634.5	22.95 ± 0.97	703.91 ± 25.77	0.0284 ± 0.0003	9.40 ± 0.05	132.8 ± 0.7	315.2 ± 0.8	0.1943 ± 0.0010	2.8 ± 0.1
A20/ICE08R15	533.2	613.03 ± 18.34	9519.40 ± 343.82	0.0288 ± 0.0001	9.82 ± 0.05	2894.2 ± 9.3	323.0 ± 0.5	0.1883 ± 0.0004	2.5 ± 0.1
A21/ICE08R-16	768.3	2695.05 ± 42.48	8840.71 ± 267.10	0.0291 ± 0.0001	9.82 ± 0.05	3557.7 ± 19.3	302.6 ± 0.8	0.1876 ± 0.0008	32.1 ± 0.5
A22/ICE08R-17	518.0	2193.71 ± 62.77	290.23 ± 11.56	0.0298 ± 0.0009	9.71 ± 0.16	184.9 ± 0.6	1094.8 ± 3.7	0.1994 ± 0.0014	16.3 ± 0.5
A24	731.1	80.74 ± 2.75	1005.24 ± 41.24	0.0287 ± 0.0001	9.72 ± 0.11	430.8 ± 1.3	306.6 ± 0.6	0.1903 ± 0.0005	5.3 ± 0.2
A27	647.5	188.69 ± 6.12	1301.25 ± 55.46	0.0292 ± 0.0001	9.89 ± 0.07	353.7 ± 1.6	302.5 ± 0.4	0.1889 ± 0.0006	23.1 ± 0.8
A32	340.8	22.83 ± 0.53	13648.03 ± 646.24	0.0291 ± 0.0001	9.88 ± 0.05	*97.6 ± 1.5*	*301.5 ± 0.9*	*0.1936 ± 0.0008*	11.8 ± 0.3
A35	646.3	130.20 ± 3.75	249.55 ± 11.12	0.0279 ± 0.0008	9.86 ± 0.12	*20.2 ± 0.1*	*322.0 ± 1.3*	*0.1945 ± 0.0015*	78.60 ± 2.3
SISZ									
RET-1	605.1	15.33 ± 0.51	3803.82 ± 139.32	0.0289 ± 0.0001	9.81 ± 0.04	5099.4 ± 13.4	294.7 ± 0.4	0.1871 ± 0.0005	-

[a] All errors are reported at the 1 σ level. Results reported in italics represent samples with blank contributions >20%.
[b] Helium data obtained for samples indicated with asterisks were previously reported by Macpherson et al. (2005a).

IV.6 Discussion

Our study of Icelandic geothermal fluids and subglacial basalts provides further evidence that the neon isotope systematics of the Icelandic mantle appear to be decoupled from that of helium. The highest neon (and argon) isotope ratios are observed in glasses along the WRZ and are associated with $^{3}He/^{4}He$ ratios of ~17 R_A. The NRZ is characterized by MORB-like $^{3}He/^{4}He$ ratios yet some glass samples fall close to the air-solar mixing line in three-isotope neon space. Along the ERZ, however, which is the segment of the neovolcanic zones with the highest $^{3}He/^{4}He$ ratios ($\geq 18R_A$), both the neon and argon systematics are dominated by an atmospheric component. Finally, Vestfirðir has the highest $^{3}He/^{4}He$ values observed for Iceland to date yet the geothermal fluids show an excess in nucleogenic ^{21}Ne.

In the following discussion, we assess the likely effects contributing to the decoupling of the He and Ne isotope systematics observed throughout Iceland. We consider both elemental and isotopic heterogeneity of the Icelandic mantle source and the possibility of mixing between primordial mantle and depleted/degassed MORB-like mantle components. In addition, we evaluate the effects of atmospheric contamination and shallow-level degassing – both processes associated with the transfer of mantle-derived volatiles to the surficial environment.

IV.6.1 Isotope variations in neon

The neon isotope composition of basalts collected along the Icelandic neovolcanic zones shows that neon represents a mixture of atmospheric and mantle-derived neon. Thus, variations in neon isotopes observed in these samples, corrected for atmospheric contamination, bear fundamental information on processes occurring within the Icelandic mantle. In contrast, the excess of nucleogenic ^{21}Ne in geothermal fluids from Vestfirðir, without a corresponding enrichment in ^{20}Ne (relative to ^{22}Ne), represents a tracer mainly

produced in the crust and thus is unrelated to processes occurring within Icelandic magmatic systems.

IV.6.1.1 Nucleogenic neon

Vestfirðir is composed of the oldest rocks in Iceland (varying in age from ~15 Myr in the west to about 9 Myr in the southeast; McDougall et al., 1984; Hardarson et al., 1997). Thus, we suggest that the ^{21}Ne enrichment in geothermal fluids from this region are consistent with nucleogenic Ne production in the Icelandic crust and subsequent release to the circulating fluids, as observed previously in other crustal fluids and natural gas samples (e.g., Bottomley et al., 1984; Kennedy et al., 1990; Ballentine and O'Nions, 1992; Hiyagon and Kennedy, 1992; Kennedy, 1992; Ballentine, 1997). The 'nucleogenic' ^{21}Ne isotope is generated by the $^{18}O(\alpha,n)^{21}Ne$ and $^{24}Mg(n, \alpha)^{21}Ne$ reactions (Wetherill, 1954), with the former reaction being the dominant one for Earth's mantle (Yatsevich and Honda, 1997), resulting in an increase of the $^{21}Ne/^{22}Ne$ ratio over time. Since the α-particles are derived from U and Th decay, the production of radiogenic ^{4}He and nucleogenic ^{21}Ne (^{21}Ne*) are directly coupled and, therefore, low $^3He/^4He$ ratios should correlate with high $^{21}Ne/^{22}Ne$ (δ^{21}Ne) ratios. However, geothermal fluids from Vestfirðir show no such relationship (Fig. IV.3b). We suggest that the He-Ne systematics of the fluids may reflect different release mechanisms of ^{4}He and ^{21}Ne* into the circulating groundwaters (due to different production sites in crustal rocks). This would result in differences in $^4He/^{21}Ne^*$ between water and surrounding rock. In this respect, it was suggested that differences in $^3He/^4He$ ratios between circulating fluids and rocks of the Carnmenellis granite reflected dissimilar formation mechanisms and release kinetics of ^{3}He and ^{4}He (Martel et al., 1990).

IV.6.1.2 Correction for atmospheric neon

The neon isotope composition of all samples (basalts and geothermal fluids) can be corrected for atmospheric contamination by assuming that neon represents a binary mixture of atmospheric and mantle-derived neon. Air-corrected $^{21}Ne/^{22}Ne$ ratios ($^{21}Ne/^{22}Ne_{ex}$) are obtained by extrapolating any data point to the primordial $^{20}Ne/^{22}Ne$ ratio along a line that passes through the air value (Moreira et al., 1995; Graham, 2002). The primordial, 'solar' neon component in Earth's mantle is often assumed to be best represented by present-day solar wind (i.e., $^{20}Ne/^{22}Ne = 13.8$; Benkert et al., 1993; Kallenbach et al., 1997). In this respect, the observation of $^{20}Ne/^{22}Ne$ values $\geq 13.0 \pm 0.2$ in plume-related rocks from the Kola Peninsula were interpreted as evidence that neon was incorporated into the deep mantle from unfractionated solar wind (Yokochi and Marty, 2004). Alternatively, it has been suggested that Ne-B, i.e., implanted solar neon sampled in gas-rich meteorites and in lunar soils with a $^{20}Ne/^{22}Ne$ ratio of 12.52 ± 0.18, is the initial 'solar' component within Earth's mantle (Black, 1972; Trieloff et al., 2000; Trieloff et al., 2002; Ballentine et al., 2005). As noted in Section IV.5.2.2, the highest $^{20}Ne/^{22}Ne$ ratio in Icelandic lavas obtained from step-wise crushing is 12.85 (Trieloff et al., 2000; excluding the Dice data from Harrison et al., 1999), comparable within error to the $^{20}Ne/^{22}Ne$ ratio of Ne-B. Thus, we adopt here the isotope composition of Ne-B as the value for 'solar' mantle neon; we note, however, that the general conclusions of this study are virtually independent of this choice.

We calculate air-corrected $^{21}Ne/^{22}Ne$ ratios ($^{21}Ne/^{22}Ne_{ex}$) for 17 subglacial glasses (i.e., 12 samples from the WRZ; 3 from the NRZ; and 2 from the ERZ) and 8 fluid samples (i.e., 2 samples for the WRZ; 4 from the NRZ; 1 from the SNVZ; and 1 from the SISZ) for which the measured neon isotope compositions are distinguishable from air at the 1 σ uncertainty level. As all these samples are located within the neovolcanic zones, we can assume that they do not contain (crustal) nucleogenic ^{21}Ne as in the case of fluids from Vestfirðir which are excluded

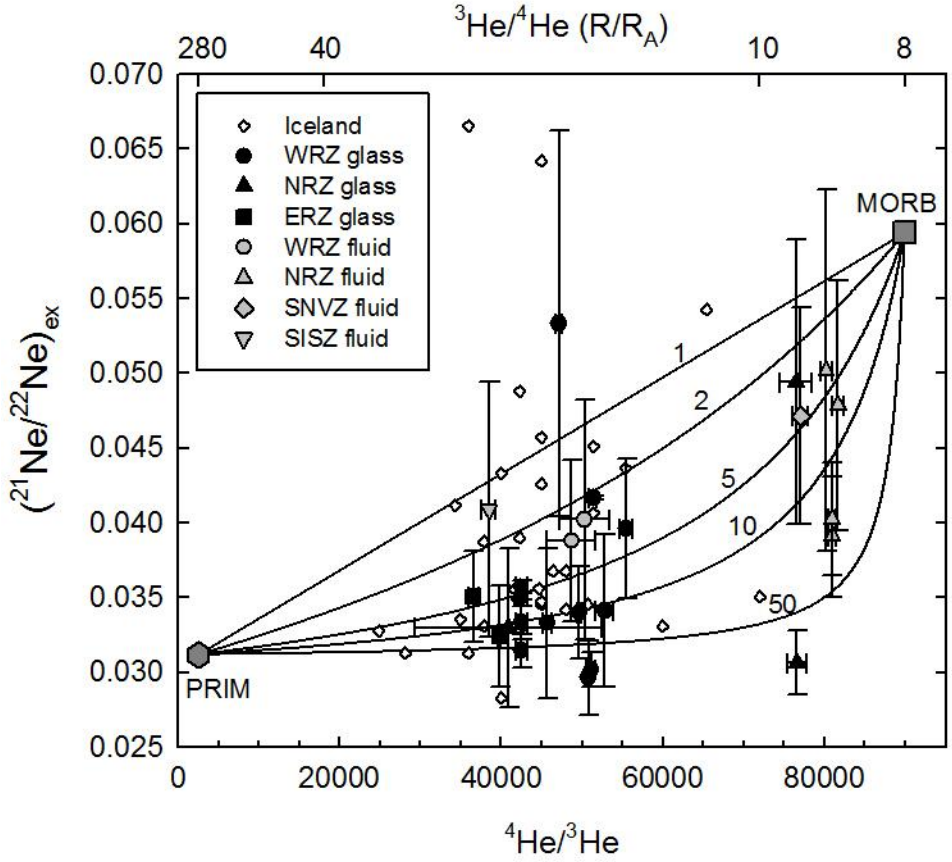

Figure IV.8: $^{21}Ne/^{22}Ne_{ex}$ (i.e., $^{21}Ne/^{22}Ne$ ratios corrected for atmospheric contamination) versus $^4He/^3He$ ratios and binary mixing curves between a primordial mantle endmember and a MORB-like component (see section IV.6.1.3 for details). The curvature of the hyperbolic mixing lines is described by $r = (^3He/^{22}Ne)_{MORB}/(^3He/^{22}Ne)_{PRIM}$. 'Iceland' data from Trieloff et al. (2000), Dixon et al. (2000; 2003), and Moreira et al. (2001). Error bars indicate 1 σ uncertainties.

from this evaluation. The $^{21}Ne/^{22}Ne_{ex}$ ratios from this study are shown as a function of measured $^4He/^3He$ ratios in Figure IV.8 together with data of Icelandic basalts from Trieloff et al. (2000), Dixon et al. (2000; 2003), and Moreira et al. (2001). Our new $^{21}Ne/^{22}Ne_{ex}$ values vary between 0.0296 ± 0.0025 and 0.0533 ± 0.0129 and fall in the range of values observed in previous studies. The lowest $^{21}Ne/^{22}Ne_{ex}$ values are similar to the solar $^{21}Ne/^{22}Ne$ ratio (0.03118; Trieloff and Kunz, 2005), whereas the highest $^{21}Ne/^{22}Ne_{ex}$ values observed in Iceland are close to $^{21}Ne/^{22}Ne_{ex}$ = 0.0594, which is the $^{21}Ne/^{22}Ne$ ratio obtained by

extrapolating the MORB trajectory from Sarda et al. (1988) to the $^{20}Ne/^{22}Ne$ ratio of Ne-B. While individual segments of the axial rift zones in Iceland show a range in $^{21}Ne/^{22}Ne_{ex}$ values, each segment has a distinct *average* $^{21}Ne/^{22}Ne_{ex}$ ratio, i.e., $^{21}Ne/^{22}Ne_{ex} = 0.0337$ along the ERZ (n = 2), 0.0364 along the WRZ (n = 14), and 0.0422 along the NRZ (n = 7), respectively.

One possible explanation for the variable $^{21}Ne/^{22}Ne_{ex}$ values observed in OIB and MORB is that the mantle itself is heterogeneous with respect to the helium to neon elemental ratio (Moreira et al., 2001). In this case, different mantle reservoirs have evolved from the same helium and neon isotope compositions but distinct $^{3}He/^{22}Ne$ ratios, and in-growth of ^{21}Ne (and ^{4}He) from the decay of U and Th over time has generated a range in $^{21}Ne/^{22}Ne_{ex}$ (and $^{3}He/^{4}He$) ratios, according to:

$$(^{21}Ne/^{22}Ne)_{ex} = (^{21}Ne/^{22}Ne)_0 + (^{3}He/^{22}Ne)\,(^{21}Ne^*/^{4}He)\,[(^{4}He/^{3}He)_m - (^{4}He/^{3}He)_0)], \qquad (IV.1)$$

where $^{4}He/^{3}He_m$ is the measured helium isotope ratio, $^{21}Ne^*/^{4}He$ is the mantle production ratio (4.5×10^{-8}; Yatsevich and Honda, 1997), and $(^{21}Ne/^{22}Ne)_0 = 0.03118$ and $(^{4}He/^{3}He)_0 = 2580$ (= 280 R_A) are the primordial ('solar') neon and helium isotope compositions of the mantle from Trieloff and Kunz (2005) and Black (1972), respectively (see section IV.6.1.3 for details on the choice of endmember compositions). Moreira et al. (2001) proposed that the lower $^{21}Ne/^{22}Ne_{ex}$ ratios and higher $^{4}He/^{3}He$ ratios in Icelandic basalts compared to lavas from Loihi Seamount are consistent with a lower $^{3}He/^{22}Ne$ ratio in the Icelandic mantle source. However, we note that $^{21}Ne/^{22}Ne_{ex}$ values of Icelandic lavas and geothermal fluids (this work; Dixon et al., 2003) are highly variable - in Iceland as a whole and within individual rift zone segments (e.g., the WRZ and NRZ). If mantle heterogeneity was the cause of the range in $^{21}Ne/^{22}Ne_{ex}$ observed in Iceland, then the $^{3}He/^{22}Ne$ ratio (derived from Eqn. IV.1) must vary between ~0.1 and 10 in the mantle source. It is hard to envisage a means to preserve distinct domains within the Icelandic mantle source characterized by $^{3}He/^{22}Ne$ ratios that differ by a factor of ~ 100 for the duration of Earth history. Therefore, we propose that the He-Ne characteristics of Icelandic

lavas and geothermal fluids are more satisfactorily explained by binary mixing. In the next section, we explore mixing between a relatively undegassed, primordial mantle endmember and a second endmember characterized by depleted/degassed MORB-mantle.

IV.6.1.3 Binary mixing

The hyperbolic relationship between $^{21}Ne/^{22}Ne_{ex}$ and $^{4}He/^{3}He$ observed in Figure IV.8 can be interpreted as mixing between two endmembers, either two mantle reservoirs or different magmas (Moreira et al., 2001; Graham, 2002). We assume here that one component has a MORB-like He-Ne isotope signature, while the second endmember is characterized by a primordial isotope composition. The curvature of the observed trends is described by $r = (^{3}He/^{22}Ne)_{MORB}/(^{3}He/^{22}Ne)_{PRIM}$, where 'PRIM' refers to the primordial component. As noted in the previous section (IV.6.1.2), we assume here that Ne-B ($^{21}Ne/^{22}Ne = 0.03118$; Trieloff and Kunz, 2005) provides the best estimate for the primordial neon component in Earth's mantle. In the case of helium, the $^{3}He/^{4}He$ ratio of 120 R_A of Jupiter's atmosphere (Mahaffy et al., 1998) is often taken as the primordial value. However, present day solar wind shows a significantly higher $^{3}He/^{4}He$ ratio of ~330 R_A (Benkert et al., 1993), whereas meteorites record a $^{3}He/^{4}He$ ratio between ~280 and 300 R_A for trapped helium (Mazor et al., 1970; Black, 1972). We adopt here the isotope composition associated with the Ne-B component reported by Black (1972) as the value for primordial helium, i.e., $(^{4}He/^{3}He)_{PRIM} = 2580 \pm 200$ (= 280 R_A). The MORB endmember, on the other hand, is described by the ratio $(^{4}He/^{3}He)_{MORB} =$ 90,000 (= 8 R_A).

Figure IV.8 shows that the Iceland data from this study and previously published data (Dixon et al., 2000; Trieloff et al., 2000; Moreira et al., 2001; Dixon, 2003) do not fall onto a single mixing curve, as noted previously by Dixon et al. (2000). Instead, the r-values required to describe the data for Icelandic subglacial basalts range from 1 to ≥ 50 for the majority of the

samples. We note that two data points reported by Dixon (2000; 2003) require lower r-values, close to 0.01. R-values greater than 1 for most samples are consistent with a higher $^{3}He/^{22}Ne$ ratio of the MORB endmember compared to the $^{3}He/^{22}Ne$ ratio of the primordial mantle component. Thus, the data require an enrichment of He relative to Ne in the MORB component or a relative depletion of He in the primordial component, or both, prior to mixing. Furthermore, the wide range in r-values can only be explained by highly variable elemental fractionation in one or both endmembers.

We note that the mixing relationships observed in Figure IV.8 also reveal a systematic variation in the proportion of MORB-like mantle admixed to the primordial mantle component for the different segments of the Icelandic neovolcanic zones. Subglacial glasses and geothermal fluids collected along the NRZ, as well as the single fluid sample from the SNVZ, plot closest to the MORB endmember, indicating that samples from northern Iceland and Snæefellsnes record the largest contribution of MORB-like mantle material. In contrast, the He-Ne systematics of glasses from the ERZ (A27 and A23) require a significantly lower MORB mantle input, i.e., these samples lie closest to the primordial mantle endmember. Thus, the proportion of the primordial mantle component appears to be greatest in melts erupting in southern Iceland.

IV.6.2 Helium to neon elemental ratios - Recent helium depletion

The binary mixing model requires that the helium to neon elemental ratio in one or both mantle endmembers in Iceland (i.e., the primordial and MORB-like mantle components) was fractionated prior to mixing. We can evaluate whether Icelandic basalts show evidence of such elemental fractionation by estimating their air-corrected helium to neon elemental ratios ($^{4}He/^{21}Ne^{*}$ and $^{3}He/^{22}Ne_{s}$). By combining the amount of nucleogenic $^{21}Ne^{*}$ and solar $^{22}Ne_{s}$ with the measured helium abundances, we can determine the relative elemental ratio of ^{4}He to

nucleogenic $^{21}Ne^*$ ($^4He/^{21}Ne^*$) and of ^3He to solar ^{22}Ne ($^3He/^{22}Ne_s$) for Icelandic subglacial basalts.

The amount of mantle-derived (solar) ^{22}Ne for each sample is

$$^{22}Ne_s = [^{22}Ne_m] \times f_{22}, \qquad \text{(IV.2)}$$

where $^{22}Ne_m$ is the measured ^{22}Ne abundance and f_{22} is the proportion of mantle-derived neon, given by

$$f_{22} = (^{20}Ne/^{22}Ne_m - {}^{20}Ne/^{22}Ne_{air}) / (^{20}Ne/^{22}Ne_s - {}^{20}Ne/^{22}Ne_{air}). \qquad \text{(IV.3)}$$

Thus, the ratio of primordial ^3He to solar ^{22}Ne is

$$^3He/^{22}Ne_s = (^3He/^4He_m \times [^4He]_m) / (^{22}Ne_s). \qquad \text{(IV.4)}$$

The amount of nucleogenic $^{21}Ne^*$ is obtained from

$$^{21}Ne^* = {}^{22}Ne_s \times (^{21}Ne/^{22}Ne_{ex} - {}^{21}Ne/^{22}Ne_s). \qquad \text{(IV.5)}$$

We emphasize that we adopt the isotope composition of Ne-B as the value for 'solar' mantle neon to calculate the $^3He/^{22}Ne_s$ and $^4He/^{21}Ne^*$ ratios for all samples shown in Figure IV.9a. Both elemental ratios are slightly higher if 'solar' neon is assumed to be represented by present-day solar wind; the following observations, however, are independent from the choice of the primordial ('solar') neon endmember (see Honda and Patterson, 1999; Graham, 2002 for comparison).

The $^3He/^{22}Ne_s$ ratio of our samples is compared to the $^4He/^{21}Ne^*$ ratio in Figure IV.9a. Data for MORB glasses from the Mid-Atlantic Ridge (MAR) (Moreira and Allègre, 2002), Kolbeinsey Ridge (Macpherson et al., 2005b), and Reykjanes Ridge (de Leeuw, 2007), as well as other OIB samples are shown for comparison. The helium to neon elemental ratios of the MORB popping rock 2ΠD43 (Sarda et al., 1988; Moreira et al., 1998) plot close to the point defined by the theoretical production ratio of radiogenic ^4He to nucleogenic $^{21}Ne^*$ (2.2×10^7; Yatsevich and Honda, 1997) and the estimated primordial $^3He/^{22}Ne$ ratio of Earth's mantle

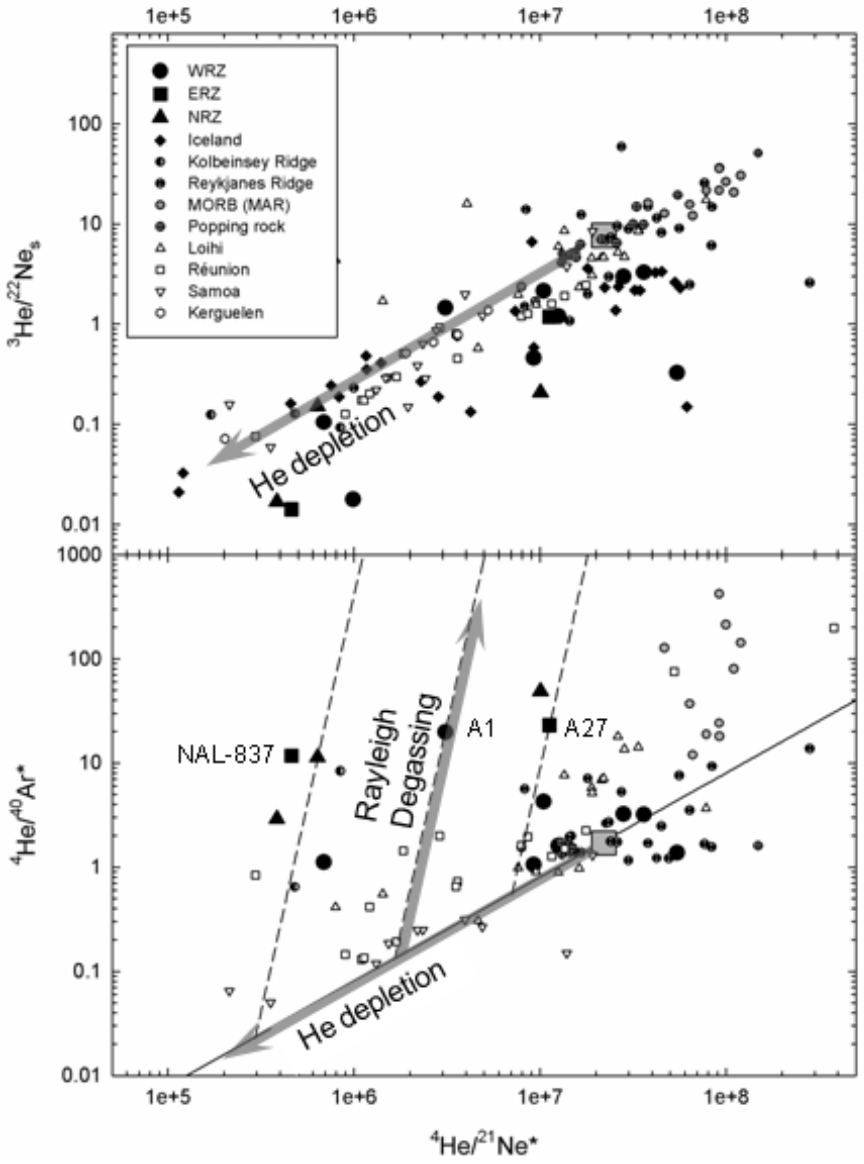

Figure IV.9: a) $^3He/^{22}Ne_s$ and b) $^4He/^{40}Ar^*$ versus $^4He/^{21}Ne^*$ for Icelandic subglacial basalts, as well as MORB samples from the MAR (Sarda et al., 1988; Moreira and Allègre, 2002), Kolbeinsey Ridge (Macpherson et al., 2005a), and Reykjanes Ridge (de Leeuw, 2007), and OIB samples from Loihi (Honda et al., 1993; Valbracht et al., 1997; Trieloff et al., 2000), Réunion (Hanyu et al., 2001; Trieloff et al., 2002), Kerguelen (Valbracht et al., 1996), and Samoa (Poreda and Farley, 1992). The grey square shows theoretical values for Earth's mantle, i.e., $^4He/^{21}Ne^* = 2.2 \times 10^7$ (Yatsevich and Honda, 1997), $^3He/^{22}Ne = 7.7$ (Honda and McDougall, 1998), and $^4He/^{40}Ar^* = 2.9$ (Jochum et al., 1983; Graham, 2002). All $^3He/^{22}Ne_s$ and $^4He/^{21}Ne^*$ ratios are calculated under the assumption that Ne-B represents the primordial, 'solar' neon component. Three degassing trajectories for open-system Rayleigh degassing are illustrated in the lower panel (see section IV.6.3.2 for details).

(7.7; Honda and Mcdougall, 1998), indicating that helium and neon are relatively unfractionated in that sample. However, most other MORB glasses from the MAR and Reykjanes Ridge are enriched in He relative to Ne, whereas OIB samples and submarine glasses from the Kolbeinsey Ridge have He/Ne elemental ratios that are less than the $^{4}He/^{21}Ne^{*}$ production and the primordial $^{3}He/^{22}Ne_{s}$ ratios.

Our data from the Icelandic neovolcanic zones agree with the general trend for OIB; He/Ne elemental ratios of the majority of Icelandic subglacial glasses are lower than the theoretical values for the mantle, suggesting that Icelandic basalts are depleted in He relative to Ne. Only samples MID-1 (this work), Dice (Harrison et al., 1999; Trieloff et al., 2000) and ice-9g (Dixon et al., 2000) from Miðfell (Dagmálafell), which is the location with the highest $^{20}Ne/^{22}Ne$ ratios observed in Iceland, plot close to the theoretical values for Earth's mantle. We note that glasses from individual segments of the Icelandic rift zones record a wide range – over two orders of magnitude – in the degree of He depletion with respect to Ne, consistent with elemental fractionation which is highly variable. Since Icelandic glasses follow the linear correlation with an observed slope of ~1, defined by MORB and OIB samples, the fractionation of the He/Ne ratio must be a relatively recent event otherwise the $^{4}He/^{21}Ne^{*}$ ratios would approach the production ratio due to ingrowth of radiogenic ^{4}He and nucleogenic $^{21}Ne^{*}$. Thus, low He/Ne elemental ratios observed in Icelandic basalts are probably not due to helium depletion in the mantle source itself. Instead, Icelandic parental melts may be depleted in helium with respect to the heavier noble gases due to more compatible behavior of helium during low-degree partial melting or, alternatively, extensive diffusive helium loss during ascent of primordial mantle material. These scenarios, discussed in more detail in section IV.6.5, are expected to result in a concomitant fractionation of the helium to argon elemental ratio ($^{4}He/^{40}Ar^{*}$).

IV.6.3 Helium to argon elemental ratios – Degassing

The ^{40}Ar content measured for each glass sample is corrected for the presence of atmospheric argon assuming that all the ^{36}Ar is atmosphere-derived:

$$^{40}Ar^{*} = [^{36}Ar_{m}] \times [(^{40}Ar/^{36}Ar)_{m} - (^{40}Ar/^{36}Ar)_{air}], \qquad \text{(IV.6)}$$

where $^{36}Ar_{m}$ and $(^{40}Ar/^{36}Ar)_{m}$ are the measured ^{36}Ar abundance and argon isotope ratio, respectively, and $(^{40}Ar/^{36}Ar)_{air}$ is the air ratio (= 295.5). The $^{4}He/^{40}Ar^{*}$ ratios, calculated from the measured He content and $^{40}Ar^{*}$ derived from Eqn. (IV.6), are given in Table IV.4 and shown as a function of ^{40}Ar abundances in Figure IV.7b. Air-like $^{40}Ar/^{36}Ar$ ratios (i.e., no evidence of radiogenic Ar) preclude calculation of $^{4}He/^{40}Ar^{*}$ in 5 samples. The $^{4}He/^{40}Ar^{*}$ ratios range from 0.8 to 78; however, the majority of the glasses from the three segments of the Icelandic neovolcanic zones plot near values observed in popping rocks (1.5 ± 0.5; Moreira et al., 1998) and the theoretical mantle production ratio of ~2.9 (1.6 to 4.2) calculated on the basis of U, Th and K concentrations (Jochum et al., 1983; Graham, 2002).

Low $^{4}He/^{40}Ar^{*}$ values between ~1 and 4.2 may indicate that the majority of Icelandic basalts have not experienced significant gas loss, since equilibrium degassing leads to increased $^{4}He/^{40}Ar^{*}$ ratios in the residual magma due to the solubility contrast between He and Ar in basaltic melts (Jambon et al., 1986). However, low $^{4}He/^{40}Ar^{*}$ ratios, i.e., equal to or lower than the mantle production ratio, can also be explained by both extensive non-equilibrium degassing (Gonnermann and Mukhopadhyay, 2007) and equilibrium degassing of a melt that has been previously depleted in helium relative to neon and argon (Valbracht et al., 1996; Graham, 2002; Hopp and Trieloff, 2008). These two scenarios are illustrated in figures IV.10 and IV.9b, respectively, where we compared the $^{4}He/^{40}Ar^{*}$ values to the $^{4}He/^{21}Ne^{*}$ ratios for MORB, OIB and Icelandic subglacial glasses. Most Icelandic basalts – with the exception of sample MID-1 – plot above the linear array with an observed slope of ~1 defined by other OIB samples that includes the point defined by the theoretical $^{4}He/^{40}Ar^{*}$ and

$^{4}He/^{21}Ne^{*}$ production ratios. In other words, Icelandic glasses show higher $^{4}He/^{40}Ar^{*}$ ratios for a given $^{4}He/^{21}Ne^{*}$ value compared to the majority of other OIB samples. Next, we explore if the He-Ne-Ar relationships are consistent with either non-equilibrium degassing (Gonnermann and Mukhopadhyay, 2007) or, alternatively, open-system equilibrium degassing of a melt that has previously been depleted in helium relative to neon and argon.

IV.6.3.1 Non-equilibrium degassing

Gonnermann and Mukhopadhyay (2007) recently proposed that the distinct He-Ne-Ar characteristics of submarine MORB and OIB glasses can be explained by non-equilibrium open-system degassing. According to their model, noble gases are kinetically fractionated during degassing depending on their relative diffusivities (where $D_{Ar} \approx D_{Ne} \approx 0.001\ D_{He}$; Lux, 1987). If the time available for degassing is short compared to the characteristic diffusion time of argon, degassing is in disequilibrium, and helium will be lost preferentially to neon and argon from the ascending melt. Thus, non-equilibrium degassing may result in He/Ne and He/Ar ratios in MORB and OIB lavas that are lower than the initial elemental ratios of the parental melt, contrary to the effects of equilibrium degassing which results in higher residual He/Ne and He/Ar ratios compared to the initial values (section IV.6.3.2). However, the solubility of noble gases also depends on the CO_2 and H_2O content of the magma (e.g., Nuccio and Paonita, 2000), so that more helium is lost from a parental melt which has a higher initial CO_2 content. Consequently, Gonnermann and Mukhopadhyay (2007) suggested that the lower helium concentrations of some OIB glasses compared to MORB samples can be explained by non-equilibrium open-system degassing of OIB parental melts with high initial CO_2 concentrations.

In order to model non-equilibrium degassing of Icelandic melts, we adopt $^{3}He/^{22}Ne$, $^{4}He/^{21}Ne$, and $^{4}He/^{40}Ar$ ratios of 7.7 (Honda and Mcdougall, 1998), 2.2×10^{7} (Yatsevich and

Honda, 1997), and 2.9 (Graham, 2002), respectively, for the mantle source. Furthermore, we assume a helium isotope composition of 26 R_A (i.e., the highest $^3He/^4He$ ratio observed in our study for subglacial glasses from the neovolcanic zones) and a ^3He concentration of 10^{-8} cm^3STP/g from Gonnermann and Mukhopadhyay (2007) for the OIB parental melt. Since noble gas solubilities and, hence, magma degassing depend on the pressure (depth) of eruption, we assume a maximum eruption pressure of ~170 bar, i.e., the hydrostatic pressure generated by the overlying Quaternary Icelandic ice sheet with a maximum thickness of ~2000 m (Hubbard et al., 2006) and a typical density of glacial ice of 0.85 g/cm^3 (Paterson, 1994). The time available for degassing, t_{degas}, is expressed as the characteristic diffusion time of argon in basalt melt, i.e., $\tau_{Ar} = a^2/D_{Ar}$, where D_{Ar} is the diffusivity for argon and a is the characteristic half-thickness of melt separating individual bubbles (see Gonnermann and Mukhopadhyay, 2007, for details). If the time available for degassing is similar to τ_{Ar}, degassing is close to equilibrium. However, if $t_{degas} \ll \tau_{Ar}$, there is insufficient time for diffusion of all noble gases to the bubble-melt interface and degassing is in disequilibrium.

Figure IV.10a shows the solution grid for non-equilibrium degassing of an Icelandic OIB parental melt erupting under 2000 m of glacial ice (at ~170 bar). Any point that falls within the solution field represents the derived He-Ne-Ar content of the degassed melt for a specific initial CO_2 abundance and degassing time at a pressure of 170 bar. Initial CO_2 concentrations vary between ~0.07 and 0.65 wt.% (i.e., the range of CO_2 concentrations estimated for parental OIB magmas from Gonnermann and Mukhopadhyay, 2007) and characteristic degassing times, t_{degas}, range from $10^{-2}\tau_{Ar}$ to $10^{-0.25}\tau_{Ar}$. Figure IV.10a confirms that at low values of t_{degas}, degassing may result in He/Ne and He/Ar ratios in the melt that are lower than the initial elemental ratios of the parental melt. For example, the isopleth for an initial CO_2 content of 0.65 wt.% illustrates that both the $^4He/^{21}Ne^*$ and the $^4He/^{40}Ar^*$ ratio in the melt will be lower than the initial ratios for short degassing times, i.e., for values of

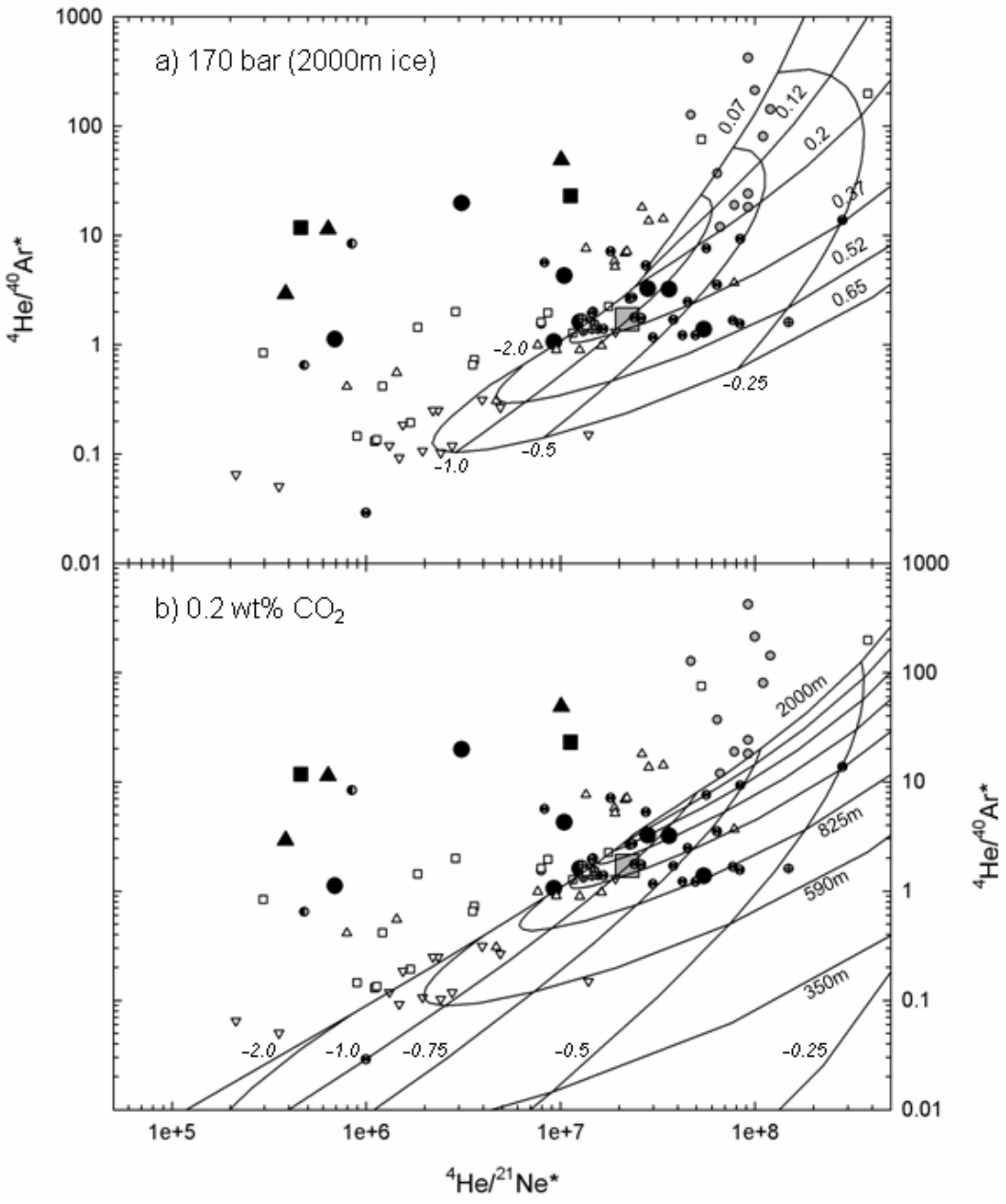

Figure IV.10: $^{4}He/^{40}Ar^{*}$ versus $^{4}He/^{21}Ne^{*}$ for Icelandic subglacial basalts as well as other MORB and OIB samples, and model results for non-equilibrium degassing of a parental melt with an initial ^{3}He abundance of 10^{-8} $cm^{3}STP/g$ and initial $^{3}He/^{4}He = 26\ R_A$, $^{4}He/^{21}Ne^{*} = 2.2 \times 10^{7}$, and $^{4}He/^{40}Ar^{*} = 2.9$. a) Solution grid for degassing at 170 bar (i.e., ~2000 m of overlying glacial ice), initial CO_2 concentrations between ~0.07 and 0.65 wt.%, and characteristic degassing times between $10^{-2}\tau_{Ar}$ and $10^{-0.5}\tau_{Ar}$. b) Solution grid for degassing of a melt with an initial CO_2 content of 0.2 wt.% erupting under 350 to 2000 m of overlying ice. Characteristic degassing times (italic numbers) are shown as values of $\log_{10}(t_{degas}/\tau_{Ar})$ Symbols and data sources as in Figure IV. 9.

$\log_{10}(t_{degas}/\tau_{Ar}) < -0.65$. With increasing values of t_{degas},, degassing will tend towards equilibrium, at which point elemental fractionation will be controlled solely by the relative solubilities of the noble gases (see section IV.6.3.2); therefore, under these circumstances, the He/Ne and He/Ar ratios will start to progressively increase.

Figure IV.10a reveals that the solution field for 2000 m of overlying glacial ice does not encompass the Icelandic data – either as a whole or within individual rift zone segments. This observation indicates that non-equilibrium degassing at 170 bar cannot account for our Icelandic He-Ne-Ar data. However, our choice of 2000 m for the thickness of the glacial ice sheet may not be valid: indeed, it has been shown recently that some table mountains in Iceland experienced their final eruptive phase during the last deglaciation when substantial ice sheet thinning had already started (Licciardi et al., 2007). Therefore, in Figure IV.10b, we model disequilibrium degassing at lower pressures, illustrated for a parental melt with an initial CO_2 content of 0.2 wt.%. We note that the range of solutions for a thinner overlying ice sheet during eruption also fails to capture the entire Icelandic data array. Therefore, we conclude that the noble gas systematics of Icelandic lavas cannot be explained satisfactorily by non-equilibrium degassing.

IV.6.3.2 Equilibrium degassing

Moreira and Sarda (2000) suggested that the He-Ne-Ar systematics of OIB samples can be explained by open-system equilibrium degassing (Rayleigh distillation), where exsolved gas bubbles are continuously lost from the ascending magma. In this scenario, the concentration of dissolved volatiles is in equilibrium with the coexisting gaseous bubbles. Consequently, the elemental fractionation is controlled solely by the relative solubilities of the noble gases, and the He/Ne and He/Ar ratios will progressively increase during open-system degassing, described by:

$$R = R_i \times f^{(1 - \alpha)}, \qquad (V.7)$$

where R is the He/Ne or He/Ar ratio in the residual melt phase, R_i is the ratio between the two volatiles initially present in the melt, *f* is the fraction of He remaining, and α is the ratio of the solubility constants of the considered volatiles, i.e., $\alpha = S_{He}/S_{Ne} = 1.8$ or $S_{He}/S_{Ar} = 7.4$ (Lux, 1987). We suggest that as a result of a primary fractionation event in the mantle, Icelandic parental melts are depleted in He relative to Ne and Ar (see section IV.6.5.), and that subsequent open-system equilibrium degassing leads to highly increased $^4He/^{40}Ar^*$ ratios in the residual melt phase. As shown in Figure IV.9b, Icelandic basalts appear to be significantly more degassed than both the majority of OIB xenoliths that are thought to trap volatiles at depth in the mantle and basalts from Loihi Seamount which were emplaced at ≥ 1200 m water depth. Low hydrostatic pressures during the subglacial eruption of Icelandic lavas likely promote such extensive degassing. However, we note that subglacial glasses from Miðfell plot close to the point defined by the theoretical mantle production ratios for $^4He/^{21}Ne^*$ and $^4He/^{40}Ar^*$. This observation suggests that these melts are not significantly degassed, which, in turn, implies that their composition most closely represents the noble gas isotope signature of the Icelandic mantle source.

IV.6.4 Elemental ratios and helium abundance

In order to test if this 2-step model (He depletion followed by open-system degassing) is appropriate for Icelandic basalts, we compare the $^4He/^{21}Ne^*$ and $^4He/^{40}Ar^*$ ratios with measured helium abundances in Figure IV.11. In general, the $^4He/^{21}Ne^*$ and $^4He/^{40}Ar^*$ values of MORB and OIB samples are positively correlated with He concentrations, as noted previously by Matsuda and Marty (1995) and Honda and Patterson (1999). This trend appears

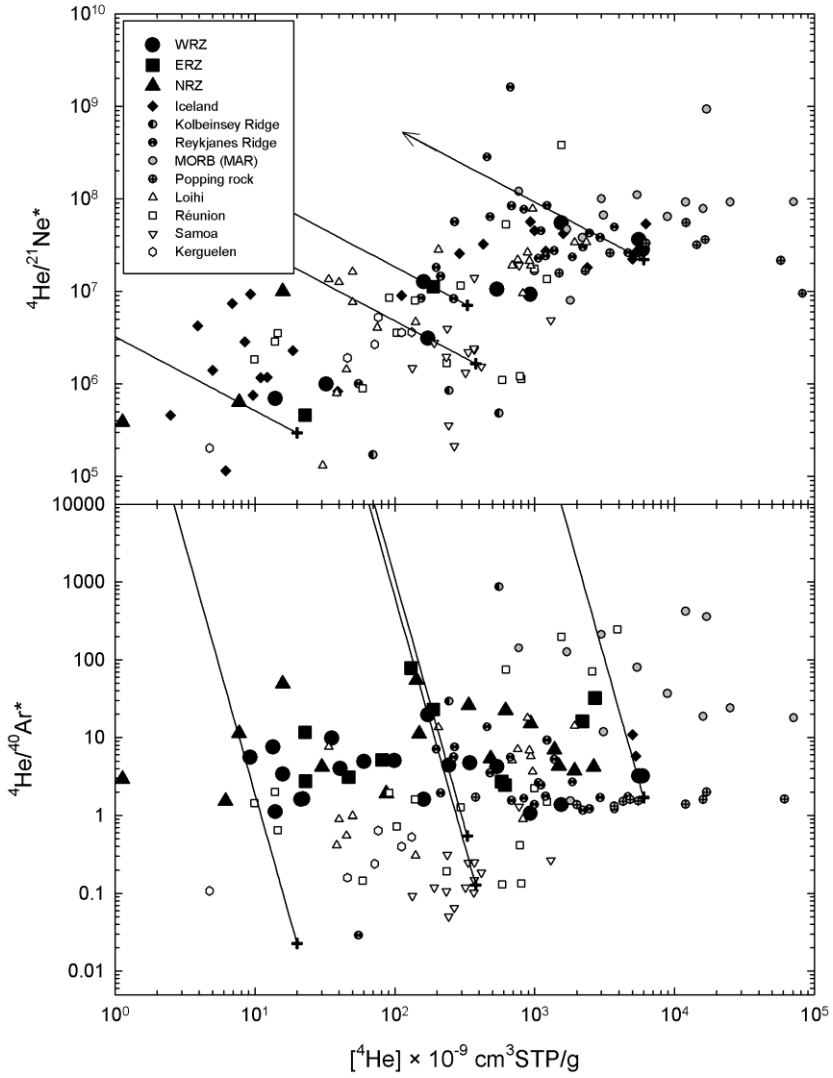

Figure IV.11: a) $^4He/^{21}Ne^*$ and b) $^4He/^{40}Ar^*$ versus helium concentrations. Rayleigh distillation trajectories are shown for samples MID-1, A1, NAL-837, and A27. Data sources as in Figure IV.9.

consistent with depletion of He relative Ne and Ar in OIB parental melts, inducing lower He/Ne and He/Ar ratios, as well as lower He concentrations in OIB compared to MORB samples. However, Icelandic basalts show greater $^4He/^{40}Ar^*$ values at low He concentrations compared to other OIB localities as a result of extensive Rayleigh degassing, possibly due to lower confining pressures during eruption.

The four trajectories for open-system equilibrium degassing shown in Figure IV.11 (for samples MID-1, A1, NAL-837, and A27) illustrate that Rayleigh degassing leads to significantly higher $^4He/^{40}Ar^*$ values of the residual melt, while the $^4He/^{21}Ne^*$ ratios are only slightly increased with decreasing He abundances due to the lower He to Ne solubility ratio (i.e., $S_{He}/S_{Ne} < S_{He}/S_{Ar}$). We note that the degassing trajectories in Figure IV.11 are based on estimates for the initial He/Ne and He/Ar ratios of the melt and the degree of degassing, *f*, obtained from Eqn. IV.7 for each sample. For example, Figure IV.9b shows that the He-Ne-Ar characteristics of sample A1 can be explained by a melt with $^4He/^{21}Ne^*_i \approx 1.65 \times 10^6$ and $^4He/^{40}Ar^*_i \approx 0.13$ that has lost ~55% of its initial He content due to Rayleigh degassing. Thus, since the melt retained ~173×10^{-9} cm^3STP/g helium, the initial ^4He concentration was ~380×10^{-9} cm^3STP/g. In contrast, the initial ^4He abundance of the melt that generated sample MID-1 was an order of magnitude higher, i.e., approximately 6000×10^{-9} cm^3STP/g. These estimated helium concentrations for Icelandic parental melts are significantly lower than the ^4He concentration estimates of ~3×10^{-4} cm^3STP/g and 9×10^{-5} cm^3STP/g for OIB and MORB parental melts, respectively, from Gonnermann and Mukhopadhyay (2007). This observation appears consistent with a primary fractionation event in the mantle that has depleted Icelandic parental melts in helium.

IV.6.5 Helium depletion in Icelandic parental melts

Our study of Icelandic subglacial basalts, together with previous studies of basaltic glasses, phenocrysts and xenoliths from Loihi Seamount (Honda et al., 1993; Valbracht et al., 1997; Trieloff et al., 2000), Réunion (Hanyu et al., 2001; Trieloff et al., 2002), Kerguelen (Valbracht et al., 1996), and Samoa (Poreda and Farley, 1992), suggest that the He/Ne and He/Ar elemental ratios in parental OIB melts are consistently lower than in MORB melts and lower than the theoretical values for Earth's mantle. This requires a mechanism that can

deplete He relative to Ne and Ar, while the latter two volatiles remain essentially unfractionated relative to each other.

Hopp and Trieloff (2007) recently proposed that the substantially lower He concentrations observed in OIB samples compared to MORB samples result from fractionation of noble gases during partial melting of the primitive mantle source. Due to more compatible behavior of He compared to Ne and Ar, low-degree partial melting of primitive, high-$^{3}He/^{4}He$ ratio mantle material generates a melt that is depleted in He relative to Ne and Ar. As the melt ascends into the shallower asthenospheric region, it mixes with higher-degree, MORB-type melts that show no fractionation-induced He deficit. A corollary of this model is that the He content of the high-$^{3}He/^{4}He$ ratio source may be very similar to the concentration in the MORB source. An issue with this model, as noted by Hopp and Trieloff (2007), is that crystal-melt partition coefficients for noble gases are not well known at present, and argon may in fact behave compatibly during mantle melting (Watson et al., 2007). Better knowledge of noble gas partition coefficients is required to assess if this model is valid.

Alternatively, Morgan and Morgan (2007; 2008) suggested that ^{3}He is concentrated in primordial 'plums' within a plum-pudding mantle. During ascent of primordial mantle material, helium - but not the heavier noble gases - diffuses from the high-$^{3}He/^{4}He$ ratio plums into neighbouring low-$^{3}He/^{4}He$ ratio, He-poor components. Subsequent partial melting of the easier-to-melt plums within the rising mantle material generates OIB melts that are depleted in He relative to Ne and Ar. More extensive (second-stage) melting of the refractory material, into which He has diffused, produces He-rich MORB melts at shallower depths beneath mid-ocean ridges.

In either scenario, high-$^{3}He/^{4}He$ ratio mantle material, likely residing deep in the mantle (e.g., Hahm et al., 2009), is depleted in helium relative to neon and argon by a primary fractionation event. Subsequent variable binary mixing between the low-$^{3}He/^{22}Ne$ ratio

primordial mantle component and the high-$^{3}He/^{22}Ne$ ratio MORB endmember at shallower depths accounts for the hyperbolic relationship observed in He-Ne isotope space for Icelandic subglacial basalts (Fig. IV.8).

IV.7 Summary and conclusions

Our new combined He-Ne(-Ar) study of Icelandic geothermal fluids and subglacial basalts confirms that the different segments of the neovolcanic zones in Iceland are characterized by distinct noble gas signatures. While the neon (and argon) isotope data are mostly masked by addition of an atmospheric component, it is still possible to discern the mantle and crustal processes controlling the He-Ne relationships. The ^{21}Ne excess in geothermal samples from Vestfirðir is consistent with nucleogenic Ne production in the Icelandic crust and subsequent release to the circulating fluids. Subglacial glasses, on the other hand, show that neon in Icelandic basalts is derived from both depleted MORB-like mantle and a relatively undegassed, 'solar' mantle source.

The He-Ne systematics of subglacial basalts from the Icelandic neovolcanic zones are consistent with binary mixing between two endmembers, one with a MORB-like isotope signature and the other with a more primordial isotope composition. The binary mixing model requires a relative depletion of He relative to neon in the primordial component and/or a He enrichment in the MORB endmember. The helium to neon elemental ratios ($^{4}He/^{21}Ne^{*}$ and $^{3}He/^{22}Ne_{s}$) of the majority of Icelandic subglacial basalts are indeed lower than in MORB samples and lower than the theoretical values for the mantle, confirming that recent elemental fractionation of mantle helium with respect to mantle neon and argon has occurred. Helium may be depleted in Icelandic parental melts due to either more compatible behavior during low-degree partial melting or more extensive diffusive loss relative to the heavier noble gases.

However, extensive open-system equilibrium degassing, likely due to low hydrostatic pressures during the subglacial eruption of Icelandic lavas, leads to higher $^{4}He/^{40}Ar^{*}$ values of Icelandic basalts compared to other OIB samples. Since most melts from the Icelandic neovolcanic zones have lost much of their magmatic gas prior to or during eruption, they are highly susceptible to contamination with atmospheric gases, either before or after emplacement below the glacial ice. Thus, the neon and argon systematics of most Icelandic glasses are dominated by the air-derived component. Only basalts collected at Miðfell (Dagmálafell) within the WRZ consistently plot near the theoretical values for Earth's mantle, suggesting that melts erupted at this particular location were the least affected by primary He depletion and subsequent degassing. Thus, the melts are less susceptible to air contamination and preserve the highest $^{20}Ne/^{22}Ne$ and $^{40}Ar/^{36}Ar$ ratios observed in Iceland to date.

Overall, we conclude that the He-Ne-Ar systematics of Icelandic subglacial glasses are imprinted with the overlapping effects of He depletion relative to Ne and Ar in the parental melt, binary mixing between a primordial and a MORB-like mantle component, followed by equilibrium degassing, and atmospheric contamination.

IV.8 Acknowledgements

We thank Kareen Prade and Ólafur Patrick Ólafsson for assistance in sample collection, and we acknowledge Björn Oddsson for collecting the geothermal samples from Kverkfjöll. We are grateful to Björn S. Harðarson for suggestions of sampling locations of phyric lavas from Vestfirðir. This work was supported by NSF Grant EAR-0439122. Additional support for sample collection came from EAR-0537340, EAR-0537618 and the Nordic Volcanological Center, Iceland.

Chapter IV has been submitted, in full, for publication in *Geochimica et Cosmochimica Acta* as Füri, E., D.R. Hilton, S.A. Halldórsson, P.H. Barry, D. Hahm, T.P. Fischer, and K. Grönvold, Decoupling of the He and Ne isotope systematics of the Icelandic mantle; the role of He depletion, magma mixing, and degassing fractionation. The dissertation author was the primary investigator and lead author of this paper and conducted all the analyses presented herein.

Chapter V Helium isotope variations in submarine basalts from the Central Indian Ridge, 17º-21ºS: New evidence for ridge-hotspot interaction

V.1 Abstract

We report new helium abundance and isotope results for basaltic glasses from the Central Indian Ridge (CIR) axis between the Marie Celeste and the Egeria fracture zones (i.e., between 16.7° and 20.6°S), and the adjacent Gasitao, Three Magi, and Rodrigues ridges, as well as for olivine separates from the Mascarene Islands (Réunion, Mauritius, and Rodrigues). Helium isotope ratios measured in the glasses range from 7.1 to 12.2 R_A (where R_A = air $^3He/^4He$), and lie between the values expected for depleted MORB mantle (8 ± 1 R_A) and the $^3He/^4He$ ratio of lavas sampled on Réunion Island (11.5-14.1 R_A). The highest $^3He/^4He$ values (up to 12.2 R_A) are found in glasses recovered off-axis, from the Three Magi and the Gasitao ridges. Along the CIR axis, MORB-like $^3He/^4He$ ratios are found in the vicinity of the Egeria Fracture Zone in the south, and there is a marked increase to values up to ~11 R_A between ~19° and 20°S. The lowest $^3He/^4He$ values (< 8 R_A) are found immediately south of the Marie Celeste Fracture Zone, where incompatible trace element ratios (e.g., La/Sm) are the highest. We propose that the low $^3He/^4He$ ratios in the north can be explained by closed-system radiogenic ^4He in-growth in either 1) an "ancient" Réunion hotspot mantle component, embedded into the sub-ridge mantle when the migrating CIR passed over the hotspot at ~34 Ma, or, alternatively, 2) trace element enriched MORB mantle. In contrast, we conclude that the high $^3He/^4He$ ratios on the CIR axis adjacent to the Gasitao Ridge, as well as along the off-axis volcanic ridges, are consistent with lateral flow of hotspot mantle material from Réunion (~ 1100 km to the west) into the sub-ridge mantle of the CIR.

V.2 Introduction

Geophysical and geochemical observations have revealed that a significant portion of the global mid-ocean ridge system is influenced by hotspots located up to 1400 km away (Schilling, 1991). In locations where a hotspot is close to a spreading ridge (e.g., Iceland, Amsterdam-St. Paul, Azores, Easter, Galápagos, and Réunion), lateral flow of upwelling hotspot mantle along the base of the lithosphere towards and along the mid-ocean ridge results in increased melt production and crustal thickness, as well as elevated topography and negative gravity anomalies at the ridge axis (Ito and Lin, 1995a; Ito and Lin, 1995b). Furthermore, mixing of hotspot mantle with the sub-ridge mantle generates enriched trace element signatures (e.g., high La/Sm ratios) as well as variations in Sr, Nd, and Pb isotope ratios of basalts erupted at the ridge (Hart et al, 1973; Schilling, 1973; Schilling et al., 1982; Schilling et al., 1985; Hanan et al., 1986; Ito et al., 2003).

Mid-ocean ridge basalts (MORB) sampled away from hotspots display $^{3}He/^{4}He$ ratios of 8 ± 1 R_A (where $R_A = {}^{3}He/^{4}He$ of air), whereas ocean islands basalts (OIB) from Iceland, Hawaii, Galápagos, Samoa and Réunion show higher $^{3}He/^{4}He$ ratios (Graham et al., 2002). Nearly all of Earth's ^{3}He is primordial (i.e., it was trapped during Earth formation), whereas ^{4}He is continuously produced by the radioactive decay of U and Th. Thus, the distinct helium signatures of MORB and OIB suggest that the MORB source has evolved with a higher time-integrated $(U+Th)/^{3}He$ ratio than the source of hotspots. Consequently, helium isotopes are a powerful tool for studying ridge-hotspot interaction; introduction of high-$^{3}He/^{4}He$ mantle material from a nearby hotspot to the sub-ridge mantle will generate MORB lavas with high helium isotope ratios. Within the Indian Ocean Basin, for example, marked increases in $^{3}He/^{4}He$ ratios up to 14.1 R_A and 16.4 R_A have been observed on the Southwest Indian Ridge near the Bouvet hotspot (Kurz et al., 1998) and on the Southeast Indian Ridge near the

Amsterdam-St. Paul hotspot (Graham et al., 1999; Burnard et al., 2002; Nicolaysen et al., 2007), respectively.

In this contribution, we study the interaction between the Central Indian Ridge (CIR) and the off-axis Réunion hotspot. We performed an extensive helium isotope survey of the CIR axis between 16.7ºS and 20.6ºS, and the adjacent Gasitao Ridge, Three Magi Ridges, and Rodrigues Ridge (Fig. V.1). In addition, we determined the helium characteristics of olivine separates from the Mascarene Islands (Réunion, Mauritius, and Rodrigues). Our new data show that basalts from the CIR and off-axis volcanic ridges record a Réunion-like helium isotope signature. We discuss the dynamics of mixing between different mantle components in this region of the Indian Ocean Basin, and we also evaluate the effects of shallow-level magmatic processes (i.e., post-eruptive radiogenic ^{4}He in-growth, degassing and fractional crystallization) that play an important role in the helium inventory of any oceanic basalt.

V.3 Geologic setting and background

The CIR, which separates the African and Indo-Australian plates, extends southward from the Carlsberg Ridge near the equator towards the Rodrigues Triple Junction (20.5ºS, 70ºE), where it branches into the Southeast and the Southwest Indian ridges. In this study, we target the CIR segment bounded by the Marie Celeste FZ (Fracture Zone) to the north and the Egeria FZ to the south (Fig. V.1). The ridge axis is shallower along this segment, and left-stepping offsets shift it westward towards the island of Réunion (Parson et al., 1993).

At ~34 Ma, the north-eastward migrating CIR passed over the Réunion hotspot (Duncan et al., 1990), which is presently located ~1100 km to the west of the ridge axis. The Réunion hotspot formed the Deccan Trap flood basalts, the Chagos-Maldive-Laccadive Ridge, the Mascarene Plateau, as well as the Mascarene Islands, comprised of the islands of Réunion,

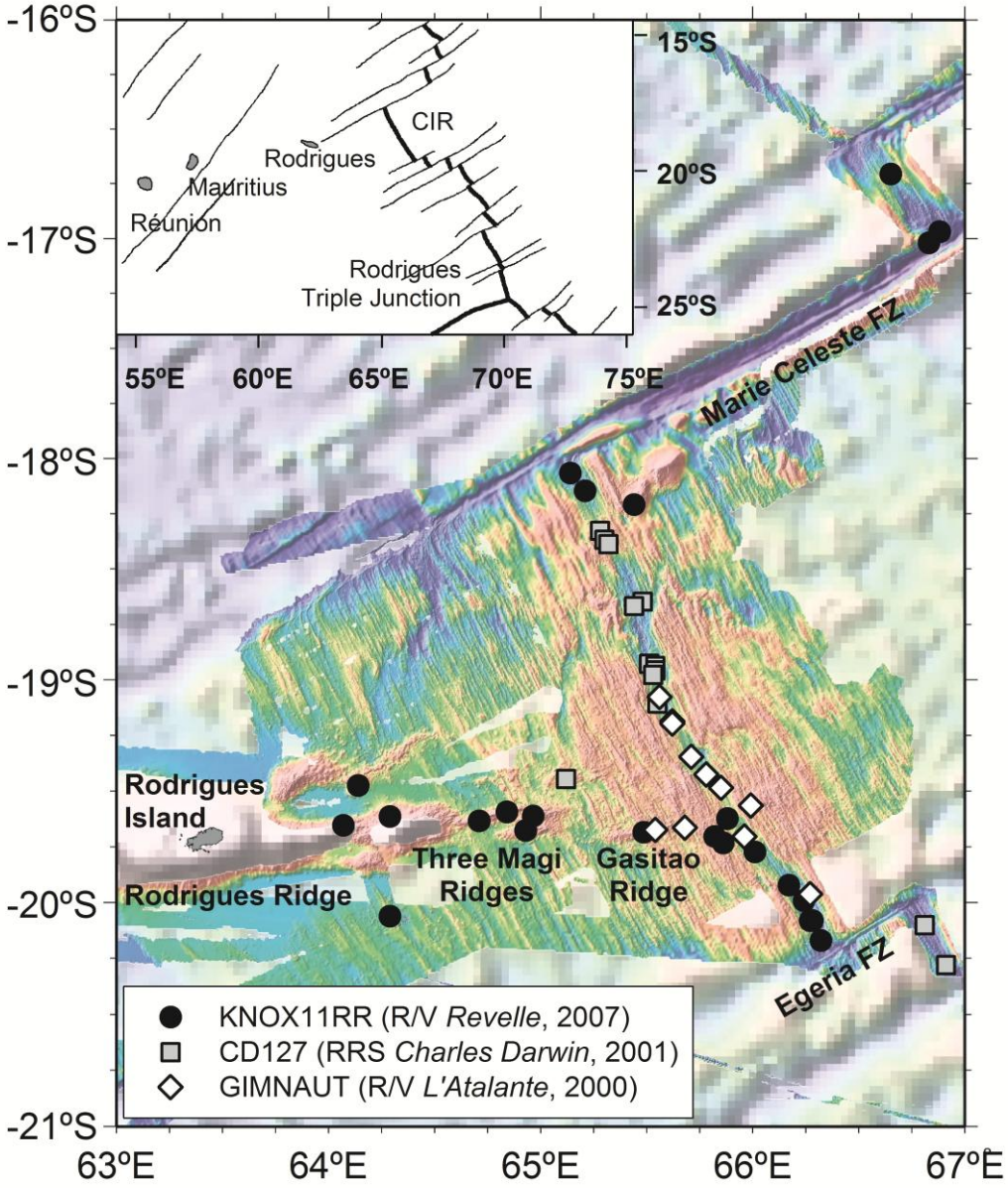

Figure V.1: Bathymetric map of CIR and the adjacent Gasitao Ridge, the Three Magi Ridges, and the Rodrigues Ridge. The three levels of shading for the bathymetry data represent a) pale colors, bathymetry "predicted" from satellite altimetry (Smith and Sandwell, 1997); b) intermediate colors, previous multibeam bathymetric data from R/V *Marion Dufresne* (1998; Dyment et al., 1999), *L'Atalante* (2000; Dyment et al., 2000), and *Hakuho-Maru* (2007; Okino et al., 2008); c) dark colors, multibeam bathymetric data collected by R/V *Revelle* (2007; this study). The symbols indicate the location of samples collected during the KNOX11RR (black circles), CD127 (gray squares) and GIMNAU (open diamonds) cruises. The inset shows the Mascarene Islands (Réunion, Mauritius, and Rodrigues) to the west of the CIR, as well as the Rodrigues Triple Junction.

Mauritius, and Rodrigues (Duncan et al., 1989, Duncan et al., 1990). Réunion Island represents the most recent expression of the hotspot. The island is made up of two volcanoes: Piton des Neiges, which was active between ~2 Ma and 43 ka, and the still active Piton de la Fournaise, where volcanic activity began ~360 kyr ago (McDougall, 1971). Mauritius is considered to be located on the former site of the Réunion hotspot. Volcanic activity on Mauritius started with a shield-building stage at 7-8 Ma (Older Series), with later stages at 2-3 Ma (Intermediate Series) and 0.2-0.7 Ma (Younger Series) (McDougall and Chamalaun, 1969). Rodrigues Island was formed at 1.5 Ma (McDougall et al., 1965); it lies at the eastern end of the Rodrigues Ridge, an east-west trending volcanic ridge that is 8-10 Ma old (Duncan etal., 1990). Smaller en-échelon volcanic ridges at 18-20°S - the Three Magi Ridges and the Gasitao Ridge – appear to extend the Rodrigues Ridge to the near vicinity of the CIR (Fig. V.1) (Dyment et al., 1999; Dyment et al., 2000).

Morgan (1978) proposed that the Rodrigues Ridge was formed by volcanism above a channel of upwelling Réunion hotspot mantle, deflected towards the ridge axis as the CIR migrated north-eastward away from the hotspot. In this scenario, a geochemical signature from the Réunion hotspot would be expected on the CIR axis at ~19.5°S, i.e., at the intersection of the ridge axis with a line projected through the Réunion and Rodrigues islands. While Mahoney et al. (1989) indeed found a Réunion-like isotope signature (low εNd, high $^{87}Sr/^{86}Sr$, high $^{207}Pb/^{204}Pb$ and high $^{206}Pb/^{204}Pb$) in basalt glasses from the CIR, the geochemical anomaly was only observed in the vicinity of the Marie Celeste FZ, i.e., further north than predicted by Morgan (1978). In addition, a more detailed study showed that basalts collected between the Marie Celeste FZ and the Rodrigues Triple Junction record a systematic decrease in incompatible element concentrations and ratios towards the south (Murton et al., 2005). The trace element and radiogenic isotope characteristics of CIR basalts appeared consistent with the presence of an enriched mantle source near the Marie Celeste FZ and

normal MORB-like mantle in the south. Thus, Mahoney et al. (1978) and Murton et al. (2005) proposed that Réunion hotspot mantle is migrating eastward along the Marie Celeste FZ towards the CIR, where it is forced southwards and mixes with depleted MORB mantle.

To investigate in more detail the influence of the Réunion hotspot on the CIR, Nauret et al. (2006) targeted a suite of basalts collected both on and off the CIR axis between 18° and 20°S. While they confirmed that basalts near the Marie Celeste FZ are enriched in incompatible trace elements, they showed that the composition of Réunion lavas is not a suitable endmember for the observed Sr-Nd-Pb isotope characteristics of most on-axis samples. Only off-axis lavas from the Gasitao Ridge, as well as a single on-ridge sample collected at 19.95ºS, recorded a Réunion source signature. Therefore, Nauret et al. (2006) proposed that Réunion hotspot material flows eastward towards the CIR on a trajectory that impinges the ridge at ~19.9°S, which agrees with the scenario initially described by Morgan (1978). Consequently, the mantle source enrichment in the vicinity of the Marie Celeste FZ, ~100 km to the north, cannot be related to influx of mantle material from Réunion.

While trace element and Sr-Nd-Pb isotope data clearly show the presence of an enriched component in the sub-ridge mantle of the CIR, the only helium isotope ratios that have so far been reported for four basalts from this region of the CIR range from 7.26 to 8.96 R_A (Mahoney et al., 1989), and are undistinguishable from the range associated with depleted MORB mantle (8 ± 1 R_A; Graham et al., 2002). In contrast, both historic and prehistoric lavas from Piton de la Fournaise, the presently active volcano on La Réunion, show that the Réunion hotspot is characterized by significantly higher $^3He/^4He$ ratios of ~11.8-14.5 R_A (Kaneoka et al., 1986; Staudacher et al., 1986; Graham et al., 1990; Staudacher et al., 1990; Hanyu et al., 2001; Trieloff et al., 2002; Hopp and Trieloff, 2005). Thus, any interaction of the CIR with the Réunion hotspot is expected to result in helium isotope values greater than 8 ± 1 R_A in basalts erupted on the ridge axis.

V.4 Sampling and analytical techniques

We collected submarine pillow basalts by dredging during the KNOX11RR cruise (November 2007) of the R/V *Revelle* along the CIR axis (between 16.7°S and 20.1°S), and the adjacent Gasitao Ridge, Three Magi Ridges, and Rodrigues Ridge (Füri et al., 2008). We recovered variable amounts of fresh glass from 24 out of a total of 38 locations (Fig. V.1). This sample set was supplemented by 12 glass samples from the GIMNAUT cruise (Nauret et al., 2006) and 14 glass samples from the cruise CD127 (Murton et al., 2005). In addition, we collected subaerial olivine phenocryst-rich lavas on Rodrigues, Mauritius, and Réunion, as well as xenoliths from Piton Chisny (Réunion).

Submarine glasses were analyzed for major elements by electron microprobe, and trace element abundances were determined using 1) a Thermo X-series II ICP-MS for samples from the KNOX11RR cruise; 2) a ICP-MS PlasmaQuad turbo 2+ for samples from the GIMNAUT cruise (Nauret et al., 2006); and 3) laser ablation ICP-MS on samples from the cruise CD127 (Murton et al., 2005). Olivine separates from the Mascarene Islands were analyzed by electron microprobe at Washington State University. For each sample, between 6 and 12 grains of olivine were analyzed for their major element chemistry in order to calculate their Mg numbers (= MgO/(MgO+FeO) × 100) - a measure of their evolutionary history.

A total of 51 basaltic glass samples, as well as 21 olivine separates, were analyzed for their helium isotope and abundance characteristics on a MAP 215 noble gas mass spectrometer by crushing. In the case of glasses, we selected fresh chips, free of phenocrysts and surface alteration using a binocular microscope. For phenocrysts, we made sure that crystals did not have any adhering matrix. In all cases, an effort was made to choose a small number of large grains to minimize the surface area to volume ratio and help preserve vesicles and/or inclusion in the samples. However, we note that olivine phenocrysts from Rodrigues and Mauritius are significantly smaller than the phenocrysts in lavas from Réunion.

After pre-cleaning in a 1:1 acetone-methanol mixture, approximately 50-170 mg of glass (i.e., typically between 1 to 10 chips) or 0.5-1 g of olivines, respectively, were loaded into on-line, electro-magnetic crushers (see description by Scarsi, 2000) connected to the preparation line of the MAP 215 noble gas mass spectrometer and pumped overnight to ultra-high vacuum. Crushing of the samples was achieved by externally accelerating a magnetized steel slug up and down within the crusher for 2 minutes at a frequency of ~120 impacts per minute. The volatiles released upon crushing were purified in the mass spectrometer preparation line by sequential exposure to a 750ºC hot Ti-getter, an activated charcoal trap (held at -196ºC), a SAES getter, and a cryogenic trap lined with activated charcoal (held at < 20 K). Helium was released from the cryogenic trap by increasing the temperature to 35 K, whereas Ne was released at 90 K. Sample $^{3}He/^{4}He$ ratios and $^{4}He/^{20}Ne$ ratios were measured in static mode and calibrated against standard aliquots of air (= 1 R_A) run at least twice a day under identical experimental conditions. Prior to each individual sample run, an analytical blank of the entire system was measured. The blanks (average $\leq 0.5 \times 10^{-9}$ cm^3STP^4He) were subtracted from each sample helium measurement. The blank contribution to the ^{4}He signal was less than 0.5 % for all basaltic glass samples (except for the exceptionally He-poor sample D29-1) and xenoliths from Piton Chisny. In contrast, olivine phenocrysts showed a significantly higher blank contribution between 1 and 11 % for samples from Réunion, and between 7 and 65 % for samples from Mauritius and Rodrigues, respectively, due to low He contents and/or small samples sizes. Analytical blanks for ^{20}Ne were also subtracted from each sample neon measurement, with any remaining neon considered an estimate of air ^{20}Ne. However, only samples D29-1, RU07-11, and RG07-01 showed a significant air ^{20}Ne contribution, indicated by low X values of 3.5, 22.3, and 4.5, respectively, where $X = (^{4}He/^{20}Ne)_{sample}/(^{4}He/^{20}Ne)_{air}$. Therefore, we corrected the measured helium isotope ratios and

helium concentrations of these three samples for the effects of air contamination (see tables V.1 and V.2 for details).

V.5 Results

Helium isotope ratios ($^3He/^4He$) and concentrations for olivine separates from the Mascarene Islands are given in Table V.1. In Table V.2, we report the abundance and isotope composition of He, as well as chondrite-normalized La/Sm ratios, for 51 submarine basalt glasses from the Central Indian Ocean. Helium isotope ratios are reported in the form of R/R_A, where R is the $^3He/^4He$ ratio measured in the sample and R_A is the atmospheric $^3He/^4He$ ratio of 1.4×10^{-6}. For samples D29-1, RU07-11, and RG07-01, we report air-corrected helium isotope ratios (R_c/R_A) and abundances ($[He]_c$).

V.5.1 Olivine samples from the Mascarene Islands

The helium contents of four olivine separates from xenoliths collected at Piton Chisny (Réunion) range from 158 to 917 ($\times 10^{-9}$ cm^3STP/g) (Table V.1; Fig. V.2a). In contrast, the helium abundances of all olivine phenocrysts from the Mascarene Islands are significantly lower and vary between 0.5 and 20.3 ($\times 10^{-9}$ cm^3STP/g). Phenocrysts from Mauritius and Rodrigues, i.e., the smallest olivine grains, show the lowest helium abundances. Mg numbers of the olivine separates range from 79.0 ± 2.5 to 88.0 ± 0.5 (Table V.1; Fig. V.2b). We note that olivine grains within individual samples from Mauritius and Rodrigues show a wider range in Mg numbers than those from samples collected on Réunion.

Our new helium isotope ratios for olivine phenocrysts and xenoliths from Réunion vary between 11.9 and 14.1 R_A and agree with the values observed in previous studies (~11.8-14.5 R_A; Kaneoka et al., 1986; Staudacher et al., 1986; Graham et al., 1990; Staudacher et al., 1990; Hanyu et al., 2001; Trieloff et al., 2002; Hopp and Trieloff, 2005)). The mean $^3He/^4He$

Table V.1: Helium characteristics of olivine samples from the Mascarene Islands[a].

Sample ID[b]	Latitude (S)	Longitude (E)	Age/Unit[c]	Weight (mg)	$^3He/^4He$ (R/R_A)	[He] cm^3STP/g ($\times 10^{-9}$)	Mg number[d]
Rodrigues							
RG07-01	19°40'53.5"	63°24'57.7"		425.2	*5.35 ± 0.43*	*1.45 ± 0.01*	80.9 ± 2.0 (n = 10)
RG07-14	19°41'55.2"	63°27'10.4"		688.9	5.60 ± 0.67	0.53 ± 0.01	83.4 ± 2.2 (n = 12)
RG07-15	19°40'07.1"	63°27'24.0"		488.8	7.43 ± 0.41	0.98 ± 0.01	81.1 ± 2.1 (n = 10)
RG07-17	19°44'55.1"	63°23'24.7"		615.8	8.40 ± 0.25	5.28 ± 0.01	79.0 ± 2.5 (n = 12)
RG07-20	19°41'45.4"	63°23'33.1"		542.1	8.41 ± 0.21	11.81 ± 0.02	82.8 ± 3.3 (n = 10)
Mauritius							
MR07-05	20°26'54.5"	57°20'48.8"	Older Series	541.6	8.64 ± 0.77	0.72 ± 0.01	83.3 ± 2.2 (n = 10)
MR07-06	20°13'00.0"	57°29'56.0"	Older Series	497.3	7.71 ± 0.37	1.85 ± 0.01	84.5 ± 0.4 (n = 10)
MR07-09	20°20'09.8"	57°46'44.3"	Older Series	650.3	10.36 ± 0.29	5.71 ± 0.01	82.7 ± 0.8 (n = 8)
MR07-10	20°21'16.5"	57°44'40.4"	Older Series	483.1	7.36 ± 0.33	1.97 ± 0.01	83.7 ± 1.3 (n = 9)
La Réunion							
RU07-01B	21°13'08.2"	55°48'25.4"	PDLF 4 (AD2002)	1068.4	12.53 ± 0.22	18.32 ± 0.02	84.2 ± 0.2 (n = 10)
RU07-02	21°13'15.1"	55°48'26.2"	PDLF 4 (AD1931)	1080.9	12.88 ± 0.31	14.09 ± 0.01	84.0 ± 0.2 (n = 10)
RU07-03	21°13'20.0"	55°48'23.3"	PDLF 4 (AD1998)	479.5	12.45 ± 0.52	15.20 ± 0.03	84.0 ± 0.7 (n = 6)
RU07-05	21°16'45.4"	55°47'43.1"	PDLF 4 (AD2007	736.2	13.71 ± 0.20	10.43 ± 0.01	84.5 ± 0.2 (n = 10)
RU07-08	21°15'18.2"	55°42'08.3"	PDLF 4 (AD1937)	959.8	12.61 ± 0.27	20.31 ± 0.02	83.3 ± 0.6 (n = 10)
RU07-10	21°53'14.6"	55°26'24.9"	Younger Oceanite Series	904.3	12.54 ± 0.28	3.05 ± 0.01	87.7 ± 0.9 (n = 10)
RU07-11	21°53'11.0"	55°26'15.2"	Younger Oceanite Series	701.1	*11.96 ± 0.54*	*2.39 ± 0.01*	88.0 ± 0.5 (n = 10)
RU07-12	21°55'52.4"	55°23'29.4"	Younger Oceanite Series	1019.7	12.84 ± 0.23	14.40 ± 0.01	84.3 ± 0.4 (n = 11)
CH07-01	21°13'53.6"	55°39'44.3"	PDLF 3	831.7	13.95 ± 0.25	917.27 ± 0.21	85.3 ± 0.5 (n = 11)
CH07-02	21°13'49.9"	55°39'55.8"	PDLF 3	669.7	13.66 ± 0.22	195.23 ± 0.11	85.3 ± 0.1 (n = 10)
CH07-04	21°13'49.8"	55°39'57.1"	PDLF 3	834.7	14.09 ± 0.23	157.99 ± 0.05	84.5 ± 0.3 (n = 11)
CH07-07	21°13'52.1"	55°39'55.9"	PDLF 3	893.3	13.58 ± 0.15	367.20 ± 0.09	84.1 ± 0.3 (n = 10)

[a] All errors are reported at the 1 σ level. Results listed in italics represent air-corrected He isotope ratios $R_C/R_A = [(R/R_A \times X) - 1]/(X - 1)$ and He contents $[He]_C = ([He] \times (X - 1))/X$, where $X=(^4He/^{20}Ne)/(^4He/^{20}Ne)_{air}$.

[b] Samples labeled CH07-0X represent xenoliths collected at Piton Chisny (Réunion).

[c] 'Older Series': shield-building stage (7-8 Ma) of Mauritius (McDougall and Chamalaun, 1969); 'Younger Oceanite Series': Piton des Neiges (0.43-2.1 Ma); PDLF3: Piton de la Fournaise, Phase 3 (5-60 ka); 'PDLF4': Piton de la Fournaise, Phase 4 (present – 5 ka) (Chevallier and Bachelery, 1981; Chevallier and Vatin-Perignon, 1982; Montaggioni et al., 1988).

[d] Mg number = [MgO/(MgO+FeO)] × 100; n = number of olivine grains analyzed.

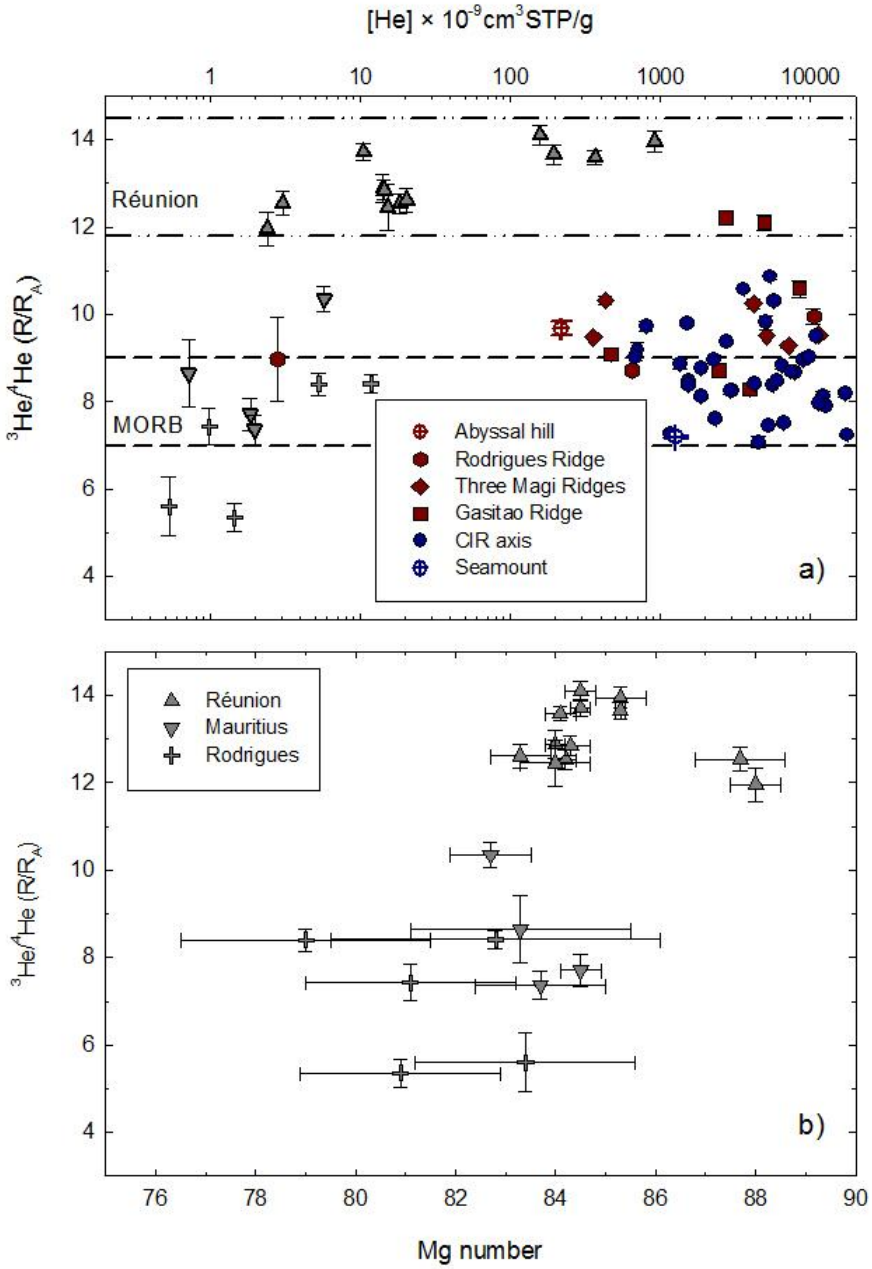

Figure V.2: a) Helium isotope ratios ($^3He/^4He$) versus helium concentrations of olivine separates from the Mascarene Islands (Réunion, Mauritius, and Rodrigues), as well as submarine basalt glasses from the CIR axis, the Gasitao Ridge, the Three Magi Ridges, the Rodrigues Ridge. Helium isotope ratios are shown as R/R_A, where $R = {}^3He/{}^4He$ ratio in the sample and $R_A = {}^3He/{}^4He$ ratio of air. The horizontal dashed lines indicate the range of values expected for MORB ($8 \pm 1R_A$, Graham et al., 2002) and the composition of lavas from Réunion Island (~11.8-14.5 R_A, (Kaneoka et al., 1986; Staudacher et al., 1986; Graham et al., 1990; Staudacher et al., 1990; Hanyu et al., 2001; Trieloff et al., 2002; Hopp and Trieloff, 2005). b) $^3He/^4He$ ratios of olivines are plotted as a function of their measured Mg number.

ratios of phenocrysts from Piton des Neiges (PDN 1) and Piton de la Fournaise (PDLF 4) are 12.45 ± 0.45 R_A (n = 5) and 12.84 ± 0.51 R_A (n = 3), respectively, whereas xenoliths from Piton Chisny (PDLF 3) show slightly higher values of 13.82 ± 0.24 R_A (n = 4). In contrast, the $^3He/^4He$ ratios of olivine phenocrysts from Mauritius and Rodrigues are lower and range from 7.4 to 10.4 R_A and 5.3 to 8.4 R_A, respectively. Hanyu et al. (2001) previously reported $^3He/^4He$ ratios of ~11.8 R_A for Older Series lavas on Mauritius, and a value of ~8 R_A for two samples from Rodrigues; however, they were unable to determine the He isotope composition of some samples due to very low helium abundances.

Figure V.2a shows that $^3He/^4He$ ratios correlate with He abundances for the olivine separates. The lowest $^3He/^4He$ values are measured in samples from Mauritius and Rodrigues, i.e., the phenocrysts with the lowest He contents. In contrast, Figure V.2b reveals that there is no clear correlation between $^3He/^4He$ ratios and Mg numbers – either for the Mascarene Islands data set as a whole or for the individual islands. Addition of crustal-derived radiogenic ^4He is expected to occur simultaneously with magma differentiation in the crust which, in turn, would be traced by lower Mg numbers. However, low $^3He/^4He$ ratios do not correspond to lower Mg values. Therefore, we suggest that post-eruptive radiogenic in-growth of ^4He from the alpha-decay of U and Th may have effectively lowered the $^3He/^4He$ values of olivines with low He contents. Since phenocrysts from Mauritius and Rodrigues are smaller in size and significantly older than those collected on Réunion Island, their low He isotope values appear consistent with addition of radiogenic helium; thus, their measured $^3He/^4He$ ratios likely represent minimum values.

V.5.2 Submarine glasses from the Central Indian Ocean

V.5.2.1 Major and trace element chemistry

The majority of submarine basalts recovered from the CIR axis and the adjacent Gasitao, Three Magi, and Rodrigues ridges are tholeiitic, with some samples from the off-axis ridges having alkaline affinity. MgO and SiO_2 contents range from 6.6 to 14.4 wt.% and from 44.7 to 51.8 wt.%, respectively (Fig. V.3; Appendix V.1), and glasses from the off-axis volcanic structures generally have higher MgO and lower SiO_2 contents compared to on-axis samples (Fig. V.3).

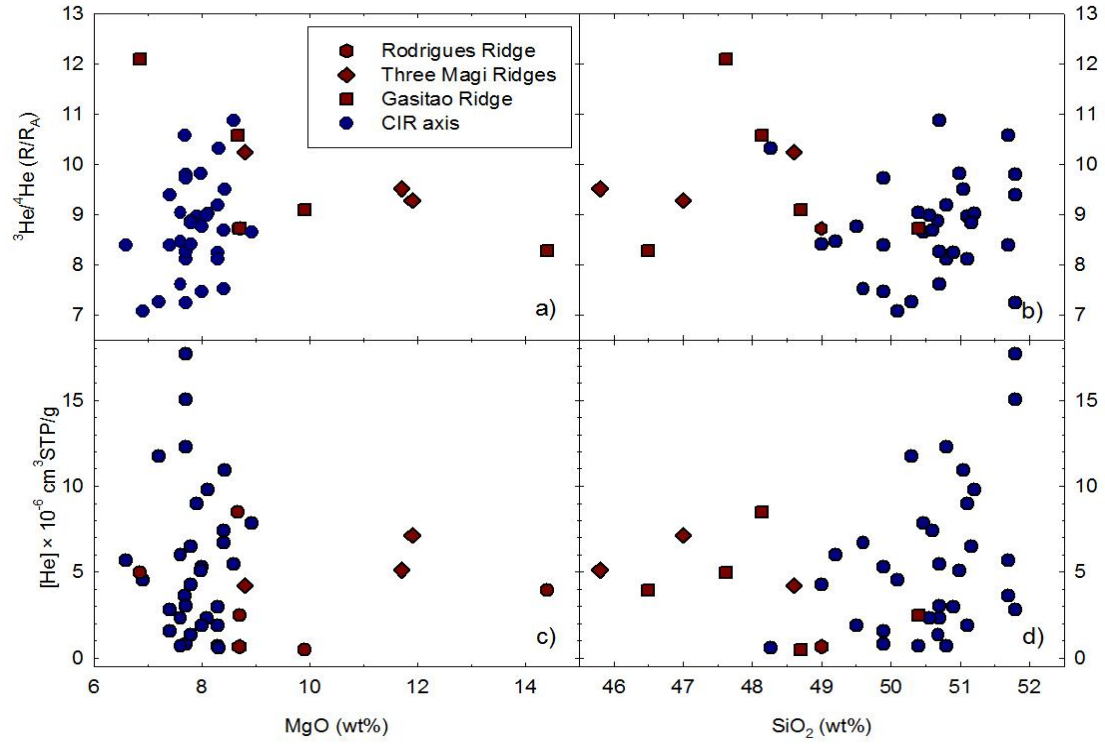

Figure V.3: Helium isotope ratios ($^3He/^4He$) and helium concentrations of Central Indian Ocean basalt glasses plotted against the MgO content (left) and the SiO_2 content in wt.% (right).

Glasses from both the CIR axis and the off-axis ridges are characterized by a wide range in chondrite-normalized La/Sm ratios, $(La/Sm)_N$, encompassing typical N-MORB-like ratios (< 0.7; Schilling et al., 1983) through values as high as 2.09 and 1.74, respectively (Table V.2). The highest $(La/Sm)_N$ is observed in sample RC1, which was collected from the western flank of the axial valley (Murton et al., 2005). We note that both Murton et al. (2005) and Nauret et al. (2006) previously concluded that the variations in incompatible element concentrations and ratios observed along the CIR axis must reflect the presence of a trace element enriched mantle source. Melting models fail to account for the observed variations in trace element characteristics (Murton et al., 2005), and the lack of a correlation between the Na_2O content and bathymetry suggests that there are no significant variations in the degree of partial melting along the CIR axis (Nauret et al., 2006).

V.5.2.2 Helium abundances and isotope ratios

Helium abundances in submarine glasses are extremely variable and range from 219 to 17,675 ($\times 10^{-9}$ cm^3STP/g) (Table V.2; Fig. V.2a). Only sample D29-1 from the Rodrigues Ridge shows a significantly lower (air-corrected) helium content of 2.2×10^{-9} cm^3STP/g. Helium isotope ratios of the glass samples vary between 7.1 and 12.2 R_A (Fig. V.2a), i.e., between values expected for depleted MORB mantle (8 ± 1 R_A, Graham et al., 2002) and the helium isotope composition of lavas from Réunion Island with a mean value of 13.1 ± 0.7 R_A (this study; see section V.5.1). We note that duplicate analyses of samples DR08-1 and D22-1 confirm that the reproducibility in $^3He/^4He$ ratios is good. In addition, samples D3-3 and D3-9 show $^3He/^4He$ ratios of 7.91 R_A and 7.96 R_A, respectively, illustrating that distinct pillow basalt fragments recovered in a particular dredge show homogeneous helium isotope compositions.

Table V.2: Helium characteristics of submarine basalt glasses from the CIR axis and the adjacent Gasitao, Three Magi, and Rodrigues ridges[*].

Sample ID	Latitude (ºS)	Longitude (ºE)	Depth (m)	Weight (mg)	$^3He/^4He$[d] (R/R_A)	[He][d] cm^3STP/g ($\times10^{-9}$)	$(La/Sm)_N$[e]
CIR axis							
D1-1[a]	-16.70	66.65	3146	75.0	8.11 ± 0.11	12264 ± 13	1.12
D3-3[a]	-16.96	66.88	4272	82.6	7.91 ± 0.02	12719 ± 3	1.36
D3-9[a]	-16.96	66.88	4272	79.8	7.96 ± 0.02	11423 ± 4	1.34
D2-1[a]	-17.01	66.83	4038	77.3	8.19 ± 0.09	17022 ± 4	1.13
D8-2[a]	-18.05	65.14	3202	75.3	7.08 ± 0.14	4532 ± 7	1.22
D9-1[a]	-18.13	65.21	3127	71.2	7.25 ± 0.08	11710 ± 2	1.58
RC19[c]	-18.31	65.28	2823	124.6	7.61 ± 0.05	2333 ± 1	1.47
RC20[c]	-18.35	65.3	2788	134.6	7.46 ± 0.04	5305 ± 2	1.72
RC21[c]	-18.37	65.32	2765	124.9	7.51 ± 0.04	6671 ± 2	1.82
RC7[c]	-18.63	65.48	2996	69.4	8.38 ± 0.03	5642 ± 1	1.31
RC5[c]	-18.65	65.44	3120	57.9	9.38 ± 0.04	2785 ± 1	1.25
RC10[c]	-18.91	65.51	3064	135.6	10.86 ± 0.06	5434 ± 2	0.81
RC12[c]	-18.92	65.54	3099	132.5	9.80 ± 0.07	15010 ± 4	0.79
RC13[c]	-18.94	65.54	3039	65.2	7.24 ± 0.03	17675 ± 5	0.73
RC4[c]	-18.96	65.53	3068	54.5	8.96 ± 0.06	8987 ± 2	1.34
DR11-1[b]	-19.05	65.56	3020	73.0	9.19 ± 0.16	705 ± 1	1.31
RC1[c]	-19.09	65.55	2853	51.6	9.72 ± 0.11	805 ± 1	2.09
PL20-2[b]	-19.17	65.62	2695	110.2	9.02 ± 0.03	9776 ± 3	0.53
PL01-5[b]	-19.18	65.62	3012	106.7	9.50 ± 0.03	10897 ± 3	0.89
DR06-1[b]	-19.33	65.71	2885	59.4	9.81 ± 0.15	5088 ± 2	0.97
DR05-1[b]	-19.41	65.78	3061	67.6	8.86 ± 0.10	1353 ± 1	0.64
PL11-1[b]	-19.47	65.85	2879	52.1	8.97 ± 0.09	2295 ± 1	0.54
DR02-3[b]	-19.55	65.99	2120	56.9	8.65 ± 0.07	7854 ± 2	0.59
DR01-1[b]	-19.55	65.94	2130	54.3	10.57 ± 0.03	3598 ± 1	0.80
D17-1[a]	-19.61	65.88	2742	112.8	8.76 ± 0.02	1867 ± 1	0.97
DR03-1[b]	-19.69	65.96	2990	60.6	8.83 ± 0.07	6464 ± 2	0.82
D15-1[a]	-19.76	66.01	2794	76.6	8.68 ± 0.01	7401 ± 4	0.62
D14-1[a]	-19.91	66.17	3267	73.4	8.46 ± 0.02	5987 ± 1	0.72
DR10-1[b]	-19.95	66.27	3070	114.5	10.31 ± 0.06	573 ± 1	0.59
D13-1[a]	-19.98	66.24	3511	67.4	8.26 ± 0.03	3004 ± 3	0.51
D12-2[a]	-20.07	66.27	3550	71.3	8.41 ± 0.03	4275 ± 1	0.54
D11-2[a]	-20.07	66.28	3370	71.1	8.46 ± 0.03	1540 ± 1	n.d.
D10-2[a]	-20.16	66.32	3483	71.1	8.38 ± 0.04	1537 ± 1	0.49
D6[c]	-20.09	66.81	3900	61.8	8.24 ± 0.07	2941 ± 1	0.69
RC23[c]	-20.27	66.91	3520	63.8	8.11 ± 0.04	1866 ± 1	0.41
RC18[c]	-20.6	68.2	2853	54.2	9.03 ± 0.09	688 ± 1	0.54
Seamount							
D6-2[a]	-18.22	65.41	2048	72.6	7.18 ± 0.03	1270 ± 3	1.19

Table V.2: Continued

Sample ID	Latitude (°S)	Longitude (°E)	Depth (m)	Weight (mg)	$^3He/^4He$[d] (R/R_A)	[He][d] cm^3STP/g ($\times 10^{-9}$)	$(La/Sm)_N$[e]
Gasitao Ridge							
D18-2[a]	-19.72	65.86	2216	119.8	9.09 ± 0.06	470 ± 1	0.95
D19-2[a]	-19.69	65.82	2176	118.2	8.72 ± 0.05	2453 ± 1	0.51
DR09-1[b]	-19.65	65.68	2071	61.1	10.58 ± 0.19	8496 ± 2	0.59
DR08-1[b]	-19.66	65.54	2110	59.6	12.10 ± 0.18	4954 ± 2	0.45
				48.5	12.21 ± 0.17	2727 ± 127	
D20-5[a]	-19.70	65.49	2002	114.8	8.28 ± 0.05	3949 ± 8	0.49
Three Magi Ridges							
D5_1.5[c]	-19.43	65.12	2226	54.0	10.24 ± 0.11	4197 ± 1	1.74
D22-1[a]	-19.62	64.97	1687	128.9	9.28 ± 0.06	7128 ± 12	n.d.
				61.0	9.52 ± 0.01	11425 ± 3	
D24-6[a]	-19.67	64.95	2019	158.3	10.32 ± 0.09	430 ± 1	0.42
D25-2[a]	-19.58	64.84	2123	156.4	9.48 ± 0.04	358 ± 1	0.71
D26-2[a]	-19.62	64.71	1785	119.5	9.51 ± 0.02	5103 ± 4	0.75
Rodrigues Ridge							
D29-1[a]	-19.60	64.29	1820	124.3	*8.97 ± 1.21*	*2.2 ± 0.1*	1.65
D34-1[a]	-19.46	64.14	2134	119.0	8.72 ± 0.03	650 ± 1	0.64
D30-3[a]	-19.64	64.07	2156	135.0	9.95 ± 0.17	10551 ± 9	0.59
Abyssal hill							
D37-2[a]	-20.05	64.29	2833	171.3	9.67 ± 0.17	219 ± 1	0.91

* All errors are reported at the 1 σ level. n.d., no data available.

[a] Samples collected on the KNOX11RR cruise (R/V *Revelle*, 2007; Füri et al., 2008).

[b] Samples collected on the GIMNAUT cruise (R/V *L'Atalante*, 2000; Nauret et al., 2006).

[c] Samples collected on the CD127 cruise (RRS *Charles Darwin*, 2001; Murton et al., 2005).

[d] R and [He] are the measured He isotope ratio and He concentration, respectively. For sample D29-1, we report the air-corrected He isotope ratio $R_C/R_A = [(R/R_A \times X) - 1]/(X - 1)$ and He content $[He]_C = ([He] \times (X - 1))/X$, where = $(^4He/^{20}Ne)/(^4He/^{20}Ne)_{air}$.

[e] $(La/Sm)_N$ is the chondrite-normalized La/Sm ratio, i.e., $(La/Sm)_N = (La/Sm)_m/(La/Sm)_{CI}$, where $(La/Sm)_{CI} \approx 1.6$ (McDonough and Sun, 1995).

A previous study reported He isotope ratios of 7.26-8.96 R_A for a series of four basalts from this region of the CIR, i.e., values that are undistinguishable from the range associated with normal MORB (Mahoney et al., 1989). Our study reveals that most glasses recovered from the CIR axis have MORB-like $^3He/^4He$ ratios; however, 9 out of the 36 samples show helium isotope ratios > 9 R_A (i.e., 9.2-10.9 R_A). The majority of glasses from the off-axis volcanic ridges - the Three Magi Ridges, the Gasitao Ridge, and the Rodrigues Ridge – have helium isotope ratios significantly greater than MORB values, i.e., 9 out of the 13 samples have $^3He/^4He$ ratios > 9 R_A, and an abyssal hill sampled ~40 km to the south of the Rodrigues Ridge also shows an elevated helium isotope ratio of 9.7 R_A. The highest $^3He/^4He$ ratio of 12.21 R_A, observed on the Gasitao Ridge, is indistinguishable from the helium isotope composition of lavas from Réunion. We conclude that the high He isotope ratios of submarine glasses recovered between ~19° and 20°S are consistent with a contribution of helium derived from a high-$^3He/^4He$ mantle source.

V.5.2.3 Geographic variations

In Figure V.4, we show the isotope composition and concentration of helium, as well as $(La/Sm)_N$ ratios, for submarine glasses collected along the CIR axis and the off-axis volcanic ridges as a function of latitude and longitude, respectively. Figure V.4a reveals that MORB-like $^3He/^4He$ ratios are observed in glasses recovered on the CIR axis in the vicinity of the Marie Celeste FZ, i.e., in the northern part of the study area. We note that a glass sample recovered from a near-ridge seamount south of the Marie Celeste FZ (sample D6-2) also records a low $^3He/^4He$ ratio of 7.2 R_A, indistinguishable from the values observed on the ridge axis in this region. There is a marked increase in a southerly direction to values >10 R_A between ~19° and 20°S along the ridge axis before values decrease to ~8 R_A close to the Egeria FZ in the south. The glasses from the southern part of the ridge are characterized by

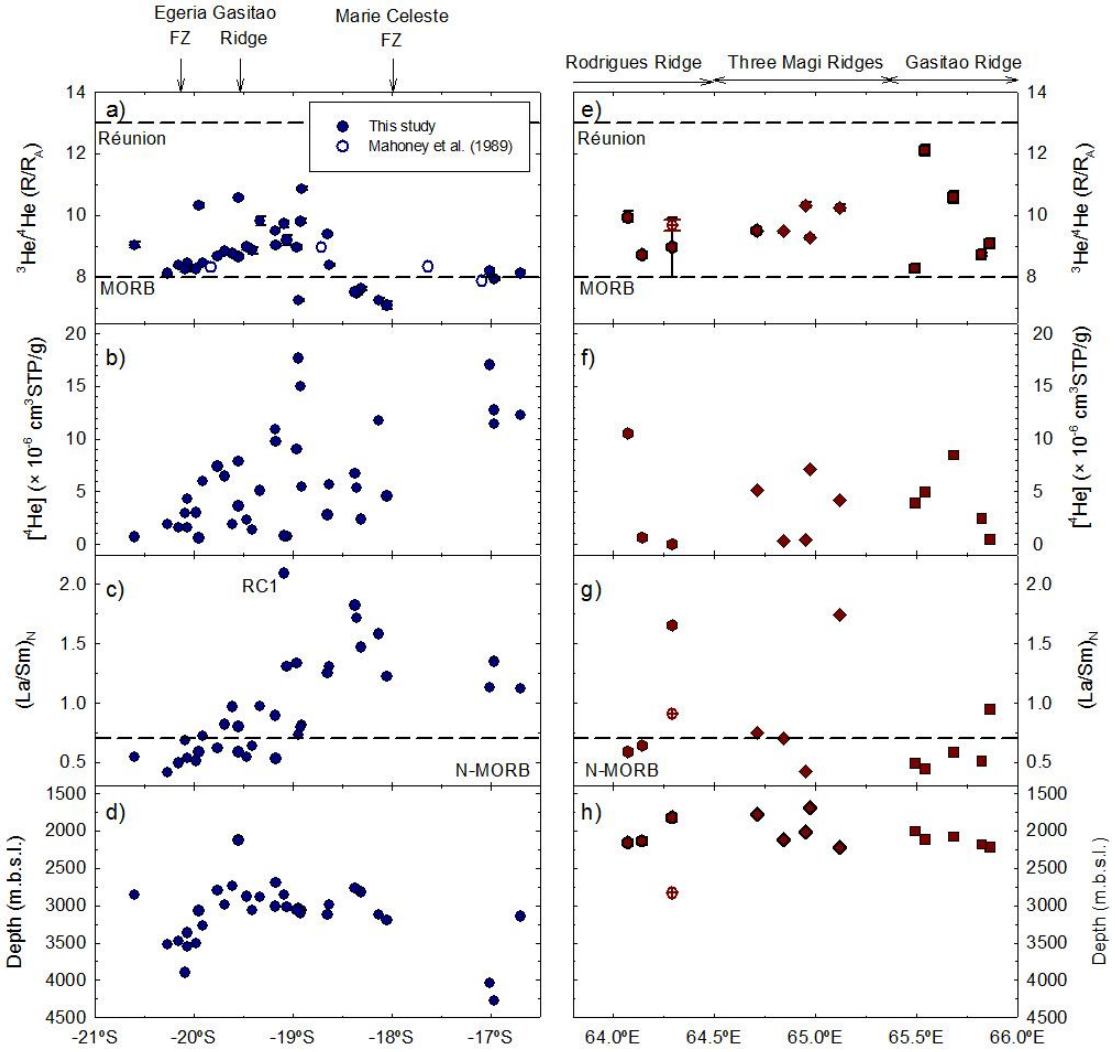

Figure V.4: Helium isotope ratios ($^3He/^4He$), helium concentrations, chondrite-normalized La/Sm $(La/Sm)_N$ ratios, and depth of sampling (in meters below sea level; m.b.s.l.) of submarine basalt glasses from the CIR axis (as a function of latitude; left panel) and from the off-axis volcanic structures (as a function of longitude; right panel). Also shown are the helium isotope ratios of four basalts obtained previously by Mahoney et al. (1989). Helium isotope ratios for depleted MORB mantle (8 ±1 R_A, Graham et al., 2002) and lavas from Réunion Island (~13.0 R_A; this study), as well as the chondrite-normalized La/Sm $(La/Sm)_N$ ratios for MORB (Schilling et al., 1983), are indicated by the horizontal dashed lines. Sample RC1 was collected from the edge of the axial valley (Murton et al., 2005).

low $^3He/^4He$ and low He concentrations ($\leq 5 \times 10^{-6}$ cm^3STP/g), as well as low $(La/Sm)_N$ ratios. Overall, however, $^3He/^4He$ values do not correlate with helium concentrations (Fig. V.2; Fig. V.4b) or $(La/Sm)_N$ ratios (Fig. V.4c) along the CIR. The highest He abundances ($> 10 \times 10^{-6}$

cm^3STP/g) are measured in glasses collected to the north of the Marie Celeste FZ and in the central part of the studied ridge segment (Fig. V.4b). In contrast, the highest $(La/Sm)_N$ ratios, characteristic of an enriched mantle component, are observed immediately south of the Marie Celeste FZ (Fig. V.4c) where $^3He/^4He$ ratios are the lowest (Fig. V.4a).

Glasses from the off-axis volcanic ridges do not record any systematic variations in $^3He/^4He$ ratios, He concentrations, or $(La/Sm)_N$ ratios with increasing distance from the CIR axis. Helium isotope ratios range from 8.7 to 12.2 R_A at the Gasitao Ridge, i.e., the volcanic ridge closest to the CIR, whereas the Three Magi and Rodrigues ridges show $^3He/^4He$ ratios of 9.5-10.3 R_A and 8.7-9.9 R_A, respectively (Fig. V.4e). Helium abundances are highly variable from east to west, and glasses from each individual volcanic ridge show a wide range in helium concentrations (Fig. V.4f). While the majority of glasses have low $(La/Sm)_N$ ratios (i.e., < 1), two samples from the Three Magi and Rodrigues ridges show $(La/Sm)_N$ ratios of 1.74 and 1.65, respectively (Fig. V.4g). However, the distinct trace element signatures of these two samples do not correlate with anomalous helium isotope ratios or abundances.

V.6 Discussion

Our helium isotope survey reveals that submarine glasses recovered from the CIR record a range in $^3He/^4He$ ratios, between values expected for depleted MORB mantle and the helium isotope composition of lavas from Réunion Island. Glasses sampled both to the north of the Marie Celeste FZ and to the south of the Egeria FZ show $^3He/^4He$ ratio that are undistinguishable from the range associated with normal MORB. However, an enriched, high-$^3He/^4He$ ratio component is present in the sub-ridge mantle between ~19° and 20°S, as well as in the mantle beneath the off-axis volcanic ridges to the west of the CIR. As the focus of this study is to identify the mantle endmember helium systematics, and to understand the dynamics of mantle mixing in this region, we first define the intrinsic helium characteristics of the

different mantle sources by evaluating other mechanisms capable of modifying the volatile inventory of submarine basalts. While pillow basalts recovered from the off-axis structures are older and in part manganese-encrusted, the "zero age" of lavas erupted on the CIR axis renders any post-eruptive in-growth of ^{4}He insignificant. However, shallow level magmatic processes and pre-eruptive radiogenic ^{4}He in-growth are considered in the following sections.

V.6.1 Effects of shallow level magmatic processes

V.6.1.1 Off-axis glasses: Post-eruptive ^{4}He in-growth

In the case of post-eruptive in-growth, ^{3}He/^{4}He ratios can be lowered with time by the addition of ^{4}He from the decay of U and Th. Therefore, it is important to evaluate the effect of radiogenic He production on the ^{3}He/^{4}He values of glasses from the off-axis volcanic ridges which may not be zero-age. Dredged samples from the Rodrigues Ridge range in age from 8 to 10 Ma (Duncan, 1990), whereas samples from the easternmost Gasitao Ridge provide ages of 0.4 and 1.8 Ma (Dyment et al., 2001). We can estimate the maximum amount of radiogenic ^{4}He produced over time in basalts erupted off-axis, according to (Graham et al., 1987):

$$^4He^* = 2.80 \times 10^{-8} [U] (4.35 + Th/U) T \ (cm^3STP/g) \qquad (V.1)$$

where T is the time in Myr, [U] is the uranium concentration in ppm, and Th/U is the atomic ratio (see Appendix V.9.2 and Nauret et al., 2006). Thus, we calculate a radiogenic ^{4}He production of ~2-17 ($\times 10^{-9}$ cm^{3}STP/g) for samples from the Gasitao Ridge. Under the very unlikely condition of complete transfer of ^{4}He* from the glass matrix (where it is produced) to the vesicle phase, post-eruptive ^{4}He in-growth may have modified the helium isotope composition of sample D18-2 which shows the highest [U] and lowest [^{4}He]. For this sample, the amount of radiogenic ^{4}He produced in 1.8 Myr is ~4% of the total helium abundance, and the initial ^{3}He/^{4}He ratio may have been 9.4 R_A – slightly higher than the ratio of 9.1 R_A observed today. In contrast, ~20-100 ($\times 10^{-9}$ cm^{3}STP^{4}He*/g) may have been produced in the

older basalts from the Rodrigues Ridge; thus, post-eruptive ^{4}He in-growth may have modified the initial ^{3}He/^{4}He ratio of the He-poor samples D29-1 and D34-1. In this case, the ^{3}He/^{4}He ratios of 9.0 and 8.7 R_A measured in these samples today represent minimum values, and the helium isotope ratios of basalts from the Rodrigues Ridge may have been significantly higher than typical MORB values.

V.6.1.2 On-axis glasses: Degassing

Degassing plays an important role in the helium inventory of any oceanic basalt (Bottinga and Javoy, 1990; Marty and Zimmermann, 1999; Hilton et al., 2000b; Moreira and Sarda, 2000). Virtually all oceanic basalts are supersaturated with respect to CO_2 – the carrier of magmatic helium – when they erupt, resulting in the formation of CO_2-rich gas bubbles and loss of helium from the melt phase (Sarda and Graham, 1990). Since the solubility of CO_2 decreases as the confining pressure decreases (Dixon et al., 1995; Jendrzejewski et al., 1997, basaltic melts erupting at shallow water depths (i.e., under low hydrostatic pressures) will lose a higher proportion of their primary volatile inventory. In addition, the solubility of CO_2 is controlled by the water content of the magma; for example, an increase in the water content of a basaltic melt from ~0.2 to 1 wt.% H_2O (at 200 bar) would decrease the CO_2 solubility from 100 to 50 ppm (Dixon et al., 1995). Thus, a water-rich magma will lose its dissolved CO_2 more efficiently than an anhydrous melt. Consequently, a combination of high water contents and shallow eruption depths will promote extensive degassing, and a lower concentration of helium is to be expected for a melt erupting under such conditions.

We recovered submarine glasses from the CIR axis between 2120 and 4270 m water depths (Table V.2; Fig. V.4d). Figure V.4d illustrates that between the Marie Celeste and the Egeria FZ, the depth of the CIR is greatest in the south. In addition, Murton et al. (2005) noted that water concentrations of CIR basalts, determined for a subset of samples by Fourier

transform laser spectroscopy, decrease southward along the ridge axis. Thus, due to a greater confining pressure at eruption and low water concentrations, the melts from the southern end of the CIR segment are expected to retain their primary helium inventory more efficiently. However, our data reveal that the helium contents of glasses collected near the Egeria FZ are the lowest (Fig. V.4b). In addition, helium abundances are highly variable for a given water depth. These observations lead us to conclude that the confining (i.e., hydrostatic) pressure and/or the water content are not the major controls on the observed variations in helium abundances of CIR basalts. *We note that major volatile content (H_2O and CO_2) measurements by secondary ion mass spectrometry (SIMS) on all glass samples from the KNOX11RR cruise are in progress; these data will allow a more quantitative evaluation of the relationship between major volatile abundances and helium concentrations.*

Alternatively, fractional crystallization in a shallow magma chamber increases the extent of gas loss from a melt (Marty and Zimmermann, 1999; Burnard et al., 2002). Since volatiles (e.g., He and CO_2) are expected to behave incompatibly, their effective concentrations in a melt increase during fractional crystallization and eventually exceed the solubility limits at the magma chamber pressure. Consequently, CO_2-rich bubbles form and, as other volatile species partition between the melt and the vapor phase, magmas are depleted in mantle-derived volatiles. Therefore, helium abundances are expected to correlate positively with a crystal fractionation index (e.g., the MgO content) if the extent of crystallization was the main control on the volatile solubility. However, Figure V.3 shows that the helium abundances of our sample set do not show a clear decrease with decreasing MgO content, that is, with increasing fractional crystallization. On-axis samples are characterized by highly variable helium concentrations for a relatively narrow range (6.6 to 8.9 wt.%) of MgO contents. This suggests that the observed variations in helium abundances along the CIR axis cannot be explained by varying degrees of fractional crystallization alone.

We conclude that shallow level magmatic processes can be ruled out as the major controls on the wide helium concentration contrasts observed in basalts collected along the CIR axis. However, the role of degassing will be evaluated in more detail in a separate contribution. We propose that the helium systematics of on-axis basalts are the result of mixing between different mantle sources with distinct helium inventories. Next, we discuss the helium characteristics of these different mantle components.

V.6.2 Enriched mantle at ~18°S: Pre-eruptive ^{4}He in-growth

The highest $(La/Sm)_N$ ratios along the CIR axis, characteristic of an enriched mantle source, are observed in basaltic glasses collected immediately south of the Marie Celeste FZ. However, glasses from this region show the lowest $^{3}He/^{4}He$ ratios (<8 R_A), and their Sr-Nd-Pb isotope characteristics differ from the composition of lavas presently erupting on Réunion (Nauret et al., 2006). Consequently, the trace element enriched mantle material cannot be supplied by direct influx from Réunion towards the CIR. As an alternative explanation, we evaluate if on-axis melts in this region may be sampling 1) an "ancient" Réunion hotspot mantle component or 2) metasomatized (i.e., trace element enriched) MORB-like mantle.

V.6.2.1 "Ancient" Réunion hotspot mantle

Fisk et al. (1989) and White et al. (1990) showed that both trace element ratios and Sr-Nd-Pb isotope systematics of basalts sampled along the Réunion hotspot track during Ocean Drilling Program (ODP) Leg 115 are variable. The basalts record a clear increase in $^{87}Sr/^{86}Sr$ and $^{206}Pb/^{204}Pb$ ratios, as wells as a decrease in εNd values with time. These compositional changes were attributed to temporal variations in the degree of mixing between the upwelling Réunion hotspot mantle and shallower asthenospheric mantle (Duncan et al., 1990; White et al., 1990). As the CIR was located closer to the Réunion hotspot in the past, the higher-

temperature and lower viscosity and density regime associated with the spreading ridge resulted in enhanced entrainment of depleted MORB-mantle by the ascending hotspot material. In this respect, studies of other hotspots located close to spreading ridges (e.g., Iceland, Bouvet, Galápagos, and Easter) have revealed that the isotope characteristics of OIB lavas show mixing trends with MORB-like mantle (Hanan and Schilling, 1989; Hauri et al., 1994). Thus, as the Réunion hotspot was centered under the CIR, mixing of the two mantle components generated basalts with lower $^{87}Sr/^{86}Sr$ and $^{206}Pb/^{204}Pb$ ratios, as well as higher εNd values compared to lavas presently erupting on Réunion (Duncan et al., 1990; White et al., 1990). These trace element and Sr-Nd-Pb isotope characteristics resemble the composition of basalts presently erupting near the Marie Celeste FZ, i.e., at the northern end of the studied CIR segment (Nauret et al., 2006). If an "ancient" Réunion hotspot component is still present in the mantle beneath the CIR, it must have been isolated from mixing with ambient MORB-like mantle over the past 34 Ma in order to retain a distinct trace element and Sr-Nd-Pb isotope composition; however, radiogenic ^{4}He in-growth from the decay of U and Th will have modified the initial $^{3}He/^{4}He$ ratio.

In order to evaluate if an "ancient" Réunion mantle component represents a suitable endmember for the helium characteristics of basalts collected near the Marie Celeste FZ, we need to estimate the He and (U+Th) content of this reservoir. Vlastélic et al. (2006) showed that the Réunion hotspot source has preserved a Th/U ratio of 3.9, similar to the bulk Earth value (Rocholl and Jochum, 1993) and identical to the Th/U ratio measured in sample D9-1 collected in the vicinity of the Marie Celeste FZ. Assuming 10% partial melting in the sub-ridge mantle and quantitative partition of uranium from the solid phase into the melt, we estimate a uranium concentration of 35 ppb for the mantle source on the basis of the uranium content of sample D9-1 ([U] = 0.35 ppm; Appendix V.9.2). Therefore, we adopt an initial $^{3}He/^{4}He$ ratio of 13.0 R_A (i.e., the helium isotope composition of lavas presently sampled on

Réunion Island), [U] = 35 ppb, Th/U = 3.9, and a corresponding ^{4}He production ratio of 2.33 × 10^{-7} cm^{3}STP/ppm U/Ma (Ozima, 2002). The helium concentration of the Réunion hotspot component, however, is difficult to constrain. The primary helium content of different mantle reservoirs cannot be determined through direct measurements of volcanic materials, and models predict a wide range of ^{4}He concentrations between ~0.5 to 50 × 10^{-6} cm^{3}STP^{4}He/g for the OIB mantle source (e.g., Porcelli and Ballentine, 2002; van Keken et al., 2002). The highest source estimates are based on steady-state, layered mantle models, with the assumption that the lower mantle represents the source of OIB and has remained a closed system over Earth history (Porcelli and Wasserburg, 1995). In contrast, significantly lower OIB source estimates are derived from studies of ^{3}He and magma flux rates at Kilauea (Hilton et al., 1997).

Figure V.5 shows that for an initial helium concentration of 50 × 10^{-6} cm^{3}STP^{4}He/g, the helium isotope ratio in the mantle source would decrease by only ~0.5 % after 34 Myr of radiogenic ^{4}He in-growth in a closed system. In order to shift the ^{3}He/^{4}He ratio to a value of 7.2 R_A, i.e., the ratio observed in basalts collected near the Marie Celeste FZ today, a significantly lower initial helium content of ~0.35 × 10^{-6} cm^{3}STP^{4}He/g is required. However, enhanced entrainment of depleted MORB-mantle by the ascending hotspot material in the past may have resulted in a lower helium isotope ratio of the trace element enriched mantle component compared to lavas currently erupting on Réunion. In this respect, we note that Older Series (5-8 Ma) lavas on Mauritius, located on the former site of the Réunion hotspot, have ^{3}He/^{4}He ratios of only ~8-11.8 R_A (this study; Hanyu et al., 2001), consistent with a higher proportion of helium derived from a MORB-like reservoir. Nonetheless, an enriched mantle component with an initial ^{3}He/^{4}He ratio of ~8-12 R_A still requires a low primary helium content of only 0.4-2.5 × 10^{-6} cm^{3}STP^{4}He/g for a decrease of the helium isotope composition to a value of ~7.2 R_A by radiogenic in-growth over 34 Myr.

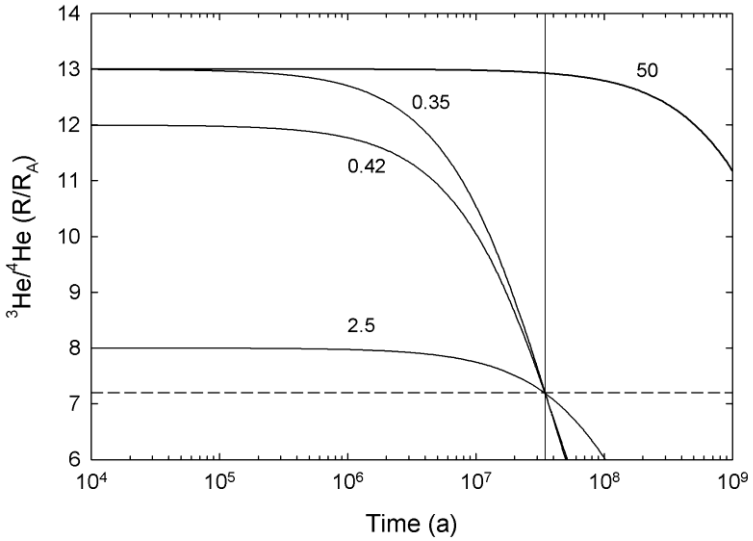

Figure V.5: Predicted time-dependent evolution of the $^3He/^4He$ ratio (R/R_A) of an "ancient" Réunion mantle component due to radiogenic ^4He in-growth from decay of U and Th over 34 Ma. Curves are modeled for a mantle reservoir with [U] = 35 ppb, Th/U = 3.9, a ^4He production ratio of 2.32×10^{-7} cm^3STP/ppm U/Ma (Ozima, 2002), and an initial He composition of a) 13 R_A and 50×10^{-6} cm^3STP^4He/g, b) 13 R_A and 0.35×10^{-6} cm^3STP^4He/g, c) 12 R_A and 0.42×10^{-6} cm^3STP^4He/g, and d) 8 R_A and 2.5×10^{-6} cm^3STP^4He/g. The horizontal dashed line indicates the helium isotope ratio observed in CIR glasses near the Marie Celeste FZ, i.e., $^3He/^4He = 7.2$ R_A. See section V.6.2.1 for details.

The above calculations illustrate that the helium characteristics of glasses collected south of the Marie Celeste FZ can be explained by closed-system radiogenic ^4He in-growth in an "ancient" Réunion mantle component. However, the helium concentration in this mantle reservoir must be extremely low, i.e., comparable to the lowest concentration estimates for the OIB source and even lower than estimates for the MORB source (~4-15 $\times 10^{-6}$ cm^3STP^4He/g, Porcelli et al., 2002). This may either indicate that the Réunion hotspot source is characterized by a low intrinsic helium inventory or, alternatively, that significant degassing occurred during or after ascent of the upwelling hotspot material into the shallower mantle region. We note that the strong helium depletion observed in many OIB samples has been explained by extensive near-surface degassing (e.g., Hilton et al., 1997; Hilton et al., 2000b; Gonnermann

and Mukhopadhyay, 2007); a corollary of these models is that the He content of the high-$^3He/^4He$ ratio OIB source may be very similar to the concentration in the MORB source.

V.6.2.2 Metasomatized MORB mantle

Alternatively, Nauret et al. (2006) suggested that lavas collected near the Marie Celeste FZ may be derived from fertilized MORB-like mantle, as recently suggested for enriched basalts from the mid-Atlantic Ridge south of the Kane FZ. Donnelly et al. (2004) suggested that the generation of enriched MORB (E-MORB) requires two stages: depleted upper mantle is first fertilized (i.e., enriched in incompatible trace elements) by low-degree melts at subduction zones; the metasomatized mantle is then recycled to mid-ocean ridges where it is melted to greater extent to form E-MORB. Furthermore, they concluded that convective mantle mixing occurs on a time scale of ~300 Myr, comparable to the stirring times proposed for the upper mantle by Allègre et al. (1995) on the basis of helium isotope ratios observed in MORB.

For this scenario, we assume that the E-MORB reservoir is initially characterized by a helium isotope composition expected for normal MORB mantle (8 ± 1 R_A, Graham et al., 2002). During convective transport of the fertilized mantle component to the ridge, radiogenic in-growth of ^4He lowers the $^3He/^4He$ ratio. Adopting the U-Th characteristics discussed in the previous section (i.e., [U] = 35 ppb, Th/U = 3.9, and a ^4He production ratio of 2.32×10^{-7} $cm^3STP/ppm\ U/Ma$; Ozima, 2002), we calculate a radiogenic ^4He contribution of 2.4×10^{-6} cm^3STP^4He/g in 300 Myr. Thus, for MORB mantle with an initial helium concentration of 4-15×10^{-6} cm^3STP^4He/g (Porcelli et al., 2002) and a helium isotope composition of 8 R_A, the $^3He/^4He$ ratio will decrease to 5-6.9 R_A. These values are comparable to, yet slightly lower than the ratios observed in glasses near the Marie Celeste FZ.

In summary, we conclude that the helium characteristics of the basalts sampled near the Marie Celeste FZ can be explained by both melting of an ancient Réunion hotspot mantle component and fertilized MORB mantle; in either case, the initial He isotope composition has been modified by pre-eruptive in-growth of radiogenic ^{4}He over time. We emphasize that the trace element enriched, low-^{3}He/^{4}He ratio mantle component is only observed in the vicinity of the Marie Celeste FZ; lavas erupting near the Egeria FZ, ~150 km to the south, record normal MORB-like trace element and helium characteristics. Thus, these observations call for a mechanism whereby distinct, small-scale heterogeneities can remain isolated in the ambient shallow mantle for 10s to 100s of Myr.

V.6.3 Interaction of the CIR with the Réunion hotspot

Our helium isotope survey reveals that ^{3}He/^{4}He ratios significantly greater than MORB values are observed between ~19° and 20°S along the CIR axis (Table V.2; Fig. V.4), i.e., close to the present-day intersection of the CIR and the off-axis volcanic structures. Furthermore, high He isotope values up to 12.2 R_A along the Gasitao Ridge, the Three Magi Ridges, and the east-west oriented Rodrigues Ridge show that an enriched mantle component is present beneath these volcanic ridges to the west of the CIR axis. Thus, our data appear consistent with influx of an eastward-flowing tongue of high-^{3}He/^{4}He mantle material from the Réunion hotspot into the sub-ridge mantle of the CIR, along an eastward trajectory that impinges the ridge at ~19.5°S.

Morgan (1978) suggested that in the case of off-axis hotspots, a pipe-like flow from the hotspot to the adjacent mid-ocean ridge axis may develop. As the ridge migrates away from the initially ridge-centered hotspot, it is continuously fed by preferential flow of enriched mantle material along a thermally induced sublithospheric channel (Schilling, 1985; Schilling, 1991; Kincaid et al., 1995). Flow along the channel can be sustained for hotspot-ridge

separations up to ~1400 km, whereas greater distances appear to inhibit interaction due to increased fluid viscosities caused by cooling along the flow path (Schilling, 1985; Schilling, 1991; Kincaid et al., 1995). At the intersection of the sublithospheric channel and the ridge axis, enhanced volcanism generates seamounts and islands which eventually form ridge-perpendicular volcanic ridges on the oceanic plate as it is moving away from the ridge (Morgan, 1978). In this scenario, the off-axis volcanic ridges will have the same age as the underlying crust, i.e., their ages will increase with increasing distance from the ridge axis. However, Duncan et al. (1990) noted that the entire Rodrigues Ridge formed at 8-10 Ma without a westward age progression, and the Gasitao Ridge also appears to be younger than the underlying crust (Dyment, 2001). These observations are inconsistent with the notion of generation of volcanic lineaments to the west of the CIR by a pipe-like channel supplying hotspot mantle material to the ridge axis.

Alternatively, Dyment et al. (2001) proposed that the Rodrigues Ridge, the Three Magi Ridges, and the Gasitao Ridge result from filling of tensional cracks in the lithosphere. Mittelstaedt and Ito (2005) showed that mantle upwelling at an off-axis hotspot influences the lithospheric stress field between the hotspot and the nearby spreading ridge, resulting in the formation of volcanic lineaments along areas of high integrated tension. Thus, the volcanic ridges to the west of the CIR axis do not require a pipe-like sub-lithospheric channel, and upwelling Réunion hotspot mantle may be expanding outward as a broad, pancake-like gravity current along the base of the lithosphere (Ito et al., 1997; Albers and Christensen, 2001).

Since the thickness of oceanic lithosphere increases as the square root of its age, thinning of the lithosphere towards the CIR axis may provide the gravitational driving force that causes the expanding Réunion hotspot mantle to flow ‘upslope’ towards the ridge axis (Kincaid et al., 1995; Kincaid et al., 1996; Sleep, 1996). In this case, shallowing of the base of the lithosphere, combined with additional thinning induced by tension, will trigger

decompression melting along the flow path of the hotspot material (Sleep, 1996). Consequently, continuous melt extraction processes are expected to progressively deplete the expanding hotspot mantle material in incompatible elements, generating geochemical gradients (i.e., a decrease in La/Sm, $^{87}Sr/^{86}Sr$, and $^{206}Pb/^{204}Pb$ ratios, as well as an increase in $^{143}Nd/^{144}Nd$) along the flow path towards the sub-ridge region, as observed along the Easter-Salas y Gomez Seamount Chain for example (Pan and Batiza, 1998; Kingsley and Schilling, 1998; Cheng et al., 1999). Mellor (1998) showed that basalts from the Rodrigues Ridge record similar gradients in Sr and Nd isotope ratios, as well as a decrease in La/Sm ratios from 6.74 to 0.44 with increasing distance from Réunion Island, consistent with progressive depletion of the hotspot component by melting en route to the CIR. However, the geochemical gradients along the Rodrigues Ridge can also be explained by enhanced entrainment of a depleted mantle component along the flow path. In this respect, Nauret et al. (2006) noted that the trace element and isotope systematics of basalts from the Gasitao Ridge require mixing of Réunion hotspot material with MORB-like mantle (Nauret et al., 2006). Furthermore, Intermediate and Younger Series lavas from Mauritius and Rodrigues show $^{3}He/^{4}He$ ratios of 6.5-8.4 R_A (Hanyu et al., 2001), suggesting that these late-stage lavas were derived from a source that is dominated by a MORB-like mantle component.

Our study reveals that trace element ratios and $^{3}He/^{4}He$ values of glasses recovered along the flow path of Réunion mantle, i.e., along the Rodrigues Ridge, the Three Magi Ridges, and the Gasitao Ridge, are variable. Furthermore, $^{3}He/^{4}He$ ratios as high as 12.2 R_A at the Gasitao Ridge, ~1000 km away from the Réunion hotspot, show that some domains of the expanding hotspot material must retain their intrinsic helium isotope characteristics. We propose that the observed variations in helium isotope ratios and trace element (La/Sm) signatures can be explained by binary mixing between high-degree partial melts derived from the high-$^{3}He/^{4}He$ Réunion mantle component, and small-degree partial melts from a MORB-

like mantle reservoir. High-degree partial melting of the hotspot component, progressively depleted along the flow path by melt extraction processes, results in lower trace element ratios (i.e., $(La/Sm)_N$) than generally observed for an enriched mantle source. In contrast, very small degrees of partial melting of an isotopically MORB-like mantle endmember produces basalts with $^3He/^4He$ values of 8 ± 1 R_A and an excess of incompatible elements, i.e., $(La/Sm)_N$ ratios > 0.7. Depending on the relative proportions of each mantle component sampled by the erupting lavas, the $^3He/^4He$ ratios will encompass a range of values, between the helium isotope composition of lavas from Réunion Island and normal MORB.

V.7 Conclusions

Submarine basalts recovered from the CIR segment bounded by the Marie Celeste and the Egeria fracture zones record a range in helium isotope composition. Low $^3He/^4He$ ratios observed immediately south of the Marie Celeste FZ can be explained by closed-system radiogenic ^4He in-growth in an "ancient" Réunion mantle component or, alternatively, fertilized MORB mantle. In contrast, high $^3He/^4He$ ratios (i.e., up to 12.2 R_A) observed in basaltic glasses collected between ~19° and 20°S along the CIR axis, as well as along the adjacent Gasitao Ridge, Three Magi Ridges, and Rodrigues Ridge are consistent with lateral flow of hotspot mantle from Réunion towards the CIR, over a distance of ~1100 km. The helium and trace element characteristics of basalts from the volcanic ridges to the west of the CIR axis can be explained by variable degrees of melting and binary mixing of Réunion hotspot mantle and an isotopically MORB-like mantle component.

V.8 Acknowledgments

We would like to thank Captain T. Desjardins and the crew of the R/V *Revelle* for their dedicated support at sea. We thank B. Murton for major and trace element analyses of submarine glasses collected during the KNOX11RR cruise, and we are grateful to Scott Cornelius (Washington State University) for major element analyses of olivine separates from the Mascarene Islands. The KNOX11RR cruise was funded by UC Ship Funds, and work at the Fluids and Volatiles Laboratory was supported by NSF grant OCE-0726573.

V.9 Appendix

V.9.1 Major element data of submarine basalts

Sample ID	SiO_2 (%)	TiO_2 (%)	Al_2O_3 (%)	Fe_2O_3 (%)	MnO (%)	MgO (%)	CaO (%)	Na_2O (%)	K_2O (%)	P_2O_5 (%)	total (%)
D1-1	50.76	1.23	15.07	10.00	0.17	7.66	11.18	2.87	0.25	0.14	99.33
D2-1	n.d.	n.d.	n.d.	n.d.	n.d.	n.d.	n.d.	n.d.	n.d.	n.d.	n.d.
D3-3	n.d.	n.d.	n.d.	n.d.	n.d.	n.d.	n.d.	n.d.	n.d.	n.d.	n.d.
D6-1	n.d.	n.d.	n.d.	n.d.	n.d.	n.d.	n.d.	n.d.	n.d.	n.d.	n.d.
D8-2	50.06	1.42	16.75	9.58	0.16	6.95	11.07	2.89	0.33	0.17	99.37
D9-1	50.35	1.55	15.52	10.00	0.17	7.17	10.97	2.93	0.48	0.20	99.35
D10-2	49.90	0.92	17.37	8.91	0.15	7.45	12.58	2.12	0.04	0.07	99.51
D11-2	n.d.	n.d.	n.d.	n.d.	n.d.	n.d.	n.d.	n.d.	n.d.	n.d.	n.d.
D12-2	49.00	0.66	18.62	7.57	0.13	7.78	13.30	2.03	0.04	0.05	99.17
D13-1	50.68	1.05	17.38	9.42	0.16	7.74	12.39	2.21	0.05	0.09	101.16
D14-1	49.21	1.04	16.68	9.21	0.15	7.56	12.14	2.27	0.11	0.09	98.44
D15-1	50.55	1.12	15.65	10.30	0.17	8.40	11.82	2.43	0.09	0.09	100.62
D17-3	49.72	1.18	14.81	10.20	0.18	7.94	11.92	2.60	0.20	0.12	98.86
D18-2	48.66	0.86	17.18	9.08	0.18	9.87	11.20	2.28	0.05	0.06	99.41
D19-2	50.41	0.95	15.78	9.67	0.17	8.68	12.43	2.24	0.05	0.07	100.44
D20-5	46.50	0.90	14.68	10.22	0.18	14.38	10.24	2.45	0.04	0.05	99.66
D22-1	47.02	1.12	15.56	10.54	0.48	11.94	10.34	2.56	0.16	0.11	99.79
D24-6	n.d.	n.d.	n.d.	n.d.	n.d.	n.d.	n.d.	n.d.	n.d.	n.d.	n.d.
D25-2	n.d.	n.d.	n.d.	n.d.	n.d.	n.d.	n.d.	n.d.	n.d.	n.d.	n.d.
D26.2	45.76	0.91	16.21	11.34	0.21	11.65	10.14	2.48	0.08	0.06	98.84
D26-3	44.67	0.82	14.60	11.02	0.29	14.43	9.02	2.21	0.08	0.06	97.20
D29-1	n.d.	n.d.	n.d.	n.d.	n.d.	n.d.	n.d.	n.d.	n.d.	n.d.	n.d.
D30-3	n.d.	n.d.	n.d.	n.d.	n.d.	n.d.	n.d.	n.d.	n.d.	n.d.	n.d.
D34.1	49.05	1.06	15.85	10.35	0.17	8.74	12.35	2.41	0.11	0.08	100.17
D37-2	n.d.	n.d.	n.d.	n.d.	n.d.	n.d.	n.d.	n.d.	n.d.	n.d.	n.d.

V.9.1 Trace element data of submarine basalts

Sample ID	Li	Rb	Sr	Y	Zr	Nb	Cs	Ba	La	Ce	Pr	Nd	Sm	Eu	Gd	Tb	Dy	Ho	Er	Tm	Yb	Lu	Hf	Ta	Pb	Th	U
	ppm	ppm	ppm	ppm	ppm	ppm	ppm	ppm	ppm	ppm	ppm	ppm	ppm	ppm	ppm	ppm	ppm	ppm	ppm	ppm	ppm	ppm	ppm	ppm	ppm	ppm	ppm
D1-1	5.23	4.00	156.6	28.8	97.4	6.26	0.05	49.1	5.56	14.09	2.10	10.26	3.11	1.17	4.08	0.73	4.75	0.99	2.88	0.43	2.83	0.42	2.34	0.40	0.89	0.55	0.16
D2-1	3.69	3.38	117.1	22.6	130.5	9.36	0.04	35.4	4.34	11.00	1.62	7.89	2.40	0.88	2.85	0.54	3.58	0.78	2.22	0.34	2.11	0.32	3.19	0.63	0.54	0.42	0.11
D3-3	3.63	4.73	127.0	22.8	155.3	14.02	0.06	48.6	5.79	13.97	1.97	9.23	2.67	0.95	3.05	0.57	3.73	0.79	2.26	0.34	2.13	0.32	3.73	0.96	0.59	0.62	0.17
D6-1	2.19	3.30	182.0	19.9	105.3	8.03	0.05	52.8	5.71	14.94	2.12	10.22	2.99	1.12	3.37	0.62	4.06	0.86	2.41	0.36	2.18	0.32	2.62	0.58	0.66	0.50	0.16
D8-2	6.05	7.44	178.3	34.1	126.2	8.01	0.10	68.9	8.01	19.81	2.89	13.75	4.09	1.43	5.06	0.89	5.65	1.19	3.34	0.51	3.28	0.48	3.05	0.28	1.10	0.90	0.24
D9-1	7.60	16.35	231.5	34.0	138.5	12.62	0.31	116.9	11.40	26.51	3.67	16.58	4.50	1.55	5.34	0.92	5.74	1.19	3.33	0.51	3.27	0.48	3.31	0.79	1.69	1.38	0.35
D10-2	4.65	0.50	90.4	26.1	53.9	1.51	0.01	8.3	1.85	6.07	1.10	6.07	2.36	0.90	3.35	0.64	4.24	0.91	2.69	0.41	2.69	0.40	1.48	0.06	0.61	0.12	0.04
D11-2	n.d.	n.d.	n.d.	n.d.	n.d.	n.d.	n.d.	n.d.	n.d.	n.d.	n.d.	n.d.	n.d.	n.d.	n.d.	n.d.	n.d.	n.d.	n.d.	n.d.	n.d.	n.d.	n.d.	n.d.	n.d.	n.d.	n.d.
D12-2	4.05	0.40	96.5	18.2	29.0	1.45	0.01	8.7	1.36	4.24	0.75	4.17	1.58	0.68	2.26	0.44	2.92	0.65	1.93	0.28	1.89	0.28	0.77	0.06	1.38	0.10	0.04
D13-1	5.05	0.60	90.8	28.4	81.9	1.88	0.01	10.2	2.15	6.94	1.25	6.94	2.61	0.98	3.73	0.70	4.67	1.02	2.95	0.45	2.96	0.44	2.19	0.10	0.54	0.15	0.06
D14-1	4.89	1.62	108.8	26.5	74.4	3.27	0.02	22.6	2.96	8.42	1.39	7.34	2.55	0.97	3.57	0.66	4.40	0.94	2.74	0.42	2.77	0.41	1.95	0.20	0.51	0.26	0.08
D15-1	4.42	0.98	109.7	29.6	79.5	2.53	0.01	15.6	2.79	8.40	1.45	7.78	2.83	1.06	3.91	0.72	4.85	1.04	3.00	0.47	3.05	0.45	2.04	0.17	0.57	0.20	0.07
D17-3	4.84	2.86	146.4	28.3	95.6	5.14	0.03	38.5	4.52	11.91	1.85	9.24	2.97	1.13	3.95	0.72	4.70	1.00	2.86	0.44	2.85	0.42	2.30	0.35	0.68	0.40	0.13
D18-2	7.63	0.91	170.3	26.5	74.4	2.13	0.02	17.3	3.82	15.91	1.51	7.59	2.52	0.97	3.43	0.64	4.28	0.94	2.78	0.44	2.91	0.44	1.75	0.39	13.34	0.37	0.16
D19-2	5.37	0.80	91.0	27.4	60.8	2.01	0.01	11.7	1.93	5.97	1.06	6.03	2.35	0.93	3.48	0.65	4.37	0.95	2.76	0.42	2.78	0.42	1.70	0.09	0.55	0.15	0.05
D20-5	4.93	0.31	114.1	26.0	68.7	1.41	0.01	7.9	1.98	6.81	1.21	6.73	2.50	1.01	3.54	0.65	4.28	0.91	2.64	0.40	2.62	0.39	1.79	0.07	1.75	0.13	0.05
D22-1	n.d.	n.d.	n.d.	n.d.	n.d.	n.d.	n.d.	n.d.	n.d.	n.d.	n.d.	n.d.	n.d.	n.d.	n.d.	n.d.	n.d.	n.d.	n.d.	n.d.	n.d.	n.d.	n.d.	n.d.	n.d.	n.d.	n.d.
D24-6	2.12	0.18	73.0	13.7	66.5	0.71	0.00	1.1	0.69	2.43	0.46	2.63	1.01	0.44	1.36	0.29	2.07	0.47	1.41	0.22	1.45	0.23	1.67	0.06	0.11	0.03	0.01
D25-2	2.07	0.75	139.7	13.5	135.1	3.61	0.01	8.5	1.57	4.75	0.80	4.20	1.39	0.59	1.67	0.32	2.17	0.48	1.35	0.21	1.31	0.20	3.17	0.25	0.20	0.09	0.03
D26.2	5.93	1.30	153.4	18.7	49.2	1.17	0.02	8.8	1.92	7.19	0.91	4.72	1.60	0.65	2.25	0.42	2.85	0.63	1.87	0.30	2.02	0.31	1.15	0.11	3.83	0.16	0.05
D26-3	n.d.	n.d.	n.d.	n.d.	n.d.	n.d.	n.d.	n.d.	n.d.	n.d.	n.d.	n.d.	n.d.	n.d.	n.d.	n.d.	n.d.	n.d.	n.d.	n.d.	n.d.	n.d.	n.d.	n.d.	n.d.	n.d.	n.d.
D29-1	0.94	1.89	129.2	6.1	138.3	11.29	0.03	21.8	1.92	4.26	0.58	2.64	0.72	0.35	0.83	0.15	1.00	0.21	0.61	0.09	0.58	0.09	3.27	0.58	0.16	0.30	0.06
D30-3	2.47	0.34	85.0	15.2	110.7	1.89	0.01	3.2	1.34	4.38	0.76	4.15	1.43	0.59	1.80	0.36	2.45	0.53	1.54	0.24	1.48	0.23	2.70	0.15	0.18	0.06	0.02
D34.1	4.80	1.38	112.9	24.9	76.9	2.84	0.02	18.1	2.46	7.58	1.26	6.81	2.42	0.96	3.38	0.62	4.11	0.88	2.56	0.38	2.49	0.37	2.00	0.11	1.47	0.21	0.08
D37-2	4.13	2.37	76.0	22.6	123.0	7.39	0.04	27.8	3.02	7.73	1.21	6.22	2.09	0.77	2.65	0.52	3.53	0.78	2.26	0.35	2.21	0.34	3.24	0.48	0.34	0.30	0.07

Chapter VI Concluding remarks

In this dissertation, I studied the origin, transport and behavior of volatiles (noble gases and CO_2) at four different geologic settings – a) the SAFZ, a transform plate boundary, b) the Costa Rica margin, a convergent plate boundary, c) Iceland, a ridge-centered hotspot, and d) the Central Indian Ridge, a mid-ocean ridge segment near an off-axis hotspot. In this chapter, I summarize the main findings and conclusions drawn from the work presented in the preceding chapters, and I conclude with a discussion of future research directions in noble gas geochemistry.

Our study of submarine cold seep fluids at Extrovert Cliff in Monterey Bay (Chapter II) demonstrates that 1) the CAT meter and OTIS, with the addition of copper sampling coils, are capable of capturing and preserving fluids for post-recovery analyses of dissolved volatiles, and 2) we are able to produce a near-continuous volatile record over prolonged deployments, up to 18 weeks or more. Thus, the modified instrumentation has the potential to revolutionize studies relying on detailed, quasi-continuous time series records of dissolved volatile variations. In Monterey Bay, the helium and neon characteristics of the sampled cold seep fluids are highly variable on time scales of only a few hours due to the combined effects of noble gas stripping by a hydrocarbon phase (methane or oil) in the subsurface and an episodic input of mantle-derived helium. We conclude that the active strike-slip faults and subsidiary cross faults that cut across Monterey Bay provide the conduits for mantle fluids to traverse the crust and impart elevated $^3He/^4He$ ratios (up to 2.3 R_A) to groundwaters that are dominated by air-derived noble gases (i.e., from equilibration with the atmosphere and from entrainment of excess air in the recharge region).

In Chapter III, we discussed the He-CO_2 isotope and abundance systematics of submarine seep fluids sampled at the Costa Rica fore-arc. Fluids collected at three seep sites

(Mound 11, Mound 12, and Jaco Scar) record a small contribution of mantle helium, possibly derived from the lithospheric mantle of the subducting Cocos Plate or from oceanic igneous basement rocks related to the Galápagos hotspot or the Caribbean Large Igneous Province. At Mound 12, anaerobic oxidation of ascending dissolved methane generates DIC with $\delta^{13}C_{\sum CO2}$ values between -68‰ to -60‰. In contrast, at the more active Mound 11, higher $\delta^{13}C_{\sum CO2}$ values are consistent with a large contribution of DIC originating from deep methanogenesis, only slightly diluted by DIC derived from anaerobic oxidation of methane and/or oxidation of marine organic matter. In addition, the quasi-continuous time series records reveal that the carbon emissions and fluid flow rates fluctuate remarkably over the 12-month sampling period. In spite of the significant spatial and temporal variability, we conclude that the total extrapolated carbon output (CO_2 plus methane) from mound structures at the Costa Rica fore-arc is significantly lower than the carbon that is potentially available by subducted sedimentary input via the trench. This suggests that the loss of slab-derived carbon in the fore-arc region is a negligible part of the carbon mass balance for the Costa Rica subduction zone, and most of the carbon being subducted in Costa Rica must be recycled to the (deeper) mantle, i.e., the zone of arc magma generation and beyond.

Chapter IV was directed at the noble gas isotope and abundance characteristics of Icelandic subglacial lavas and geothermal fluids. Our study confirmed that geothermal fluids, subglacial glasses, and phenocrysts are characterized by a wide range in helium isotope ratios, encompassing typical MORB-like ratios through values as high as 36.8 R_A. While neon in all geothermal fluids is dominated by an atmospheric component, samples from the northwest peninsula (Vestfirðir) show a small excess of nucleogenic ^{21}Ne, likely produced in-situ and released to circulating fluids. In contrast, geothermal fluids from the neovolcanic zones show evidence of a contribution of mantle-derived neon. The decoupling of the He and Ne isotope

systematics observed in subglacial glasses is inferred to be the result of the overlapping effects of helium depletion relative to neon (and argon) in the high-$^3He/^4He$ ratio parental melt, followed by binary mixing between the primordial mantle component and a depleted/degassed MORB-like endmember at shallower depths, and extensive open-system equilibrium degassing. Helium may be depleted relative to neon in high-$^3He/^4He$ ratio parental melts due to either more compatible behavior during low-degree partial melting or more extensive diffusive loss relative to the heavier noble gases. A corollary of these conclusions is that the primary He content of the high-$^3He/^4He$ ratio source may be very similar to the concentration in the MORB source; thus, the distinct volatile concentrations and elemental ratios in MORB and OIB samples are mainly a reflection of physical processes that can fractionate one volatile element from another.

The final study (Chapter IV) targeted a segment of the Central Indian Ridge near the Réunion hotspot. Our helium isotope survey shows that basalts from the CIR axis and the adjacent Gasitao Ridge, Three Magi Ridges, and Rodrigues Ridge record a range in helium isotope compositions, between values expected for depleted MORB mantle and the helium isotope composition of lavas from Réunion Island. Low $^3He/^4He$ values (< 8 R_A) immediately south of the Marie Celeste Fracture Zone can be explained by closed-system radiogenic ^4He in-growth in 1) an "ancient" Réunion hotspot mantle component, entrained into the sub-ridge mantle when the migrating CIR passed over the hotspot at ~34 Ma, or, alternatively, 2) trace element enriched MORB mantle. In contrast, high $^3He/^4He$ ratios (up to 12.2 R_A) observed in basaltic glasses collected between ~19° and 20°S along the CIR axis, as well as along the off-axis volcanic ridges, show that Réunion hotspot material flows eastward towards the CIR, over a distance of ~1100 km, along a trajectory that impinges the CIR axis at ~19.5°S.

As we move forward towards a better understanding of the origin and geochemical behavior of the noble gases, several issues appear particularly important to address in future analytical, experimental and modeling efforts. For example, improved knowledge about the partitioning behavior of noble gases between melt and the different dominant mantle minerals (e.g., olivine and pyroxene), as well as between silicates and metal, is required to model noble gas elemental fractionation during partial melting and during core formation. Experimental determinations of crystal-melt partition coefficients for noble gases are hampered by large analytical errors, and there is a significant discrepancy in values published by different authors to date (Hiyagon and Ozima, 1986; Marty and Lussiez, 1993; Parman et al., 2005; Heber et al., 2007; Watson et al., 2007). More partition coefficient data is essential if realistic models of the distribution and transport of mantle noble gases are to be constructed.

As discussed in Chapter IV, most basaltic glasses (MORB and OIB) contain both large vesicles, carrying air-derived noble gases, and small vesicles that bear mantle noble gases. Volatiles released by conventional crushing or melting methods represent an average composition of several vesicles in a sample, and thus, are a mixture of atmospheric and mantle-derived volatiles trapped at different stages in the evolution of a melt. New analytical techniques, such as the recently developed 'bubble-by-bubble' laser ablation method (Colin et al., 2009), are now capable of releasing volatiles from select individual vesicles. Thus, the vesicles that preserve the least fractionated volatiles can be identified, and the pristine, unfractionated volatile composition of parental magmas can be better constrained. We expect future refinements and developments in analytical techniques to provide new insights into the primary volatile inventory of mantle melts as well as of different mantle reservoirs.

Advances in sample processing, measurement capabilities and modeling are critical to answer some of the fundamental questions regarding noble gases that remain to be explored. Some of these issues are:

1) Origin of noble gases in the solid Earth. As discussed in Chapter IV, there is an on-going debate on the origin of a solar-like neon component in Earth's mantle. There are two potential sources for this neon: i) solar nebula gas (Benkert et al., 1993; Kallenbach et al., 1997; Ballentine et al., 2001) or ii) implanted solar wind, called Ne-B found in gas-rich meteorites and in lunar soils (Black, 1972; Trieloff et al., 2000; 2002; Ballentine et al., 2005). Identifying which of these sources provides the primordial 'solar' neon component in Earth's mantle has profound implications for the formation and early evolution of our planet. The first scenario invokes capture of a massive early atmosphere directly from the solar nebula by magma ocean equilibration (Harper and Jacobsen, 1996), consistent with accretion of nearly full-sized planets before dissipation of the accretion disk and loss of the nebular gas. In contrast, the occurrence of an implanted solar wind component inside a large planet like Earth would suggest that the primordial noble gas signatures in the deep Earth were acquired from accreting meteorites that had been heavily irradiated by solar ions prior to their assembly to form the Earth. Such intense irradiation is likely to have occurred during an active phase of the early Sun, and only after the accretion disk had been swept clear, i.e., had lost most of its gaseous or volatile components (Trieloff et al., 2000).

2) Noble gas concentrations in different mantle reservoirs. It has been difficult to determine the volatile content of undegassed parental melts; thus, volatile abundances in different mantle domains are poorly known. While it is often assumed that noble

gas abundances in the OIB source are higher than in the MORB source, the primary noble gas inventory of the OIB reservoir remains rather unconstrained (e.g., van Keken and Ballentine, 1998; Porcelli and Ballentine, 2002).

3) Preservation of high-$^3He/^4He$ ratio mantle domains. The high $^3He/^4He$ ratios observed in OIB implies that a primitive noble gas component is still present in Earth's mantle. There have been various suggestions for isolating and preserving a high-$^3He/^4He$ ratio mantle reservoir, including storage within the transition zone, layers or blobs within the deep mantle, the D" layer or the core (Kellogg et al., 1999; Porcelli and Halliday, 2001; Allègre and Moreira, 2004; Trieloff and Kunz, 2005). Alternatively, Anderson (1993) suggested that subduction of interplanetary dust particles within seafloor sediments is the source of mantle ^3He. Further work is required to demonstrate that a primitive component is present in the mantle and to identify the reservoir of primordial noble gases in Earth's mantle.

As a final remark, we point out that current geophysical models of mantle convection find it impossible to keep a large primitive noble gas reservoir isolated in the mantle over Earth history (e.g., van der Hilst et al., 1997; van Keken and Ballentine, 1998). If indeed certain domains of the mantle have remained largely undegassed over 4.6 Ga, regardless of whole mantle convection, geophysical debates regarding the feasibility of maintaining chemically distinct blobs or layers in the mantle need resolution.

References

Aeschbach-Hertig, W., F. Peeters, U. Beyerle, and R. Kipfer (1999), Interpretation of dissolved atmospheric noble gases in natural waters, *Water Resour. Res.*, **35**(9), 2779-2792, doi:10.1029/1999WR900130.

Aeschbach-Hertig, W., F. Peeters, U. Beyerle, and R. Kipfer (2000), Palaeotemperature reconstruction from noble gases in ground water taking into account equilibration with entrapped air, *Nature*, **405**(6790), 1040-1044, doi:10.1038/35016542.

Albers M. and Christensen U. R. (2001) Channeling of plume flow beneath mid-ocean ridges. *Earth Planet. Sci. Lett.* **187**(1-2), 207-220.

Allègre C. J. and Moreira M. (2004) Rare gas systematics and the origin of oceanic islands: the key role of entrainment at the 670 km boundary layer, *Earth Planet. Sci. Lett.,* **228**(1-2), 85-92, doi:10.1016/j.epsl.2004.07.041.

Allègre C. J., Staudacher T., and Sarda P. (1987) Rare gas systematics: formation of the atmosphere, evolution and structure of the Earth's mantle, *Earth Planet. Sci. Lett.,* **81**(2-3), 127-150, doi:10.1016/0012-821X(87)90151-8.

Allègre C. J., Moreira M., and Staudacher T. (1995) $^{4}He/^{3}He$ dispersion and mantle convection. *Geophys. Res. Lett.* **22**(17), 2325-2328.

Alt, J.C., and D.A.H. Teagle (1999), The uptake of carbon during alteration of ocean crust, *Geochim. Cosmochim. Acta*, **63**(10), 1527-1535, doi:10.1016/S0016-7037(99)00123-4.

Alvarado, G.E., P. Denyer, and C.W. Sinton (1997), The 89 Ma Tortugal komatiitic suite, Costa Rica: Implications for a common geological origin of the Caribbean and Eastern Pacific region from a mantle plume, *Geology*, **25**(5), 439-442, doi:10.1130/0091-7613(1997)025 <0439:TMTKSC>2.3.CO;2.

Anderson D. L. (1993) Helium-3 from the mantle: primordial signal or cosmic dust?, *Science,* **261**, 170-176, doi:10.1126/science.261.5118.170.

Anderson D. L. (1998) A model to explain the various paradoxes associated with mantle noble gas geochemistry, *Proc. Natl. Acad. Sci.* **95**, 9087-9092.

Anderson, R.S., D.L. Orange, and S.Y. Schwartz (1990) Implications of the October 17th 1989 Loma Prieta earthquake for the emergence of marine terraces along the Santa Cruz coast, and for long term evolution of the Santa Cruz Mountains, in *Geology and tectonics of coastal California, San Francisco to Monterey*, edited by R.E. Garrison, pp. 205-224, Pac. Sect., Am. Assoc. of Pet. Geol., Bakersfield, Calif.

Andrews, J.N. (1985), The Isotopic composition of radiogenic helium and its use to study groundwater movement in confined aquifers, *Chem. Geol.*, **49**(1-3), 339-351, doi:10.1016/0009-2541(85)90166-4.

Andrews J. N. and Lee D. J. (1979) Inert gases in groundwater from the Bunter Sandstone of England as indicators of age and paleoclimatic trends, *J. Hydrol.* **41**(3-4), 233-252, 10.1016/0022-1694(79)90064-7.

Andrews, J.N., and Kay R.L.F. (1982), Natural production of tritium in permeable rocks, *Nature*, **298**(5872), 361-363, doi:10.1038/298361a0.

Ballentine C. J. (1997) Resolving the mantle He/Ne and crustal $^{21}Ne/^{22}Ne$ in well gases. *Earth Planet. Sci. Lett.* **152**(1-4), 233-249.

Ballentine C. J. and O'Nions R. K. (1992) The nature of mantle neon contributions to Vienna Basin hydrocarbon reservoirs. *Earth Planet. Sci. Lett.* **113**(4), 553-567.

Ballentine C. J. and Barfod D. N. (2000) The origin of air-like noble gases in MORB and OIB. *Earth Planet. Sci. Lett.* **180**(1-2), 39-48.

Ballentine C. J., Porcelli D., and Wieler R. (2001) Noble gases in mantle plumes, *Science,* **291**(5512), 2269, doi:10.1126/science.291.5512.2269a.

Ballentine, C.J., R. Burgess, and B. Marty (2002), Tracing fluid origin, transport and interaction in the crust, in *Noble Gases in Geochemistry and Cosmochemistry, Rev. in Mineral. and Geochem.,* vol. 47, edited by D. Porcelli, C. Ballentine, and R. Wieler, pp. 539-614, Mineral. Soc. of Am., Washington, D.C.

Ballentine C. J., Marty B., Lollar B. S., and Cassidy M. (2005) Neon isotopes constrain convection and volatile origin in the Earth's mantle, *Nature,* **433**(7021), 33-38, doi:10.1038/nature03182.

Barry, J.P., H.G. Greene, D.L. Orange, C.H. Baxter, B.H. Robison, R.E. Kochevar, J.W. Nybakken, D.L. Reed, C.M. McHugh (1996), Biologic and geologic characteristics of cold seeps in Monterey Bay, California, *Deep-Sea Res. Part I*, **43**, 1739-1762, doi:10.1016/S0967-0637(96)00075-1.

Barry, J.P., R.E. Kochevar, and C.H. Baxter (1997), The influence of pore-water chemistry and physiology on the distribution of vesicomyid clams at cold seeps in Monterey Bay: Implications for patterns of chemosynthetic community organization, *Limnol. Oceanogr.*, **42**(2), 318-328.

Barry, P. H., D. R. Hilton, M. D. Tryon, K. M. Brown, and J. T. Kulongoski (2009), A new syringe pump apparatus for the retrieval and temporal analysis of helium in groundwaters and geothermal fluids, *Geochem. Geophys. Geosyst.*, **10**, Q05004, doi:10.1029/2009GC002422.

Benkert J. P., Baur H., Signer P., and Wieler R. (1993) He, Ne, and Ar from the Solar-Wind and Solar Energetic Particles in Lunar Ilmenites and Pyroxenes, *J. Geophys. Res.,* **98**(E7), 13,147–13,162.

Bijwaard H. and Spakman W. (1999) Tomographic evidence for a narrow whole mantle plume below Iceland. *Earth Planet. Sci. Lett.* **166**(3-4), 121-126.

Black D. C. (1972) On the origins of trapped helium, neon and argon isotopic variations in meteorites - I. Gas-rich meteorites, lunar soil and breccia, *Geochim. Cosmochim. Acta,* **36**(3), 347-375, doi:10.1016/0016-7037(72)90028-2.

Boetius, A., K. Ravenschlag, C.J. Schubert, D. Rickert, F. Widdel, A. Gieseke, R. Amann, B.B. Jorgensen, U. Witte, and O. Pfannkuche (2000), A marine microbial consortium apparently mediating anaerobic oxidation of methane, *Nature*, **407**(6804), 623-626, doi:10.1038/35036572.

Bohrmann, G., K. Heeschen, C. Jung, W. Weinrebe, B. Baranov, B. Cailleau, R. Heath, V. Huehnerbach, M. Hort, D. Masson, and I. Trummer (2002), Widespread fluid expulsion along the seafloor of the Costa Rica convergent margin, *Terra Nova*, **14**(2), 69-79, doi:10.1046/j.1365-3121.2002.00400.x.

Bottinga Y. and Javoy M. (1990) MORB degassing: bubble growth and ascent. *Chem. Geol.* **81**(4), 255-270.

Bottomley D. J., Ross J. D., and Clarke W. B. (1984) Helium and neon isotope geochemistry of some ground waters from the Canadian Precambrian Shield. *Geochim. Cosmochim. Ac.* **48**(10), 1973-1985.

Brandon A. D., Graham D. W., Waight T., and Gautason B. (2007) ^{186}Os and ^{187}Os enrichments and high-^{3}He/^{4}He sources in the Earth's mantle: Evidence from Icelandic picrites. *Geochim. Cosmochim. Acta* **71**(18), 4570-4591.

Breddam K., Kurz M. D., and Storey M. (2000) Mapping out the conduit of the Iceland mantle plume with helium isotopes, *Earth Planet. Sci. Lett.,* **176**(1), 45-55, doi:10.1016/S0012-821X(99)00313-1 .

Brennwald, M.S., M. Hofer, F. Peeters, W. Aeschbach-Hertig, K. Strassmann, R. Kipfer, and D.M. Imboden (2003), Analysis of dissolved noble gases in the porewater of lacustrine sediments, *Limnol. Oceanogr. Methods,* **1**, 51-62.

Brennwald, M.S., R. Kipfer, and D.M. Imboden (2005), Release of gas bubbles from lake sediment traced by noble gas isotopes in the sediment pore water, *Earth Planet. Sci. Lett.*, **235**(1-2), 31-44, doi:10.1016/j.epsl.2005.03.004.

Bruno L. A., Baur H., Graf T., Schlüchter C., Signer P., and Wieler R. (1997) Dating of Sirius group tillites in the Antarctic Dry Valleys with cosmogenic ^{3}He and ^{21}Ne, *Earth Planet. Sci. Lett.* **147**(1-4), 37-54, doi:10.1016/S0012-821X(97)00003-4.

Burnard P. G., Stuart F. M., Turner G., and Oskarsson N. (1994) Air contamination of basaltic magmas: Implications for high ^{3}He/^{4}He mantle Ar isotopic composition. *J. Geophys. Res.-Sol. Ea.* **99**(B9), 17709-17715.

Burnard P., Graham D., and Turner G. (1997) Vesicle-specific noble gas analyses of "popping rock": Implications for primordial noble gases in Earth, *Science* **276**(5312), 568-571, doi: 10.1126/science.276.5312.568.

Burnard P. G., Graham D. W., and Farley K. A. (2002) Mechanisms of magmatic gas loss along the Southeast Indian Ridge and the Amsterdam-St. Paul Plateau. *Earth Planet. Sci. Lett.* **203**(1), 131-148.

Byrne, D.E., D.M. Davis, and L.R. Sykes (1988), Loci and maximum size of thrust earthquakes and the mechanics of the shallow region of subduction zones, *Tectonics*, **7**(4), 833-857.

Cerling T. E. and Craig H. (1994) Geomorphology and *in situ* cosmogenic isotopes, *Ann. Rev. Earth Planet. Sci.* **31**, 369-385, doi:10.1146/annurev.ea.22.050194.001421.

Chan, L.H., and M. Kastner (2000), Lithium isotopic compositions of pore fluids and sediments in the Costa Rica subduction zone: Implications for fluid processes and sediment contribution to the arc volcanoes, *Earth Planet. Sci. Lett.*, **183**(1-2), 275-290, doi:10.1016/S0012-821X(00)00275-2.

Chauvel C. and Hémond C. (2000) Melting of a complete section of recycled oceanic crust: Trace element and Pb isotopic evidence from Iceland. *Geochem. Geophys. Geosyst.* **1**(2), 1001, doi:10.1029/1999GC000002.

Cheng Q. C., Macdougall J. D., and Zhu P. (1999) Isotopic constraints on the Easter Seamount Chain source. *Contrib. Mineral. Petr.* **135**(2-3), 225-233.

Chevallier L. and Bachelery P. (1981) Evolution structurale du volcan actif du Piton de la Fournaise, Ile de la Réunion, Océan Indien occidental. Structural evolution of the Piton de la Fournaise active volcano, Réunion, western Indian Ocean. *Bulletin Volcanologique* **44**(4), 723-741.

Chevallier L. and Vatin-Perignon N. (1982) Volcano-structural evolution of Piton des Neiges, Reunion Island, Indian Ocean. *Bulletin Volcanologique* **45**(4), 285-298.

Colin A., Burnard P., and Marty B. (2009) A study of degassing at mid-oceanic ridges by bubble-by-bubble analyses, DINGUE Noble Gas workshop, Nancy, France, Abstract.

Condomines M., Grönvold K., Hooker P. J., Muehlenbachs K., O'Nions R. K., Oskarsson N., and Oxburgh E. R. (1983) Helium, oxygen, strontium and neodymium isotopic relationships in Icelandic volcanics, *Earth Planet. Sci. Lett.,* **66**(1-3), 125-136, doi:10.1016/0012-821X(83)90131-0.

Craig H., J.E. Lupton (1976) Primordial neon, helium, and hydrogen in oceanic basalts, *Earth Planet. Sci. Lett.*, **31**(3), 369-385.

Craig H., Marti K., and Wiens R. (1993) A static mass spectrometer with triple collection for nitrogen and neon isotopes. *Tech. Rep.* 93-11, Scripps Inst. Oceanogr. (San Diego), 37pp.

Curiale, J.A., D. Cameron, and D.V. Davis (1985), Biological marker distribution and significance in oils and rocks of the Monterey Formation, California, *Geochim. Cosmochim. Acta*, **49**(1), 271-288, doi:10.1016/0016-7037(85)90210-8.

Cussler, E. L. (1984), Diffusion: Mass transfer in fluid systems, 525 pp., Cambridge Univ. Press, Cambridge, U.K.

Darbyshire F. A., White R. S., and Priestley K. F. (2000) Structure of the crust and uppermost mantle of Iceland from a combined seismic and gravity study. *Earth Planet. Sci. Lett.* **181**(3), 409-428.

de Leeuw G. A. M. (2007) The noble gas and carbon systematics of divergent, convergent and strike-slip plate boundaries: Examples from the Reykjanes Ridge, Central American Arc and North Anatolian Fault Zone. Ph. D. thesis, University of California, San Diego.

de Leeuw, G.A.M., D.R. Hilton, T.P. Fischer, and J.A. Walker (2007), The He-CO_2 isotope and relative abundance characteristics of geothermal fluids in El Salvador and Honduras: New constraints on volatile mass balance of the Central American Volcanic Arc, *Earth Planet. Sci. Lett.*, **258**(1-2), 132-146, doi:10.1016/ j.epsl.2007.03.028.

DeMets, C. (2001), A new estimate for present-day Cocos-Caribbean plate motion: Implications for slip along the Central American volcanic arc, *Geophys. Res. Lett.*, **28**(21), 4043-4046, doi:10.1029/2001GL013518.

DeShon, H.R., and S.Y. Schwartz (2004), Evidence for serpentinization of the forearc mantle wedge along the Nicoya Peninsula, Costa Rica, *Geophys. Res. Lett.*, **31**(21), L21611, doi:10.1029/2004GL021179.

Dixon E. T. (2003) Interpretation of helium and neon isotopic heterogeneity in Icelandic basalts, *Earth Planet. Sci. Lett.,* **206**(1-2), 83-99, doi:10.1016/S0012-821X(02)01071-3.

Dixon E. T., Honda M., McDougall I., Campbell I. H., and Sigurdsson I. (2000) Preservation of near-solar neon isotopic ratios in Icelandic basalts, *Earth Planet. Sci. Lett.,* **180**(3-4), 309-324, doi:10.1016/S0012-821X(00)00164-3.

Dixon J. E., Stolper E. M., and Holloway J. R. (1995) An experimental study of water and carbon dioxide solubilities in mid-ocean ridge basaltic liquids. Part I: Calibration and solubility models. *J. Petrol.* **36**(6), 1607-1631.

Dogan, T., H. Sumino, K. Nagao, and K. Notsu (2006), Release of mantle helium from forearc region of the Southwest Japan arc, *Chem. Geol.*, **233**(3-4), 235-248, doi:10.1016/j.chemgeo.2006.03.008.

Donnelly K. E., Goldstein S. L., Langmuir C. H., and Spiegelman M. (2004) Origin of enriched ocean ridge basalts and implications for mantle dynamics. *Earth Planet. Sci. Lett.* **226**(3-4), 347-366.

Duncan R. A., Backman J., and Peterson L. (1989) Reunion hotspot activity through Tertiary time: Initial results from the Ocean Drilling Program, Leg 115. *J. Volcan. Geoth. Res.* **36**(1-3), 193-198.

Duncan R. A. (1990) The volcanic record of the Réunion hotspot. In *Proc. Ocean Drill. Prog., Sci. Results,* **115** (eds. R.A. Duncan, J. Backman, R.B. Dunbar and L.C. Peterson). pp 3-10.

Dyment J., Gallet Y., and the Magofond 2 Scientific Party (1999) The Magofond 2 cruise: A surface and deep tow survey on the past and present Central Indian Ridge. *InterRidge News* **8**(1), 25-31.

Dyment J., Hémond C., and the Gimnaut Scientific Party (2000) Deep-sea exploration of the Central Indian Ridge at 19ºS. *InterRidge News* **9**(2), 29-32.

Dyment J., Hémond, C., Guillou, H., Maia, M., Briais, A., Gente, P. (2001) Central Indian Ridge and Réunion Hotspot in Rodrigues area: another type of ridge-hotspot interaction? *Eos Trans.* - Am. Geophys. Union **82**, F1168 (suppl.).

Einarsson P. (2008) Plate boundaries, rifts and transforms in Iceland. In *The dynamic geology of Iceland*, Jökull (58), (eds. A. Geirsdóttir and B. Brandsdóttir). Iceland glaciological society. pp. 35-58.

Eittreim, S.L., R.J. Anima, and A.J. Stevenson (2002), Seafloor geology of the Monterey Bay area continental shelf, *Mar. Geol.*, **181**(1-3), 3-34, doi:10.1016/S0025-3227(01) 00259-6.

Ellam R. M. and Stuart F. M. (2004) Coherent He-Nd-Sr isotope trends in high $^{3}He/^{4}He$ basalts: implications for a common reservoir, mantle heterogeneity and convection, *Earth Planet. Sci. Lett.,* **228**(3-4), 511-523, doi:10.1016/j.epsl.2004.10.020

Emrich, K., and J.C. Vogel (1970), Carbon isotope fractionation during precipitation of calcium carbonate, *Earth Planet. Sci. Lett.*, **8**(5), 363-371, doi:10.1016/0012-821X(70)90109-3.

Fisher, D.M., T.W. Gardner, J.S. Marshall, P.B. Sak, and M. Protti (1998), Effect of subducting sea-floor roughness on fore-arc kinematics Pacific coast, Costa Rica, *Geology*, **26**(5), 467-470, doi:10.1130/0091-7613(1998)026 <0467:EOSSFR> 2.3.CO;2.

Fisk M. R., Duncan R. A., Baxter A. N., Greenough J. D., Hargraves R. B., and Tatsumi Y. (1989) Reunion hotspot magma chemistry over the past 65 m.y.: Results from Leg 115 of the Ocean Drilling Program. *Geology* **17**(10), 934-937.

Foulger G. R., Pritchard M. J., Julian B. R., Evans J. R., Allen R. M., Nolet G., Morgan W. J., Bergsson B. H., Erlendsson P., Jakobsdóttir S., Ragnarsson S., Stefansson R., and Vogfjörd K. (2000) The seismic anomaly beneath Iceland extends down to the mantle transition zone and no deeper. *Geophys. J. Int.* **142**(3), F1-F5.

Freeze, A.R., and J.A. Cherry (1979), *Groundwater*, 604 pp., Prentice-Hall, Englewood Cliffs, N.J.

Füri E., Hilton D. R., and the KNOX11RR Scientific Party (2008) Sampling and surveying ridge-hotspot interaction on the Central Indian Ridge, 19°S: Cruise KNOX11RR. *InterRidge News* **17**, 28-29.

Füri, E., D. R. Hilton, K. M. Brown, and M. D. Tryon (2009), Helium systematics of cold seep fluids at Monterey Bay, California, USA: Temporal variations and mantle contributions, *Geochem. Geophys. Geosyst.*, **10**, Q08013, doi:10.1029/2009GC002557.

Gasparon M., Hilton D. R., and Varne R. (1994) Crustal Contamination Processes Traced by Helium-Isotopes - Examples from the Sunda Arc, Indonesia. *Earth Planet. Sci. Lett.* **126**(1-3), 15-22.

Gieskes, J., C. Mahn, S. Day, J.B. Martin, J. Greinert, T. Rathburn, and B. McAdoo (2005), A study of the chemistry of pore fluids and authigenic carbonates in methane seep environments: Kodiak Trench, Hydrate Ridge, Monterey Bay, and Eel River Basin, *Chem. Geol.*, **220**(3-4), 329-345, doi:10.1016/j.chemgeo.2005.04.002.

Giggenbach, W.F., Y. Sano, and H. Wakita (1993), Isotopic composition of helium, and CO_2 and CH_4 contents in gases produced along the New-Zealand part of a convergent plate boundary, *Geochim. Cosmochim. Acta*, **57**(14), 3427-3455, doi:10.1016/0016-7037(93)90549-C.

Gonnermann H. M. and Mukhopadhyay S. (2007) Non-equilibrium degassing and a primordial source for helium in ocean-island volcanism, *Nature* **449**(7165), 1037-1040, doi:10.1038/nature06240.

Graham, D.W. (2002), Noble gas isotope geochemistry of mid-ocean ridge and ocean island basalts: Characterization of mantle source reservoirs, in *Noble Gases in Geochemistry and Cosmochemistry, Rev. in Mineral. and Geochem.,* vol. 47, edited by D. Porcelli, C. Ballentine, and R. Wieler, pp. 247-317, Mineral. Soc. of Am., Washington, D.C.

Graham, D. W., W. J. Jenkins, M. D. Kurz, and R. Batiza (1987), Helium isotope disequilibrium and geochronology of glassy submarine basalts, *Nature* **326**, 384-386.

Graham D., Lupton J., Albarède F., and Condomines M. (1990) Extreme temporal homogeneity of helium isotopes at Piton de la Fournaise, Réunion Island. *Nature* **347**(6293), 545-548.

Graham D. W., Johnson K. T. M., Priebe L. D., and Lupton J. E. (1999) Hotspot-ridge interaction along the Southeast Indian Ridge near Amsterdam and St. Paul islands; helium isotope evidence. *Earth Planet. Sci. Lett.* **167**(3-4), 297-310.

Greene, H.G. (1977), Geology of the Monterey Bay region, *U.S. Geol. Surv. Open File Rep.*, 77-718, 347 pp.

Greene, H.G. (1990), Regional tectonics and structural evolution of the Monterey Bay region, Central California, in *Geology and Tectonics of the Central California Coast Region, San Francisco to Monterey,* Guideb. Am. Assoc. of Pet. Geol., Pac. Sect., vol. GB 67, edited by R. E. Garrison et al., pp. 31–56, Pac. Sect. Am. Assoc. of Pet. Geol., Bakersfield, Calif.

Greene, H.G., D. Orange, and J. Barry (1993), Geological diversity of cold seep communities, Monterey Bay region, Central California, U.S.A, *Eos Trans. AGU,* **74**(43), Fall Meet. Suppl., Abstract T13C-6-578.

Greene, H.G., N. Maher, T.H. Naehr, and Orange D.L. (1999), Fluid flow in the offshore Monterey Bay region, in *Late Cenozoic Fluid Seeps and Tectonics Along the San Gregorio Fault Zone in the Monterey Bay Region, California.* Guideb. Am. Assoc. of Pet. Geol., Pac. Sect., vol. GB 76, edited by R. E. Garrison, I. W. Aiello, and J. C. Moore, pp. 1–19, Pac. Sect., Am. Assoc. of Pet. Geol., Bakersfield, Calif.

Hahm D., Castillo P. R., and Hilton D. R. (2009) A deep mantle source for high $^{3}He/^{4}He$ ocean island basalts (OIB) inferred from Pacific near-ridge seamount lavas, *Geophys. Res. Lett.*, **36**, L20316, doi:10.1029/2009GL040560

Han, M.W., and E. Suess (1989), Subduction-induced pore fluid venting and the formation of authigenic carbonates along the Cascadia continental margin: Implications for the global Ca-cycle, *Palaeogeogr. Palaeocl. Paleoecol.*, **71**(1-2), 97-118, doi:10.1016/0031-0182(89)90032-1.

Han, X.Q., E. Suess, H. Sahling, and K. Wallmann (2004), Fluid venting activity on the Costa Rica margin: new results from authigenic carbonates, *Int. J. Earth Sci.*, **9**(4), 596-611, doi:10.1007/s00531-004-0402-y.

Hanan B. B. and Schilling J.-G. (1989) Easter Microplate Evolution - Pb Isotope Evidence. *J. Geophys. Res.-Sol. Ea.* **94**(B6), 7432-7448.

Hanan B. B., Kingsley R. H., and Schilling J.-G. (1986) Pb isotope evidence in the South Atlantic for migrating ridge-hotspot interactions. *Nature* **322**(6075), 137-144.

Hanyu T., Dunai T. J., Davies G. R., Kaneoka I., Nohda S., and Uto K. (2001) Noble gas study of the Reunion hotspot; evidence for distinct less-degassed mantle sources. *Earth Planet. Sci. Lett.* **193**(1-2), 83-98.

Hardarson B. S., Fitton J. G., Ellam R. M., and Pringle M. S. (1997) Rift relocation - a geochemical and geochronological investigation of a palaeo-rift in northwest Iceland. *Earth Planet. Sci. Lett.* **153**(3-4), 181-196.

Hards V. L., Kempton P. D., and Thompson R. N. (1995) The heterogeneous Iceland plume: new insights from the alkaline basalts of the Snaefell volcanic centre. *J. Geol. Soc.* **152**, 1003-1009.

Harper C.L., and Jacobsen S.B. (1996) Noble gases and Earth's accretion, *Science,* **273**(5283), 1814-1818, doi:10.1126/science.273.5283.1814.

Harrison D., Burnard P., and Turner G. (1999) Noble gas behaviour and composition in the mantle: constraints from the Iceland Plume, *Earth Planet. Sci. Lett.,* **171**(2), 199-207, doi:10.1016/S0012-821X(99)00143-0.

Harrison D., Burnard P. G., Trieloff M., and Turner G. (2003) Resolving atmospheric contaminants in mantle noble gas analyses. *Geochem. Geophys. Geosyst.*, **4**(3), 1023, doi:10.1029/2002GC000325.

Hart S. R., Schilling J.-G., and Powell J. L. (1973) Basalts from Iceland and along the Reykjanes Ridge: Sr isotope geochemistry. *Nature Phys. Sci.* **246**(155), 104-107.

Hauff, F., K. Hoernle, P. van den Bogaard, G. Alvarado, and D. Garbe-Schönberg (2000), Age and geochemistry of basaltic complexes in western Costa Rica: Contributions to the geotectonic evolution of Central America, *Geochem. Geophys. Geosyst.*, **1**(5), 1009, doi:10.1029/1999GC000020.

Hauff, F., K. Hoernle, G. Tilton, D.W. Graham, and A.C. Kerr (2000b), Large volume recycling of oceanic lithosphere over short time scales: geochemical constraints from the Caribbean Large Igneous Province, *Earth Planet. Sci. Lett.*, **174(**3-4), 247-263, doi:10.1016/S0012-821X(99)00272-1

Hauri E. H., Whitehead J. A., and Hart S. R. (1994) Fluid Dynamic and Geochemical Aspects of Entrainment in Mantle Plumes. *J. Geophys. Res.-Sol. Ea.* **99**(B12), 24275-24300.

Heaton, T.H.E., and Vogel J.C. (1981), "Excess air" in groundwater, *J. Hydrol.*, **50**(1-3), 201-216, doi:10.1016/0022-1694(81)90070-6.

Heber V. S., Brooker R. A., Kelley S. P., and Wood B. J. (2007) Crystal-melt partitioning of noble gases (helium, neon, argon, krypton, and xenon) for olivine and clinopyroxene, *Geochim. Cosmochim. Acta,* **71**(4), 1041-1061, doi:10.1016/j.gca.2006.11.010.

Helmberger D. V., Wen L., and Ding X. (1998) Seismic evidence that the source of the Iceland hotspot lies at the core-mantle boundary. *Nature* **396**(6708), 251-255.

Hensen, C., K. Wallmann, M. Schmidt, C.R. Ranero, and Suess E. (2004), Fluid expulsion related to mud extrusion off Costa Rica - A window to the subducting slab, *Geology*, **32**(3), 201-204, doi: 10.1130/G20119.1.

Hilton D. R. (1996) The helium and carbon isotope systematics of a continental geothermal system; results from monitoring studies at Long Valley Caldera (California, U.S.A.). *Chem. Geol.* **127**(4), 269-295.

Hilton D. R., Grönvold K., O'Nions R. K., and Oxburgh E. R. (1990) Regional distribution of ^{3}He anomalies in the Icelandic crust. *Chem. Geol.* **88**(1-2), 53-67.

Hilton D.R., G.M. McMurtry and R. Kreulen (1997) Evidence for extensive degassing of the Hawaiian mantle plume from helium-carbon relationships at Kilauea volcano, *Geophys. Res. Lett.*, **24** (23), 3065-3068.

Hilton D. R., Gronvold K., Sveinbjornsdottir A. E., and Hammerschmidt K. (1998) Helium isotope evidence for off-axis degassing of the Icelandic hotspot. *Chem. Geol.* **149**(3-4), 173-187. *Earth Planet. Sci. Lett.* **173**(1-2), 53-60.

Hilton D. R., Gronvold K., Macpherson C. G., and Castillo P. R. (1999) Extreme $^{3}He/^{4}He$ ratios in northwest Iceland: constraining the common component in mantle plumes, *Earth Planet. Sci. Lett.,* **173**(1-2), 53-60, doi:10.1016/S0012-821X(99)00215-0.

Hilton D. R., Thirlwall M. F., Taylor R. N., Murton B. J., and Nichols A. (2000) Controls on magmatic degassing along the Reykjanes Ridge with implications for the helium paradox, *Earth Planet. Sci. Lett.,* **183**(1-2), 43-50, doi:10.1016/S0012-821X(00) 00253-3.

Hilton, D.R., T.P. Fischer, and B. Marty (2002), Noble gases and volatile recycling at subduction zones, in *Noble Gases in Geochemistry and Cosmochemistry, Rev. in Mineral. and Geochem.,* vol. 47, edited by D. Porcelli, C. Ballentine, and R. Wieler, pp. 319-370, Mineral. Soc. of Am., Washington, D.C.

Hilton, D.R., T.P. Fischer, C. Ramirez, E. Füri, P.H. Barry, K.M. Brown, W. Montero, and P. Denyer (2009), Helium isotopes in the seismogenic zone of Costa Rica, DINGUE Noble Gas workshop, Nancy, France.

Hiyagon H. and Ozima M. (1986) Partition of noble gases between olivine and basalt melt, *Geochim. Cosmochim. Acta,* **50**(9), 2045-2057, doi:10.1016/0016-7037(86)90258-9.

Hiyagon H. and Kennedy B. M. (1992) Noble gases in CH_4-rich gas fields, Alberta, Canada. *Geochim. Cosmochim. Acta* **56**(4), 1569-1589.

Hofmann A. W. (1997) Mantle geochemistry: The message from oceanic volcanism. *Nature* **385**(6613), 219-229.

Holzner, C.P., D.F. McGinnis, C.J. Schubert, R. Kipfer, and D.M. Imboden (2008), Noble gas anomalies related to high-intensity methane gas seeps in the Black Sea, *Earth Planet. Sci. Lett.*, **265**(3-4), 396-409, doi:10.1016/j.epsl.2007.10.029.

Honda M. and McDougall I. (1998) Primordial helium and neon in the Earth - a speculation on early degassing. *Geophy. Res. Lett.* **25**(11), 1951-1954.

Honda M., McDougall I., Patterson D. B., Doulgeris A., and Clague D. A. (1991) Possible solar noble-gas component in Hawaiian basalts. *Nature* **349**(6305), 149-151.

Honda M., McDougall I., Patterson D. B., Doulgeris A., and Clague D. A. (1993) Noble gases in submarine pillow basalt glasses from Loihi and Kilauea, Hawaii: A solar component in the Earth. *Geochim. Cosmochim. Acta* **57**(4), 859-874.

Hopp J. and Trieloff M. (2005) Refining the noble gas record of the Réunion mantle plume source: Implications on mantle geochemistry. *Earth Planet. Sci. Lett.* **240**(3-4), 573-588.

Hopp J. and Trieloff M. (2008) Helium deficit in high-^{3}He/^{4}He parent magmas: Predegassing fractionation, not a "helium paradox", *Geochem. Geophys. Geosyst.*, 9, Q03009, doi:10.1029/2007GC001833.

Horns, D.M., and K.L. Verosub (1995), Paleomagnetic investigation of Late Neogene vertical axis rotation and remagnetization in Central Coastal California, *J. Geophys. Res.*, **100**(B3), 3873-3884, doi:10.1029/94JB02169.

Hubbard A., Sugden D., Dugmore A., Norddahl H., and Pétursson H. G. (2006) A modelling insight into the Icelandic Last Glacial Maximum ice sheet. *Quaternary Sci. Rev.* **25**(17-18), 2283-2296.

Huehnerbach, V., D.G. Masson, G. Bohrmann, J.M. Bull, and W. Weinrebe (2005), Deformation and submarine landsliding caused by seamount subduction beneath the Costa Rica continental margin - new insights from high-resolution sidescan sonar data, in *Submarine slope systems: processes and products,* vol. 244, edited by D.M. Hodgson and S.S. Flint, pp. 195-205, Geological Society, London, Special Publications, doi:10.1144/GSL.SP.2005.244.01.12.

Italiano, F., G. Martinelli, and P.M. Nuccio, (2001) Anomalies of mantle-derived helium during the 1997-1998 seismic swarm of Umbria-Marche, Italy, *Geophys. Res. Lett.*, **28**(5), 839-842, doi:10.1029/2000GL012059.

Ito G. (2001) Reykjanes 'V'-shaped ridges originating from a pulsing and dehydrating mantle plume. *Nature* **411**(6838), 681-684.

Ito G. and Lin J. (1995a) Oceanic spreading center-hotspot interactions: Constraints from along-isochron bathymetric and gravity anomalies. *Geology* **23**(7), 657-660.

Ito G., Lin J., and Gable C. W. (1997) Interaction of mantle plumes and migrating mid-ocean ridges: Implications for the Galápagos plume-ridge system. *J. Geophys. Res.-Sol. Ea.* **102**(B7), 15403-15417.

Ito G., Lin J., and Graham D. (2003) Observational and theoretical studies of the dynamics of mantle plume-mid-ocean ridge interaction. *Rev. Geophys.* **41**(4), 1017.

Ito G. T. and Lin J. (1995b) Mantle temperature anomalies along the past and paleoaxes of the Galápagos spreading center as inferred from gravity analyses. *J. Geophys. Res.-Sol. Ea.* **100**(B3), 3733-3745.

Jackson M. G., Kurz M. D., Hart S. R., and Workman R. K. (2007) New Samoan lavas from Ofu Island reveal a hemispherically heterogeneous high ^{3}He/^{4}He mantle. *Earth Planet. Sci. Lett.* **264**(3-4), 360-374.

Jähne, B., G. Heinz, and W. Dietrich (1987), Measurement of the Diffusion Coefficients of Sparingly Soluble Gases in Water, *J. Geophys. Res.*, **92**(C10), 10,767–10,776.

Jambon A., Weber H., and Braun O. (1986) Solubility of He, Ne, Ar, Kr and Xe in a basalt melt in the range 1250-1600°C. Geochemical implications, *Geochim. Cosmochim. Acta* **50**(3), 401-408, doi:10.1016/0016-7037(86)90193-6.

Jendrzejewski N., Trull T. W., Pineau F., and Javoy M. (1997) Carbon solubility in mid-ocean ridge basaltic melt at low pressures (250-1950 bar). *Chem. Geol.* **138**, 81-92.

Jenkins W. J. and Clarke W. B. (1976) The distribution of ^{3}He in the western Atlantic Ocean, *Deep-Sea Res.,* **23**, 481-494.

Jochum K. P., Hofmann A. W., Ito E., Seufert H. M., and White W. M. (1983) K, U and Th in mid-ocean ridge basalt glasses and heat production, K/U and K/Rb in the mantle. *Nature* **306**(5942), 431-436.

Judd, A.G., and M. Hovland (2007), *Seabed fluid flow; the impact on geology, biology, and the marine environment*, 475 pp., Cambridge University Press, Cambridge, United Kingdom (GBR).

Judd, A.G. (2005), The global importance and context of methane escape from the seabed, *Geo-Mar. Lett.*, **23**(3-4), 147-154, doi:10.1007/s00367-003-0136-z.

Kahn, L. M., E. A. Silver, D. Orange, R. Kochevar, and B. McAdoo (1996), Surficial evidence of fluid expulsion from the Costa Rica Accretionary Prism, *Geophys. Res. Lett.*, **23**(8), 887–890.

Kallenbach, R., et al. (1997), Isotopic composition of solar wind neon measured by CELIAS/MTOF on board SOHO, *J. Geophys. Res.*, **102**(A12), 26,895–26,904.

Kaneoka I., Takaoka N., and Upton B. G. J. (1986) Noble gas systematics in basalts and a dunite nodule from Réunion and Grand Comore Islands, Indian Ocean. *Chem. Geol.* **59**(1), 35-42.

Kastner, M., H. Elderfield, W.J. Jenkins, J.M. Gieskes, and T. Gamo (1993), Geochemical and isotopic evidence for fluid flow in the western Nankai subduction zone, Japan, in *Proc. ODP Sci. Res.*, pp. 397-413.

Kellogg L. H., Hager B. H., and van der Hilst R. D. (1999) Compositional stratification in the deep mantle, *Science,* **283**(5409), 1881-1884, doi:10.1126/science.283.5409.1881.

Kempton P. D., Fitton J. G., Saunders A. D., Nowell G. M., Taylor R. N., Hardarson B. S., and Pearson G. (2000) The Iceland plume in space and time: a Sr-Nd-Pb-Hf study of the North Atlantic rifted margin. *Earth Planet. Sci. Lett.* **177**(3-4), 255-271.

Kennedy, B.M., and M.C. van Soest (2007), Flow of mantle fluids through the ductile lower crust: Helium isotope trends, *Science*, **318**(5855), 1433-1436, doi:10.1126/ science.1147537.

Kennedy B. M., Hiyagon H., and Reynolds J. H. (1990) Crustal neon: a striking uniformity. *Earth Planet. Sci. Lett.* **98**(3-4), 277-286.

Kennedy, B.M., Y.K. Kharaka, W.C. Evans, A. Ellwood, D.J. DePaolo, J. Thordsen, G. Ambats, and R.H. Mariner (1997), Mantle fluids in the San Andreas Fault system, California, *Science*, *278* (5341), 1278-1281, doi:10.1126/science.278.5341.1278.

Kerr A. C., Saunders A. D., Tarney J., Berry N. H., and Hards V. L. (1995) Depleted mantle-plume geochemical signatures: No paradox for plume theories. *Geology* **23**(9), 843-846.

Kerr, A.C., J. Tarney, A. Nivia, G.F. Marriner, and A.D. Saunders (1998), The internal structure of oceanic plateaus: inferences from obducted Cretaceous terranes in western Colombia and the Caribbean, *Tectonophysics*, **292**(3-4), 173-188, doi:10.1016/S0040-1951(98)00067-5.

Kerrick D.M. and Connolly J.A.D. (2001) Metamorphic devolatilization of subducted marine sediments and the transport of volatiles into the Earth's mantle, *Nature*, **411**, 293-296.

Kharaka, Y.K., and D.J. Specht (1988), The solubility of noble gases in crude oil at 25-100 ºC, *Appl. Geochem.*, **3**(2), 137-144, doi:10.1016/0883-2927(88)90001-7.

Kimura, G., et al. (Eds.) (1997), P*roceedings of the Ocean Drilling Program, Initial Reports*, vol. 170, Ocean Drill. Program, College Station, Tex.

Kincaid C., Ito G., and Gable C. (1995) Laboratory investigation of the interaction of off-axis mantle plumes and spreading centres. *Nature* **376**(6543), 758-761.

Kincaid C., Schilling J.-G., and Gable C. (1996) The dynamics of off-axis plume-ridge interaction in the uppermost mantle. *Earth Planet. Sci. Lett.* **137**(1-4), 29-43.

King, C.Y. (1978), Radon emanation on San-Andreas Fault, *Nature*, **271**(5645), 516-519, doi:10.1038/271516a0.

King, C.Y. (1984), Impulsive radon emanation on a creeping segment of the San-Andreas Fault, California, *Pure Appl. Geophys.*, **122**(2-4), 340-352, doi:10.1007/BF00874603.

King, C.Y. (1986), Gas geochemistry applied to earthquake prediction: an overview, *J. Geophys. Res.,* **91**(B12), 12269-12281, doi:10.1029/JB091iB12p12269.

Kingsley R. H. and Schilling J.-G. (1998) Plume-ridge interaction in the Easter Salas y Gomez seamount chain-Easter Microplate system: Pb isotope evidence. *J. Geophys. Res.-Sol. Ea.* **103**(B10), 24159-24177.

Kipfer, R., W. Aeschbach-Hertig, F. Peeters, and M. Stute (2002), Noble gases in lakes and ground waters, in *Noble Gases in Geochemistry and Cosmochemistry, Rev. in Mineral. and Geochem.,* vol. 47, edited by D. Porcelli, C. Ballentine, and R. Wieler, pp. 615-700, Mineral. Soc. of Am., Washington, D.C.

Klaucke, I., D. G. Masson, C. J. Petersen, W. Weinrebe, and C. R. Ranero (2008), Multifrequency geoacoustic imaging of fluid escape structures offshore Costa Rica: Implications for the quantification of seep processes, *Geochem. Geophys. Geosyst.*, **9**, Q04010, doi:10.1029/2007GC001708.

Kopf, A., A. Deyhle, and E. Zuleger (2000), Evidence for deep fluid circulation and gas hydrate dissociation using boron and boron isotopes of pore fluids in forearc sediments from Costa Rica (ODP Leg 170), *Mar. Geol.*, **167**(1-2), 1-28, doi:10.1016/S0025-3227(00)00026-8.

Kroopnick, P.M. (1985), The distribution of ^{13}C of $\sum CO_2$ in the world oceans, *Deep-Sea Res.*, **32**(1), 57-84.

Kulongoski, J.T., and D.R. Hilton (2002), A quadrupole-based mass spectrometric system for the determination of noble gas abundances in fluids, *Geochem. Geophys. Geosyst.*, **3***(6)*, 1032, doi:10.1029/2001GC000267.

Kulongoski, J.T., D.R. Hilton, and J.A. Izbicki (2003), Helium isotope studies in the Mojave Desert, California: implications for groundwater chronology and regional seismicity, *Chem. Geol.*, **202**(1-2), 95-113, doi:10.1016/j.chemgeo.2003.07.002.

Kulongoski, J.T., D.R. Hilton, and J.A. Izbicki (2005), Source and movement of helium in the eastern Morongo groundwater Basin: The influence of regional tectonics on crustal and mantle helium fluxes, *Geochim. Cosmochim. Acta*, **69**(15), 3857-3872, doi:10.1016/j.gca.2005.03.001.

Kurz M. D., Meyer P. S., and Sigurdsson H. (1985) Helium isotopic systematics within the neovolcanic zones of Iceland, *Earth Planet. Sci. Lett.,* **74**(4), 291-305, doi:10.1016/S0012-821X(85)80001-7.

Kurz M. D., Le Roex A. P., and Dick H. J. B. (1998) Isotope geochemistry of the oceanic mantle near the Bouvet triple junction. *Geochim. Cosmochim. Ac.* **62**(5), 841-852.

Kvenvolden, K.A., F.D. Hostettler, R.W. Rosenbauer, T.D. Lorenson, W.T. Castle, and S. Sugarman (2002), Hydrocarbons in recent sediment of the Monterey Bay National Marine Sanctuary, *Mar. Geol.*, **181**(1-3), 101-113, doi:10.1016/S0025-3227(01) 00263-8.

LaBonte, A.L., K.M. Brown, and M.D. Tryon (2007), Monitoring periodic and episodic flow events at Monterey Bay seeps using a new optical flow meter, *J. Geophys. Res.*, **112**(B2), B02105, doi:10.1029/2006JB004410.

Leifer, I., and J. Clark (2002), Modeling trace gases in hydrocarbon seep bubbles. Application to marine hydrocarbon seeps in the Santa Barbara Channel, *Russ. Geol. Geophys*, **43**(7), 613-621.

Leifer, I., J.R. Boles, B.P. Luyendyk, and J.F. Clark (2004), Transient discharges from marine hydrocarbon seeps: spatial and temporal variability, *Environ. Geol.*, **46**(8), 1038-1052, doi:10.1007/s00254-004-1091-3.

Li, L., and G. E. Bebout (2005), Carbon and nitrogen geochemistry of sediments in the Central American convergent margin: Insights regarding subduction input fluxes, diagenesis, and paleoproductivity, *J. Geophys. Res.*, **110**, B11202, doi:10.1029/2004JB003276.

Licciardi J. M., Kurz M. D., and Curtice J. M. (2007) Glacial and volcanic history of Icelandic table mountains from cosmogenic ^{3}He exposure ages. *Quaternary Sci. Rev.* **26**(11-12), 1529-1546.

Linke, P., K. Wallmann, E. Suess, C. Hensen, and G. Rehder (2005), In situ benthic fluxes from an intermittently active mud volcano at the Costa Rica convergent margin, *Earth Planet. Sci. Lett.*, **235**(1-2), 79-95, doi:10.1016/j.epsl.2005.03.009.

Lorenson, T.D., K.A. Kvenvolden, F.D. Hostettler, R.J. Rosenbauer, D.L. Orange, and J.B. Martin (2002), Hydrocarbon geochemistry of cold seeps in the Monterey Bay National Marine Sanctuary, *Mar. Geol*, **181**(1-3), 285-304, doi:10.1016/S0025-3227(01)00272-9.

Luff, R., and K. Wallmann (2003), Fluid flow, methane fluxes, carbonate precipitation and biogeochemical turnover in gas hydrate-bearing sediments at Hydrate Ridge, Cascadia Margin: Numerical modeling and mass balances, *Geochim. Cosmochim. Acta*, **67**(18), 3403-3421, doi:10.1016/S0016-7037(03)00127-3.

Lux G. (1987) The behavior of noble gases in silicate liquids: Solution, diffusion, bubbles and surface effects, with applications to natural samples. *Geochim. Cosmochim. Acta* **51**(6), 1549-1560.

Macpherson C. G., Hilton D. R., Day J. M. D., Lowry D., and Grönvold K. (2005a) High-^{3}He/^{4}He, depleted mantle and low-δ^{18}O, recycled oceanic lithosphere in the source of central Iceland magmatism, *Earth Planet. Sci. Lett.,* **233**(3-4), 411-427, doi:10.1016/j.epsl.2005.02.037.

Macpherson C. G., Hilton D. R., Mertz D. F., and Dunai T. J. (2005b) Sources, degassing, and contamination of CO_2, H_2O, He, Ne, and Ar in basaltic glasses from Kolbeinsey Ridge, North Atlantic. *Geochim. Cosmochim. Acta* **69**(24), 5729-5746.

Mahaffy P. R., Donahue T. M., Atreya S. K., Owen T. C., and Niemann H. B. (1998) Galileo probe measurements of D/H and ^{3}He/^{4}He in Jupiter's atmosphere. *Space Sci. Rev.* **84**(1-2), 251-263.

Mahoney J. J., Natland J. H., White W. M., Poreda R., Bloomer S. H., Fisher R. L., and Baxter A. N. (1989) Isotopic and Geochemical Provinces of the Western Indian-Ocean Spreading Centers. *J. Geophys. Res.-Sol. Ea.* **94**(B4), 4033-4052.

Martel D. J., Onions R. K., Hilton D. R., and Oxburgh E. R. (1990) The role of element distribution in production and release of radiogenic helium: the Carnmenellis Granite, Southwest England. *Chem. Geol.* **88**(3-4), 207-221.

Martin, J.B., D.L. Orange, T.D. Lorenson, and K.A. Kvenvolden (1997), Chemical and isotopic evidence of gas-influenced flow at a transform plate boundary; Monterey Bay, California, *J. Geophys. Res.*, **102**(B11), 24,903-24,915, doi:10.1029/97JB02154.

Martin, J.B., S.A. Day, A.E. Rathburn, M.E. Perez, C. Mahn, and J. Gieskes (2004), Relationships between the stable isotopic signatures of living and fossil foraminifera in Monterey Bay, California, *Geochem. Geophys. Geosyst.*, **5**(4), Q04004, doi:10.1029/2003GC000629.

Marty, B., and A. Jambon (1987), $C/^{3}He$ in volatile fluxes from the solid Earth - implications for carbon geodynamics, *Earth Planet. Sci. Lett.*, **83**(1-4), 16-26, doi:10.1016/0012-821X(87)90047-1.

Marty B. and Lussiez P. (1993) Constraints on rare gas partition coefficients from analysis of olivine glass from a picritic mid-ocean ridge basalt, *Chem. Geol.* **106**(1-2), 1-7, doi:10.1016/0009-2541(93)90162-C.

Marty B. and Zimmermann L. (1999) Volatiles (He, C, N, Ar) in mid-ocean ridge basalts: Assesment of shallow-level fractionation and characterization of source composition. *Geochim. Cosmochim. Ac.* **63**(21), 3619-3633.

Marty B., Gunnlaugsson E., Jambon A., Oskarsson N., Ozima M., Pineau F., and Torssander P. (1991) Gas geochemistry of geothermal fluids, the Hengill Area, southwest rift zone of Iceland. *Chem. Geol.* **91**(3), 207-225.

Matsuda J. and Marty B. (1995) The $^{40}Ar/^{36}Ar$ ratio of the undepleted mantle; a reevaluation. *Geophy. Res. Lett.* **22**(15), 1937-1940.

Matsumoto, T., T. Kawabata, J. Matsuda, K. Yamamoto, and K. Mimura (2003), $^{3}He/^{4}He$ ratios in well gases in the Kinki district, SW Japan: surface appearance of slab-derived fluids in a non-volcanic area in Kii Peninsula, *Earth Planet. Sci. Lett.*, **216**(1-2), 221-230, doi:10.1016/S0012-821X(03)00479-5.

Mau, S., H. Sahling, G. Rehder, E. Suess, P. Linke, and E. Soeding (2006), Estimates of methane output from mud extrusions at the erosive convergent margin off Costa Rica, *Mar. Geol.*, **225**(1-4), 129-144, doi:10.1016/j.margeo.2005.09.007.

Mau, S., G. Rehder, I. G. Arroyo, J. Gossler, and E. Suess (2007), Indications of a link between seismotectonics and CH_4 release from seeps off Costa Rica, *Geochem. Geophys. Geosyst.*, **8**, Q04003, doi:10.1029/2006GC001326.

Mazor E. (1972) Paleotemperatures and other hydrological parameters deduced from noble gases dissolved in groundwaters, Jordan Rift Valley, Israel, *Geochim. Cosmochim. Acta* **36**(12), 1321-1336, doi:10.1016/0016-7037(72)90065-8.

Mazor E., Heymann D., and Anders E. (1970) Noble gases in carbonaceous chondrites. *Geochim. Cosmochim. Acta* **34**(7), 781-824.

McDougall I. (1971) Geochronology and evolution of young volcanic island of Réunion, Indian Ocean. *Geochim. Cosmochim. Ac.* **35**(3), 261-268.

McDougall I. and Chamalaun F. H. (1969) Isotopic dating and geomagnetic polarity studies on volcanic rocks from Mauritius, Indian Ocean. *Geol. Soc. Am. Bull.* **80**(8), 1419-1442.

McDougall I., Upton B. G. J., and Wadswort W. J. (1965) A geological reconnaissance of Rodriguez Island Indian Ocean. *Nature* **206**(4979), 26-27.

McDougall I., Kristjansson L., and Saemundsson K. (1984) Magnetostratigraphy and geochronology of northwest Iceland. *J. Geophy. Res.* **89**(NB8), 7029-7060.

McIntosh, K.D., and M.K. Sen (2000), Geophysical evidence for dewatering and deformation processes in the ODP Leg 170 area offshore Costa Rica, *Earth Planet. Sci. Lett.*, **178**(1-2), 125-138, doi:10.1016/S0012-821X(00)00069-8.

McIntosh, K. D., and E. A. Silver (1996), Using 3D seismic reflection data to find fluid seeps from the Costa Rica Accretionary Prism, *Geophys. Res. Lett.*, **23**(8), 895–898.

Mellor S. H. (1998) The geochemistry, petrology, and petrogenesis of lavas from the submarine flanks of Réunion Island (western Indian Ocean): implications for magma genesis and the mantel source. *Ph. D. Thesis, Greenwich*, 297 pp.

Mertz D. F., Devey C. W., Todt W., Stoffers P., and Hofmann A. W. (1991) Sr-Nd-Pb isotope evidence against plume-asthenosphere mixing north of Iceland. *Earth Planet. Sci. Lett.* **107**(2), 243-255.

Milkov, A.V., G.E. Claypool, Y.J. Lee, W.Y. Xu, G.R. Dickens, and W.S. Borowski (2003), In situ methane concentrations, at Hydrate Ridge, offshore Oregon: New constraints on the global gas hydrate inventory from an active margin, *Geology*, **31(**10), 833-836, doi:10.1130/G19689.1.

Mittelstaedt E. and Ito G. (2005) Plume-ridge interaction, lithospheric stresses, and the origin of near-ridge volcanic lineaments. *Geochem. Geophys. Geosyst.*, 6, Q06002.

Montaggioni L., Nativel P., Cadet T., Faure G., Bachelery P., and Naim O. (1988) La Réunion, Ile Maurice; géologie et aperçus biologiques, plantes et animaux. Réunion and Mauritius; their geology and a quick look at plant and animal biology. *Guides Geologiques Regionaux* **1988**, 192.

Montelli R., Nolet G., Dahlen F. A., and Masters G. (2006) A catalogue of deep mantle plumes: New results from finite-frequency tomography. *Geochem. Geophys. Geosyst.*, 7, Q11007, doi:10.1029/2006GC001248.

Moore J.C., and D. Saffer (2001), Updip limit of the seismogenic zone beneath the accretionary prism of southwest Japan: an effect of diagenetic to low-grade metamorphic processes and increasing effective stress, *Geology*, **29**(2), 183–186, doi:10.1130/0091-7613(2001)029<0183:ULOTSZ> 2.0.CO;2.

Moreira M. and Sarda P. (2000) Noble gas constraints on degassing processes. *Earth Planet. Sci. Lett.* **176**(3-4), 375-386.

Moreira M. and Allègre C. J. (2002) Rare gas systematics on Mid Atlantic Ridge (37-40°N). *Earth Planet. Sci. Lett.* **198**(3-4), 401-416.

Moreira M., Staudacher T., Sarda P., Schilling J.-G., and Allègre C. J. (1995) A primitive plume neon component in MORB: The Shona ridge-anomaly, South-Atlantic (51-52°S). *Earth Planet. Sci. Lett.* **133**(3-4), 367-377.

Moreira M., Kunz J., and Allègre C. (1998) Rare gas systematics in popping rock: Isotopic and elemental compositions in the upper mantle. *Science* **279**(5354), 1178-1181.

Moreira M., Breddam K., Curtice J., and Kurz M. D. (2001) Solar neon in the Icelandic mantle: new evidence for an undegassed lower mantle, *Earth Planet. Sci. Lett.,* **185**(1-2), 15-23, doi:10.1016/S0012-821X(00)00351-4.

Moreira M., Blusztajn J., Curtice J., Hart S., Dick H., and Kurz M. D. (2003) He and Ne isotopes in oceanic crust: implications for noble gas recycling in the mantle, *Earth Planet. Sci. Lett.,* **216**(4), 635-643, doi:10.1016/S0012-821X(03)00554-5.

Morgan J. P. and Morgan W. J. (2007) Several plume 'paradoxes' can be resolved by a plume-fed asthenosphere. *EGU 2007,* Vienna. A-10146 (abstr.)

Morgan J. P. and Morgan W. J. (2008) Two-stage melting and noble gases. *EGU 2008,* Vienna. A-10727 (abstr.)

Morgan W. J. (1978) Rodriguez, Darwin, Amsterdam. A second type of hotspot island. *J. Geophys. Ress* **83**(NB11), 5355-5360.

Morris, J., R. Valentine, and T. Harrison (2002), ^{10}Be imaging of sediment accretion and subduction along the northeast Japan and Costa Rica convergent margins, *Geology*, **30**(1), 59-62, doi:10.1130/0091-7613(2002)030<0059:BIOSAA> 2.0.CO;2.

Murton B. J., Tindle A. G., Milton J. A., and Sauter D. (2005) Heterogeneity in southern Central Indian Ridge MORB: Implications for ridge-hot spot interaction. *Geochem. Geophys. Geosyst.*, 6, Q03E20.

Nadeau, R.M., and D. Dolenc (2005), Nonvolcanic tremors deep beneath the San Andreas Fault, *Science*, **307**(5708), 389-389, doi:10.1126/science.1107142.

Nauret F., Abouchami W., Galer S. J. G., Hofmann A. W., Hemond C., Chauvel C., and Dyment J. (2006) Correlated trace element-Pb isotope enrichments in Indian MORB along 18-20 ºS, Central Indian Ridge. *Earth Planet. Sci. Lett.* **245**(1-2), 137-152.

Newman, A. V., S. Y. Schwartz, V. Gonzalez, H. R. DeShon, J. M. Protti, and L. M. Dorman (2002), Along-strike variability in the seismogenic zone below Nicoya Peninsula, Costa Rica, *Geophys. Res. Lett.*, **29**(20), 1977, doi:10.1029/2002GL015409.

Nicolaysen, K. P., F. A. Frey, J. J. Mahoney, K. T. M. Johnson, and D. W. Graham (2007), Influence of the Amsterdam/St. Paul hot spot along the Southeast Indian Ridge between 77° and 88°E: Correlations of Sr, Nd, Pb, and He isotopic variations with ridge segmentation, *Geochem. Geophys. Geosyst.*, 8, Q09007.

Niedermann S., Bach W., and Erzinger J. (1997) Noble gas evidence for a lower mantle component in MORBs from the southern East Pacific Rise: Decoupling of helium and neon isotope systematics. *Geochim. Cosmochim. Acta* **61**(13), 2697-2715.

Nuccio P. M. and Paonita A. (2000) Investigation of the noble gas solubility in H_2O-CO_2 bearing silicate liquids at moderate pressure II: the extended ionic porosity (EIP) model. *Earth Planet. Sci. Lett.* **183**(3-4), 499-512.

Nur, A.M., and J.S. Walder (1990), Time-dependent hydraulics of the Earth's crust, in T*he role of fluids in crustal processes*, pp. 113-127 , Natl. Acad. Press, Washington, D.C.

Obara, K. (2002), Nonvolcanic Deep Tremor Associated with Subduction in Southwest Japan, *Science*, **296**, 1679-1681, doi:10.1126/science.1070378.

Okino K., Ichikawa Y., and Tamaki T. (2008) Detailed morphology of the Central Indian Ridge between 20deg15S and 15deg30S: implication for hotspot-ridge interaction. In *Proc. Jpn. Geoscience Union (JPGU),* J164-002.

Orange, D.L., H.G. Greene, D. Reed, J.B. Martin, C.M. McHugh, W.B.F. Ryan, N. Maher, D. Stakes, and J. Barry (1999), Widespread fluid expulsion on a translational continental margin: Mud volcanoes, fault zones, headless canyons, and organic-rich substrate in Monterey Bay, California, *Geol. Soc. Am. Bull.*, **111**(7), 992-1009, doi:10.1130/0016-7606(1999)111<0992:WFEOAT>2.3.CO;2..

Ozima M. and Podosek F.A. (2002) *Noble Gas Geochemistry*. Cambridge University Press, United Kingdom (GBR). 286 pp.

Pan Y. C. and Batiza R. (1998) Major element chemistry of volcanic glasses from the Easter Seamount Chain: Constraints on melting conditions in the plume channel. *Journal of J. Geophys. Res.-Sol. Ea.* **103**(B3), 5287-5304.

Parai R., Mukhopadhyay S., and Lassiter J. C. (2009) New constraints on the HIMU mantle from neon and helium isotopic compositions of basalts from the Cook-Austral Islands. *Earth Planet. Sci. Lett.* **277**(1-2), 253-261.

Parman S. W., Kurz M. D., Hart S. R., and Grove T. L. (2005) Helium solubility in olivine and implications for high $^3He/^4He$ in ocean island basalts, *Nature,* **437**(7062), 1140-1143, doi:10.1038/nature04215.

Parson L. M., Patriat P., Searle R. C., and Briais A. R. (1993) Segmentation of the Central Indian Ridge between 12º12'S and the Indian Ocean Triple Junction. *Mar. Geophys. Res.* **15**(4), 265-282.

Paterson W. S. B. (1994) *The Physics of Glaciers*. Pergamon Press, Elsevier Science Ltd.. New York.

Peeters, F., U. Beyerle, W. Aeschbach-Hertig, J. Holocher, M.S. Brennwald, and R. Kipfer (2003), Improving noble gas based paleoclimate reconstruction and groundwater dating using $^{20}Ne/^{22}Ne$ ratios, *Geochim. Cosmochim. Acta*, **67**(4), 587-600, doi:10.1016/S0016-7037(02)00969-9.

Pili, E., B.M. Kennedy, M.S. Conrad, J.P. Gratier, and F. Poitrasson (1998), Isotope constraints on the involvement of fluids in the San Andreas fault system, California, *Mineral. Mag.*, **62A**(2), 1182-1183, doi:10.1180/minmag.1998.62A.2.284.

Polak G., Kononov I., Tolstikhin I., Mamyrin B. A., and Khabarin L. V. (1976) The helium isotopes in thermal fluids. In *Thermal and Chemical Problems of Thermal Waters.* Intl. Assoc. Hydrogeol. Sci. 119. pp. 17-33.

Porcelli D. and Ballentine C. J. (2002) Models for the distribution of terrestrial noble gases and the evolution of the atmosphere, in *Noble Gases in Geochemistry and Cosmochemistry, Rev. in Mineral. and Geochem.,* vol. 47, edited by D. Porcelli, C. Ballentine, and R. Wieler, pp. 412-480, Mineral. Soc. of Am., Washington, D.C.

Porcelli D. and Halliday A. N. (2001) The core as a possible source of mantle helium, *Earth Planet Sci. Lett.,* **192**(1), 45-56, doi:10.1016/S0012-821X(01)00418-6.

Porcelli D. and Wasserburg G. J. (1995) Mass transfer of helium, neon, argon, and xenon through a steady state upper mantle. *Geochim. Cosmochim. Ac.* **59**(23), 4921-4937.

Poreda R. and di Brozolo F. R. (1984) Neon isotope variations in Mid-Atlantic Ridge basalts. *Earth Planet. Sci. Lett.* **69**(2), 277-289.

Poreda R., Schilling J.-G., and Craig H. (1986) Helium and hydrogen isotopes in ocean-ridge basalts north and south of Iceland. *Earth Planet. Sci. Lett.* **78**(1), 1-17.

Poreda R. J. and Farley K. A. (1992) Rare gases in Samoan xenoliths. *Earth Planet. Sci. Lett.* **113**(1-2), 129-144.

Poreda, R.J., A.W.A. Jeffrey, I.R. Kaplan, and H. Craig (1988), Magmatic helium in subduction-zone natural gases, *Chem. Geol.*, **71**, 199-210, doi:10.1016/0009-2541(88)90115-5.

Poreda R. J., Craig H., Arnórsson S., and Welhan J. A. (1992) Helium isotopes in Icelandic geothermal systems: I. ^{3}He, gas chemistry, and ^{13}C relations. *Geochim. Cosmochim. Acta* **56**(12), 4221-4228.

Ranero, C.R., and R. von Huene (2000), Subduction erosion along the Middle America convergent margin, *Nature*, **404**(6779), 748-752, doi:10.1038/35008046.

Ranero, C. R., I. Grevemeyer, H. Sahling, U. Barckhausen, C. Hensen, K. Wallmann, W. Weinrebe, P. Vannucchi, R. von Huene, and K. McIntosh (2008), Hydrogeological system of erosional convergent margins and its influence on tectonics and interplate seismogenesis, *Geochem. Geophys. Geosyst.*, **9**, Q03S04, doi:10.1029/2007GC001679.

Rathburn, A.E., M.E. Perez, J.B. Martin, S.A. Day, C. Mahn, J. Gieskes, W. Ziebis, D. Williams, and A. Bahls (2003), Relationships between the distribution and stable isotopic composition of living benthic Foraminifera and cold methane seep biogeochemistry in Monterey Bay, California, *Geochem. Geophys. Geosyst.*, **4**(12), 1106, doi:10.1029/2003GC000595.

Reid, M.R., and D.W. Graham (1996), Resolving lithospheric and sub-lithospheric contributions to helium isotope variations in basalts from the southwestern US, *Earth Planet. Sci. Lett.*, **144**(1-2), 213-222, doi:10.1016/0012-821X(96)00166-5.

Reimer, G.M. (1984), Prediction of central California earthquakes from soil-gas helium fluctuations, *Pure Appl. Geophys.*, **122**(2-4), 369-375, doi:10.1007/BF00874605.

Reimer, G.M. (1990), Helium increase, *Nature*, **347**(6291), 342-342, doi:10.1038/347342a.

Rice, J.R. (1992), Fault stress states, pore pressure distributions, and the weakness of the San Andreas Fault, in *Fault mechanics and Transport Properties in Rocks*, editors B. Evans and T.-F. Wong, pp. 475-503, Academic Press, San Diego, Calif.

Rocholl A. and Jochum K. P. (1993) Th, U and other trace elements in carbonaceous chondrites: Implications for the terrestrial and solar system Th/U ratios. *Earth Planet. Sci. Lett.* **117**, 265-278.

Rogers, G. and H. Dragert (2003), Episodic tremor and slip on the Cascadia subduction zone: the chatter of silent slip, *Science*, **300**, 1942-1943, doi:10.1126/science.1084783.

Saffer, D.M., E.A. Silver, A.T. Fisher, H. Tobin, and K. Moran (2000), Inferred pore pressures at the Costa Rica subduction zone: implications for dewatering processes, *Earth Planet. Sci. Lett.,* **177**(3-4), 193-207, doi:10.1016/S0012-821X(00)00048-0.

Sahling, H., D. G. Masson, C. R. Ranero, V. Hühnerbach, W. Weinrebe, I. Klaucke, D. Bürk, W. Brückmann, and E. Suess (2008), Fluid seepage at the continental margin offshore Costa Rica and southern Nicaragua, *Geochem. Geophys. Geosyst.*, **9**, Q05S05, doi:10.1029/2008GC001978.

Saito, S., and D. Goldberg (2001), Compaction and dewatering processes of the oceanic sediments in the Costa Rica and Barbados subduction zones: estimates from in situ physical property measurements, *Earth Planet. Sci. Lett.*, **191**(3-4), 283-293, doi:10.1016/S0012-821X(01)00403-4.

Sano, Y., and B. Marty (1995), Origin of carbon in fumarolic gas from island arcs, *Chem. Geol.*, **119**(1-4), 265-274, doi:10.1016/0009-2541(94)00097-R.

Sano Y., Urabe A., Wakita H., Chiba H., and Sakai H. (1985) Chemical and isotopic compositions of gases in geothermal fluids in Iceland. *Geochem. J.* **19**(3), 135-148.

Sarda P. (2004) Surface noble gas recycling to the terrestrial mantle. *Earth Planet. Sci. Lett.* **228**(1-2), 49-63.

Sarda P. and Graham D. (1990) Mid-ocean ridge popping rocks: implications for degassing at ridge crests. *Earth Planet. Sci. Lett.* **97**(3-4), 268-289.

Sarda P., Staudacher T., and Allègre C. J. (1985) $^{40}Ar/^{36}Ar$ in MORB glasses: constraints on atmosphere and mantle evolution. *Earth Planet. Sci. Lett.* **72**(4), 357-375.

Sarda P., Staudacher T., and Allègre C. J. (1988) Neon isotopes in submarine basalts, *Earth Planet. Sci. Lett.,* **91**(1-2), 73-88, doi:10.1016/0012-821X(88)90152-5.

Scarsi P. (2000) Fractional extraction of helium by crushing of olivine and clinopyroxene phenocrysts; effects on the $^{3}He/^{4}He$ measured ratio. *Geochim. Cosmochim. Acta* **64**(21), 3751-3762.

Schilling J.-G. (1973) Iceland mantle plume: geochemical Study of Reykjanes Ridge. *Nature* **242**(5400), 565-571.

Schilling J.-G. (1985) Upper mantle heterogeneities and dynamics. *Nature* **314**(6006), 62-67.

Schilling J.-G. (1991) Fluxes and excess temperatures of mantle plumes inferred from their interaction with migrating mid-ocean ridges. **352**(6334), 397-403.

Schilling J.-G., Kingsley R. H., and Devine J. D. (1982) Galápagos hot spot-spreading center system, 1, Spatial petrological and geochemical variations (83ºW-101ºW). *J. Geophys. Res.* **87**(NB7), 5593-5610.

Schilling J.-G., Zajac M., Evans R., Johnston T., White W., Devine J. D., and Kingsley R. (1983) Petrologic and geochemical variations along the Mid-Atlantic Ridge from 29ºN to 73 ºN. *Am. J. Sci.* **283**(6), 510-586.

Schilling J.-G., Thompson G., Kingsley R., and Humphris S. (1985) Hotspot-migrating ridge interaction in the South-Atlantic. *Nature* **313**(5999), 187-191.

Schlosser P., Stute M., Dorr H., Sonntag C., and Munnich K. O. (1988) Tritium/^{3}He dating of shallow groundwater, *Earth Planet. Sci. Lett.,* **89**(3-4), 353-362, doi:10.1016/0012-821X(88)90122-7.

Schmidt, M., C. Hensen, T. Morz, C. Muller, I. Grevemeyer, K. Wallmann, S. Mau, and N. Kaul (2005), Methane hydrate accumulation in "Mound 11" mud volcano, Costa Rica forearc, *Mar. Geol.*, **216**(1-2), 83-100, doi:10.1016/j.margeo.2005.01.001.

Shaw A. M., Hilton D. R., Macpherson C. G., and Sinton J. M. (2001) Nucleogenic neon in high $^{3}He/^{4}He$ lavas from the Manus back-arc basin: a new perspective on He-Ne decoupling, *Earth Planet. Sci. Lett.,* **194**(1-2), 53-66, doi:10.1016/S0012-821X(01) 00539-8.

Shaw, A.M., D.R. Hilton, T.P. Fischer, J.A. Walker, and G.E. Alvarado (2003), Contrasting He-C relationships in Nicaragua and Costa Rica: insights into C cycling through subduction zones, *Earth Planet. Sci. Lett.*, **214**(3-4), 499-513, doi:10.1016/S0012-821X(03)00401-1.

Shaw A. M., Hilton D. R., Fischer T. P., Walker J. A., and de Leeuw G. A. M. (2006) Helium isotope variations in mineral separates from Costa Rica and Nicaragua: Assessing crustal contributions, timescale variations and diffusion-related mechanisms. *Chem. Geol.* **230**(1-2), 124-139.

Shipley, T. H., and G. F. Moore (1986), Sediment accretion, subduction, and dewatering at the base of the trench slope off Costa Rica: A seismic reflection view of the décollement, *J. Geophys. Res.*, **91**(B2), 2019–2028.

Shipley, T. H., P. L. Stoffa, and D. F. Dean (1990), Underthrust sediments, fluid migration paths, and mud volcanoes associated with the accretionary wedge off Costa Rica: Middle America Trench, *J. Geophys. Res.*, **95**(B6), 8743–8752.

Simpson, H.J., and W.S. Broecker (1973), A new method for determining total carbonate ion concentration in saline waters, *Limnol. Oceanogr.*, **18**(3), 426-440.

Sinton, C. W., R. A. Duncan, and P. Denyer (1997), Nicoya Peninsula, Costa Rica: A single suite of Caribbean oceanic plateau magmas, *J. Geophys. Res.*, **102**(B7), 15,507–15,520.

Sleep N. H. (1996) Lateral flow of hot plume material ponded at sublithospheric depths. *Journal of J. Geophys. Res.-Sol. Ea.* **101**(B12), 28065-28083.

Smith, S.P. (1985), Noble gas solubility in water at high temperature, *Eos Trans. AGU,* **66** (18), Spring Meet. Suppl., Abstract V22B-02.

Smith W. H. F. and Sandwell D. T. (1997) Global sea floor topography from satellite altimetry and ship depth soundings. *Science* **277**(5334), 1956-1962.

Solomon, E.A., M. Kastner, H. Jannasch, G. Robertson, and Y. Weinstein (2008), Dynamic fluid flow and chemical fluxes associated with a seafloor gas hydrate deposit on the northern Gulf of Mexico slope, *Earth Planet. Sci. Lett.*, **270**(1-2), 95-105, doi:10.1016/j.epsl.2008.03.024.

Southward, A.J., E.C. Southward, P.R. Dando, G.H. Rau, H. Felbeck, and H. Flugel (1981), Bacterial symbionts and low $^{13}C/^{12}C$ Ratios in tissues of Pogonophora indicate unusual nutrition and metabolism, *Nature*, **293**(5834), 616-620, doi:10.1038/293616a0.

Spinelli, G. A., and D. M. Saffer (2004), Along-strike variations in underthrust sediment dewatering on the Nicoya margin, Costa Rica related to the updip limit of seismicity, *Geophys. Res. Lett.*, **31**, L04613, doi:10.1029/2003GL018863.

Spinelli, G.A., and M.B. Underwood (2004), Character of sediments entering the Costa Rica subduction zone: Implications for partitioning of water along the plate interface, *Island Arc*, **13**(3), 432-451, doi: 10.1111/j.1440-1738.2004.00436.x.

Stakes, D.S., D. Orange, J.B. Paduan, K.A. Salamy, and N. Maher (1999), Cold-seeps and authigenic carbonate formation in Monterey Bay, California, *Mar. Geol.*, **159**(1-4), 93-109, doi:10.1016/S0025-3227(98)00200-X.

Starkey N. A., Stuart F. M., Ellam R. M., Fitton J. G., Basu S., and Larsen L. M. (2009) Helium isotopes in early Iceland plume picrites: Constraints on the composition of high $^{3}He/^{4}He$ mantle. *Earth Planet. Sci. Lett.* **277**(1-2), 91-100.

Staudacher T. and Allègre, C. J. (1988) Recycling of oceanic crust and sediments: the noble gas subduction barrier, *Earth Planet. Sci. Lett.,* **89**(2), 173–183, doi:10.1016/0012-821X(88)90170-7.

Staudacher T., Kurz M. D., and Allègre C. J. (1986) New noble-gas data on glass samples from Loihi Seamount and Hualalai and on dunite Samples from Loihi and Réunion Island. *Chem. Geol.* **56**(3-4), 193-205.

Staudacher T., Sarda P., and Allègre C. J. (1990) Noble gas systematics of Réunion Island, Indian Ocean. *Chem. Geol.* **89**(1-2), 1-17.

Stuart F., Turner G., and Taylor R. (1994) He-Ar isotope systematics of fluid inclusions; resolving mantle and crustal contributions to hydrothermal fluids. In *Noble gas geochemistry and cosmochemistry* (ed. J. Matsuda). Terra Scientific Publishing Company, Tokyo. pp. 261-277.

Stute, M., M. Forster, H. Frischkorn, A. Serejo, J.F. Clark, P. Schlosser, W.S. Broecker, and G. Bonani (1995), Cooling of tropical Brazil (5ºC) during the Last Glacial Maximum, *Science*, **269**(5222), 379-383, doi:10.1126/science.269.5222.379..

Stute, M., T. Torgersen, G. Winkler, and P. Schlosser (2005), Helium isotope measurements on matrix fluids from the SAFOD drillcore, *Eos Trans. AGU,* **86**(52), Fall Meet. Suppl., Abstract T21A-0453.

Sugisaki, R., T. Ito, K. Nagamine, and I. Kawabe (1996), Gas geochemical changes at mineral springs associated with the 1995 southern Hyogo earthquake (M = 7.2), Japan, *Earth Planet. Sci. Lett.*, **139**(1-2), 239-249, doi:10.1016/0012-821X(96)00007-6.

Sun S. S., Tatsumoto M., and Schilling J.-G. (1975) Mantle Plume Mixing Along the Reykjanes Ridge Axis: Lead Isotopic Evidence. *Science* **190**(4210), 143-147.

Tatsumi, Y., and S. Eggins (1995), *Subduction zone magmatism*, 211 pp., Blackwell Science, Cambridge, MA, United States (USA).

Taylor R. N., Thirlwall M. F., Murton B. J., Hilton D. R., and Gee M. A. M. (1997) Isotopic constraints on the influence of the Icelandic plume. *Earth Planet. Sci. Lett.* **148**(1-2), E1-E8.

Tedesco D., Nagao K., and Scarsi P. (1998) Noble gas isotopic ratios from historical lavas and fumaroles at Mount Vesuvius (southern Italy): constraints for current and future volcanic activity, *Earth Planet. Sci. Lett.,* **164**(1-2), 61-78, doi:10.1016/S0012-821X(98)00167-8.

Thirlwall M. F. (1995) Generation of the Pb isotopic characteristics of the Iceland plume. *J. Geol. Soc.* **152**, 991-996.

Thirlwall M. F., Gee M. A. M., Taylor R. N., and Murton B. J. (2004) Mantle components in Iceland and adjacent ridges investigated using double-spike Pb isotope ratios. *Geochim. Cosmochim. Acta* **68**(2), 361-386.

Thordsen, J.J., W.C. Evans, Y.K. Kharaka, B.M. Kennedy, and M. van Soest (2005), Chemical and isotopic composition of water and gases from the SAFOD wells: Implications to the dynamics of the San Andreas Fault at Parkfield, California, *Eos Trans. AGU,* **86**(52), Fall Meet. Suppl., Abstract T23E-08.

Tolstikhin I. and Kamenski I. (1969) Determination of groundwater age by the T-^{3}He method, *Geochem. Int.* **6**(4), 810-811.

Torgersen T. and Jenkins W. J. (1982) Helium isotopes in geothermal systems: Iceland, The Geysers, Raft River and Steamboat Springs. *Geochim. Cosmochim. Acta* **46**(5), 739-748.

Torres, M.E., J.P. Barry, D.A. Hubbard, and E. Suess (2001), Reconstructing the history of fluid flow at cold seep sites from Ba/Ca ratios in vesicomyid clam shells, *Limnol. Oceanogr.*, **46**(7), 1701-1708.

Toutain, J.P., and J.C. Baubron (1999), Gas geochemistry and seismotectonics: A review, *Tectonophysics*, **304**(1-2), 1-2, doi:10.1016/S0040-1951(98)00295-9.

Trieloff M. and Kunz J. (2005) Isotope systematics of noble gases in the Earth's mantle: possible sources of primordial isotopes and implications for mantle structure, *Phys. Earth Planet. In.,* **148**(1), 13-38, doi:10.1016/j.pepi.2004.07.007.

Trieloff M., Kunz J., Clague D. A., Harrison D., and Allègre C. J. (2000) The nature of pristine noble gases in mantle plumes, *Science* **288**(5468), 1036-1038, doi: 10.1126/ science.288.5468.1036.

Trieloff M., Kunz J., and Allègre C. J. (2002) Noble gas systematics of the Réunion mantle plume source and the origin of primordial noble gases in Earth's mantle, *Earth Planet. Sci. Lett.,* **200**(3-4), 297-313, doi:10.1016/S0012-821X(02)00639-8.

Trieloff M., Falter M., and Jessberger E. K. (2003) The distribution of mantle and atmospheric argon in oceanic basalt glasses. *Geochim. Cosmochim. Acta* **67**(6), 1229-1245.

Trull, T.W., M.R. Perfit, and M.D. Kurz (1990), He and Sr isotopic constraints on subduction contributions to Woodlark Basin volcanism, Solomon Islands, *Geochim. Cosmochim. Acta*, **54***(2)*, 441-453, doi:10.1016/0016-7037(90)90332-F.

Tryggvason K., Husebye E. S., and Stefansson R. (1983) Seismic image of the hypothesized Icelandic hot spot. *Tectonophysics* **100**(1-3), 97-118.

Tryon, M., K. Brown, L. Dorman, and A. Sauter (2001), A new benthic aqueous flux meter for very low to moderate discharge rates, *Deep Sea Res. Part I,* **48**(9), 2121-2146, doi:10.1016/S0967-0637(01)00002-4.

Tryon, M., D.R. Hilton, K. Brown, G. Wheat, G.M. McMurtry, W. Brueckmann, H. Niemann, A.L. LaBonte, E. Füri, U. Schacht, and R. Hansman (2006), Observations at forearc carbonate mounds offshore Costa Rica, *Eos Trans. AGU*, **87**(52), Fall Meet. Suppl. Abstract V41B-1714.

Tryon, M., C.G. Wheat, and D.R. Hilton (2009), Fluid sources and pathways of the Costa Rica erosional convergent margin, submitted to *Geochem. Geophys. Geosyst*., doi:10.1029/2009GC002818.

Tryon, M. D., and K. M. Brown (2001), Complex flow patterns through Hydrate Ridge and their impact on seep biota, *Geophys. Res. Lett.*, **28**(14), 2863–2866.

Tryon, M.D., K.M. Brown, and M.E. Torres (2002), Fluid and chemical flux in and out of sediments hosting methane hydrate deposits on Hydrate Ridge, OR, II: Hydrological processes, *Earth Planet. Sci. Lett.*, **201**(3-4), 541-557, doi:10.1016/S0012-821X(02) 00732-X.

Tryon, M.D., K.M. Brown, M.E. Torres, A.M. Trehu, J. McManus, and R.W. Collier (1999), Measurements of transience and downward fluid flow near episodic methane gas vents, Hydrate Ridge, Cascadia, *Geology*, **27**(12), 1075-1078, doi:10.1130/0091-7613(1999)027<1075:MOTADF>2.3.CO;2.

Umeda, K., G. F. McCrank, and A. Ninomiya (2007), Helium isotopes as geochemical indicators of a serpentinized fore-arc mantle wedge, *J. Geophys. Res.*, **112**, B10206, doi:10.1029/2007JB005031.

Umeda, K., Y. Ogawa, K. Asamori, and T. Oikawa (2006), Aqueous fluids derived from a subducting slab: Observed high ^{3}He emanation and conductive anomaly in a non-volcanic region, Kii Peninsula southwest Japan, *J. Volcanol. Geoth. Res.*, **149**(1-2), 47-61, doi:10.1016/j.jvolgeores.2005.06.005.

Valbracht P. J., Honda M., Matsumoto T., Mattielli N., McDougall I., Ragettli R., and Weis D. (1996) Helium, neon and argon isotope systematics in Kerguelen ultramafic xenoliths: implications for mantle source signatures. *Earth Planet. Sci. Lett* **138**(1-4), 29-38.

Valbracht P. J., Staudacher T., Malahoff A., and Allègre C. J. (1997) Noble gas systematics of deep rift zone glasses from Loihi Seamount, Hawaii. *Earth Planet. Sci. Lett* **150**(3-4), 399-411.

van der Hilst R. D., Widiyantoro S., and Engdahl E. R. (1997) Evidence for deep mantle circulation from global tomography, *Nature,* **386**, 578-584, doi:10.1038/386578a0.

van Keken P. E. and Ballentine C. J. (1998) Whole-mantle versus layered mantle convection and the role of a high-viscosity lower mantle in terrestrial volatile evolution, *Earth Planet. Sci. Lett.*, **156**(1-2), 19-32, doi:10.1016/S0012-821X(98)00023-5.

van Keken P. E., Hauri E. H., and Ballentine C. J. (2002) Mantle mixing: The generation, preservation, and destruction of chemical heterogeneity. *Ann. Rev. Earth Pl. Sci.* **30**, 493-525.

Vannucchi, P., and H. Tobin (2000), Deformation structures and implications for fluid flow at the Costa Rica convergent margin, ODP Sites 1040 and 1043, Leg 170, *J. Struct. Geol.*, **22**(8), 1087-1103, doi:10.1016/S0191-8141(00)00027-4.

Vlastélic I., Lewin E., and Staudacher T. (2006) Th/U and other geochemical evidence for the Réunion plume sampling a less differentiated mantle domain. *Earth Planet. Sci. Lett.* **248**(1-2), 379-393.

von Huene, R., C.R. Ranero, W. Weinrebe, and K. Hinz (2000), Quaternary convergent margin tectonics of Costa Rica, segmentation of the Cocos Plate, and Central American volcanism, *Tectonics*, **19**(2), 314-334, doi:10.1029/1999TC001143.

Watson E. B., Thomas J. B., and Cherniak D. J. (2007) ^{40}Ar retention in the terrestrial planets, *Nature,* **449**(7160), 299-304, doi:10.1038/nature06144.

Weiss, R.F. (1971), Solubility of helium and neon in water and seawater, *J. Chem. Eng. Data*, **16**(2), 235-241, doi:10.1021/je60049a019

Wetherill G. W. (1954) Variations in the Isotopic Abundances of Neon and Argon Extracted from Radioactive Minerals. *Phys. Rev.* **96**(3), 679-683.

White W. M., Cheatham M. M., Duncan R. A. (1990) Isotope geochemistry of Leg 115 basalts and inferences on the history of the Réunion mantle plume. In *Proc. Ocean Drill. Prog., Sci. Results,* **115** (eds. R.A. Duncan, J. Backman, R.B. Dunbar and L.C. Peterson). pp 53-61.

Whiticar, M.J. (1999), Carbon and hydrogen isotope systematics of bacterial formation and oxidation of methane, *Chem. Geol.*, **161**(1-3), 291-314, doi:10.1016/S0009-2541(99)00092-3.

Wiersberg, T., and J. Erzinger (2007), A helium isotope cross-section study through the San Andreas Fault at seismogenic depths, *Geochem. Geophys. Geosyst.*, **8**, Q01002, doi:10.1029/2006GC001388.

Wolfe C. J., Bjarnason I. T., VanDecar J. C., and Solomon S. C. (1997) Seismic structure of the Iceland mantle plume. *Nature* **385**(6613), 245-247.

Yatsevich I. and Honda M. (1997) Production of nucleogenic neon in the Earth from natural radioactive decay. *J. Geophys. Res.-Sol. Ea.* **102**(B5), 10291-10298.

Yokochi R. and Marty B. (2004) A determination of the neon isotopic composition of the deep mantle. *Earth Planet. Sci. Lett* **146**(1-2), 3-34.

Zhao D. P. (2004) Global tomographic images of mantle plumes and subducting slabs: insight into deep Earth dynamics. *Phys. Earth Planet. In.* **146**(1-2), 3-34.

Zimmer, M. M., T. P. Fischer, D. R. Hilton, G. E. Alvarado, Z. D. Sharp, and J. A. Walker (2004), Nitrogen systematics and gas fluxes of subduction zones: Insights from Costa Rica arc volatiles, *Geochem. Geophys. Geosyst.*, **5**, Q05J11, doi:10.1029/2003GC000651.

Zindler A. and Hart S. (1986) Chemical Geodynamics. *Ann. Rev. Earth Planet. Sci.* **14**, 493-571.

Zoback, M., S. Hickman, and W. Ellensworth (2006), Structure and properties of the San Andreas fault in central California: preliminary results from the SAFOD experiment, *Geophys. Res. Abstr.*, **8**, Abstract 02474.